Computational Study of Linear and Nonlinear Optical Properties of Single Molecules and Clusters of Organic Electro-Optic Chromophores

Kerry Garrett

A dissertation
submitted in partial fulfillment of the
requirements for the degree of

Doctor of Philosophy

University of Washington

2015

Reading Committee:

Larry Dalton, Chair

Xiaosong Li

Rob Synovec

Program Authorized to Offer Degree:
Chemistry

University of Washington

Abstract

Computational Study of Linear and Nonlinear Optical Properties
of Single Molecules and Clusters
of Organic Electro-Optic Chromophores

Kerry Garrett

Chair of the Supervisory Committee:
Professor Larry Dalton
Department of Chemistry

Organic electro-optic (OEO) materials integrated into silicon-organic hybrid (SOH) devices afford significant improvements in size, weight, power, and bandwidth (SWAP) performance of integrated electronic/photonic systems critical for current and next generation telecommunication, computer, sensor, transportation, and defense technologies. Improvement in molecular first hyperpolarizability, and in turn electro-optic activity, is crucial to further improvement in the performance of SOH devices. The timely preparation of new chromophores with improved molecular first hyperpolarizability requires theoretical guidance; however, common density functional theory (DFT) methods often perform poorly for optical properties in systems with substantial intramolecular charge transfer character. The first part of this dissertation describes the careful evaluation of popular long-range correction (LC) and range-separated hybrid (RSH) density functional theory (DFT) for definition of structure/function relationships crucial for the optimization of molecular first hyperpolarizability, β. In particular, a benchmark set of well-characterized OEO chromophores is used to compare calculated results with the corresponding experimentally measured linear and nonlinear optical properties; respectively, the wavelength of the peak one-photon absorption energy, λ_{max}, and β. A goal of this work is to systematically determine the amount of exact exchange in LC/RSH-DFT methods required for accurately computing these properties for

a variety OEO chromophores. High-level electron correlation (post-Hartree-Fock) methods are also investigated and compared with DFT. Included are results for the computation of β using second-order Møller-Plesset perturbation theory (MP2) and the double-hybrid method, B2PLYP. The second part of this work transitions from single-molecule studies to computing bulk electronic and nonlinear optical properties of molecular crystals and isotropic ensembles of a high-β chromophore, YLD124. Of particular interest are phenomena such as aggregation and the effect of intermolecular interactions on EO activity.

TABLE OF CONTENTS

LIST OF FIGURES

LIST OF TABLES

GLOSSARY

ωB97 ('wB97'): tunable LR exchange-correlation functional developed by Head-Gordon and coworkers

ωB97xD ('wB97xD'): tunable SR and LR exchange-correlation functional with empirical atom-atom dispersion correction developed by Head-Gordon and coworkers

-D: denotes dispersion correction when added to a DFT method, e.g. wB97x-D

B2PLYP-D: Dispersion corrected form of B2PLYP

B2PLYP: Combination of correlation energy functionals of B3LYP and second-order Møller-Plesset Perturbation

B3LYP: hybrid DFT functional using three-parameter Becke exchange with Lee-Yang-Parr correlation functional

BLA: bond-length alternation

BLYP: pure DFT method using Becke 88 exchange functional and Lee-Yang-Parr correlation functional

BODIPY: boron dipyrrin- acceptor group

CAM-B3LYP: Coulomb-attentuated (long-range corrected) method to B3LYP, developed by Handy and coworkers

CCD: charge-coupled device, commonly used for digital imaging of spectroscopic events (i.e., converts incoming photons into electron charges that are translated into digital output)

$CHCl_3$: chloroform

CLD: D-π-A system with polyene bridge

CPHF: coupled-perturbed Hartree-Fock

CPKS: coupled-perturbed Kohn-Sham

CT: charge transfer

D/A: Donor/Acceptor, usually in the context of molecular orbital overlap

DAAP: (diarylamino)phenyl- donor moiety

DFT: density functional theory

EO: Electro-optic

FTC: D-π-A system with thienylenevinylene bridge

HF: Hartree-Fock theory

HOMO: highest occupied molecular orbital

HRS: hyper-Rayleigh scattering

KS: Kohn-Sham

LC-ωPBE ('LC-wPBE'): long-range correction to PBE functional, developed by Vydrov and coworkers

LC-BLYP: Long-range correction to BLYP, developed by Tawada and coworkers

LR: 'long-range' in the context of long-range interactions; 'linear response' in the context of LR-TDDFT equations

LUMO: lowest unoccupied molecular orbital

M062X: variation on Minnesota functional 2006, developed by Truhlar and coworkers

MO: molecular orbital

MP2: Second-order Møller-Plesset Perturbation

NLO: Non-linear optical

Nd:YAG: neodymium-doped yttrium aluminium garnet; a crystal that is used as a lasing medium for solid-state lasers

OEO: organic electro-optic

PCM: polarizable continuum method

PMMA: poly-(methyl)-methacrylate

SCRF: self-consistent reaction field

SHG: second-harmonic generation

SIE: self-interaction error

SOH: silicon-organic hybrid device

SR: short-range

TBDMSO: tert-butyl dimethyl silyl protecting group

TCF: tricyanofuran acceptor moiety

TCP: tricyanopyrrole acceptor moiety

TD: time-dependent

TLM: two-level model

UV-vis: Ultra-Violet/visible

WFT: wavefunction theory

XC: exchange-correlation

ACKNOWLEDGMENTS

I would like to thank my Ph.D. advisor, Prof. Larry Dalton. I first met Larry in Eugene, OR where he was being awarded the 2011 Linus Pauling Award. Larry's dedication to science is truly inspiring. In addition to his years of accomplishments, he is also very personable and humble. Larry has generously helped me through pivotal changes in my graduate school experience. It has been a wonderful privilege to work with such an accomplished person who also possesses such a kind and magnanimous spirit.

I would also like to thank all of the members of my Ph.D. committee: Professors Munira Khalil, Xiaosong Li, Rob Synovec, and Eli Shlizerman. Prof. Khalil has served as a committee member on all of my graduate exams over the years and has always made me feel at ease during the stressful closed door sessions. Prof. Li has a great eye for detail and has also helped me understand the greater impact of my research. Prof. Synovec has been vital to my education. He has shown me a lot of generosity and support over the years. Finally, I am so glad to have Prof. Shlizerman on my committee. He is excellent teacher who taught me many useful coding skills that I have put to use in this work. His scientific computing class was a blast!

I would like to thank all of the members of the Dalton, Isborn (of UC Merced), Robinson, Li, and Reid groups who have all played an important part in my education. I give special thanks to Dr. Delwin Elder. I feel incredibly blessed to have shared my time in graduate school with Delwin as my mentor who has been a positive light for me and all of us in the group. He selflessly dedicates countless hours of his time to others and his presence makes an enormous difference to us all.

I would also love to thank the wonderful undergraduate researchers I've worked with

over the years: Graham, Shawn, Phoebe, and Brian. I learned a lot from all of them and being around their enthusiasm and energy helped remind me why I came to graduate school.

Finally, I would also like to thank all of the wonderful staff of the UW chemistry department: Jim Earnshaw, Paul Miller, Richard Ketcham, Lon Buck, Jerry Chan, Diana Knight, Ashley Zigler, Marianne Cavelti, and many others. They keep things running smoothly for all of us. Thank you all!

DEDICATION

To my family, fellow students and mentors.

Chapter 1

INTRODUCTION

1.1 Overview

Modern telecommunications relies on the speed by which large amounts of digital information can be delivered; hence, materials with large bandwidths that can transmit signals with low loss or interference are crucial [104]. Electro-optic (EO) materials meet these criteria while offering stability and processability at a low cost [44], [52]. The key requirement of an EO device is that it contains nonlinear optical (NLO) materials capable of manipulating photonic signals upon application of an electromagnetic field, thus generating an altered field with respect to its frequency, phase, or other physical property. This phenomena is known as the *electro-optic effect* [23]. Inorganic nonlinear optical (NLO) materials such as lithium niobate, $LiNbO_3$, have been traditionally used for the manipulation of photonic signals due mainly to their high damage threshold and optical transparency at telecommunication wavelengths [254], [159], [101], [165]. Such inorganic materials, however, also have limited NLO response and require high driving voltages to achieve optimal performance. In contrast, a number of organic electro-optic (OEO) materials have been shown to offer a much higher EO activity than their inorganic counterparts, as well as a myriad of other favorable properties, including fast response time and ease of structural modification to suit various applications [55], [57], [19], [49], [50]. The integration of OEO materials into silicon photonic waveguide devices (silicon-organic hybrid, SOH, technology) has led to state-of-the-art defining bandwidth, drive voltage, power efficiency, and device size [197], [64], [184], [141], [242], [185], [4], [149]. Success has also been achieved using OEO polymeric materials for a variety of photonics applications, including next generation optical data-transmission, computing and imaging and sensing [56], [120], [54], [20], [136], [93], [214], [204], [205], [72]. The challenge

remains in minimizing optical loss associated with these organic materials [58], [12]. Current interdisciplinary research in organic electro-optics is focused on overcoming this challenge, with a combination of theoretical, synthetic, and spectroscopic methods [79], [117], [115], [13]. By utilizing a variety of cutting-edge technologies, it is possible that losses observed in the organic EO device may be overcome by enhancing the EO activity of the organic NLO material.

An objective of this dissertation is determining the accuracy and reliability of computed electronic and optical properties of OEO systems with comparison to measurement. When theory is expected to not match measured data precisely, as when comparing gas phase calculations to heterogeneous solution-phase media for example, or when measured data is not available, the focus instead turns to identifying trends in the computed properties. The computational method most used in this dissertation is density functional theory (DFT) due to its favorable accuracy-to-cost ratio.

The first half of this work focuses on investigating the accuracy of DFT methods for predicting linear and nonlinear optical properties of specific OEO materials of interest. Specifically, properties such as electronic transition energies and static and dynamic first hyperpolarizability are related to modifications in the structure of these OEO materials. Computational methods of particular interest are long-range corrected (LC) DFT methods and electron-correlated wavefunction methods, in particular second-order Møller-Plesset Perturbation Theory (MP2). The combination of DFT and MP2 will be examined using a double-hybrid method, B2PLYP. The computational methods investigated herein are compared to experimental measurement. The second part of this work discusses the transition from single-molecule studies to computing bulk properties of both ordered and disordered molecular systems. Of particular interest are phenomena such as aggregation and the effect of molecular ordering on EO activity. Trends in simulated absorbance spectra and hyperpolarizabilities of monomers, dimers, and trimers of OEO systems are studied.

A brief background of nonlinear optics and the electro-optic effect is described in the following sections of this chapter. Electronic structure methods used in this dissertation,

including Hartree-Fock (HF) theory, MP2, and DFT, are also briefly introduced.

1.2 Second-order Nonlinear Optical Materials

In most forms of spectroscopy, the goal is to measure the optical response of a material when it undergoes radiation [71]. This radiation is characterized by an oscillating electric field which, when applied to a sample, generates a set of induced dipoles in the sample, thereby, giving rise to a macroscopic frequency-dependent polarization, P [23]. In the case of linear optics, whereby the intensity of incident light is relatively weak, the polarization depends linearly on the electric field strength, E, such that

$$P_i^{\omega} = \chi_i^{(0)} + \chi_{ij}^{(1)}(\omega;\omega)E^{\omega}, \tag{1.1}$$

where the coefficient, $\chi^{(1)}$, is known as the *linear susceptibility* and is related to the medium's index of refraction, η, and henceforth, its dielectric properties, all of which are frequency-dependent. Here, the summation over common indices (with $i, j, k = 1, 2, 3$) applies to the Einstein convention [68], [139].

In the case of linear optics, the light may still be delayed or deflected, but the frequency of light being absorbed by the sample is the same as that being emitted. This is not the case when the intensity of light is significant, such as with high-intensity lasers [211]. In this case, the associated field is strong enough to distort the molecular structure and force constants of the *medium*, which can produce nonlinear optical (NLO) effects by changing the frequency of light emitted, as illustrated in the case of second-harmonic generation (SHG) [23] in Figure 1.1. It is important to note that nonlinearity is a property of the medium by which light passes through, not of the light itself. As an example, organic electro-optic materials consist of many optically active molecular units, known as *chromophores*. The nonlinear optical activity in OEO materials is a result of the extended π-electron conjugation of the chromophore, in which the delocalized electron density may be polarized easily in response to an applied electric field. Since it is a nonlinear optical material, the polarization has a nonlinear dependence with respect to the applied electric field, which can be physically

observed by the output of frequencies that are distinctly different than that of the incident light [233]. These NLO effects can be treated as a weak perturbation on top of the linear response; thus, can be modeled by re-writing the polarization as a power series expansion about E as follows

$$P_i^{\omega} = \chi_i^{(0)} + \chi_{ij}^{(1)}(\omega;\omega)E_j^{\omega} + \chi_{ijk}^{(2)}(\omega;\omega_1,\omega_2)E_j^{\omega_1}E_k^{\omega_2} + \chi_{ijkl}^{(3)}(\omega;\omega_1,\omega_2,\omega_3)E_j^{\omega_1}E_k^{\omega_2}E_l^{\omega_3} + \ldots, \quad (1.2)$$

where $\chi^{(2)}(\omega;\omega_1,\omega_2)$ and $\chi^{(3)}(\omega;\omega_1,\omega_2,\omega_3)$ are the second- and third-order nonlinear optical susceptibilities, respectively, and are ranked with respect to the linear susceptibility and each other such that $\chi^{(1)} >> \chi^{(2)} >> \chi^{(3)} >> \ldots$, etc.

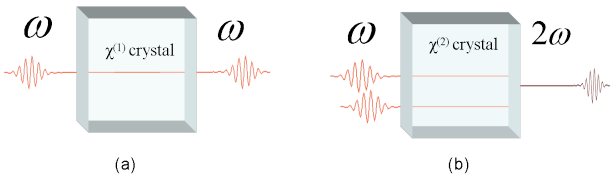

Figure 1.1: **Geometric interpretation of linear and nonlinear optical processes.** (a) linear optical process in which there is one incident field, characterized by a frequency ω, which remains unchanged after passing through the linear optical medium; (b) an example of a nonlinear optical process: second harmonic generation (SHG), in which there are multiple fields being applied to the sample which, in-phase, will constructively add up at the $\chi^{(2)}$ crystals exit face to form a third wave with output frequency, 2ω.

The above equations describe solutions in the bulk phase; the analogous equations which describe the polarization of the electron density in response to an applied external field for a single molecule can be written as

$$p_i^{\omega} = \mu_i^{(0)} + \alpha_{ij}(\omega;\omega)E_j^{\omega} + \beta_{ijk}(\omega;\omega_1,\omega_2)E_j^{\omega_1}E_k^{\omega_2} + \gamma_{ijkl}(\omega;\omega_1,\omega_2,\omega_3)E_j^{\omega_1}E_k^{\omega_2}E_l^{\omega_3} + \ldots, \quad (1.3)$$

where $\mu_i^{(0)}$ is the permanent ground state dipole moment and α_{ij} is the linear polarizability, and β_{ijk} and γ_{ijkl} denote the molecular first and second hyperpolarizabilities, respectively.

The physical properties of a material will dictate the order of nonlinear optical response;

of these physical properties, molecular symmetry is of chief importance. Unlike odd-order susceptibility terms, a nonzero $\chi^{(2)}_{ijk}$ requires a bulk system with net asymmetry. On the single-molecule level, this requires that a molecule be intrinsically noncentrosymmetric (i.e., has no center of inversion) and, thus, have a non-zero first hyperpolarizability, β [46]. By definition, the first hyperpolarizability, β, is the ease to which a molecule can be asymmetrically polarized in response to an applied electric field. When excited by an oscillating electric field of light, the electrons along the length of conjugated chain interact, showing a preferential shift from one direction relative to the other. In the case of a bulk material that is constructed from many molecularly asymmetric chromophores, the need for overall noncentrosymmetry imposes the *additional* requirement of molecular alignment in order to achieve a finite macroscopic second-order nonlinear optical activity. Figure 1.2 shows different examples of ensemble ordering in organic NLO materials supplemented by illustrations of ordering in dipolar spheroids similar to illustrations in Refs [194] and [116].

Efforts to optimize β in OEO materials have inspired a variety of different chromophore designs over the past several decades [131], [12] [3], [13]. Since the 1970s, second-order NLO chromophores have been developed based on the donor-π-acceptor (D-π-A) structure model, in which a conjugated π-electron bridge is unsymmetrically capped on one end with an electron-donating group and on the other by an electron-accepting group, so to impart an electronic bias while still in the ground state, as shown in Figure 1.3 [168]. Research into optimizing the β response of these dipolar chromophores relies on tuning of the electron density distribution through chemical modification of the D-π-A constituents [60], [112], [38], [29], [39], [73]. In practice, one of the most successful acceptor moieties is tricyanofuran (TCF), commonly linked through a π-conjugated thienylenevinylene (FTC-type) or polyene (CLD-type) bridge to a substituted aniline donor, as shown in Figure 1.4 [5].

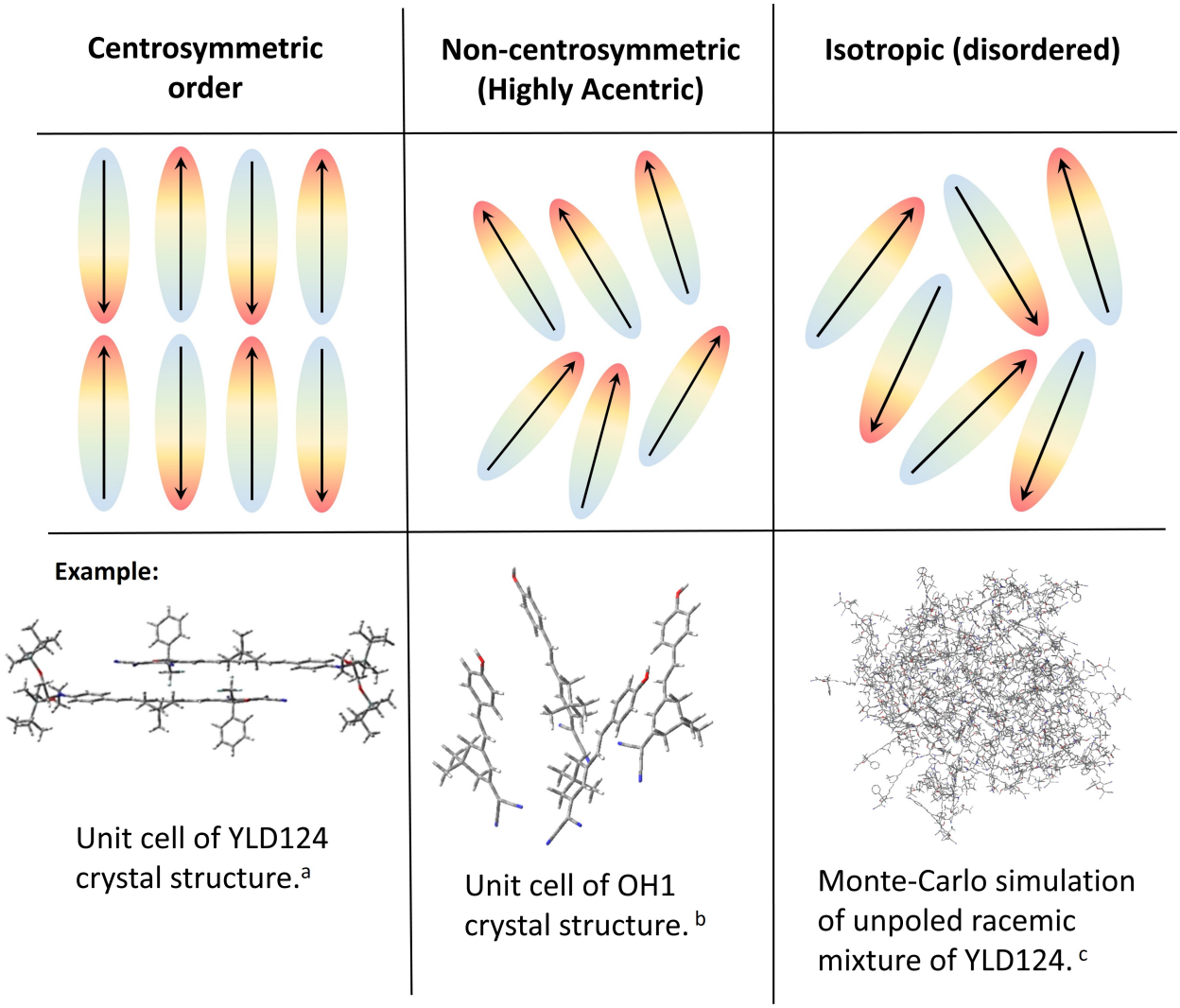

Figure 1.2: **Different Types of Ensemble Order in Molecular D-π-A materials.** (Left:) Centrosymmetric order (no acentric) is observed in crystals of YLD124 ([a] Ref [122]); whereas, (Center:) non-centrosymmetric (highly acentric) behavior has been shown to occur in crystals for some small dipolar chromophores, such as OH1 ([b] Refs [41], [160]). (Right:) Unpoled polymer thin films containing highly dipolar chromophores, like YLD124, are generally isotropic (disordered) ([c] Ref [232]).

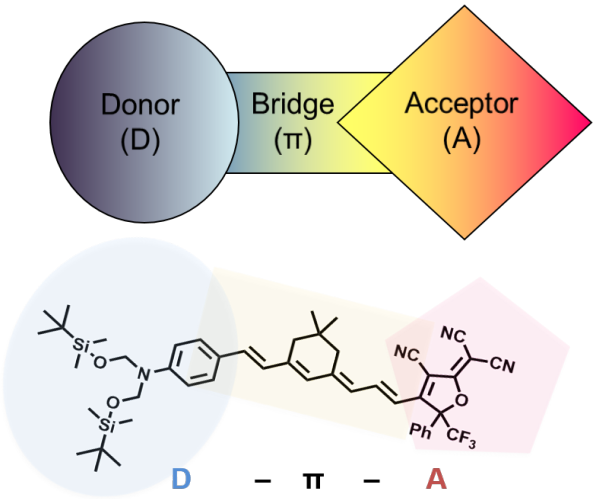

Figure 1.3: **Donor-π-Acceptor (D-π-A) motif** A π-conjugated bridge connects an electron-donating (D) group with an electron-withdrawing (or accepting, A) group on either end of the chromophore.

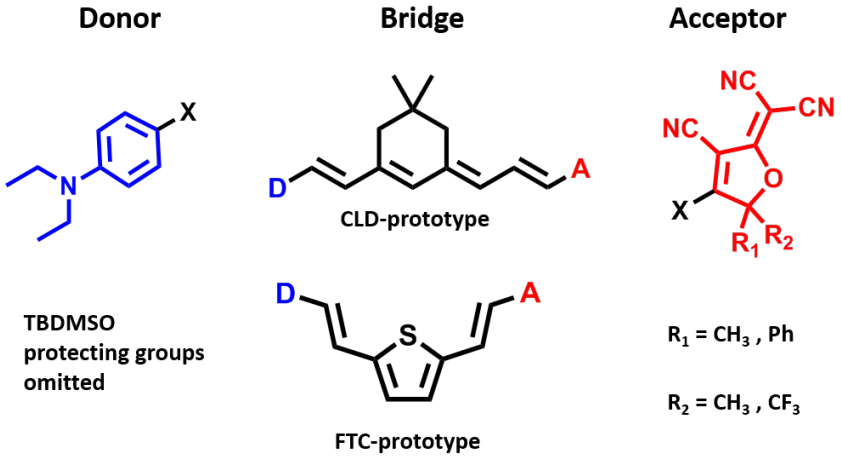

Figure 1.4: **Common successful D-π-A motifs.** The combination of tricyanofuran (TCF) acceptor with a thienylenevinylene (FTC-type) or polyene (CLD-type) bridge has resulted in numerous high-β chromohpores.

As a general rule, stronger electron density donors and acceptors and increased conjugated bridge length lead to larger β [50]. This phenomenon may be rationalized by considering a two-state theoretical approximation developed by Oudar and Chemla [183] for the dependence of the principal nonresonant hyperpolarizability tensor element (oriented along the dipolar axis) on the contributions from frontier orbitals. This 'two-level model' (TLM) approximation can be expressed as

$$\beta(\omega_3;\omega_1,\omega_2) = \frac{\omega_{eg}^2(3\omega_{eg}^2+\omega_1\omega_2-\omega_3^2)|\mu_{ge}|^2\Delta\mu_{ge}}{\hbar^2(\omega_{ge}^2-\omega_1^2)(\omega_{ge}^2-\omega_2^2)(\omega_{ge}^2-\omega_3^2)}, \tag{1.4}$$

where μ_{ge} and $\hbar\omega_{eg} = \Delta E_{ge}$ are the dipole matrix element and transition energy, respectively, between the ground state (g) and the first strongly allowed charge-transfer excited state (e); $\mu_{ge} = \langle g|\mu_z|e\rangle$ is also called the *transition dipole moment*. The dipolar nature of these compounds is signified by the term, $\Delta\mu_{ge} = (\mu_{z,e} - \mu_{z,g})$, which accounts for the electrons preferential shift upon excitation. Given the direct dependence on this term, this model implies that second-order nonlinear optical response relies heavily on the relative magnitudes of the excited-state, μ_{ee} and ground- state μ_{gg} dipole moments. Additonally, the quadratic dependence on the transition dipole moment, μ_{ge}, implies that the second-order nonlinear optical response may also be enhanced by increasing the "allowedness" or charge-transfer corresponding to this transition. The outgoing frequency "ω_3" is the frequency obtained by mixing of the incident frequencies ω_1 and ω_2 with energy conserved, $\omega_3 = \omega_1 + \omega_2$ [47]. For the linear electro-optic (Pockels) effect, $\omega_3 = -\omega$, $\omega_1 = \omega$, and $\omega_2 = 0$, such that the two-state approximation of β is [156], [117],

$$\beta(-\omega;\omega,0) = \frac{\omega_{eg}^2(3\omega_{eg}^2-\omega^2)|\mu_{ge}|^2\Delta\mu_{ge}}{\hbar^2(\omega_{ge}^2-\omega^2)(\omega_{ge}^2)(\omega_{ge}^2-\omega^2)} = \frac{(3\omega_{eg}^2-\omega^2)|\mu_{ge}|^2\Delta\mu_{ge}}{\hbar^2(\omega_{ge}^2-\omega^2)^2} \tag{1.5}$$

The frequency dependence can be separated into a product of static hyperpolarizability, $\beta(0)$, and a dispersion factor, $g(\omega)$:

$$\beta(-\omega;\omega,0) = g(\omega)\beta(0),$$

where the static hyperpolarizability and dispersion correction are, respectively,

$$\beta(0) = \frac{3|\mu_{ge}|^2 \Delta\mu_{ge}}{\hbar^2 \omega_{ge}^2},$$
$$g(\omega) = \frac{3\omega_{eg}^2 - \omega^2)}{3(\omega_{ge}^2 - \omega^2)^2} \tag{1.6}$$

Another special case for second-harmonic generation can be derived from Equation 1.4, in which $\omega_3 = 2\omega_1 = 2\omega_2 = 2\omega$, then

$$\beta(2\omega; \omega, \omega) = \frac{3\omega_{eg}^2 |\mu_{ge}|^2 \Delta\mu_{ge}}{\hbar^2(\omega_{ge}^2 - \omega^2)(\omega_{ge}^2 - 4\omega^2)} \tag{1.7}$$

and here the dispersion factor, $g(\omega)$, becomes:

$$g(\omega) = \frac{\omega_{eg}^4}{(\omega_{ge}^2 - \omega^2)(\omega_{ge}^2 - 4\omega^2)} \tag{1.8}$$

Each of these dispersion corrections are particularly useful for comparing theory to measurement (see Chapter 2 for more details).

1.3 The Linear Electro-optic (Pockels) Effect

The linear electro-optic (i.e., Pockels) effect is the control or modulation of the refractive index of a second-order NLO material by application of a low-frequency (dc $\sim$ 10 THz) electric field [1]. Mathematically, this effect can be described by expanding the refractive index, η, as a power series in the strength of the components of the applied field, E [23], [252], [234]:

$$\eta_i = \eta_i^{(0)} - \frac{1}{2} r_{ijk} \eta_i^3 E_k - \frac{1}{2} K_{ijkl} \eta_i^3 E_{kl} + \ldots, \tag{1.9}$$

[1]The dc field is low-frequency with respect to the optical field $\sim 2 \times 10^{14}$ Hz.

where r_{ijk} is the Pockels effect tensor and K_{ijkl} is the Kerr (quadratic electr-optic) effect tensor. Focusing on non-centrosymmetric materials in which the Pockels effect is dominant, we may truncate to first-order as follows:

$$\Delta\eta = \eta_i - \eta_i^{(0)} = -\frac{1}{2} r_{ijk} \eta_i^3 E_k \tag{1.10}$$

The refractive index of the material changes linearly with the applied electric field. The linear electro-optic effect is relevant to noncentrosymmetric materials because the linear electro-optic coefficient, r_{ijk}, is linearly proportional to the second-order susceptibility, $\chi^{(2)}_{ijk}$, [50], [12]

$$r_{ijk} = -\frac{2}{\eta_i^2 \eta_j^2} \chi^{(2)}_{ijk}, \tag{1.11}$$

where the frequency-dependence is consistent with the linear electro-optic effect.

1.3.1 Electro-optic Modulators

The Pockels effect is important for applications which involve electrical-to-optical signal transduction. A change in refractive index affects the speed of light passing through the material, thus a beam of light passing through will undergo a phase shift that is proportional to the distance traveled through the material. Devices known as electro-optic modulators (EOMs) are designed to make use of this effect [198], [126]. One of the simplest EO modulator designs is the Mach-Zehnder device [51], [188], [162], [154], shown in Figure 1.5, in which an incoming optical signal is split into two paths: one unaltered signal and the other which travels through an EO material embedded between a pair of electrodes. A voltage is applied to the electrodes which induces a change in refractive index of the EO material. In turn, this causes a phase shift in the light passing through the material. After traveling through the electrodes, the perturbed signal is recombined with the unaltered signal, thus interference occurs that results in either an increase in the overall wave amplitude or cancellation. This result may be interpreted as a binary output of either “1” or “0”, respectively. Destructive

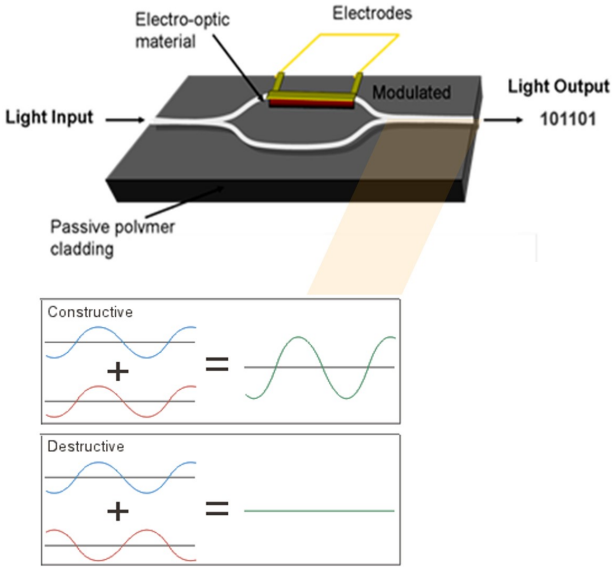

Figure 1.5: **Schematic representation of a Mach-Zehnder device.** The Mach-Zehnder device is a type of EO modulator that can be used for electrical-to-optical signal transduction. Such a device could take an electrical signal from a computer and produce superfast data transfer via optical signals.

interference results only if the voltage is sufficient to shift the phase of the modulated light by π radians. This voltage is known as the *half-wave voltage*, V_π, given by [12]

$$V_\pi = \frac{\lambda d}{2(\eta^3 r)_{eff} L}, \tag{1.12}$$

where $(\eta^3 r)_{eff}$ is the effective electro-optic coefficient, d is the distance between electrodes, L is the sample thickness, and λ is the wavelength of the light. Drive voltage, device size, and EO coefficient of the material are all commonly used as figures of merit for EO devices. Smaller device size and lower drive voltage make for a better device, thus, by improving the EO coefficient, device size and/or drive voltage can be reduced.

1.3.2 Electric-field Poling

The application of an electric field is, for many OEO applications, meant to induce order in intrinsically disordered systems, such as a polymer thin film doped with an electro-optic

dye [56]. Due to the highly dipolar nature of many OEO chromophores, they tend to exhibit limited ferroelectric ordering at a high density [116], [55]. In order to overcome these dipolar interactions, a strong[2] dc field can be applied to OEO polymeric materials in a method known as emphelectric-field poling [50]. In the case of *contact* poling, the film is first heated near its glass transition temperature (T_g) to increase the mobility of the chromophores. While in this mobile state, a voltage is applied to electrodes at both ends of the film, thereby subjecting the chromophores to a strong electric field. The chromophores align with the field and are then frozen in position by cooling the film [213], [73]. A schematic of electric-field poling is shown in Figure 1.6. In this illustration, the molecule rotates to align to a poling (z) axis, where θ is the angle between the molecular dipole, $\vec{\mu}$, and the poling field, $\vec{E}$ [19].

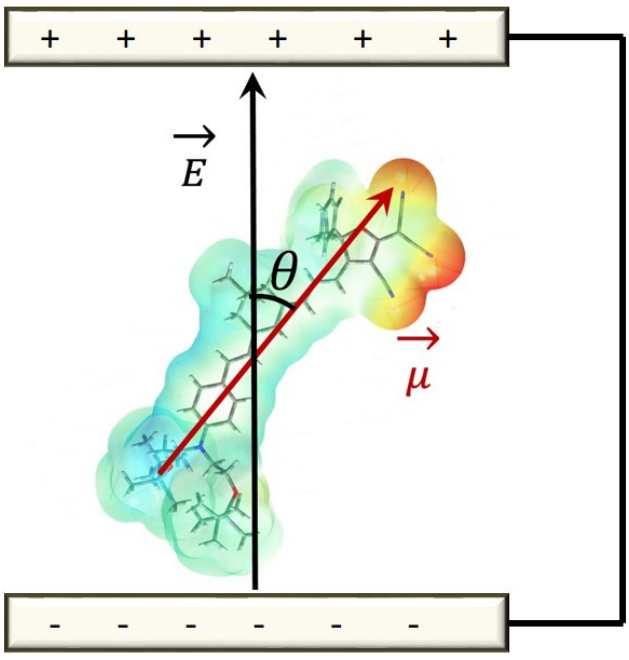

Figure 1.6: **Electric-field poling of a dipolar electro-optic chromophore.** The molecule rotates to align to a poling (z) axis, where θ is the angle between the molecular dipole, $\vec{\mu}$, and the poling field, $\vec{E}$. This schematic was inspired by a similar illustration in Ref [116].

[2]Reported as high as 10^6 V/cm, according to Ref [25].

1.4 Connection between Macroscopic and Microscopic Second-order Nonlinear Optical Response

It is important to connect this macroscopic NLO property to the microscopic NLO response of the material's constituent molecules, namely the first hyperpolarizability, β. Understanding the behavior on the molecular level helps in enhancing the EO response of the bulk material which is necessary for improving EO devices. For this purpose, it is convenient to examine the tensor elements that are coincident with the molecular symmetry axis (laboratory z-axis) such that one can relate the principle element of the nonlinear susceptibility tensor, $\chi^{(2)}_{zzz}$, to the molecular parameters by [50]

$$\chi^{(2)}_{zzz} = N\beta_{zzz}\langle cos^3(\theta)\rangle g(\omega) \tag{1.13}$$

where N (molecules/cm^3) denotes the number density of active molecules that interact with the incident optical field, β_{zzz} is the hyperpolarizability tensor element along the symmetry axis and is dependent on the frequency of the incident light field. The $\langle cos^3(\theta)\rangle$ term denotes the average molecular acentric order parameter denoting the extent of chromophore alignment relative to the laboratory z axis. The quantity $g(\omega)$ is the Lorentz-Onsager local field factor. The z laboratory axis is parallel to the applied poling field (in electric field poled materials), as well as the field vectors of the optical and electrical operating fields in the case of an electro-optic device.

Mathematical connections between molecular and macroscopic second-order NLO properties were derived in the 1970s and 1980s regarding different types of organic materials. The first model came from Chemla and others in 1975 [36] called the *oriented gas model* which was developed for organic crystals. According to this model, molecular interactions are completely neglected and the first hyperpolarizabilities (β) of the molecules are added up while accounting for different molecular orientations to give the macroscopic second-order susceptibility. In 1983, Shen and others developed an expression similar to Equation 1.13 for molecular orientation of of monolayer adsorbates by second-harmonic generation (SHG) [94]. Singer and others extended this analysis to liquid crystals and poled polymer films [47],

[213]. For these models, the effect of intermolecular interactions on β, hence also on $\chi^{(2)}_{zzz}$, is either completely overlooked or treated insufficiently by local field factors [18]. Improved models which account for intermolecular interactions, H-bonding, and other effects occurring within the bulk material are necessary to accurately describe the macroscopic NLO response [247], [88], [212]. This is a topic of active research and is discussed further in Chapter 4.

As noted in Equation 1.11, the linear electro-optic coefficient, r_{ijk}, is linearly proportional to the second-order susceptibility, $\chi^{(2)}_{ijk}$, thus it can be related to β using Equation 1.13. Upon application of a low-frequency (dc) field, the dominant elements of the Pockels effect tensor are r_{333} and r_{133}. As a simplification, r_{ijk}, is symmetric in its first two indices and can be expressed in contracted notation, r_{ik}; thus, $r_{333} = r_{33}$ and $r_{133} = r_{13}$. Furthermore, due to symmetry, $r_{33} = 3r_{13}$, thus it is sufficient to study just one of these quantities. The relationship between r_{33} in the direction of the applied field along with χ_{zzz} is given by

$$r_{33} = \left| \frac{2\chi^{(2)}_{zzz}}{\eta^4} \right|, \tag{1.14}$$

where η is the refractive index of the material. It follows, based on the relationship between $\chi^{(2)}$ and β that

$$r_{33} = \left| \frac{2N\beta_{zzz}\langle cos^3(\theta)\rangle g(\omega)}{\eta^4} \right|. \tag{1.15}$$

This EO coefficient[3] is a figure-of-merit for EO materials and is measured in units of pm/V.

In summary, the above equations demonstrate the three most important factors in the optimization of $\chi^{(2)}_{zzz}$ and, consequently, r_{33}: the chromophore number density (N), molecular first hyperpolarizability (β), and the acentric order parameter; all of which must be optimized simultaneously. Much recent progress has been made by guiding the improvement of materials to yield larger molecular hyperpolarizabilities and loading parameters, $N\langle cos^3(\theta)\rangle$ [115], [221], [48], [158], [52].

---

[3]From now on, the term 'linear' will be implied since this work focuses solely on materials in which the Pockels effect dominates.

1.5 Characterization of Second-Order NLO Materials

The electro-optic coefficient of a material can be characterized using Attenuated Total Reflection (ATR) and Teng-Man (Simple Reflection) methods [173], [62], [37], [230], [92]. For molecular properties of interest, the linear electro-optic effect hyperpolarizability, $\beta_{zzz}(-\omega;\omega,0)$, cannot be directly measured [117], however, the second-harmonic hyperpolarizability, $\beta_{HRS}(-2\omega;\omega,\omega)$, can be measured with hyper-Rayleigh scattering (HRS) [43], [13], [50]. An approximate conversion between β_{HRS} and β_{zzz} was determined by Cyvin and Decius [46], as

$$\beta_{HRS} \approx \sqrt{\frac{6}{35}}\beta_{zzz},$$

where β_{zzz} is roughly 42% of the orientationally averaged β_{HRS} because β_{zzz} is largest component in the hyperpolarizability tensor. For this reason, calculated hyperpolarizabilities are often compared to measured $\beta_{HRS}(-2\omega;\omega,\omega)$ values [117], [79]. This comparison is the main topic of Chapter 2.

1.6 Calculation of Molecular Hyperpolarizabilities

The Stark energy, W, describes the evolution of the total electronic energy of a system of particles in the presence of an applied electric field, E. The molecular polarizability and hyperpolarizabilities derived from a power series expansion of W in terms of E are given by [227]

$$W(E) = W_0 + \mu_i E_i + \alpha_{ij} E_i E_j + \beta_{ijk} E_i E_j E_k + \gamma_{ijkl} E_i E_j E_k E_l + \ldots, \tag{1.16}$$

where the summation over common indices (with $i, j, k = 1, 2, 3$) is implied. Quantum-mechanical (QM) algorithms use the Hellman-Feynman theorem [13], from which the dipole moment can be expressed as a partial derivative of electronic energy with respect to the applied field:

$$\mu_i = -\left.\frac{\partial W(E)}{\partial E_i}\right|_{E=0} \tag{1.17}$$

Higher derivatives can be similarly expressed and is implied that each derivative is evaluated at zero field strength (E=0), as follows:

$$\alpha_{ij} = -\frac{\partial^2 W(E)}{\partial E_i \partial E_j} = \frac{\partial \mu_i}{\partial E_j}, \tag{1.18}$$

$$\beta_{ijk} = -\frac{\partial^3 W(E)}{\partial E_i \partial E_j \partial E_k} = \frac{\partial^2 \mu_i}{\partial E_j \partial E_k}, \tag{1.19}$$

and

$$\gamma_{ijkl} = -\frac{\partial^4 W(E)}{\partial E_i \partial E_j \partial E_k \partial E_l} = \frac{\partial^3 \mu_i}{\partial E_j \partial E_k \partial E_l}, \tag{1.20}$$

and so on. Thus, theoretically evaluating α, β, or γ for a system of particles requires differentiation of the total electronic energy or dipole moment, μ, either numerically using the finite-field method (FFM) [105] or analytically using the coupled-perturbed Hartree Fock (CPHF) method [172], [171], [152].

1.7 Electronic Structure Theory

1.7.1 The Schrödinger equation

The main problem underlying quantum mechanics is to solve the Schrödinger equation [191], [155]

$$H\Psi = E\Psi \tag{1.21}$$

where H is the time-independent hamiltonian operating on the normalized square-integrable wavefunction, Ψ. The wavefunction describes all of the properties of the physical system in question. Term by term, the hamiltonian can be broken up into the following [6]:

$$H = T_e + T_n + V_{ee} + V_{en} + V_{nn}, \tag{1.22}$$

in which the electronic and nuclear terms are denoted by subscripts e and n, respectively. In more detail, H is a sum of kinetic energy terms

$$T_e = -\frac{1}{2}\sum_i^N \nabla_i^2 \text{ and } T_n = -\frac{1}{2}\sum_n^M \frac{\nabla_n^2}{m_n},$$

and potential energy terms

$$V_{ee} = \sum_{i<j}^N \frac{1}{r_{ij}},\ V_{en} = -\sum_i^N \sum_A^M \frac{Z_A}{r_{in}}, \text{ and } V_{nn} = \sum_{A<B}^M \frac{Z_A Z_B}{r_{AB}}$$

for each the electron-electron, electron-nuclear, and nuclear-nuclear interactions, respectively. There is no known analytical solution to this many-body problem, hence, one must apply a series of approximations to achieve a tractable result.

Note that without applying any simplifications to the hamiltonian, the resulting molecular wavefunction will be a function of the coordinates of both the electrons and nuclei of the system. The first simplification is to rewrite the hamiltonian such that it and its resulting solutions are only functions of the electronic coordinates. This is known as the Born-Oppenheimer approximation [22], [114], in which the slow-moving nuclei are considered stationary point charges such that all of the nuclear terms of the hamiltonian are constants. In effect, this reduces the hamiltonian to its electronic form

$$\begin{aligned} H \approx H_{el} &= \sum_{i=1}^N \left(-\frac{1}{2}\nabla_i^2 - \sum_{A=1}^M \frac{Z_A}{r_{iA}} \right) + \sum_{i=1}^N \sum_{j>i}^N \frac{1}{r_{ij}} \\ &= \sum_{i=1}^N h_i + \sum_{i=1}^N \sum_{j>i}^N \frac{1}{r_{ij}} + V_{nn} \end{aligned} \tag{1.23}$$

Here we add the nuclear repulsion operator, V_{nn}, as a constant (assuming a stationary geometry) to H_{el} to give the total energy. H_{el} can be solved exactly for hydrogenic systems. In order to solve H_{el} for systems containing many electrons, further simplifications are necessary. While fixing the nuclear configuration of the system is easier to solve than the complete molecular hamiltonian, it is still not possible to calculate the electronic orbitals and energies *exactly* for nontrivial systems. Hence, to solve for a molecular system containing many electrons, the Hartree-Fock (HF) method [89] is commonly used for this purpose.

1.7.2 Hartree-Fock (HF) Equations

In general, the HF method gives an approximate solution of the electronic Schrodinger equation using the hamiltonian H_{el}, as obtained from the Born-Oppenheimer approximation, and builds on this by further stipulating that the trial wavefunction Ψ be chosen as a *single* Slater determinant, i.e. an antisymmetric product, of mutually orthonormal one-electron states [227]. Neglecting relativistic effects allows us to describe the electron spin as consisting of two possible states, either aligned opposite (β) or along (α) with the magnetic field. Thus, the one-electron wavefunctions, $\chi_n(x)$, each consist of the product of a *spatial* orbital $\psi(r)$ depending on the position of the electron and a restricted set of *spin* orbitals $\alpha(\omega)$ or $\beta(\omega)$ depending only on the spin of the electron:

$$\chi_n(\vec{x}) = \psi(r) \begin{cases} \alpha(\omega) \\ \beta(\omega) \end{cases}$$

With this convention, the trial determinantal wavefunction may be written as:

$$\Psi(\vec{x}_1, \vec{x}_2, ..., \vec{x}_N) = \frac{1}{\sqrt{N!}} \begin{vmatrix} \chi_1(\vec{x}_1) & \chi_2(\vec{x}_1) & \dots & \chi_N(\vec{x}_1) \\ \chi_1(\vec{x}_2) & \chi_2(\vec{x}_2) & \dots & \chi_N(\vec{x}_2) \\ \vdots & \vdots & & \vdots \\ \chi_1(\vec{x}_N) & \chi_2(\vec{x}_N) & \dots & \chi_N(\vec{x}_N) \end{vmatrix} \tag{1.24}$$

(1.25)

The one-electron wavefunctions $\chi_n(x)$ are then determined by minimizing the functional, ε, for the energy expectation value:

$$\varepsilon[\Psi] = \frac{\left\langle \Psi | \hat{H} | \Psi \right\rangle}{\langle \Psi | \Psi \rangle},$$

according to the variational principle, which states that the minimum energy obtained by this method will always be greater than the true energy, E_0, of the ground state hamiltonian such that $\varepsilon \geq E_0$. In fact, $\varepsilon = E_0$ if and only if Ψ is exactly equal to the wave function of the ground state of the studied system; which is never the case, given the inherent assumptions

of this method. The HF energy will always be greater than the true energy.

The Hartree-Fock equations results from determining the total energy of the system, $E = \langle\Psi|\,\hat{H}\,|\Psi\rangle$ (based on a normalized wavefunction), by using the single Slater determinant as the trial wavefunction. To solve for E, first recognize the separate "one-electron" and "two-electron" terms of the electronic Hamiltonian. From Equation 1.7.1, the electronic hamiltonian, H_{el}, is already separated into a *one-electron operator* $\mathbf{h}_i = -\frac{1}{2}\nabla_i^2 - \sum_{A=1}^{M}\frac{Z_A}{r_{iA}}$ (of the i-th electron) and a *two-electron operator* $\frac{1}{r_{ij}}$ (involving electrons i and j). The one-electron operator, $\mathbf{h}_i$, describes the kinetic and potential energy of the i-th electron in the field of the nuclei. It is commonly referred to as the "core-Hamiltonian", H_i^{core}; henceforth, we will use this notation to clearly distinguish the operator $\mathbf{h}_i$ from the value h_i. The total energy is then

$$\langle\Psi|\,\hat{H}\,|\Psi\rangle = \sum_{i=1}^{N} H_i^{core} + \frac{1}{2}\sum_{i=1}^{N}\sum_{j=1}^{N}(J_{ij} - K_{ij}) + V_{nn}, \tag{1.26}$$

where $H_i^{core} = -\frac{1}{2}\nabla_i^2 - \sum_{A=1}^{M}\frac{Z_A}{r_{iA}}$ is the one electron operator, as previously defined, and J and K are the two-electron parts known as the Coulomb and Exchange operators, respectively. The *Coulomb* term accounts for electron-electron repulsion between i, j pairs and is explicitly defined as [114]

$$\mathbf{J}_i|\chi_j(\vec{x}_2)\rangle = \langle\chi_i(\vec{x}_1)|\frac{1}{r_{ij}}|\chi_i(\vec{x}_1)\rangle|\chi_j(\vec{x}_2)\rangle, \tag{1.27}$$

and the non-classical *exchange* term is given as,

$$\mathbf{K}_i|\chi_j(\vec{x}_2)\rangle = \langle\chi_i(\vec{x}_1)|\frac{1}{r_{ij}}|\chi_j(\vec{x}_1)\rangle|\chi_i(\vec{x}_2)\rangle, \tag{1.28}$$

originates from antisymmetrization of the trial wavefunction. (The minus sign on the exchange term in Equation 1.32 comes from antisymmetrization). **J** and **K** appear very similar, however, look closer and see that $|\chi_j(\vec{x}_2)\rangle$ is multiplied on both sides of Equation 1.7.2 describing **J**; whereas, $|\chi_j(\vec{x}_2)\rangle$ and $|\chi_i(\vec{x}_2)\rangle$ are "exchanged" in Equation 1.28 for **K**.

As a result of variational calculus, one can show that finding the one-electron wavefunctions that correspond with the lowest total energy the system, according to the variational

principle, is equivalent to solving the eigenfunction equation:

$$\hat{F}\chi_i = \varepsilon_i \chi_i, \tag{1.29}$$

where F is known as the *Fock* operator and is given by

$$\hat{F}_i = H_i^{core} + \sum_j^N (\mathbf{J}_j - \mathbf{K}_j), \tag{1.30}$$

The Fock operator is a one-electron operator meaning that it takes each i^{th} electron in the system and describes its kinetic energy and its attraction to all of the nuclei (in H_i^{core}), as well as its repulsion to the sum of all the other electrons (in an effective potential, $\nu^{HF} = \sum_j^N (\mathbf{J}_j - \mathbf{K}_j)$). Therefore, the orbital energies may be solved using

$$\varepsilon_i = \langle \chi_i | \hat{F}_i | \chi_i \rangle = h_i + \sum_j^N (J_{ij} - K_{ij}), \tag{1.31}$$

thus giving rewriting the total energy of the system in terms of the orbital energies gives:

$$E = \sum_{i=1}^N \varepsilon_i - \frac{1}{2} \sum_{i=1}^N \sum_{j=1}^N (J_{ij} - K_{ij}) + V_{nn} \tag{1.32}$$

These equations, having the form of a one-electron Schrödinger equation, are the *Hartree-Fock equations* that characterize the optimal (lowest-energy) one-electron wavefunctions to be used in the Slater determinant. One must note a few things about these equations, however. They appear deceptively simple, given that $\hat{F}$ has a similar form as the electronic hamiltonian (Equation 1.7.1). But, upon close inspection, one notices that $\hat{F}$ depends on the wavefunctions of all of the electrons! Thus, the Fock operator couples the N equations, and makes Equation 1.29 a nonlinear Schödinger equation. To solve the eigenfunction equation requires iterative methods.

Solving the Hartree-Fock Equations

1.7.3 Basis Sets

In order to solve the Hartree-fock equations, it is necessary to first guess the initial form of the wavefunctions, use them in the two-electron integrals, and continue this cycle until

convergence of the energies and wavefunctions is obtained. In order to solve a many-electron system numerically, it is useful to introduce a set of known spatial *basis functions* such that the differential Hartree-Fock equations can be reformulated as a system of algebraic equations to be solved iteratively by standard techniques.

Take $\{\phi_m\}$ to represent a set of basis functions for the space of square integrable functions where our solution lives (i.e., Hilbert space). In this example, we will think of these basis functions as atomic orbitals centered at each of the nuclei. Then one can approximate the i-th spatial wavefunction by a linear combination of such Q basis functions :

$$\psi_i(r) = \sum_{m=1}^{Q} C_{mi}\phi_m(r) \tag{1.33}$$

The above expression is not exact since it does not completely sum over all terms which fully describe the space. For simplicity, it is common practice to use deficient basis sets, just as long as one chooses these functions carefully to describe the physics of the problem appropriately.

1.7.4 Roothaan's Equations

To obtain the HF equations in matrix form [130], one begins by expanding $\psi_m(\vec{r}_1)$ in the chosen basis,

$$F(\vec{r}_1)\sum_m C_{mi}\phi_m(\vec{r}_1) = \epsilon_i \sum_m C_{mi}\phi_m(\vec{r}_1) \tag{1.34}$$

and then multiplying from the left by $\phi_p^*(\vec{r}_1)$ and integrating over the whole equation, to obtain:

$$\sum_m \left\{ \int d\vec{r}_1 \phi_p^*(\vec{r}_1) f(\vec{r}_1)\phi_m(\vec{r}_1) \right\} C_{mi} = \epsilon_i \sum_m \left\{ \int d\vec{r}_1 \phi_p^*(\vec{r}_1)\phi_m(\vec{r}_1) \right\} C_{mi} \tag{1.35}$$

This results in the left-side integral, called the *Fock* matrix $F_{pm} = \int d\vec{r}_1 \phi_p^*(\vec{r}_1) f(\vec{r}_1)\phi_m(\vec{r}_1)$, and the right-side, the *overlap* matrix, $S_{pm} = \int d\vec{r}_1 \phi_p^*(\vec{r}_1)\phi_m(\vec{r}_1)$. Then Equation 1.35 sim-

plifies to just,

$$\sum_m F_{pm} C_{mi} = \epsilon_i \sum_m S_{pm} C_{mi}. \tag{1.36}$$

This result is known as the system of *Roothaan equations*:

$$FC = SC\epsilon \tag{1.37}$$

Here, the matrix ϵ is diagonal and contains the energies, ϵ_i, of each of i-th element. Furthermore, C is the $Q \times Q$ *coefficient* matrix whose n-th column denotes the expansion coefficients of ψ_n in the basis set $\{\phi_m\}$. For example, the first column of C contains the coefficients which describe ψ_1, the second column for ψ_2, and so on. Hence, solving for the coefficient matrix C that solves the Roothaan equation is equivalent to solving for the optimal molecular orbitals that go into the Slater determinant to solve for the wavefunction, ψ.

In order to solve Equation 1.37, it is first necessary to obtain an explicit expression for the Fock Matrix, F, and for this purpose, we must rewrite it in terms of the density matrix, P:

$$P_{pm} = 2 \sum_i^{N/2} C_{pi} C_{mi}^* \tag{1.38}$$

such that if we rewrite the two-electron operator as

$$(ij|kl) = \int \int \phi_i^*(x_1) \phi_j(x_1) \frac{1}{r_{12}} \phi_k^*(x_2) \phi_l(x_2) dx_1^3 dx_2^3 \tag{1.39}$$

then the Fock matrix may be written as the following:

$$F_{pm} = \int d\vec{r}_1 \phi_p^*(1) f(1) \phi_m(1) \tag{1.40}$$

$$= \int d\vec{r}_1 \phi_p^*(1) h(1) \phi_m(1) + \sum_a^{N/2} \int d\vec{r}_1 \phi_p^*(1) [2J_a(1) - K_a(1)] \phi_m(1) \tag{1.41}$$

$$= H_{pm}^{core} + \sum_{kl} P_{kl} [(pm|kl) - \frac{1}{2}(pk|lm)] \tag{1.42}$$

$$= H_{pm}^{core} + G_{pm} \tag{1.43}$$

where G_{pm} represents the two-electron part of the Fock matrix.

Now that the Fock matrix has been reformulated to depend on the density matrix, one may step back from these equations and analyze how the Hartree-Fock method will proceed:

- The first step of the procedure is to guess a density matrix, P, thereby guessing the charge density, $\rho(r)$, which describes the positions of the electrons.

- This charge density is then used to calculate an *effective* one-electron potential $\nu^{HF}(r_1)$, according to the expression of the closed-shell Fock operator.

- Thus, one obtains an effective one-electron hamiltonian, i.e., Fock operator, such that we can determine the set of states, ψ_i, describing the electron in the presence of the effective potential.

This process is repeated until $\nu^{HF}(r_1)$ remains constant. In other words, convergence is reached once the effective electrostatic field that produced a given charge density is identical to the field that would be calculated from that charge density. This process is commonly known as the *self-consistent field* (SCF) method.

1.7.5 Møller-Plesset Perturbation Theory

Despite being a relatively simple and inexpensive approach to solving the electronic Schrödinger equation, a major shortcoming of Hartree-Fock (HF) theory is that it fundamentally lacks electron correlation (with exception of *Fermi correlation*, which is upheld by the HF exchange integral). When treated with HF, each electron of the system responds to a net repulsion energy that describes all other electrons in the system (shown in Equations 1.30 and 1.31). The use of a single Slater determinant means that the spatial distribution of all $N-1$ other electrons is described only be a set of orbitals. This method captures the big picture, but invites error by allowing individual electrons to approach each other more closely than would

be allowed if their motion was correlated. Adding in electron correlation is a small correction to the HF energy, however, plays a significant role in the accurate determination of many molecular properties.

If we assume that the HF wavefunction and energy are close to the real answer, then perturbation theory can be used to add in a small correction to get closer to the true electronic Schrödinger equation. Thus, we can generate a hamiltonian which accounts for both HF and a perturbative correction, $\mathbf{H} = \mathbf{H}^{HF} + \lambda\mathbf{V}$ where $\mathbf{H}^{HF}$ is the unperturbed operator that is the sum of Fock operators,

$$\mathbf{H}^{HF} = \sum_{i=1}^{N} \mathbf{F}_i = \sum_{i=1}^{N} [H_i^{core} + \sum_{j}^{N} (\mathbf{J}_j - \mathbf{K}_j)], \tag{1.44}$$

and V is the a perturbation operator with dimensionless ordering parameter λ. This ordering parameter will eventually be set to unity, but for now it provides a convenient way to improve $\mathbf{H}^{HF}$ by getting closer to the energies and wavefunctions that describe $\mathbf{H}$. This approach to adding correlation to HF is known as Møller-Plesset (MP) perturbation theory [175], [114]. Henceforth, the $\mathbf{H}^{HF}$ will be denoted H_0 to denote the zeroth order component consistent with perturbation theory. It follows that the exact wavefunctions and energies are expanded in a Taylor series in λ [71]

$$\mathscr{E}_i = E_i^{(0)} + \lambda E_i^{(1)} + \lambda^2 E_i^{(2)} + ... \tag{1.45}$$

where $E_i^{(n)}$ is the n^{th} order energy, and

$$|\Psi_i\rangle = |\Psi_i^{(0)}\rangle + \lambda|\Psi_i^{(1)}\rangle + \lambda^2|\Psi_i^{(2)}\rangle + ... \tag{1.46}$$

We want to express the n^{th} order quantities in terms of the zeroth-order energies and matrix elements of the perturbed operator, V, with unperturbed wavefunctions, such that $\langle\Psi_i^{(0)}|V|\Psi_j^{(0)}\rangle$. Therefore, following intermediate normalization [227], substituting these expansions into $H\Psi_i = \mathscr{E}_i\Psi_i$ gives the zeroth order expression for HF,

$$H_0|\Psi_i^{(0)}\rangle = E_i^{(0)}|\Psi_i^{(0)}\rangle \tag{1.47}$$

where $\Psi_i^{(0)}$ is the HF determinant and $E_i^{(0)}$ is a sum of molecular orbital energies,

$$E_i^{(0)} = \langle \Psi_i^{(0)} | H_0 | \Psi_i^{(0)} \rangle = \langle \Psi_i^{(0)} | \sum_{i=1}^{N} \mathbf{F}_i | \Psi_i^{(0)} \rangle = \sum_{i=1}^{N} \varepsilon_i \tag{1.48}$$

and higher order terms which include the perturbation,

$$H_0|\Psi_i^{(1)}\rangle + V|\Psi_i^{(0)}\rangle = E_i^{(0)}|\Psi_i^{(1)}\rangle + E_i^{(1)}|\Psi_i^{(0)}\rangle,$$
$$H_0|\Psi_i^{(2)}\rangle + V|\Psi_i^{(1)}\rangle = E_i^{(0)}|\Psi_i^{(2)}\rangle + E_i^{(1)}|\Psi_i^{(1)}\rangle + E_i^{(2)}|\Psi_i^{(0)}\rangle \tag{1.49}$$

and so on.

Multiplying each of these higher order equations by $\langle \Psi_i^{(0)}|$ and using orthogonality ($\langle \Psi_i^{(0)} | \Psi_i^{(n)} \rangle = 0$) gives the following n^{th} order energies, where $n = 0$ was already shown above,

$$E_i^{(1)} = \langle \Psi_i^{(0)} | V | \Psi_i^{(0)} \rangle \tag{1.50}$$

$$E_i^{(2)} = \langle \Psi_i^{(0)} | V | \Psi_i^{(1)} \rangle \tag{1.51}$$

The first-order energy correction accounts for the double-counting of the electron-electron repulsion in the zeroth-order term. Thus, the sum of the zero and first-order Møller Plesset energies is exactly the HF energy, comparing with Equation 1.32:

$$E^{HF} = E^{(0)} + E^{(1)} = \langle \Psi_i^{(0)} | H_0 | \Psi_i^{(0)} \rangle + \langle \Psi_i^{(0)} | V | \Psi_i^{(0)} \rangle = \langle \Psi_i^{(0)} | H_0 + V | \Psi_i^{(0)} \rangle \tag{1.52}$$

For this reason, the first-order perturbation correction called "MP1" is simply equivalent to HF. Electron correlation energy is not encountered until second-order, called "MP2". The second-order correction energy involves a sum over doubly excited determinants,

$$E^{(2)} = \sum \sum_{i<j}^{occ} \sum \sum_{a<b}^{unocc} \frac{[(ij||ab)]^2}{(\epsilon_a + \epsilon_b - \epsilon_i - \epsilon_j)} \tag{1.53}$$

where ϵ_i and ϵ_j are energies of occupied molecular orbitals, and ϵ_a and ϵ_b are energies of unoccupied molecular orbitals. The integrals $(ij||ab) = \langle \phi_i \phi_j | \phi_a \phi_b \rangle - \langle \phi_i \phi_j | \phi_b \phi_a \rangle$ over filled (i and j) and empty (a and b) MOs account for changes in electron-electron interactions as a result of electron promotion. The integrals $(ij||ab)$ are related to the basis functions by

$$\langle \phi_i \phi_j | \phi_a \phi_b \rangle = \sum_{\mu} \sum_{\nu} \sum_{\lambda} \sum_{\sigma}^{basis functions} c_{\mu i} c_{\nu j} c_{\lambda a} c_{\sigma b} (\mu\nu|\lambda\sigma) \tag{1.54}$$

where $(\mu\nu|\lambda\sigma)$ are the two electron integrals that are given by

$$(\mu\nu|\lambda\sigma) = \langle\phi_\mu(1)\phi_\nu(1)|\frac{1}{r_{12}}|\phi_\lambda(2)\phi_\sigma(2)\rangle \tag{1.55}$$

It is important to note that MPn method is not variational, so the MPn energy can be less than the true energy, typically depending on the order of perturbation correction. Ideally, odd-ordered methods are systematically above the true energy whereas even-ordered methods are below, eventually converging to the true value at high orders [114].

1.7.6 Density Functional Theory

We thus far have considered two solutions to the Schrødinger equation: Hartree-Fock theory and a correlated wavefunction method, Møller -Plesset perturbation theory. Now we consider an entirely different approach based on the charge density, $\rho(\vec{r})$. The electronic wavefunction is of 4N variables (3N spatial and N spin); whereas, $\rho(\vec{r})$ can be described locally by 3 coordinates, r_x, r_y, r_z. A common misconception is that all DFT methods are based on only these 3 coordinates, thereby reducing the cost significantly. However, the most common implementation of DFT comes from Kohn-Sham (KS) theory which introduce orbitals into DFT in order to describe the kinetic energy in a manner analogous to HF (after all, what is the kinetic energy of an electron cloud?). In fact, KS-DFT takes identical formulas for the kinetic, electron-nuclear, and electron-electron repulsion energies from HF [114]. Therefore, similar to HF, KS-DFT depends on 3N spatial variables. However, unlike HF, KS-DFT is based on formulating an exact solution for an idealized many-body problem (the uniform electron gas), thus providing a solution for electron correlation. Therefore, KS-DFT presents a correlated method that is an improvement over HF [137] and also has significantly lower computational cost (scales like $\mathscr{O}(N^3)$) than correlated wavefunction methods such as MP2 ($\mathscr{O}(N^5)$), configuration interaction (CI), and coupled-cluster methods (CCSD$\sim \mathscr{O}(N^3)$).

The entire field of DFT methods owes to the Hohenberg-Kohn (H-K) theorems from their paper published in 1964 [99]. The first is an existence theorem, which states that there is a unique relationship between the electronic density, $\rho(\vec{r})$ and the external potential, $V_{ext}(\vec{r})$

and, in turn, since $V_{ext}(\vec{r})$ fixes $H = T + V_{en} + V_{ee}$, any ground state property is a unique functional of the ground state density. Specifically, this enables one to find the total ground state energy by the minimization of the charge density functional $E[\rho]$,

$$E[\rho] = V_{en}[\rho] + T[\rho] + V_{ee}[\rho] \tag{1.56}$$

where V_{en} describes the electron-nuclear interaction, T is the kinetic energy of the electrons, and V_{ee} is the Coulombic electron-electron repulsion. Thus, the exact ground state energy exists provided that the exact ground state density can be found. To help in this search of the true g.s. energy is the second H-K theorem, which proves that the energy obtained from a trial density,

$$\rho_{trial} = N \int |\Psi(\vec{r}_1, \vec{r}_2, ..., \vec{r}_N)|^2 d_\omega d\vec{r}_1 d\vec{r}_2 ... d\vec{r}_N, \tag{1.57}$$

where N is the number of electrons and d_ω is integrable over spin variable of electron 1, is an upper bound to the true ground state energy, such that

$$E[\rho_{trial}] \geq E[\rho_0],$$

where ρ_0 is the exact ground state density, and ρ_{trial} is varied until E is minimal using the constraint that $\int \rho[\vec{r}] d\vec{r} = N_{elec}$. Thus the problem is solved using the electronic density, $\rho = |\Psi|^2$ instead of using the wavefunction directly, $\Psi(\vec{r}_1, \vec{r}_2, ..., \vec{r}_N)$.

The main problems with using the density are that the functional, $E[\rho]$, is proven to exist but is unknown, and that the kinetic energy, $T[\rho]$, and exchange energy, $E_x[\rho]$, are also unknown. Kohn-Sham (KS) DFT provides a solution to these problems. KS-DFT works by separating $E[\rho]$ into a simple large part of known variables and a small complicated part of unknowns. To do so requires constructing a fictitious reference system of non-interacting electrons which is constructed to have the same electron density as the system of interest, thus $\rho_{ref} = \rho_0$. By using an external potential V_{ext} that models the interacting system, the actual forms of the electron correlation and difference between the kinetic energy of the fictitious reference system and the interacting system can be determined. It is not straightforward to compute the kinetic energy operator from the density. For this reason, Kohn-Sham

theory borrows from HF theory by using a Slater determinant to get the kinetic energy of the non-interacting reference system,

$$T_{ref}[\rho_{ref}] = -\frac{1}{2}\sum_{i}^{N}\langle\chi_i|\nabla_i^2|\chi_i\rangle, \tag{1.58}$$

where χ_i is the i^{th} Kohn-Sham orbital and $\rho_{ref} = \sum_{i=1}^{N}\sum_{\omega}|\chi_i(\vec{r},\omega)|^2$. Then the charge density functional of the real system is written as

$$E[\rho] = T_{ref}[\rho] + V_{ne}[\rho] + J[\rho] + V_{nn}[\rho] + E_{xc}[\rho], \tag{1.59}$$

where the first four terms are known quantities, explicitly defined the kinetic energy of the reference system (Equation 1.58), the Coulombic interaction between an electron cloud and the nucleus,

$$V_{en}[\rho] = \sum_{A=1}^{M}\sum_{i=1}^{N} Z_A\langle\rho_i|\frac{1}{|r_1 - R_A|}|\rho_i\rangle \tag{1.60}$$

and the repulsion of electrons within the cloud,

$$J[\rho] = \frac{1}{2}\sum_{i=1}^{N}\sum_{j=1}^{N}\langle\rho_i\rho_j|\frac{1}{|r_1 - r_2|}|\rho_i\rho_j\rangle \tag{1.61}$$

and the nuclear repulsion given by a constant,

$$V_{nn}[\rho] = \sum_{A=1}^{M}\sum_{B=1}^{M}\frac{Z_A Z_B}{|R_A - R_B|} \tag{1.62}$$

All of the unknown terms are swept into the exchange-correlation functional, $E_{xc}[\rho]$. This term is known as a "catch-all" because it has to correct for the other terms from Equations 1.58 and 1.61. It corrects for kinetic correlation which is slower on average than the non-interacting system and it also corrects for the lack of electron correlation in the V_{ee} term, thereby partially removing self-interaction error (SIE). Thus, the exchange-correlation term is given by,

$$E_{xc}[\rho] = (T[\rho] - T_{ref}[\rho]) + (V_{ee}[\rho] - J[\rho]) \tag{1.63}$$

The main difficulty in all of this is that $E[\rho]$ is unknown. Thus, the second HK theorem is applied in which the approximated energy is minimized in a variational way. The Lagrange method yields a set of one-electron KS equations which have to be solved iteratively:

$$h^{KS}\chi_i^{KS} = \epsilon_i^{KS}\chi_i^{KS}.$$

Similar to the Fock equations of HF theory, the KS hamiltonian is given by

$$h^{KS}(r_1) = -\frac{1}{2}\nabla_1^2 - \sum_A \frac{Z_A}{|r_1 - R_A|} + \int \frac{\rho(\vec{r_2})}{|r_1 - r_2|} d\vec{r_2} + \nu_{xc}(r_1) \tag{1.64}$$

where $\nu_{xc}(r_1) = \frac{\partial E_{xc}}{\partial \rho}$ is the exchange correlation potential and a functional derivative of E_{xc}. The major difference between Equation 1.64 and Equation 1.30, is the "effective potential", V_{eff}, which in HF theory is $\sum_{j=1}^{N}(\mathbf{J}_j - \mathbf{K}_j)$, but in KS-DFT is $V_{KS}(r_1) = \int \frac{\rho(\vec{r_2})}{|r_1 - r_2|} d\vec{r_2} + \nu_{xc}(r_1)$. Similar to the summary provided in Ref. [179], the properties of KS-DFT and HF based methods are given in Table 1.1.

The promise of KS-DFT is that by determining the exact form of the exchange-correlation energy E_{xc}, the solution of the Kohn-Sham equations can then generate the true ground state energy of the total Hamiltonian of the Schrödinger equation! Thus, while HF theory offers only an approximate solution at best, the Kohn-Sham approach is in principle exact. The catch is that the exact form of E_{xc} is unknown, so much of DFT is in the art of finding the best functional form for this energy given a particular molecular system. For this purpose, a jungle of DFT methods exist. For a recent colorful perspective on the current state of DFT from a man who is passionate about the subject, none other than A. Becke (namesake of exchange functional in **B**LYP and **B3**LYP), I recommend the reader see Ref. [15].

Quantity	**Hartree-Fock Theory**	**KS-DFT**
System definition	Ψ, Slater determinant	$\rho(\vec{r}) = \sum_i \lvert\Psi_i(\vec{r})\rvert^2$
Variational condition	$\delta E[\Psi] = \frac{\partial E}{\partial \Psi} = 0$	$\delta E[\rho] = \frac{\partial E}{\partial \rho} = 0$
Effective potential	$\nu^{HF}(r_1) = \sum_{j=1}^{N}(\mathbf{J}_j - \mathbf{K}_j)$	$V^{KS}(r_1) = \int \frac{\rho(\vec{r_2})}{\lvert r_1 - r_2\rvert} d\vec{r_2} + \nu_{xc}(r_1)$
Total Energy	$E = \sum_{i=1}^{N} \varepsilon_i + V_{nn} - \frac{1}{2}\sum_{i=1}^{N}\sum_{j=1}^{N}(J_{ij} - K_{ij})$	$E[\rho] = T_{ref}[\rho] + V_{ne}[\rho] + J[\rho] + V_{nn}[\rho] + E_{xc}[\rho]$
Orbital equation	$\hat{F}\chi_i^{HF} = \varepsilon_i^{HF}\chi_i^{HF}$	$h^{KS}\chi_i^{KS} = \epsilon_i^{KS}\chi_i^{KS}$

Table 1.1: **Similarities between KS-DFT and HF theories.**

References

[3] A. J. P. Akelaitis et al. "Synthesis and electro-optic properties of amino-phenyl-thienyl donor chromophores". In: *Opt. Mater. (Amsterdam, Neth.)* 30 (2008), pp. 1504–1513.

[4] L. Alloatti et al. "100 GHz Silicon-Organic Hybrid Modulator". In: *Light: Science and Applications* 3.5 (2014), E173.

[5] J. Andzelm et al. "Performance of DFT Methods in the Calculation of Optical Spectra of TCF-Chromophores." In: *J. Chem. Theory Comput.* 5 (2009).

[6] P. Atkins. *Molecular quantum mechanics (2nd ed.)* Oxford [Oxfordshire] ; New York: Oxford University Press., 1983.

[12] D. H. Bale. "Nonlinear Optical Materials Characterization Studies Employing Photostability, Hyper-Rayleigh Scattering, and Electric Field Induced Second Harmonic Generation Techniques." Thesis. 2007.

[13] D. H. Bale et al. "Dielectric Dependence of the First hyperpolarizability for Electro-Optic Chromophores". In: *J. Phys. Chem. B.* 115 (2011).

[15] A. Becke. “Perspective: Fifty years of density functional theory in chemical physics”. In: *J. Chem. Phys.* 140 (2014), 18A301.

[18] S. D. Bella, M. Ratner, and T. Marks. “Design of Chromophoric Molecular Assemblies with Large Second-Order Optical Nonlinearities. A Theoretical Analysis of the Role of Intermolecular Interactions.” In: *J. Am. Chem. Soc.* 114 (1992), pp. 5842–5849.

[19] S. Benight et al. “Reduced Dimensionality in Organic Electro-Optic Materials: Theory and Defined Order”. In: *J. Phys. Chem. B.* 114 (2010), pp. 11949–11956.

[20] A.F. Benner et al. In: *IBM J. Res. Dev.* 49 (2005), p. 755.

[22] M. Born and R. Oppenheimer. “Zur Quantentheorie der Molekeln.” In: *Ann. Phys.* 84 (1927), p. 457.

[23] R. Boyd. *Nonlinear Optics*. San Diego, CA, USA: Academic Press, Inc., 1992.

[25] J.L. Bredas and S. Marder. “CHEM 535B – SPRING 2003, Chapter 9 – Nonlinear Optics”. Accessed Nov. 2015 via quiz2.chem.arizona.edu/chem535/.

[29] D.M. Casimier et al. “Demonstration of a Low Vpi-L Modulator with GHz Bandwidth Based on Electro-Optic Polymer-Clad Silicon Slot Waveguides”. In: *Proc. SPIE* 5351 (2004), pp. 243–252.

[36] D. S. Chemla, J. L. Oudar, and J. Jerphagnon. “Origin of the second-order optical susceptibilities of crystalline substituted benzene”. In: *Phys. Rev. B* 12 (1975), p. 4534.

[37] A. Chen et al. *In Modified attenuated total reflection for the fast and routine electro-optic measurement of nonlinear optical polymer thin films, Organic Thin Films for Photonics Applications*. Long Beach, CA. 1997.

[38] Y.J. Cheng et al. “Demonstration of a Low Vpi-L Modulator with GHz Bandwidth Based on Electro-Optic Polymer-Clad Silicon Slot Waveguides”. In: *Chem. Mater.* 19 (2007), pp. 1154–1163.

[39] Y.J. Cheng et al. "Donor-Acceptor thiolated polyenic chromophores exhibiting large optical nonlinearity and excellent photostability". In: *Chem. Mater.* 20.15 (2008), pp. 5047–5054.

[41] E.Y. Choi, M. Jazbinsek, and O.P. Kwon. "Control of Nucleation of Organic Electrooptic Phenolic Polyene Crystals by Highly Polar Liquid Additive". In: *Crystal Growth & Design* 12.1 (2012), pp. 495–498.

[43] K. Clays and A. Persoons. "Hyper-Rayleigh Scattering in Solution." In: *Rev. Sci. Instrum.* 63 (1992), pp. 3285–3289.

[44] CMDITR. *Photonics Wiki.* 2015. URL: `www.photonicswiki.org`.

[46] S. J. Cyvin, J. E. Rauch, and J. C. Decius. "Theory of Hyper-Raman Effects (Nonlinear Inelastic Light Scattering): Selection Rules and Depolarization Ratios for the Second-Order Polarizability". In: *J. Chem. Phys.* 43 (1965).

[47] Singer K. D., Kuzyk M. G., and Sohn J. E. "Second-Order Nonlinear-Optical Processes in Orientationally Ordered Materials: Relationship between Molecular and Macroscopic Properties". In: *J. Opt. Soc. Am. B* 4 (1987), p. 968.

[48] L. R. Dalton. "Rational design of organic electro-optic materials". In: *J. Phys.: Condens. Matter* 15 (2003), R897.

[49] L. R. Dalton and W. H. Steier. *Broadband Optical Modulators: Science, Technology, and Applications, Polymer Modulators.* New York, NY, USA: Taylor and Francis, 2011, pp. 221–254.

[50] L. R. Dalton, P. A. Sullivan, and D. H. Bale. "Electric Field Poled Organic Electro-optic Materials: State of the Art and Future Prospects". In: *Chem. Rev.* 110 (2010), pp. 25–55.

[51] L. R. Dalton et al. "From molecules to optochips: organic electro-optic materials." In: *Journal of Materials Chemistry* 9.9 (1999), pp. 1905–1920.

[52] L. R. Dalton et al. *Organic electro-optic silicon photonic materials and devices.* 2007.

[54] Larry R. Dalton and K. S. Lee. *Polymers for Photonic Applications I: Advances in Polymer Science*. 2002.

[55] L.R. Dalton. "Organic electro-optic materials." In: *Pure Appl. Chem.* 76.7-8 (2004), pp. 1421–1433.

[56] L.R. Dalton et al. "Low (Sub-Volt) Halfwave Voltage Polymeric Electro-optic Modulators Achieved by Controlling Chromophore Shape". In: *Science* 288 (2000), p. 119.

[57] L.R. Dalton et al. "Organic Electro-Optic Materials". In: *Organic Thin Films for Photonic Applications*. Chap. 3, pp. 13–33.

[58] L.R. Dalton et al. "Progress toward Device-Quality Second-Order Nonlinear Optical Materials. 1. Influence of Composition and Processing Conditions on Nonlinearity, Temporal Stability, and Optical Loss". In: *Chem. Mater.* 10 (1998), pp. 146–155.

[60] J. A. Davies et al. "Rational Enhancement of Second-Order Nonlinearity: Bis-(4-methoxyphenyl)hetero-aryl-amino Donor-Based Chromophores: Design, Synthesis, and Electrooptic Activity". In: *J. Am. Chem. Soc* 130 (2008), pp. 10565–10575.

[62] V. Dentan et al. In: *Opt. Commun.* 69 (1989), pp. 379–383.

[64] R. Ding and et al. "Demonstration of a Low Vpi-L Modulator with GHz Bandwidth Based on Electro-Optic Polymer-Clad Silicon Slot Waveguides". In: *Opt. Express* 18 (2010), pp. 15618–15623.

[68] A. Einstein. "Die Grundlage der allgemeinen Relativitatstheorie." In: *Ann. der Physik* 49 (1916), pp. 769–822.

[71] T. Engel and P. Reid. *Physical Chemistry, 3rd Ed.* San Francisco, CA, USA: Pearson Ed., Inc., 2013.

[72] J.F. Federici et al. In: *Semicond. Sci. Technol.* 20 (2005), S266.

[73] K. Firestone. "Frequency-agile hyper-Rayleigh scattering studies of nonlinear optical chromophores". Thesis. 2005.

[79] K. Garrett et al. “Optimum Exchange for Calculation of Excitation Energies and Hyperpolarizabilities of Organic Electro-optic Chromophores”. In: *Journal of Chemical Theory and Computation* 10.9 (2014), pp. 3821–3831.

[88] M. Guillame, E. Botek, and B. Champagne. “Theoretical investigations of the linear and second-order nonlinear susceptibilities of the 3-methyl-4-nitropyridine-1-oxyde (POM) crystal”. In: *J. Chem. Phys.* 121 (2004), pp. 7390–7400.

[89] D.R. Hartree. In: *Proc. Cambridge Phil. Soc.* 24 (1928), p. 111.

[92] L. M. Hayden et al. “Second-order nonlinear optical measurements in guest-host and side-chain polymers.” In: *Journal of Applied Physics* 68 (1990), p. 456.

[93] L.M. Hayden et al. In: *J. Polym. Sci. (B) Polym. Phys* 41 (2003), p. 2492.

[94] T.F. Heinz, W.K. Tom, and Y. R. Shen. “Determination of molecular orientation of monolayer adsorbates by optical second harmonic generation”. In: *Phys. Rev. A* 28.3 (1983), p. 1883.

[99] P. Hohenberg and W. Kohn. “Inhomogeneous electron gas.” In: *Phys. Rev.* 136 (1964), B864.

[101] J. Huo, K. Liu, and X. Chen. “1x2 Precise Electro-Optic Switch In Periodically Poled Lithium Niobate”. In: *Opt. Express* 18 (2010), p. 15603.

[104] Cisco Systems Inc. *Cisco Visual Networking Index: Global Mobile Data Traffic Forecast Update, 2014-2019.* Accessed Nov. 9, 2015 from www.cisco.com. 2015.

[105] C. M. Isborn et al. “Comparison of Static First Hyperpolarizabilities Calculated with Various Quantum Mechanical Methods.” In: *J. Phys. Chem. A.* 111 (2007).

[112] S.-H. Jang et al. In: *Chem. Mater.* 18 (2006), pp. 2982–2988.

[114] F. Jensen. *Introduction to Computational Chemistry.* West Sussex, England: Wiley and Sons, 2006.

[115] W. Jin et al. “Benzocyclobutene barrier layer for suppressing conductance in nonlinear optical devices during electric field poling”. In: *Appl. Phys. Lett.* 104 (2014), p. 243304.

[116] L. E. v.d.L. Johnson. “Multi-Scale Modeling of Organic Electro-Optic Materials”. Thesis. 2012.

[117] L. E. v.d.L. Johnson, B. H. Robinson, and L. R. Dalton. “Optimizing Calculations of Electronic Excitations and Relative Hyperpolarizabilities of Electrooptic Chromophores”. In: *Accounts of Chemical Research* 47 (2014), pp. 3258–3265.

[120] O. Kaliski. *Organics for Electro-optical Applications*. 2002.

[122] W. Kaminsky. *Report: Crystal Structure Report for Dalton-Reid, ID-YLD124*. Sample Submitted by Peter Johnston. 2012. URL: `cad4.cpac.washington.edu/structures`.

[126] S. Karna and A. Yeates. *Nonlinear Optical Materials: Theory and Modeling.* Washington, DC: American Chemical Society., 1996.

[130] T.H. Kim. *An Iterative Technique for Solving the N-electron Hamiltonian: The Hartree-Fock method.* Accessed: December 2012 via web.mit.edu/kimt/www/8.06/.

[131] T. Kinnibrugh et al. “Influence of isomerization on nonlinear optical properties of molecules.” In: *J. Phys. Chem. B.* 110.27 (2006), pp. 13512–22.

[136] M.J. Kobrinsky et al. In: *Intel Technol. J.* 8 (2004), p. 129.

[137] W. Koch and M. C. Holthausen. *A Chemist's Guide to Density Functional Theory (2nd Ed.).* Weinheim: Wiley-VCH, 2001.

[139] L. Kollros. “Albert Einstein en Suisse Souvenirs.” In: *Helv. Phys. Acta. Supp.* 4 (1956), pp. 271–281.

[141] D. Korn. “Silicon-Organic Hybrid (SOH) IQ Modulator Using the Linear Electro-Optic Effect for Transmitting 16QAM at 112 Gbit/s”. In: *Opt. Express* 12 (2013), pp. 13219–13227.

[149] M. Lauermann et al. “16QAM Silicon-Organic Hybrid (SOH) Modulator Operating with 0.6 Vpi and 19 fJ/bit at 112 Gbit/s”. In: *IEEE J. Lightwave Technol.* (2014).

[152] A. Lee and S. Colwell. “The determination of hyperpolarizabilities using density functional theory with nonlocal functionals”. In: *The Journal of Chemical Physics* 101 (1994), p. 9704.

[154] M. Lee et al. “Broadband Modulation of Light by Using an Electro-Optic Polymer.” In: *Science* 298 (2002), pp. 1401–1403.

[155] I. Levine. *Quantum chemistry (6th ed.)* Upper Saddle River, N.J.: Pearson Prentice Hall., 2009.

[156] H. Li. “Nonlinear Optical Properties of Potential Sensitive Dyes”. Thesis. 2007.

[158] Y. Liao et al. “Systematic study of the structure-property relationship of a series of ferrocenyl nonlinear optical chromophores”. In: *J. Am. Chem. Soc.* 127 (2005), p. 2758.

[159] S.-T. Lin and C.-S. Hsieh. “Triple-Wavelength Nd-Laser System By Cascaded Electro-Optic Periodically Poled Lithium Niobate Bragg Modulator”. In: *Opt. Express* 20 (2012), p. 29659.

[160] T.C. Lin et al. “Molecular Origins of the High-Performance Nonlinear Optical Susceptibility in a Phenolic Polyene Chromophore: Electron Density Distributions, Hydrogen Bonding, and ab Initio Calculations”. In: *The Journal of Physical Chemistry C* 117.18 (2013), pp. 9416–9430.

[162] A. Liu et al. “A high-speed silicon optical modulator based on a metal-oxide-semiconductor capacitor.” In: *Nature* 427 (2004), pp. 615–618.

[165] H. Lu et al. “6-Micron Interaction Length Electro-Optic Modulation Based On Lithium Niobate Photonic Crystal Cavity”. In: *Opt. Express* 20 (2012), p. 20884.

[168] S. R. Marder. “Organic nonlinear optical materials: where we have been and where we are going”. In: *Chem. Commun.* (2006), pp. 131–134.

[171] R. McWeeny. “Perturbation Theory for Fock-Dirac Density Matrix”. In: *Phys. Rev.* 126 (1962), p. 1028.

[172] R. McWeeny. “Some recent advances in density matrix theory”. In: *Rev. Mod. Phys.* 32 (1960), pp. 335–369.

[173] F. Michelotti et al. In: *Appl. Phys. Lett.* 67 (1995), pp. 2765–2767.

[175] C. Moller and M. S. Plesset. “Note on approximation treatment for many-electron systems.” In: *Phys. Rev.* 46 (1934), p. 618.

[179] H. Naundorf. “Short Introduction to Quantum Chemistry Methods.” In: (2005). Institute of Physical and Theoretical Chemistry, Freie Universitat Berlin.

[183] J. L. Oudar and D. S. Chemla. “Hyperpolarizabilities of the Nitroanilines and their Relations to the Excited State Dipole Moment”. In: *J. Chem. Phys.* 66 (1977), p. 2664.

[184] R. Palmer. “Low Power Mach-Zehnder Modulator in Silicon-Organic Hybrid Technology”. In: *IEEE Photonics Technol. Lett.* 25 (2013), pp. 1226–1229.

[185] R. Palmer et al. “High-Speed, Low Drive-Voltage Silicon-Organic Hybrid Modulator Based on a Binary-Chromophore Electro-Optic Material”. In: *IEEE Photonics Technol. Lett.* (2014).

[188] M. Paniccia, V. Krutul, and S. Koehl. *White Paper: Introducing Intel’s Advances in Silicon Photonics*. 2004.

[191] A. D. Polyanin and V. F. Zaitsev. *Handbook of Nonlinear Partial Differential Equations*. 2000 N.W. Corporate Blvd., Boca Raton, Florida 33431: Chapman and Hall/CRC Press, 2004, pp. 779–782.

[194] B.H. Robinson, L.E. Johnson, and B.E. Eichinger. “Relation of System Dimensionality and Order Parameters”. In: *J. Phys. Chem. B* 119.7 (2015), pp. 3205–3212.

[197] Y. Salamin et al. “Direct Conversion of Free Space Millimeter Waves to Optical Domain by Plasmonic Modulator Antenna”. In: *Nano Letters* (Article ASAP).

[198] T. Saleh. *Fundamentals of Photonics. (1st Ed.)* New York, New York: Wiley-Interscience Publications., 1991.

[204] A. Schneider, M. Stillhart, and P. Gunter. *Highly Efficient Generation of THz Pulses Using Laser Pulses at Telecommunication Wavelengths*. 2006.

[205] A. Schneider et al. "Generation of terahertz pulses through optical rectification in organic DAST crystals: Theory and experiment". In: *J. Opt. Soc. Am. B* 23 (2006), p. 1822.

[211] Y. R. Shen. *The Principles of Nonlinear Optics*. New York, New York: Wiley, Inc., 1984.

[212] D. Silva et al. "Self Aggregation and Optical Absorption of Stilbazolium Merocyanine in Chloroform". In: *J. Phys. Chem. B* 118 (2014).

[213] K. D. Singer, J. E. Sohn, and S. J. Lalama. "Second harmonic generation in poled polymer films." In: *Applied Physics Letters* 49.5 (1986), p. 248.

[214] A.M. Sinyukov et al. In: *Appl. Phys. Lett.* 85 (2004), p. 5827.

[221] P.A. Sullivan and L.R. Dalton. "Theory Inspired Development of Organic Electro optic Materials". In: *Accounts of Chemical Research* 43.1 (2010), pp. 10–18.

[227] A. Szabo and N. Ostlund. *Modern Quantum Chemistry*. New York: McGraw-Hill, 1982.

[230] C. C. Teng and H. T. Man. "Simple reflection technique for measuring the electro-optic coefficient of poled polymers." In: *Applied Physics Letters* 56 (1990), p. 1734.

[232] A. Tillack. "Electro-Optic Material Design Criteria Derived from Condensed Matter Simulations Using the Level-of-Detail Coarse-Graining Approach." Thesis. 2015.

[233] A. Tokmakoff. *5.74 Introductory Quantum Mechanics II, Spring 2009. (Massachusetts Institute of Technology: MIT OpenCourseWare)*. Accessed: January 2011 via www.ocw.mit.edu; License: Creative Commons BY-NC-SA.

[234] F. Trager. *Springer Handbook of Lasers and Optics, 2nd Ed.* Berlin ; New York: Springer Science and Business Media, 2012.

[242] C. Weimann et al. "Silicon-Organic Hybrid (SOH) Frequency Comb Sources for Terabit/s Data Transimission". In: *Opt. Express* 22.3 (2014), pp. 3629–3647.

[247] K. Wu, J. Snijders, and C. Lin. "Reinvestigation of Hydrogen Bond Effects on the Polarizability an Hyperpolarizability of Urea Molecular Clusters". In: *J. Chem. Phys. B.* 106 (2002), pp. 8954–8958.

[252] F. Zernike and J. E. Midwinter. *Applied Nonlinear Optics.* Mineola, NY: Dover Publications, Inc., 1973.

[254] X. Zhou et al. "One-Dimensional Model Of A Plasma-Electrode Optical Switch Driven By One-Pulse Process". In: *Opt. Express* 14 (2006), p. 2880.

Chapter 2

DETERMINING AN ACCURATE AND AFFORDABLE METHOD FOR COMPUTING MOLECULAR HYPERPOLARIZABILITY

In the quest to design better organic NLO materials with theory as a guide, it is necessary to develop a computational method that can reliably predict the electronic properties of interest for a variety of donor, acceptor, and bridge combinations. Density functional theory (DFT) is the method of choice for many organic molecules, including large conjugated systems such as those studied in this work, due to its favorable accuracy/cost ratio [224], [5]. Furthermore, the development of time-dependent density functional theory (TDDFT) [28] has made it possible to theoretically predict excited state properties of large molecules with good accuracy [2], [79], [67], [5]. Many useful optical properties such as the peak one-photon absorption energy, λ_{max}, excited state dipole moments, μ_e, and static and dynamic polarizabilities and hyperpolarizabilities, can be readily calculated using TDDFT [63], [105], [190], [164], [216]. Although both DFT and TDDFT are exact theories, using standard approximate exchange-correlation (XC) functionals leads to a few well-known limitations. Due to overdelocalization error, also known as self-interaction error (SIE) [67], [66], which results from using an approximate form of the exchange interaction, DFT is known to overestimate polarization and Rydberg excitation energies and underestimate bandgaps and reaction barrier heights [229], [150]. DFT has also been reported to overestimate the hyperpolarizabilities of π-conjugated systems, and neither asymptotic far-nucleus correction nor mild exchange-energy correction methods (i.e., hybrid functionals) have offered improvement [124]. Thus, even popular hybrid functionals, such as B3LYP, which lack the correct long-range exchange interaction are known to underestimate charge-transfer energies [66]. This issue is of great

consequence for systems which obey the D-π-A motif due to the pairing of electron-rich and electron-deficient end-groups which lend to significant intramolecular charge-transfer. Thus, alternative methods have been explored for accurately predicting important linear and non-linear optical properties of these conjugated molecular systems.

The long-range correction (LC) scheme is one method which is growing in popularity for its simplicity and effectiveness in remediating some the above issues [195], [196], [111], [109]. The LC scheme was developed by Hirao and co-workers to incorporate exact exchange in the interaction between distant orbitals [102]. By its nature, the exchange integral used in Hartree-Fock (HF) theory is deemed exact, meaning that it explicitly accounts for the exchange of each and every electron in the system. Thus, the LC scheme uses the standard error function ('*erf*') to partition the electron repulsion operator, $\frac{1}{r_{12}}$, into short and long-range components, as follows:

$$\frac{1}{r_{12}} = \frac{1}{r_{12}}[erf(\omega r_{12})] + \frac{1}{r_{12}}[1 - erf(\omega r_{12})], \tag{2.1}$$

where $r_{12} = |r_1 - r_2|$ is the distance electrons 1 and 2 and ω is the adjustable *range-separation parameter* defined in atomic units of inverse length (a_0^{-1}). This method is applied to the exhange-correlation operator, E_{xc}, of a pure DFT (i.e., BLYP, VWN, and PBE) so to balance long-range (LR) HF exchange with short-range (SR) pure DFT exchange:

$$E_{xc} = E_c^{DFT} + E_x^{LR,HF} + E_x^{SR,DFT}, \tag{2.2}$$

where E_c^{DFT} is the DFT correlation functional at all ranges, $E_x^{LR,HF}$ is the long-range HF exchange functional, and $E_x^{SR,DFT}$ is the short-range DFT exchange functional.

The pure DFT exchange is conventionally described by the following exchange functional,

$$E_x^{DFT} = -\frac{1}{2}\sum_{\sigma}\int \kappa_\sigma \rho_\sigma^{4/3} d^3\mathbf{R}, \tag{2.3}$$

where ρ_σ is the density of σ-spin electrons and κ_σ is a dimensionless constant derived from the local-spin density approximation (LSDA). This approximate form of exchange leads to incorrect asymptotic behavior at large r_{12} distances. In accordance with the LC scheme,

the exchange functional is modified so that is 'borrows' the exact $-1/r$ behavior exhibited by HF. To describe the SR exchange interaction, Equation 2.3 becomes [229]

$$E_x^{(SR,DFT)} = -\frac{1}{2}\sum_{\sigma}\int \kappa_\sigma \rho_\sigma^{4/3} \times \left\{1 - \frac{4}{3}a_\sigma\left(\sqrt{\pi}\cdot erf(\frac{1}{a_\sigma}) + 2a_\sigma b_\sigma(\frac{1}{4} - a_\sigma)\right)\right\} d^3\mathbf{R}, \quad (2.4)$$

where the parameters a_σ and b_σ depend on the range-separation parameter, ω, and the cube-root of the σ-spin density, ρ_σ, and are given by coupled equations $a_\sigma = \omega\kappa_\sigma^{\frac{1}{2}}/3\sqrt{\pi}\rho_\sigma^{\frac{1}{3}}$ and $b_\sigma = [exp(\frac{-1}{a_\sigma^2}) - 1]$. The long-range exchange interaction adapt the HF exchange integral such that

$$E_x^{(LR,HF)} = -\frac{1}{2}\sum_{\sigma}\sum_{i}^{occ}\sum_{j}^{occ}\int\int \phi_{i\sigma}^*(r_1)\phi_{i\sigma}^*(r_1)\frac{erf(\omega r_{12})}{r_{12}}\phi_{j\sigma}(r_2)\phi_{j\sigma}(r_2)d^3r_1 d^3r_2, \quad (2.5)$$

where $\phi_{i\sigma}^*$ is the i^{th} σ-spin orthonormal molecular orbital. The aforementioned *range-separation parameter*, ω, sets the amount of exact exchange used in the calculation, with ω=0 giving full DFT exchange at all r_{12} distances, thus Equation 2.2 reverts back to the pure DFT functional:

$$E_{xc} = E_c^{DFT} + E_x^{DFT}, \quad (2.6)$$

and, conversely, $\omega \to \infty$ giving full exact (HF) exchange at all r_{12} distances converts Equation 2.2 to:

$$E_{xc} = E_c^{DFT} + E_x^{HF}, \quad (2.7)$$

Note that the DFT correlation remains intact regardless of ω. In practice, attentuating ω so as to replace the local DFT exchange with nonlocal HF exchange is performed by tuning the *fraction* of long-range (LR) HF exchange to DFT exchange from 0 to 1 (also called a 'mixing ratio'). For example, the default values for ω in LC-BLYP is 0.47 $bohr^{-1}$ and for LC-ωPBE is 0.40 $bohr^{-1}$. The above equations describe the inclusion of HF exchange for long-range interactions and, thus, are applied as a long-range correction ('LC') to DFT methods such as BLYP. A similar approach can be applied for tuning ω for short-range exchange interactions, as well. Handy and coworkers developed the Coulomb-attenuating three-parameter method, CAM-B3LYP, in which the ω parameter adjusts the amount of exact exchange from 20% at

short-range to 65% at long-range, with a default value of ω=0.33 $bohr^{-1}$ [249]. The *three-parameter* term refers to the inclusion of parameters, α and β (not to be confused with hyperpolarizability) respectively, into Equation 2.8 to finely tune the contributions of HF and DFT in the SR and LR regions such that

$$E_x^{LR,HF} + E_x^{SR,DFT} = \frac{1}{r_{12}}[\alpha + \beta erf(\omega r_{12})] + \frac{1}{r_{12}}\{1 - [\alpha + \beta erf(\omega r_{12})]\} \tag{2.8}$$

where α dominates the SR exchange character and β dominates the LR. The class of functionals which include adjustable short- and long-range exchange are commonly called 'range-separated hybrids' or RSH functionals. Another functional in this class is wB97xD developed by Head-Gordon and co-workers to include empirical atom-atom dispersion corrections (denoted by 'D') [30]. This functional modifies the team's earlier development, B97, so to compensate for the added dispersion correction by using 100% long-range exact exchange, 22% short-range exact exchange, and range-separation parameter, ω, of 0.2. The merits of the LC- RSH functionals, LC-BLYP, CAMB3LYP and wB97xD, are investigated in this chapter and contrasted with the results from DFTs with no long-range exchange corrections (BLYP and B3LYP). These DFT methods are also compared with the performance of a correlated wavefunction method; in particular, Møller-Plesset (MP) Perturbation Theory.

MP2 is the lowest order electron correlation correction of the MPn methods and is, thus, the most computationally accessible correlated MPn method available for relatively large molecules ($\sim$100 atoms or more). However, MP2 is still computationally expensive with comparison to DFT; standard MP2 implementations require on the order of N^5 operations compared with roughly N^3 operations using DFT. In practice, for the largest molecules studied here ($\sim$100 atoms), it may take up to two weeks (runnning on 16 processors/node) to run an MP2 static β calculation with 6-31+G* basis set; whereas, a similar calculation in DFT typically finishes in less than a day. Nevertheless, two weeks of run time is still in the realm of a routine calculation. A benefit of studying correlated wavefunction methods is that they are systematically improvable, meaning that they theoretically approach a more accurate result when paired with a larger and larger basis set [227], [45], [114]. This is

not the case for DFT. Furthermore, Champagne and coworkers showed that MP2 compares well with high-level CCSD(T) results for the static hyperpolarizability of moderately-sized molecular systems [35], [32], [225].An additional study by this group found that beyond a certain bridge length (at least 16 carbon atoms in a polybutatriene chain), MP2 was shown to overestimate β as much as double the CCSD(T) results [133]; however, the majority of the molecules considered in this study have molecular sizes that are below this size limit.

A study comparing DFT and MP2 would not be complete without also considering the 'double-hybrid' functionals. Since the exchange terms in both LC-DFT and MP2 are essentially exact, the correlation terms remain to be corrected. One strategy is to add MP2 correlation to DFT correlation, so that the exchange-correlation functional has the form [30]:

$$E_{xc} = (1 - c_{HF})E_x^{DFT} + c_{HF}E_x^{HF} + (1 - c_{MP2})E_c^{DFT} + c_{MP2}E_c^{MP2}, \tag{2.9}$$

where the mixing ratio, 'c_{HF}', is analogous to the range-separation parameter, ω, used for mixing DFT and HF exchange terms discussed earlier, and 'c_{MP2}' describes the mixing of DFT and MP2 correlation terms. The first double hybrid method, B2-PLYP, was developed by Grimme [85],[86]. According to this method, a standard Kohn-Sham DFT calculation is performed and the resulting virtual (vir) and occupied (occ) Kohn-Sham orbitals (ϕ) and orbital eigenvalues (ϵ) are then used in a MP2-like second-order perturbative (PT2) correlation energy expression [30]:

$$E_c^{PT2} = \frac{1}{4}\sum_{ij}^{occ}\sum_{ab}^{unocc}\frac{|(\phi_i\phi_a|\hat{g}|\phi_j\phi_b) - (\phi_i\phi_b|\hat{g}|\phi_j\phi_a)|^2}{\epsilon_i + \epsilon_j - \epsilon_a - \epsilon_b}, \tag{2.10}$$

where ϕ_i and ϕ_j are the occupied KS orbitals and ϕ_a and ϕ_b are the unoccupied (virtual) KS orbitals and

$$(\phi_i\phi_a|\hat{g}|\phi_j\phi_b) = \int \phi_i^*(r_1)\phi_a^*(r_1)\frac{1}{r_{12}}\phi_j(r_2)\phi_b(r_2)d^3r_1d^3r_2 \tag{2.11}$$

Using this method, we can replace 'E_c^{MP2}' in Equation 2.9 with E_c^{PT2} described by Equation 2.10. B2-PLYP combines MP2 correlation with the exchange and correlation terms in B3LYP [16], in which E_x^{DFT} is Becke 88 (B88) exchange functional [17] and E_c^{DFT} is the

Lee-Yang-Parr (LYP) correlation functional [153]. Fitting to a large set of empirical thermodynamic data yields the optimal ratios: 47% E_x^{B88} and 73% $E_C(LYP)$ with E_x^{HF} and E_c^{PT2} making up the remaining exchange and correlation parts [228], [129], [84]. Studies done by Champagne, et al. have shown that B2-PLYP tends to slightly overestimate β by 19%-46% depending on molecular bridge length in comparison to CCSD(T) values. By comparison, they found that LC-BLYP tends to underestimate β by $\sim$ 19% regardless of bridge length [32]. Also, the relatively small amount of MP2-like correlation (27%) in B2PLYP makes it insufficient for describing van der Waals (vdW) interactions. For this reason, the dispersion-corrected form of this functional, B2PLYP-D, is also examined. Similar to MP2, B2PLYP and B2PLYP-D both scale like N^5 operations.

In this work, we examine the results of second-order Møller-Plesset perturbation (MP2) to explore the effectiveness of a post-Hartree-Fock method for computing β in contrast with DFT. We also compare the DFTs for accurately and reliably determining excitation energies and briefly examine tuning of the ω parameter in LC-BLYP and CAM-B3LYP and its affect on this computed λ_{max}. In Section 1 we describe the benchmarking set of 36 molecules along with summarizing the corresponding experimental results. Section 2 gives the computational details along with a discussion of computing the hyperpolarizability, β, and comparing to experimentally measurable values. In Section 3 we show the results of the computed hyperpolarizabilites according to MP2, double hybrids, and DFT, leading to Section 4 where we conclude by stating our recommendations for the computation of β based on the various electronic structure methods studied.

2.1 Molecular Benchmark set and Summary of Experimental Results

Structures and experimental properties for the 35-molecule test set used in this study are shown in Table 2.1. Each of the molecules in this test set obey the D-π-A motif such that it contains an electron-withdrawing acceptor group linked through a π-conjugated bridge to a substituted aniline donor. Each of the 35 systems may be classified according to its

bridge-character; either of a thienylenevinylene (FTC-type) or polyene-based (CLD-type) nature [5]. Also, included are 'short-bridge' systems which contain less than one vinylene unit in the bridge. In addition to classifying the bridge character, we also classify the donor (D) and acceptor (A) parts with color-coding in Table 2.1.

The molecules consist mostly of dialkylamino donors, however, bulkier donors such as 4-(diarylamino)phenyl (DAAP) donors [38] are also studied. According to the bond-length alternation (BLA) hypothesis, aromatic groups belonging in the π-backbone are believed to hinder electronic polarization resulting in reduced β, thus various donors and bridges have been developed to amorielate this issue [169],[60]. Less aromatic groups replace the phenyl unit of the diarylamino donor in systems such as 4-(diarylamino)thienyl (JDD2) and 4-(diarylamino)pyrrolyl (JDD3) [60]. The measured hyperpolarizabilities of these chromophores (6.0$\pm$0.5 and 5.3$\pm$0.3, respectively) are larger than the benchmark YLD124 (5.2$\pm$0.2), however, similar to YLD124, they suffer from signifcant resonance enhancement at the second-harmonic (SH) frequency as evidenced by its molar absorptivity at the SH, $\epsilon_{950nm} > 27,000\ M^{-1}cm^{-1}$ [12], [60]. Theoretical studies are thus needed to clarify the intrinsic β values of these systems. Additional modifications include thiazole in place of the thienyl unit of the FTC-type bridge for the DMC chromophores [29], where it was observed that placing the nitrogen atom closer to the acceptor results in a 10% increase in β with respect to EZ-FTC. Furthermore, 10%-30% enhancements in measured β were found when comparing (di-TBDMSO-amino)phenyl donors of YLD124 and YLD156 ('TBDMSO'=tert-butyldimethylsilane) with amino-phenyl-thienyl (APT) donors which effectively lengthen the bridge by adding a thienyl unit to the donor (C3 and C2 molecules, respectively) [3]. On this note, comparing YLD124 to YLD156 or each of their analogous APT systems, one recognizes that higher measured β values are obtained for the CLD-type chromophores versus FTC-type chromophores.

Variations of the CLD-type bridge were examined in the AJY series [39]. The phenyl-tetraene bridge is appended by thio-alkyl chains in both AJY2 and AJY3, however, despite the electron-withdrawing nature of the thiols, each system was shown to have increased

β with respect to the standard, AJY1. Similar to the JDD systems, the AJY series is significantly resonance enhanced and requires theoretical study to accurately quantify the relative instrinsic β of these systems. GLD1 is the lone phenylpentacene bridge system of the CLD-type molecules [73]. The HRS results for GLD1 shows that lengthening the bridge by one polyene unit results in nearly double the β of CLD1, however, doing so also increases dipole moment and induces a bathochromic shift of $\sim$ 30nm. Nevertheless, the series DCDHF$\rightarrow$TCF1$\rightarrow$CLD1$\rightarrow$GLD1 present a nice bridge length study and will be revisited in Chapter 3. Analogous to the structural relationship between GLD1 and CLD1, the 2,2'-dithiophene bridge of the OLD3 molecule [73] shows a 40% increase in measured β with comparison to EZ-FTC, however, its λ_{max} is practically the same ($\sim$677 nm) despite including a second thienyl unit in the bridge. This suggests that the aromaticity of the thienyl ring to some extent impedes electronic polarization, as can be rationalized by the bond-length alternation (BLA) model discussed elsewhere [169], [13].

In addition to donor and bridge variations, there are twelve distinct acceptor groups studied in this set. Included are tricyanofuran (TCF) and its substituted variants (TCF1-CF3-Ph and TCF1-CF3) as well as tricyano-pyrroline (TCP), which has been suggested to be the strongest acceptor in this set based on HRS measurements of short-bridge-type molecules [112], [12]. Systems with relatively weak acceptors, boron dipyrrin (BODIPY) and 3,5-dinitropyridine (YLN144), are included for comparison of measurement to theory [69], [157].

In Table 2.1, experimental HRS measurements are reported as relative hyperpolarizabilities, $\beta_{HRS}^{sys}/\beta_{HRS}^{FTC}$, where β_{HRS}^{FTC} is the hyperpolarizability of the reference solution, EZFTC. All HRS measurements were performed at the University of Washington (UW) using a Q-switched Nd:YAG laser (Spectra-Physics Quanta-Ray GCR-170), equipped with an H_2 Raman cell and CCD detector. All experimental HRS values were measured using spectroscopic-grade chloroform at 1907nm and through external reference to EZFTC; in turn, β^{EZFTC} was determined through the Internal Reference Method (IRM) [12],[73]. HRS measurements performed by Dr. Kim Firestone and David Lao are marked by (*); otherwise, HRS mea-

surements were performed by Dr. Denise Bale. Synthesis of the selected chromophores was performed at either UW, University of Southern California (USC), or University of Central Florida [157], [69], [60], [38], [29], [118], [39], [3], [12], [73].

Errors in HRS measurements shown in Table 2.1 that were performed by Bale are reported as β_{sys}/β_{FTC} plus or minus one standard deviation from the mean of 3-4 sample runs; otherwise, measurements performed by Firestone and Lao were reported as $\beta_{sys}/\beta_{CHCl_3}$ with errors that are two standard deviations from the mean of 5 or more measurements [73], [12]. To convert the Firestone measurements to β_{sys}/β_{FTC}, the following method was used

$$\frac{\beta_{sys} \pm \delta\beta_{sys}}{\beta_{FTC} \pm \delta\beta_{FTC}} = \frac{\beta_{sys}}{\beta_{FTC}} \left[1 \pm \frac{\delta\beta_{sys}}{\beta_{sys}}\right],$$

where $\beta_{FTC}/\beta_{CHCl_3} \pm \delta\beta_{FTC}/\beta_{CHCl_3} = 2780 \pm 1440$ and describes the reference, EZFTC, in chloroform solution. Note that the error on the EZFTC measurement is not propagated[1].

[1]Similar to Bale's work, all of the HRS measurements from Firestone's work [73] are according to the external reference method (ERM) with EZFTC as the reference system; thus, the $\beta_{sys}/\beta_{CHCl_3}$ values reported in Firestone's work are a result of multiplying the ERM measurements by $\beta_{FTC}/\beta_{CHCl_3}$=2780. It is noted in Firestone's thesis that the large error on the EZFTC measurement (i.e., $\pm$1440) is not propagated in this multiplication: "Error bars only represent the deviations in the measurement relative to the standard and do not include the error in the original measurement for the standard."

Measured Data for Benchmark Chromophores		
Experimental[a] λ_{max} in $CHCl_3$ (nm, eV)	Experimental[b,c] $\beta_{HRS}^{sys}/\beta_{HRS}^{FTC}$ at 1907-nm in $CHCl_3$	Name and Structure[d]
Prototypical FTC-type systems		
676, 1.832	1.0	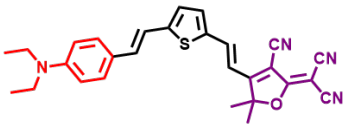 EZFTC (Reference)
754, 1.645	2.2 ± 0.3	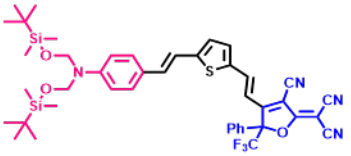 YLD156
Prototypical CLD-type systems		
691, 1.795	1.8 ± 0.08	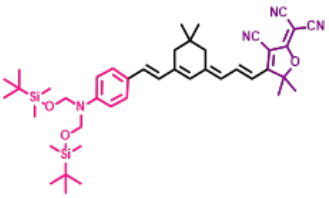 CLD1
786, 1.578	5.2 ± 0.2	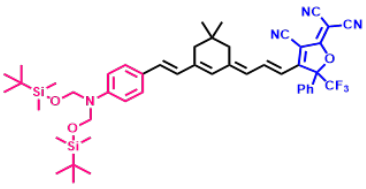 YLD124
continued on next page		

Table 2.1: **Relative first-order hyperpolarizabilties, $\beta_{HRS}^{sys}/\beta_{HRS}^{FTC}$, of selected electro-optical chromophores and their structural and optical properties, measured in $CHCl_3$.**

Experimental[a] λ_{max} in $CHCl_3$ (nm, eV)	Experimental[b,c] $\beta^{sys}_{HRS}/\beta^{FTC}_{HRS}$ at 1907-nm in $CHCl_3$	Name and Structure[d]
Bridge Variations in FTC-type systems		
677, 1.832	1.4 ± 0.1	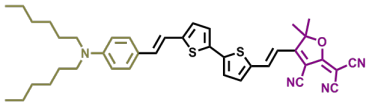 OLD3*
682, 1.818	1.1 ± 0.08	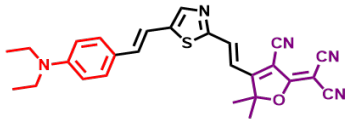 DMC3257*
645, 1.923	0.76 ± 0.07	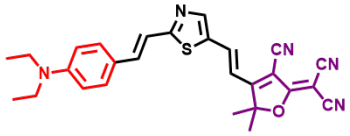 DMC3194*

continued on next page

(a) λ_{max} of the UV-Vis absorption spectrum of the molecule dissolved in chloroform. All UV-visible absorbance measurements were performed at the University of Washington (UW) using a Shimadzu 1610 UV-vis spectrophotometer.

(b) Relative hyperpolarizabilities, $\beta^{sys}_{HRS}/\beta^{FTC}_{HRS}$, reports the hyperpolarizability measured with hyper-Rayleigh scattering (HRS) and taken as a ratio with respect to the reference solution of EZFTC in chloroform. All HRS measurements were also performed at the UW using a Q-switched Nd:YAG laser (Spectra-Physics Quanta-Ray GCR-170), equipped with an H_2 Raman cell and CCD detector. All experimental HRS values were measured using spectroscopic-grade chloroform at 1907nm and through external reference to EZFTC; in turn, β^{FTC} was determined through the Internal Reference Method (IRM). HRS measurements performed by Dr. Kim Firestone and David Lao are marked by (*); other HRS measurements were performed by Dr. Denise Bale. Synthesis of the selected chromophores was performed at either UW or University of Southern California (USC), as noted by footnote (d).

Experimental[a] λ_{max} in $CHCl_3$ (nm, eV)	Experimental[b,c] $\beta_{HRS}^{sys}/\beta_{HRS}^{FTC}$ at 1907-nm in $CHCl_3$	Name and Structure[d]
Bridge Variations in CLD-type systems		
810, 1.531	5.6 ± 0.3	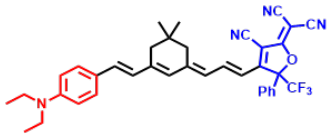 AJY1
793, 1.564	7.5 ± 1.3	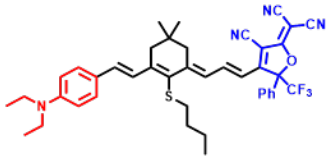 AJY2
799, 1.552	5.9 ± 0.6	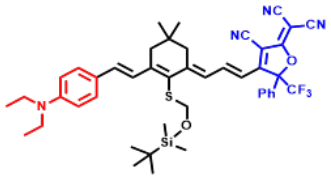 AJY3
719, 1.725	3.0 ± 0.4	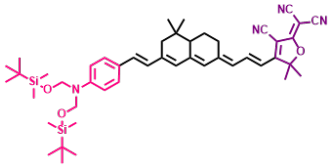 GLD1*
817, 1.518	Not available	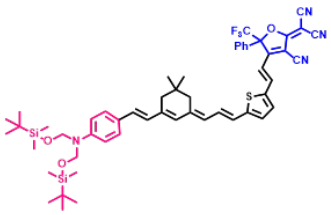 YLD130*

continued on next page

Experimental[a] λ_{max} in $CHCl_3$ (nm, eV)	Experimental[b,c] $\beta^{sys}_{HRS}/\beta^{FTC}_{HRS}$ at 1907-nm in $CHCl_3$	Name and Structure[d]
Acceptor Variations in CLD-type systems		
678, 1.829	0.90 ± 0.10	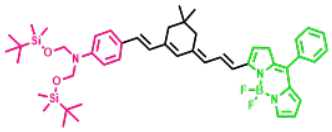 BODIPYH
682, 1.818	0.81 ± 0.01	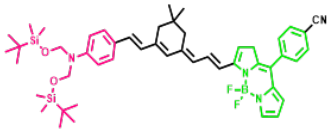 BODIPYCN
703, 1.764	1.16 ± 0.05	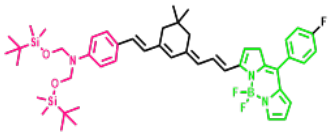 BODIPYF
707, 1.754	1.27 ± 0.09	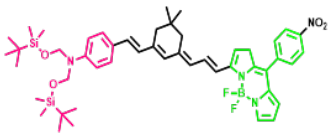 BODIPYNO2
619, 2.003	0.82 ± 0.05	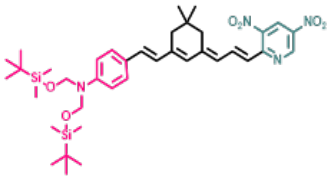 YLN144

continued on next page

(c) Errors in HRS measurements (β_{sys}/β_{FTC}) performed by Bale are reported as plus or minus one standard deviation from the mean of 3-4 sample runs. Measurements performed by Firestone and Lao were reported as $\beta_{sys}/\beta_{CHCl_3}$ with errors that are two standard deviations from the mean. To get β ratios with respect to EZ-FTC, the following method was used $\frac{\beta_{sys} \pm \delta\beta_{sys}}{\beta_{FTC} \pm \delta\beta_{FTC}} = \frac{\beta_{sys}}{\beta_{FTC}}\left[1 \pm \frac{\delta\beta_{sys}}{\beta_{sys}}\right]$, where $\beta_{FTC}/\beta_{CHCl_3} \pm \delta\beta_{FTC}/\beta_{CHCl_3} = 2780 \pm 1440$ and describes the reference, EZFTC, in chloroform solution. (**) No error was reported for C3 in Refs [12] and [3], thus the error for YLD124 was used since it has a similar $\frac{\beta_{HRS}}{\beta_{FTC}}$ and λ_{max} as C3.

Experimental[a] λ_{max} in $CHCl_3$ (nm, eV)	Experimental[b,c] $\beta_{HRS}^{sys}/\beta_{HRS}^{FTC}$ at 1907-nm in $CHCl_3$	Name and Structure[d]
Donor Variations in CLD-type systems		
722, 1.718	2.49 ± 0.09	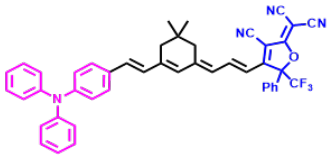 CLDDAAP1
772, 1.606	3.52 ± 0.09	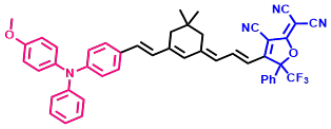 CLDDAAP2
746, 1.662	5.20 ± 0.54	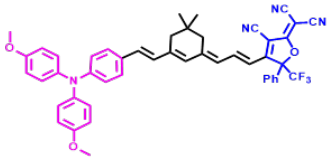 CLDDAAP3
658, 1.885	1.3 ± 0.3	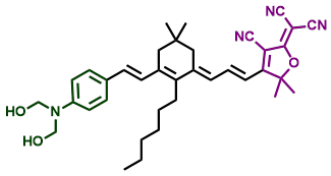 CLD5*
777, 1.596	5.7 ± 0.2**	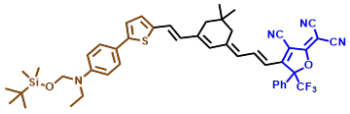 AALD2023 (C3)

continued on next page

[d] DMC3 systems were synthesized by Dr. Daniel Casmier; YLD and YLN systems by Dr. Yi Lao; CLD, DAAP, and AJY systems by Dr. Yen-Ju Cheng; OLD3 by Dr. Olivier Clot (whom also synthesized EZFTC); SHJ- (TCF1 and TCP) systems by Dr. Sei-Hum Jang; DCDHF was synthesized by Peter Johnston; AALD systems (C2,C3) by Dr. Andrew Akelaitis; JDD systems by Dr. Joshua Davies; BODIPY systems by Dr. A. Elangovan and Davies; and GLD1 was synthesized at University of Southern California. Different donor (D) and acceptor (A) groups are classified according to color-coding.

Experimental[a] λ_{max} in $CHCl_3$ (nm, eV)	Experimental[b,c] $\beta_{HRS}^{sys}/\beta_{HRS}^{FTC}$ at 1907-nm in $CHCl_3$	Name and Structure[d]
Donor Variations in FTC-type systems		
746, 1.662	2.8 ± 0.3	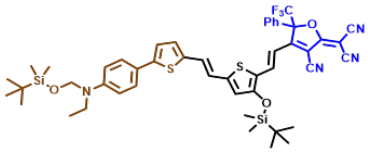 AALD1158 (C2)*
694, 1.787	1.30 ± 0.04	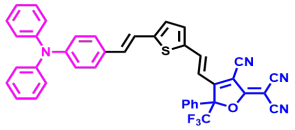 FTCDAAP1
717, 1.729	1.58 ± 0.19	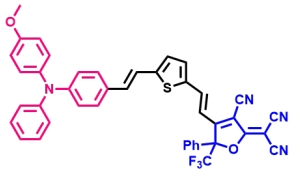 FTCDAAP2
745, 1.664	2.54 ± 0.09	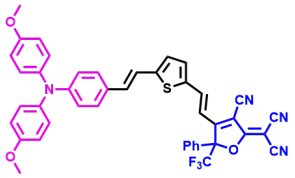 JDD1
857, 1.447	6.0 ± 0.5	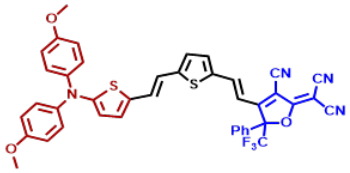 JDD2
853, 1.454	5.3 ± 0.3	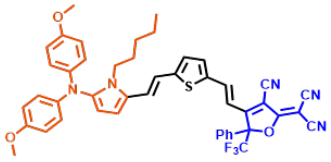 JDD3

continued on next page

Experimental[a] λ_{max} in $CHCl_3$ (nm, eV)	Experimental[b,c] $\beta_{HRS}^{sys}/\beta_{HRS}^{FTC}$ at 1907-nm in $CHCl_3$	Name and Structure[d]
Short-bridge systems		
493, 2.515	Not available	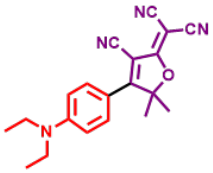 DCDHF
587, 2.112	0.332 ± 0.004	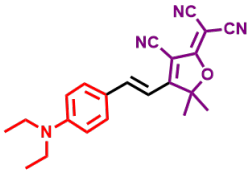 TCF1
629, 1.971	0.36 ± 0.02	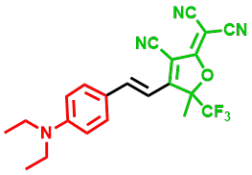 TCF1-CF3
730, 1.699	0.95 ± 0.13	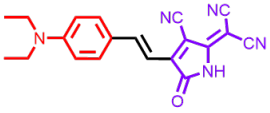 TCP0
749, 1.656	0.85 ± 0.05	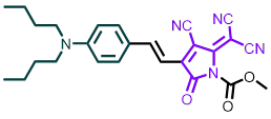 TCP1*
744, 1.667	0.89 ± 0.07	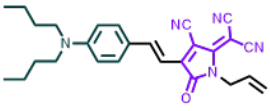 TCP2*
758, 1.636	0.98 ± 0.02	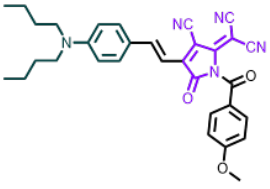 TCP3*

2.2 Computational Details

Structural modifications were made to the molecules listed in Table 2.1 by removing the tert-butyldimethylsilane (TBDMSO) protecting groups on the donor and bridge parts of selected benchmark molecules as shown in the Supporting Information (see Figure A.1). The removal of these groups was done for computational efficiency (particularly geometry optimization) and based on the assumption that the TBDMSO groups provide little contribution to the electronic properties of the D-π-A system. The benchmark set is effectively reduced from 35 to 34 systems after applying these structural modifications. The interchange occurs when the TBDMSO groups are removed from YLD124, yielding the molecule AJY1. The measured properties of these molecules are not identical. The experimental λ_{max} of AJY1 is increased (red shifted) by $\sim$24 nm compared with YLD124; similarly λ_{max} calculated using LC-BLYP red shifts by $\sim$20 nm when the TBDMSO groups are removed. Despite these differences, for simplicity the computed values for the AJY1 structure, henceforth referred to as "YLD124", are compared with measured data for YLD124. Additional calculations using LC-BLYP showed that the λ_{max} values of other modified systems typically red shift by as much as 10% upon removal of the TBDMSO groups and $\beta_{HRS}(2\omega)$ values increase by 10-20%.Although this effect is assumed negligible for this study, this relatively small red shift can result in serious resonance enhancement effects for the measured β_{HRS} [12]. Also, as shown in Figure A.1, for OLD3 and the TCP1-3 molecules, the long alkyl chains hanging from the donor were shortened to make a more compact and rigid structure for more efficient geometry optimization. Similar to the removal of TBDMSO groups, these structural changes were assumed to have negligible impact on the computed electronic properties.

All calculations were performed with the Gaussian-09 Rev D.01 electronic structure package [77]. Conformational analysis was performed on CLD1 and EZFTC structures as shown in Figure 2.1 to determine the lowest-energy configuration (see the Supporting Information and Tables A.1 and A.2 for more details). A transoid backbone with cisoid acceptor ('ttc') was determined to have the most energetically favorable geometry. A ttc configuration was

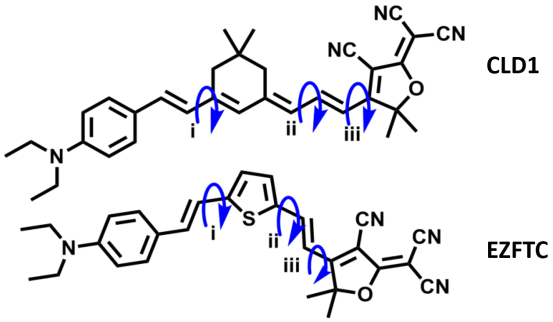

Figure 2.1: **Prototypes for CLD- and FTC-type systems** CLD1 and EZFTC molecules in trans-trans-cis (ttc) configuration. Three rotatable bonds are labeled i, ii, iii, with the donor held in constant configuration.

applied to all systems as shown in Table 2.1 and the geometry of each molecule was optimized at the B3LYP/6-31+G* level of theory using an 'ultrafine' integration grid and default settings, which choose the RMS force on all atoms to converge at a threshold of 3×10^{-4} au or less. For comparison with measurement, the chloroform solvation environment was included in each geometry optimization and property calculation. The polarizable continuum model (PCM) under the linear-response approximation (i.e., non-equilibrium excited-state solvation) was employed for this purpose [106]. All calculations were carried out according to a tightened SCF convergence criteria, requiring density matrix convergence at least 10^{-10} au.

Properties were computed with HF and various DFT methods, including BLYP and its long-range corrected (LC) version, LC-BLYP, along with the pair B3LYP and its long-range corrected variant CAM-B3LYP. For each of the long-range corrected methods, there is included a variable long-range (LR) separation parameter, that determines the ratio of DFT and exact (or HF) exchange included at a particular r_{12} distance [102], [249],[240]. This parameter was tuned from 0 to 1 (all DFT LR exchange to all HF LR exchange, respectively) to examine LR exchange effects, particularly for the computation of λ_{max}. The short-range (SR) exchange parameter for CAM-B3LYP was held at its default, 0.19, for all calculations. LC-BLYP does not include a SR exchange correction.

Excitation energies were computed using the linear response time-dependent DFT (LR-TDDFT) formalism. The excitation energy of the state with the largest oscillator strength was compared to the experimental one-photon peak absorption energy, ΔE_{max}, also denoted λ_{max} when given in wavelength. This transition occurs as an intense low-lying $\pi \rightarrow \pi^*$ transition in the measured absorbance spectrum and is characterized by significant intramolecular charge-transfer (CT) along the molecular axis. This CT transition is known to greatly impact both the linear and nonlinear optical properties of D-π-A chromophores. For device applications, it is ideal to achieve *optical transparency* for these systems such that this CT peak absorbs above the nominal 'red edge' of the visible spectrum at 700 nm but without interferring with telecommunications operating wavelengths (e.g., 1300 nm, 1550 nm) and to also have its higher-energy transitions occurring in the UV [5]. Although it is beneficial for the quality of the EO material, molecular systems that meet these criteria can present a dilemma for HRS measurements due to contamination of the signal from resonance enhancement effects occurring from large absorbance near the second harmonic (SH) of the fundamental wavelength of the measuring device. For the measurements in this study, the fundamental is 1907 nm and the SH is near 950 nm. Thus, the location of measured λ_{max} and linewidth of its corresponding peak can strongly affect the experimentally measured β value and, analogously, the predicted λ_{max} and linewidth can greatly affect the accuracy of the computed frequency-dependent β value.

To get approximate linewidths, simulated absorbance spectra were generated for all computed electronic transitions from ground (g) to n^{th} excited state (e) by fitting the computed oscillator strengths, f_{eg} of each transition to a Gaussian function [243] with full-width-half-maximum (FWHM) of $\Delta\omega$=0.45 eV, according to:

$$\frac{1}{(\sigma\sqrt{2\pi})}\sum_{n=1} {f_{eg}}^{n} \exp^{\frac{-(\omega-\omega_{eg}^{n})^2}{(2\sigma^2)}}, \tag{2.12}$$

where $\sigma = \frac{FWHM}{(2\sqrt{2ln(2)})} \approx 0.19$, describes the standard deviation. The optical properties are dependent upon molecular geometry, thus, it is implied that they are a function of the nuclear coordinates [161]. A FWHM of 0.45 eV was chosen based on the *average* linewidth measured

from experimental absorbance spectra for these molecules. (The default σ in GaussView is 0.4 eV [220]; as a point of interest, recent work toward fully non-empirical simulations of optical band shapes is described in Ref [251]).

The frequency-dependent hyperpolarizabilities consistent with hyper-Rayleigh Scattering (HRS) measurements, $\beta_{HRS}(2\omega)$, were computed at 1907 nm from analytical derivatives obtained via the coupled-perturbed Kohn-Sham (CPKS) method [124], [152]. Specifically, the second-harmonic hyperpolarizability, $\beta(-2\omega;\omega,\omega)$, was computed using CPKS and subsequently the orientational average that describes β_{HRS} was computed using the formulas of Cyvin and Decius [46] to sum over the tensor components:

$$\begin{aligned}\beta^2_{HRS} = \tfrac{6}{35}\textstyle\sum_i \beta^2_{iii} + \tfrac{20}{35}\beta^2_{ijk} \\ +\tfrac{16}{105}\textstyle\sum_{i\neq j} \beta_{iii}\beta_{jjj} + \tfrac{38}{105}\sum_{i\neq j}\beta^2_{iij} \\ +\tfrac{16}{105}[\beta_{iij}\beta_{jkk} + \beta_{jjk}\beta_{kii} + \beta_{kki}\beta_{ijj}]\end{aligned} \tag{2.13}$$

This analysis was done using MATLAB codes developed by Dr. Bruce Eichinger [131] and modified by myself to handle the output from the CPKS calculations in Gaussian-09. For comparison of the hyperpolarizability computed using CPKS-DFT, second-order Møller-Plesset Perturbation (MP2) was used to calculate static hyperpolarizability, using double numerical differentiation of the analytic gradient (first derivative of the energy) via the finite-field method (FFM). In the Gaussian-09 Rev. D.01 package, the analytic dynamic hyperpolarizability is only implemented for HF and some DFT functionals; thus, alternative methods must be used to obtain a frequency-dependent (i.e., 'dispersion-corrected') β with MP2. The MP2 static hyperpolarizability, $\beta_{HRS}(0)$, was corrected for dispersion [2] using two

[2]The term 'dispersion' is used in physics to describe the frequency-dependence of a given quantity; whereas, 'dispersion' is also commonly used in the context of electronic fluctuation due to intermolecular forces such as 'London-dispersion' forces. The DFT functionals which include a dispersion correction, 'D', refer to the latter (e.g., B2PLYP-D, wB97x-D, etc.).

methods. The first is the damped two-level model (TLM) (Equation 2.14) so as to impose the frequency-dependence, ω, consistent with HRS, $\beta_{HRS}(2\omega, \omega_{eg}, \gamma)$ [26]. The TLM fits were performed using a damping factor, γ, set to 0.45 eV for all systems (consistent with the choice of FWHM).

$$\beta_{HRS}(2\omega, \omega_{eg}, \gamma) = g(2\omega, \omega_{eg}, \gamma) \cdot \beta_{HRS}(0),$$
$$g(2\omega, \omega_{eg}, \gamma) =$$
$$\frac{\omega_{eg}^2}{2}\left(\frac{1}{(\omega_{eg}+i\gamma+2\omega)(\omega_{eg}+i\gamma+\omega)} + \frac{1}{(\omega_{eg}-i\gamma-2\omega)(\omega_{eg}-i\gamma-\omega)} + \frac{1}{(\omega_{eg}+i\gamma+\omega)(\omega_{eg}-i\gamma-\omega)}\right) \tag{2.14}$$

The TLM makes it clear that these dispersion-corrected β values depend on an accurate value for the transition energy of the molecule, ω_{eg}. (Throughout this study, ω_{eg} is taken to mean $1240/\lambda_{max}$ in units of eV). This quantity must either come from measurement, which assumes the molecule has already been synthesized, purified, and characterized, or use time-dependent theoretical methods (such as TDDFT) to obtain an approximate ω_{eg}. The use of TDDFT according to the latter is discussed more in Section 2.3. Since experimental absorbance data is available, we convert experimental λ_{max} values to ω_{eg}; thus, the frequency-dependent MP2 values according to TLM are obtained via an *empirical* fit to measured absorbance energies. This method is abbreviated as 'TLM-MP2' in the corresponding tables and figures. The second method of dispersion correction does not assume knowledge of ω_{eg} a priori. Instead, we compute analytical derivatives vis coupled-perturbed Hartree Fock (CPHF) using Gaussian-09 and apply the following correction factor [225]:

$$\beta_{HRS}(2\omega; \omega, \omega) = \Delta^{CPHF} \cdot \beta_{HRS}(0),$$
$$\Delta^{CPHF} = \frac{\beta_{HRS}^{CPHF}(2\omega; \omega, \omega)}{\beta_{HRS}^{CPHF}(0)}, \tag{2.15}$$

where the static MP2 hyperpolarizability is input for $\beta_{HRS}(0)$, thus, yielding a correlated dynamic hyperpolarizability consistent with MP2, $\beta_{HRS}^{MP2}(2\omega; \omega, \omega)$, after applying the multiplicative factor Δ^{CPHF}. This method is abbreviated as 'CPHF-MP2' in the corresponding

tables and figures. Similar to MP2, static hyperpolarizabilities are computed via the FFM in B2PLYP and B2PLYP-D and empirical TLM fits are applied to obtain frequency-dependent $\beta(2\omega)$ values, as well by the dispersion correction shown in Equation 2.15.

Due to significant errors that are sometimes attached to measured absolute hyperpolarizabilities, this study focuses solely on relative hyperpolarizabilities. 'Relative' refers to the absolute hyperpolarizability of the molecule taken as a ratio with the hyperpolarizability of a reference solution. With comparison to measured data, the reference used for all systems in this study is EZ-FTC in $CHCl_3$.

2.3 Results

2.3.1 Frequency-Dependent Hyperpolarizabilities

Calculations from HF, various DFTs, double hybrid methods, and MP2 were performed on thrity-four different molecular systems, including 16 modified molecular structures (illustrated in Figure A.1) along with 18 unmodified structures shown in Table 2.1. [3] Static and frequency-dependent hyperpolarizabilities were computed for HF and DFT via analytic derivatives using the CPHF (or CPKS) method. Static hyperpolarizabilities for MP2 and B2PLYP were computed via numerical differentiation using the FF method. Frequency-dependent hyperpolarizabilities for MP2, B2PLYP, and B2PLYP-D were obtained using TLM and multiplicative-factor dispersion-correction methods discussed in Section 2.2.

Figure 2.2 illustrates how to obtain $\beta_{HRS}(2\omega)$ from $\beta_{HRS}(0)$ using Equation 2.14 with γ=0.45 eV and UV-vis measurements of the peak CT transition for ω_{eg} (eV). The static hyperpolarizabilities were computed using MP2 and the dispersion-corrected values corresponding to 1907-nm (0.65 eV, shown as dashed line) were collected for the 'TLM-MP2' $\beta_{HRS}(2\omega)$ values. The hyperpolarizabilities are taken relative to β_{FTC}, thus the plotted values are:

[3]The unmodified structures are DCDHF, TCF1-CF3, TCF1, EZFTC, DMC3-series, BODIPY-series, TCP0, CLD5, FTCDAAP-series, CLDDAAP-series, JDD-series, AJY2 and AJY3.

$$\frac{\beta_{HRS}^{sys}(2\omega)}{\beta_{HRS}^{FTC}(2\omega)} = \frac{g_{\gamma}^{sys}(\omega, \omega_{eg})}{g_{\gamma}^{FTC}(\omega, \omega_{eg})} \frac{\beta_{HRS}^{sys}(0)}{\beta_{HRS}^{FTC}(0)} \tag{2.16}$$

where the dispersion factor, g, is defined in Equation 2.14. As expected, the dispersion correction curves have maxima near the second harmonic at 950 nm (1.3 eV) of the fundamental wavelength at 1907 nm. The resulting dispersion factors are therefore largely determined by the relative positions of the SH of the fundamental wavelength and the CT transition of the molecule, ω_{eg}, thus, the TLM partially captures the resonance enhancement effects observed in HRS measurements [12]. To illustrate this, the color-coding was chosen according to increasing experimental β_{HRS} value which visually correlates well with increasing dispersion factor and the $\beta_{HRS}(2\omega)$ resulting from the TLM-MP2 curves shown.

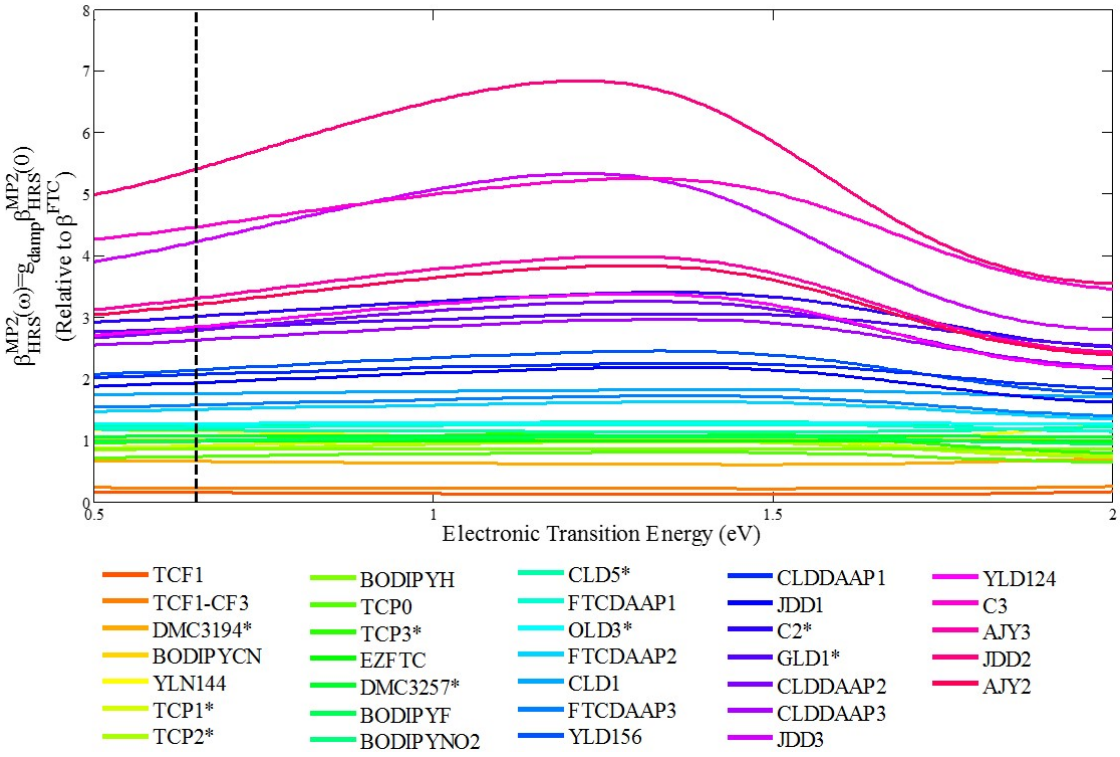

Figure 2.2: **Two-level Model Correction with Homogeneous Damping:** Determination of $\beta_{2\omega}^{MP2}$ from β_0^{MP2}. The curves show the results of Equations 2.14 and 2.16 where ω_{eg} transitions are taken from corresponding λ_{max} values of UV-vis measurements. A damping factor of γ=0.45 eV is used. The dotted line shows the fundamental wavelength used in the HRS measurements (1907 nm = 0.65 eV). The dispersion-corrected values at 1906nm are collected for the TLM fit. The molecules are listed in order of increasing measured β_{HRS}.

Figure 2.3.1 shows the TLM-MP2 results along with the results of DFT and double-hybrid methods in comparison to HRS measurements, with values given in Table A.8. Error bars on HRS measurements correspond to values in Table 2.1. HRS measurements performed by Firestone and Lao are noted by (*) next to the molecule name; otherwise, the measurements were performed by Bale. The following error analysis based on computed and measured hyperpolarizabilities is essentially comprised over 32 (out of 34) of the benchmark molecules since YLD130 and DCDHF do not have measured HRS data at 1907-nm.

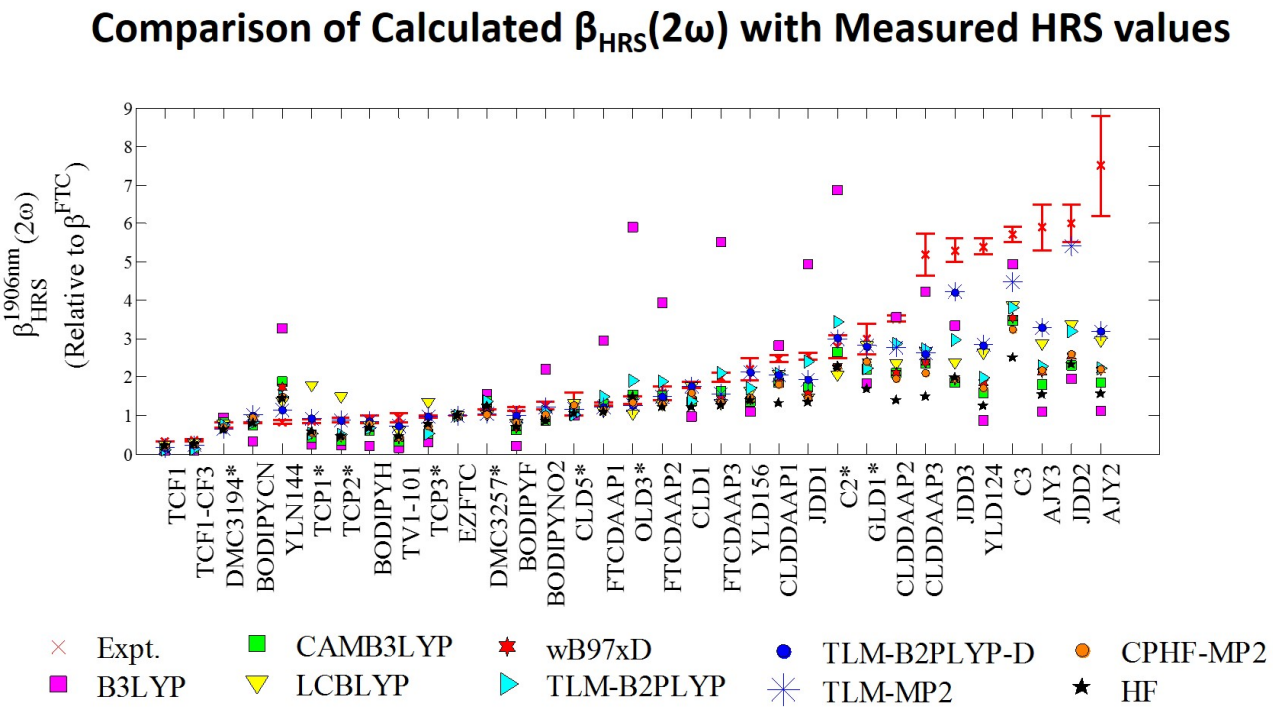

Figure 2.3: **Comparison of Theoretical Methods with Experimental Measurements of Relative Frequency-Dependent Hyperpolarizabilities.** Measurements performed by Firestone are noted by *. Experimental values correspond to those listed in Table 2.1. The molecules are listed in order of increasing measured β_{HRS}. B2PLYP-D results are nearly identical to MP2. B2PLYP-D calculations were not finished for C3, BODIPYNO2, FTCDAAP3, and CLDDAAP2.

Table 2.2 gives statistical measures for accuracy and precision for the computation of $\beta_{HRS}(2\omega)/\beta_{FTC}$ in the form of mean absolute error (MAE) and standard deviation of errors (STE), respectively. The MAE and STE values tend to increase together; in other words, methods with low accuracy also tend to be erratic (both underestimate and overestimate $\beta_{HRS}(2\omega)/\beta_{FTC}$ for different molecules). Other methods such as HF systematically underestimate β [32]. Accordingly, the long-range corrected methods which include long-range HF exchange also tend to systematically underestimate β. Of these methods, LC-BLYP has the least MAE and STE (0.906, 1.258) followed closely by wB97xD (1.049, 1.434) and CAM-B3LYP (1.110, 1.534). BLYP has the largest MAE (and STE) which are at least 6 (and 15)

times greater than the next largest MAE and STE belonging to B3LYP. Because these errors are out of range of the other methods, BLYP is not plotted in Figure 2.3.1. As for B3LYP, the computed hyperpolarizabilities are also unreliable in that they range from $\sim 100\%$ underestimated to $\sim 350\%$ overestimated compared with experimental HRS values (see a plot of relative percent errors in the Supporting Information, Figure A.4). Notably, B3LYP appears to overestimate the hyperpolarizabilities of thiophene-bridge systems, namely OLD3 and the FTCDAAP series. Comparing these results with measurement suggests that B3LYP does not correctly describe the effect that a thiophene in the bridge has on the electronic polarization of the molecule. Interestingly, all methods predict at least 50% larger β values for YLN144 compared with measurement. Because this result is unaninmous among all levels of theory, it is reasonable to question if the 3,4-dinitropyridine acceptor is better than described by the HRS measurement.

Of all of the methods, the best for computing frequency-dependent hyperpolarizability based on MAE and STE is TLM-MP2. However, MP2 comes at significantly greater cost than DFT or HF. Table 2.2 also includes the number of CPU hours (and Walltime) required for computing β of the largest molecule in the set, JDD3 (99 atoms, 424 electrons) using 16 processors per single node. Based on these results, CPKS LC-BLYP computes both static and frequency-dependent β in roughly one hundredth the time it takes MP2 to compute just static hyperpolarizability, β_0. The results of Table 2.2 are summarized in Figure 2.4.

All of the electronic structure methods underestimate β for systems with measured $\beta_{HRS}(2\omega)/\beta_{FTC} > 4$. This discrepancy between theory and experiment may be ascribed to secondary effects occurring during the measurement that may obfuscate the true intensity of the HRS scattering signal, thereby inflating the measured β. One known cause is resonance enhancement which is partially handled by the empirical TLM fit, thus giving favorable results for TLM-MP2.

Combining DFT and MP2 correlation, as is done with B2PLYP, does not show improvement over MP2 or LC-BLYP, but does show improvement over the other methods in regards to MAE. The DFT exchange and correlation parts in B2PLYP are similar to B3LYP,

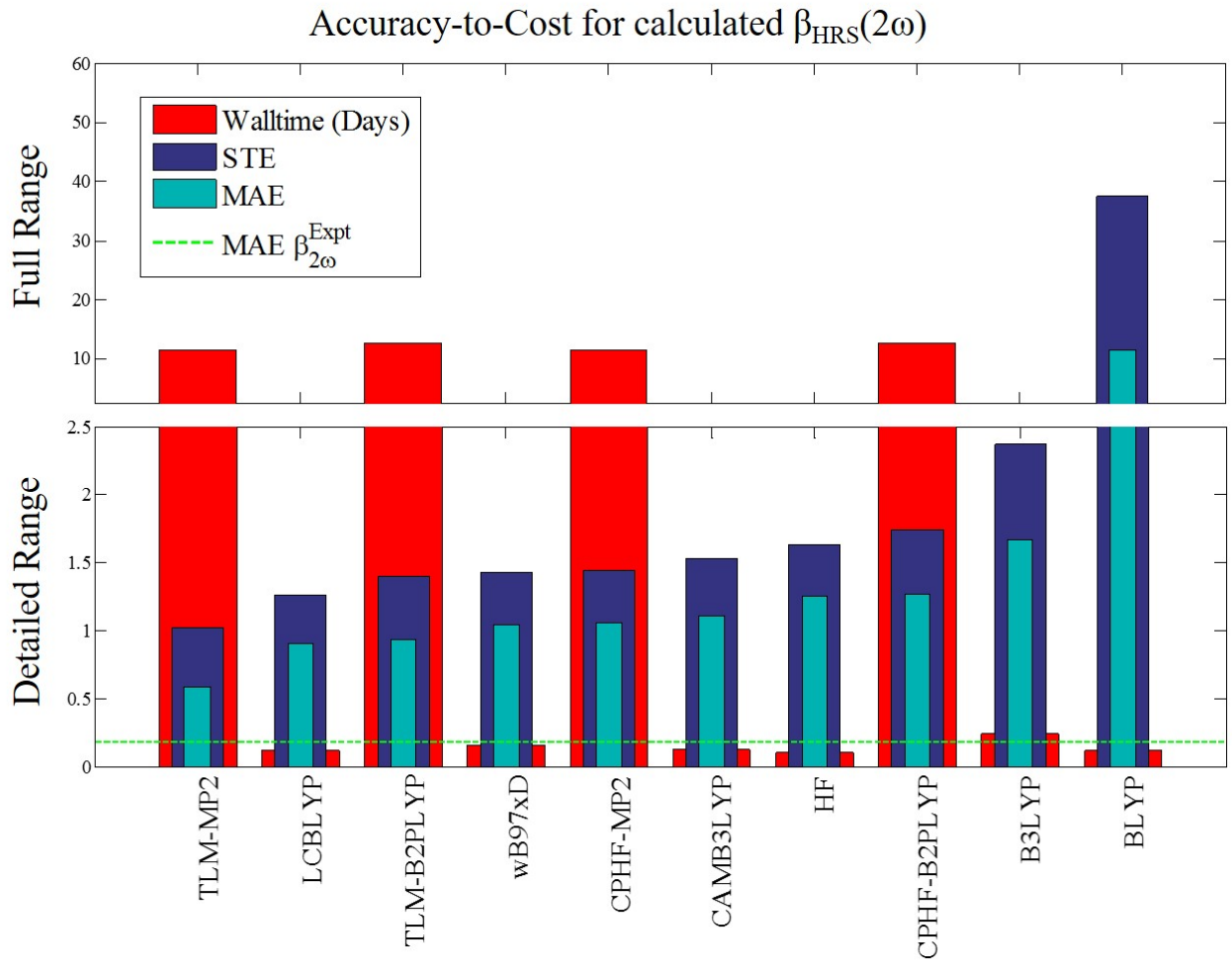

Figure 2.4: **Accuracy-to-Cost for calculated $\beta_{HRS}(2\omega)$.** TLM-MP2 is the most accurate method (MAE=0.592), however, is also the second most expensive behind TLM-B2PLYP ($\sim$ 12 days). HF is the cheapest method (2.5 hours), but is not very accurate. The best DFT method is LC-BLYP (MAE=0.906). When HF exchange is removed from LC-BLYP, resulting in BLYP, the MAE increases by a factor of 13.

which these results have shown performs poorly by itself; thus, the contribution of the MP2 correlation energy and HF exchange is certainly beneficial when compared with this mild hybrid functional. As for reliability, B2PLYP has STE that is $\sim 7\%$ larger than LC-BLYP, but is smaller than any of the other DFTs or HF. Interestingly, the B2PLYP-D β results were almost identical to the results for MP2 with only 0.2368% relative difference. For this reason, the B2PLYP-D values are not included in Table 2.2. B2PLYP-D results are shown in the plots, however, calculations for CLD5, C3, BODIPYNO2, FTCDAAP3, JDD2, and CLDDAAP2 were not completed.

The CPHF dispersion corrected methods (CPHF-MP2, etc.) according to Equation 2.15 generally underestimate β due to the HF correction factor that is < 1.2 for all molecules except for the largest, YLD130 (CPHF factor ~ 1.4). Based on MAE and STE values in Table 2.2, CPHF-MP2 is less reliable than LC-BLYP and CPHF-B2PLYP is performs only as well as HF. Based on these results, multiplying $\beta(0)$ by the CPHF correction factor to get frequency-dependent β values is not advised.

$\beta(2\omega)/\beta_{FTC}$ Method	MAE	STE	CPU hours	Walltime (days)
Expt.	0.196	–	–	–
HF	1.252	1.629	39.6	0.103
BLYP	11.492	37.636	45.5	0.119
LC-BLYP	0.906	1.258	45.7	0.119
B3LYP	1.670	2.376	93.4	0.243
CAM-B3LYP	1.110	1.534	48.6	0.126
wB97xD	1.049	1.434	59.4	0.155
TLM-MP2	0.592	1.021	4393.8	11.4
CPHF-MP2	1.060	1.450	4393.8	11.4
TLM-B2PLYP	0.938	1.400	4849.8	12.6
CPHF-B2PLYP	1.268	1.737	4849.8	12.6

Walltime=CPU hours × Number of Processors. For these calculations, 16 processors were used on 1 node.

Table 2.2: **Mean Absolute Error (MAE), Standard Deviation of Errors (STE), and Computational Cost of computed frequency-dependent hyperpolarizabilities, $\beta_{HRS}(2\omega)/\beta_{FTC}$, with various theoretical methods. MAE is taken with respect to experimental HRS measurements. STE indicates precision of each method.**

2.3.2 Static Hyperpolarizabilities

Comparison of the experimental and theoretical data is complicated by the issue of resonant enhancement and two-photon fluorescence (TPF) interference effects [12], in which the experimental HRS can be inflated by absorbance occurring near the second harmonic (2ω). Some of these issues can be mitigated with the method of experimental measurement by spectrally resolving the scattered light so to exclude the slower time-scale fluorescence phenomena, as well as other modern ultrafast laser techniques [73], [12]. By employing 1907-nm

excitation, both the input frequency and the second harmonic, 2ω, are far from the absorption bands of most chromophores of interest, thus, minimizing the resonance enhancement and TPF effects [12]. Still, some key systems have problematic molar absorptivities near the second harmonic, $\sim$ 950 nm, specifically the high-β systems such as YLD124 (ϵ_{950} $\sim$17400 $M^{-1}cm^{-1}$) and C3 (ϵ_{950} $\sim$17900 $M^{-1}cm^{-1}$) [12]. Therefore, we a priori expect some of the error between theory and measurement to be attributed to issues inherent in the measured values, not the theory per se.

In light of this, it is helpful to consider β when the dispersion (and henceforth, resonance enhancement) of these measurements are removed. This helps determine how molecular structure affects β, thus giving insight into the 'intrinsic hyperpolarizability' of the molecule. One method to get static β values from frequency-dependent measurements is by simply inverting the homogeneously damped TLM, Equation 2.14. Figure 2.3.2 shows the results of inverting Equation 2.14 with γ=0.45 eV and empirical ω_{eg} values such that the dispersion is effectively removed from the 1907-nm HRS measurements, as follows:

$$\frac{\beta_{HRS}^{sys}(0)}{\beta_{HRS}^{FTC}(0)} = \left(\frac{g_{\gamma}^{sys}(\omega,\omega_{eg})}{g_{\gamma}^{FTC}(\omega,\omega_{eg})}\right)^{-1} \frac{\beta_{HRS}^{sys}(2\omega)}{\beta_{HRS}^{FTC}(2\omega)} \tag{2.17}$$

where g is defined in Equation 2.14. The inverted dispersion factor, $\left(\frac{g_{\gamma}^{sys}(\omega,\omega_{eg})}{g_{\gamma}^{FTC}(\omega,\omega_{eg})}\right)^{-1}$, is applied to the experimental HRS values and errors. The β_0 values for HRS measurements along with the results of HF, DFT, MP2, and the double-hybrid methods are given in Table A.8.

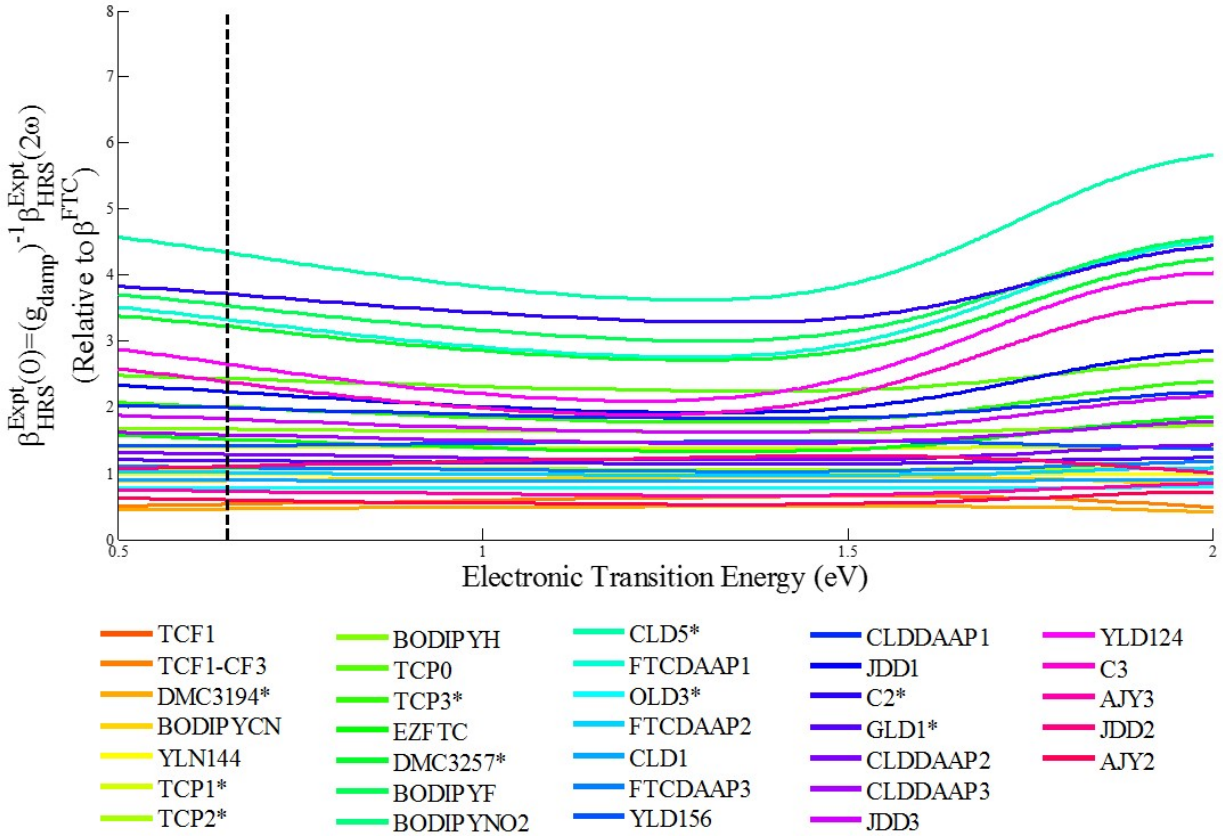

Figure 2.5: **Two-level Model Correction with Homogeneous Damping: Determination of β_0^{Expt} from $\beta_{2\omega}^{Expt}$.** The curves show the results of Equations 2.14 and 2.17 where ω_{eg} transitions are taken from corresponding λ_{max} values for UV-vis measurements for each of the molecules shown. A damping factor of γ=0.45 eV is used. The dotted line shows the fundamental wavelength used in the HRS measurements: 1906 nm = 0.65 eV. The dispersion is effectively removed from the frequency-dependent HRS measurements.

Figure 2.3.2 shows the results of HF, DFT, MP2, and the double hybrids for computing $\beta_{sys}(0)/\beta_{FTC}(0)$ in comparison to HRS measurements that have been fit with Equation 2.17. Table 2.3 gives MAE and STE values for the different theoretical methods in comparison with the inverse TLM-fitted $\beta_{HRS}^{Expt}(0)/\beta_{FTC}$, as well as the CPU hours, previously described in Table 2.2. All of the theoretical methods show smaller errors than the frequency-dependent results shown in Table 2.2, however, their rankings in error are similar. For example, BLYP

and B3LYP still have the largest MAE and STE values. One exception is that the smallest MAE and STE no longer belongs to MP2, but rather LC-BLYP. This result hints at the favorable influence that the TLM fit using empirical parameters has on matching TLM-MP2 to frequency-dependent β, as shown previously in Table 2.2. However, on an even playing field (when the resonance effects are removed from the HRS data), it appears that LC-BLYP outperforms MP2 for computing the intrinsic hyperpolarizability. This makes LC-BLYP an immensely useful tool for determining new target molecules. The results of Table 2.3 are summarized in Figure 2.7.

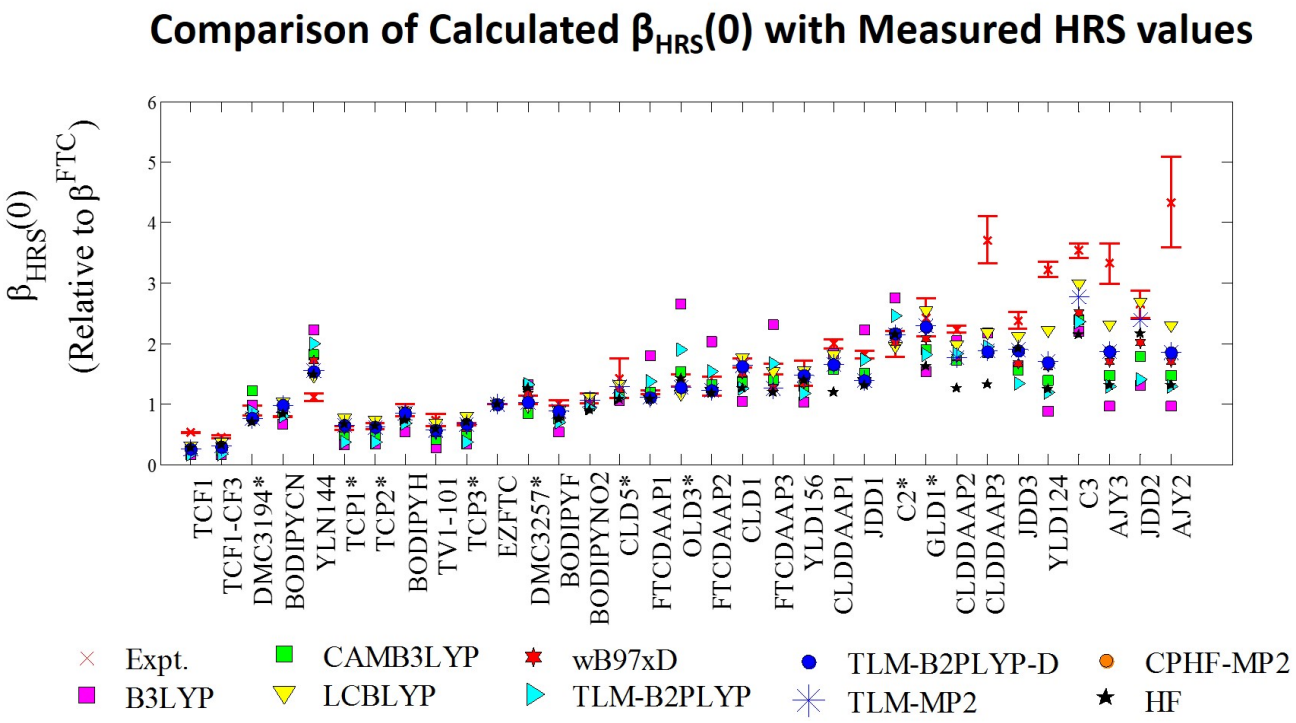

Figure 2.6: **Comparison of Theoretical Methods with Experimental Measurements of Relative Static Hyperpolarizabilities.** Measurements performed by Firestone are noted by *. Experimental values correspond to those listed in Table 2.1. The molecules are listed in order of increasing measured β_{HRS}.

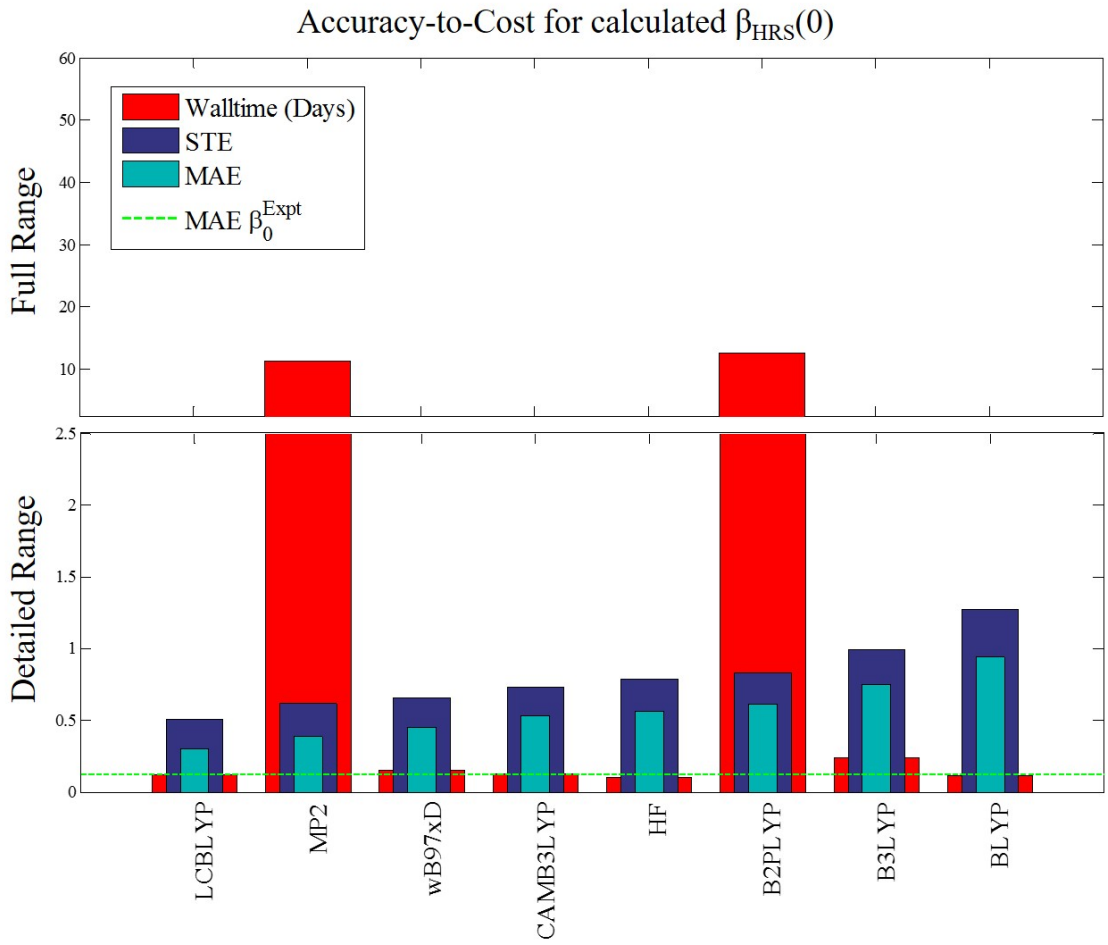

Figure 2.7: **Accuracy-to-Cost for calculated** $\beta_{HRS}(0)$**.** Upon removing dispersion effects from the experimental HRS values using the inverted TLM fit, the resulting $\beta_{HRS}^{Expt}(0)/\beta_{FTC}$ values are compared with computed static hyperpolarizabilities. All of the theoretical methods show smaller errors than the frequency-dependent results shown in Table 2.2. LC-BLYP outperforms MP2 as the most accurate method for $\beta_{HRS}(0)$ (MAE=0.300).

$\beta(0)/\beta_{FTC}$ Method	MAE	STE	CPU hours	Walltime (days)
Expt.	0.136	–	–	–
HF	0.566	0.793	39.6	0.103
BLYP	0.940	1.276	45.5	0.119
LC-BLYP	0.300	0.503	45.7	0.119
B3LYP	0.751	0.998	93.4	0.243
CAM-B3LYP	0.534	0.730	48.6	0.126
wB97xD	0.450	0.655	59.4	0.155
MP2	0.390	0.619	4393.8	11.4
B2PLYP	0.613	0.830	4849.8	12.6

Walltime=CPU hours × Number of Processors. For these calculations, 16 processors were used on 1 node.

Table 2.3: **Mean Absolute Error (MAE), Standard Deviation of Errors (STE), and Computational Cost of computed static hyperpolarizabilities, $\beta_{HRS}(0)/\beta_{FTC}$, with various theoretical methods. MAE is taken with respect to experimental HRS measurements (extrapolated to zero frequency). STE indicates precision of each method.**

2.3.3 Investigating the TLM fit

Of the methods presented here, the best for computing frequency-dependent hyperpolarizability, $\beta_{HRS}(2\omega)/\beta_{FTC}$, based on MAE and STE is TLM-MP2. It is worthy to note that this success is partly due to the use of empirical transition energy data used in the TLM fit. For example, the MAE drops from 0.906 (32% mean absolute percentage error, MAPE) using CPKS-LCBLYP to 0.444 (15% MAPE) using an empirical TLM fit applied to $\beta_{HRS}^{LCBLYP}(0)$. The latter describes a similar procedure applied to $\beta_{HRS}^{MP2}(0)$ values to give TLM-MP2; however, the MAPE resulting from TLM-LCBLYP is 3% lower than that applied to MP2 (MAPE for TLM-MP2 is 18%). The TLM-LCBLYP method also has improved reliability with STE=0.816 compared with TLM-MP2 which has STE=1.021. Thus, the influence

of the TLM fit on MP2 for computing frequency-dependent hyperpolarizabilities should be called into question. For this purpose, the accuracy of the TLM fit when using computed ω_{eg} values and applied to MP2 was investigated. To calculate the electronic transition energy, TD-DFT was employed using the long-range corrected functionals LC-BLYP and CAM-B3LYP. To see the affect that varying the amount of long-range (LR) HF exchange has on the strongest (largest oscillator strength) transition, the range-separation parameter in each functional was varied from 0 to 1. The relative percent errors of measured and computed λ_{max} (inversely proportional to ω_{eg}) with respect to the fraction of LR HF exchange are shown in the Supporting Information, see Figure A.5. These computed ω_{eg} values were then plugged into the TLM Equation 2.14 and applied to static hyperpolarizabilities computed using MP2, $\beta_{HRS}^{MP2}(0)$. The results are shown with comparison to the empirical TLM-MP2 results in Figure A.7. The mean absolute errors (MAE) and mean absolute percentage errors (MAPE) between the computed $\beta_{HRS}^{MP2}(2\omega)$ at each fraction of LR HF exchange and the corresponding measured HRS values were computed. The resulting MAPE curves for each of the 'TD-DFT-TLM' methods (DFT=LC-BLYP or CAM-B3LYP) are shown in Figure 2.8 with comparison to the MAPE for the Empirical TLM fit applied to $\beta_{HRS}^{MP2}(0)$ and $\beta_{HRS}^{LCBLYP}(0)$. The MAPE for CPKS-LCBLYP is shown for comparison to a method that derives the frequency-dependent hyperpolarizabilities via analytic differentiation rather than a multiplicative dispersion factor.

The accuracy of the TLM fit is highly dependent on the value of ω_{eg} and as a result the approximate ω_{eg} determined using TD-DFT result in MAPE that is 31-120%. The smallest MAPE of the TD-DFT-TLM fits corresponds to LC-BLYP with 0.15 LR HF exchange; whereas, the largest error corresponds to LC-BLYP with zero LR HF exchange (i.e., BLYP). The MAPE for CPKS-LCBLYP is within the smallest MAE of the TD-DFT-TLM fits ($\sim 32\%$), but has a few key advantages over the TLM fits, namely: i) frequency-dependent hyperpolarizabilities are computed using analytic differentiation, thus not only is this method more numerically stable than FFM (used for MP2), but also when the calculation is completed no additional analysis is required to obtain $\beta(2\omega)$ which makes for easier

implementation; ii) empirical parameterization is *not* necessary to obtain accurate results which makes it useful for target molecules that have not yet been synthesized, purified, and characterized with UV-vis absorbance studies; and iii) CPKS LC-BLYP is significantly more cpu affordable than MP2. For these reasons, CPKS LC-BLYP is recommended for determining frequency-dependent hyperpolarizabilities in an accurate and timely manner that does not require empirical parameterization or additional fitting. MP2 is still an excellent method for computing static hyperpolarizabilities, especially when compared to the other DFTs and HF, as well as the double hybrid methods. The major flaw of using MP2 is simply the computational cost. Instead, the cpu-affordable LC-BLYP has proven to be an exceptional DFT for computing frequency-dependent β for the organic D-π-A systems of interest to this study.

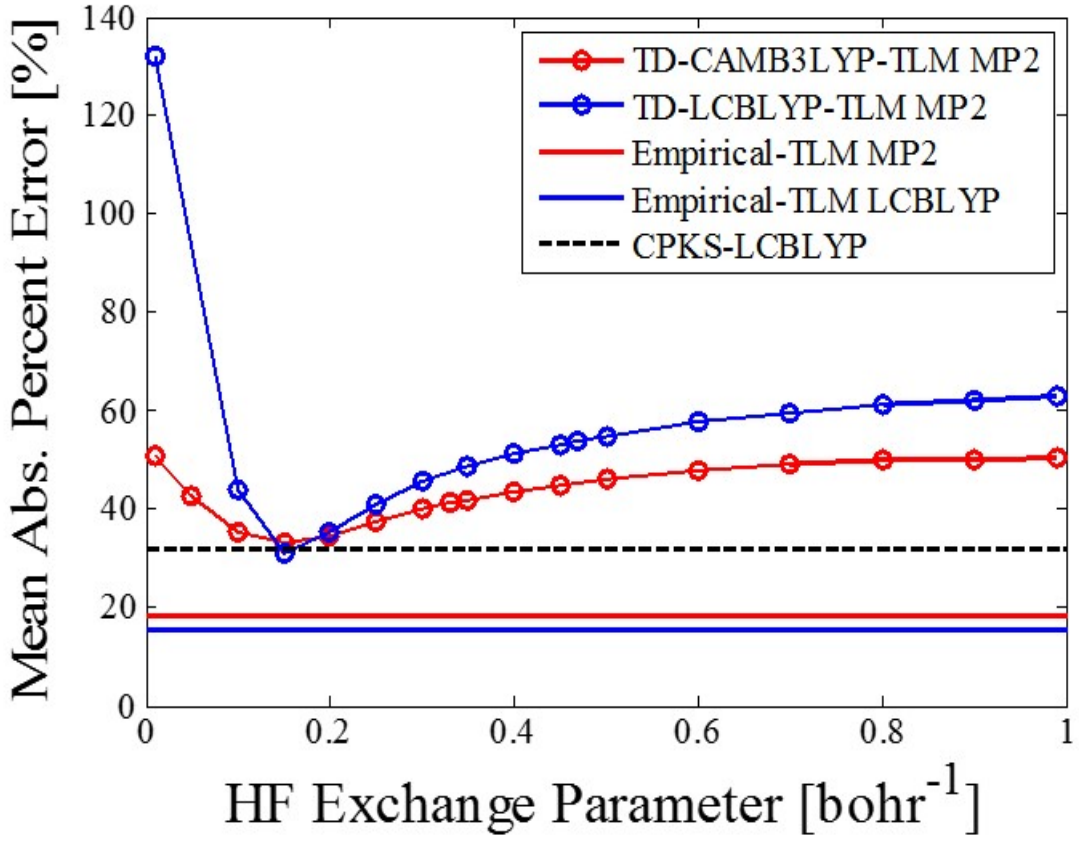

Figure 2.8: **Influence of Experimental vs. Calculated ω_{eg} in the TLM fit.** Red and blue circles represent the mean absolute percentage error [MAPE, %] between HRS measurement and different TLM fits according to the amount of LR HF exchange included in CAM-B3LYP or LC-BLYP, respectively, for computing ω_{eg} applied to $\beta_{HRS}^{MP2}(0)$. The solid red and blue lines represent the TLM fits that have measured ω_{eg} values applied to $\beta_{HRS}^{MP2}(0)$ and $\beta_{HRS}^{LCBLYP}(0)$ with MAPE values of 18% and 15%, respectively. The dotted black line is the MAPE for CPKS-LCBLYP (32%).

2.4 Summary and Conclusions

Static and frequency-dependent hyperpolarizabilities for thirty-two[4] D-π-A systems were computed from analytical differentiation using the coupled-perturbed Hartree-Fock (CPHF)

[4]There are 34 systems total of the modified set (all with measured UV-vis data); however, YLD130 and DCDHF do not have measured HRS data at 1907-nm to compare with theory

and analogous CP-Kohn-Sham (CPKS) methods applied to HF and various DFTs, including LC-BLYP, CAM-B3LYP, wB97xD, B3LYP, and BLYP. Static hyperpolarizabilities for these molecules were also computed from numerical derivatives using the finite-field method (FFM) applied to double hybrid methods (B2PLYP, B2PLYP-D) and MP2. Frequency-dependent hyperpolarizabilities for the double hybrids and MP2 were obtained by multiplying the static β values by a two-level model (TLM) fit with empirical parameterization, as well as by the ratio of frequency-dependent and static hyperpolarizability computed with CPHF, $\beta^{CPHF}(2\omega)/\beta^{CPHF}(0)$.

For each computational method, the elements of the calculated second-harmonic hyperpolarizability tensor, $\beta(-2\omega;\omega,\omega)$, were orientationally averaged and taken with respect to the hyperpolarizability of a reference molecule, EZFTC, computed at the same level of theory. The resulting $\beta^{sys}_{HRS}/\beta^{FTC}_{HRS}$ values for each molecule in the 35-benchmark set were then compared with experimental HRS values. The accuracy of each computational method was assessed by averaging the absolute error (MAE) between computed $\beta^{sys}_{HRS}/\beta^{FTC}_{HRS}$ and HRS measurement for each molecule. The reliability of each computational method was assessed by determining the standard deviation of signed errors (STE) between computed $\beta^{sys}_{HRS}/\beta^{FTC}_{HRS}$ and HRS measurement for each molecule. According to these criteria, the most accurate and reliable method for computing frequency-dependent hyperpolarizability is TLM-MP2 (MAE=0.592, STE=1.021), followed by LC-BLYP (MAE=0.906, STE=1.258). The worst methods for computing $\beta(2\omega)$ are DFTs which do not include long-range HF exchange, BLYP and B3LYP, which had MAE$>$ 1.67 and STE$>$ 2.38.

The double-hybrid method, B2PLYP, does not show improvement over MP2 or LC-BLYP, but does show improvement over the other methods in regards to MAE. As for reliability, B2PLYP has STE that is $\sim 7\%$ larger than LC-BLYP, but is smaller than any of the other DFTs or HF. The B2PLYP-D static hyperpolarizability results were almost identical to the results for MP2 with only 0.2368% relative difference.

Multiplying MP2 static hyperpolarizabilities by a CPHF dispersion correction factor, $\beta^{CPHF}(2\omega)/\beta^{CPHF}(0)$, results in frequency-dependent 'CPHF-MP2' β values that generally

underestimate the measured HRS values. This is due to the small correction factors that are < 1.2 for all molecules except for the largest, YLD130 (CPHF factor ~ 1.4). Based on MAE and STE values in Table 2.2, CPHF-MP2 (MAE=1.060, STE=1.450) is less accurate and reliable than LC-BLYP. In fact, its errors are slightly larger than another LC-DFT method, wB97xD (MAE=1.049, STE=1.434). Applying the CPHF dispersion factor to B2PLYP, the resulting 'CPHF-B2PLYP' β have similar MAE and STE as HF (MAE=1.252, STE=1.629). Based on these results, multiplying $\beta(0)$ by the CPHF correction factor to get frequency-dependent β values is not advised due to its performance being less than some LC-DFT methods (LC-BLYP and wB97xD).

All of the electronic structure methods underestimate frequency-dependent β for systems with measured $\beta_{HRS}(2\omega)/\beta_{FTC} > 4$. This discrepancy between theory and experiment may be attributed to secondary dispersion effects occurring during the measurement that may obfuscate the true intensity of the HRS scattering signal, thereby inflating the measured β_{HRS} value. Some known causes are two-photon fluorescence (TPF) and resonance enhancement, for which the latter is partially handled by the empirical TLM fit, thus giving favorable results for TLM-MP2. However, it was determined that the accuracy of the TLM-MP2 method is highly dependent on the value of ω_{eg} in the TLM fit. To test this, an approximate ω_{eg} determined using TD-DFT was used in the TLM fit resulting in mean absolute percentage errors (MAPE) between 31-120% compared with 18% (on average) for the empirical TLM fit applied to MP2. The CPKS-LCBLYP has an MAPE that is within the low range of errors ($\sim 32\%$) for the TD-DFT TLM fits, but it instead obtains $\beta(2\omega)$ from frequency-dependent perturbations via analytical derivatives thus ensuring greater generality and numerical stability than FFM. It also does not require empirical parameterization or additional fitting and it is significantly more cpu affordable than MP2. Furthermore, upon removing dispersion from the measured β_{HRS}/β_{FTC} values and comparing with computed static hyperpolarizabilities, LC-BLYP was the most accurate method (MAE=0.300) of the electronic structure methods explored here.

MP2 is overall an accurate and reliable method for computing hyperpolarizabilities of

D-π-A molecules. However, for this study, MP2 required as much as 4400 cpu hours on 16 processors per node compared with LC-BLYP which ran the same calculation using 46 cpu hours on the same hardware. Thus, for this study we found that LC-BLYP is the most cost effective electronic structure method for computing static and frequency-dependent hyperpolarizabilities compared with experimental HRS data of a structurally diverse set of well-characterized D-π-A molecules.

2.4.1 Supporting Information

Additional figures and tables are located in Appendix A.

Appendix A includes, in order:

1. Conformational Analysis of FTC and CLD type systems
2. Description of Modified Structures for Computational Studies
3. Determination of Average Absorbance FWHM for the 34 molecule test set
4. Relative Percent Error between Measured and Computed $\beta_{HRS}(2\omega)/\beta_{FTC}$
5. Discussion of absolute frequency-dependent hyperpolarizabilities
6. Computed Electronic Transition Energies using LC-BLYP and CAM-B3LYP with varying LR HF exchange
7. Computed Dynamic Hyperpolarizabilities using LC-BLYP and CAM-B3LYP with varying LR HF exchange
8. Damped TLM fit using computed ω_{eg}
9. Data Tables for Computed Static and Dynamic Relative Hyperpolarizabilities

10. Measured and Simulated Absorbance Spectra for the 34 (modified) molecule benchmark set

2.4.2 Acknowledgements

Work at University of Washington was partially supported by the National Science Foundation (STC- MDITR DMR-0120967 and DMR-0905686) and the Air Force Office of Scientific Research (FA9550-09-1-0682, FA9550-10-1-0558, and FA9550-15-1-0319) and the University of Washington Student Technology Fund (STF). I thank Prof. Larry Dalton, Dr. Delwin Elder and other members of the Dalton group for helpful discussions. This work was facilitated though the use of the AFRL Spirit supercomputer system at the DoD supercomputing resource center. I would like to thank Dr. Joshua Hendrickson who is the principal investigator for the Nanobeam Nanophotonics subproject on Spirit that I am very fortunate to be a part of. I also express special thanks to Dr. Lewis Johnson who first introduced me to electronic structure calculations using Gaussian. Dr. Johnson also studied the performance of DFT methods for computing hyperpolarizabilities of CLD1 and EZFTC during his graduate studies. I especially thank Dr. Denise Bale for providing experimental HRS and raw UV-vis data for this study.

References

[2] C. Adamo and D. Jacquemin. "The Calculations of Excited-State Properties with Time-Dependent Density Functional Theory". In: *Chem. Soc. Rev.* 42 (2013), p. 845.

[3] A. J. P. Akelaitis et al. "Synthesis and electro-optic properties of amino-phenyl-thienyl donor chromophores". In: *Opt. Mater. (Amsterdam, Neth.)* 30 (2008), pp. 1504–1513.

[5] J. Andzelm et al. "Performance of DFT Methods in the Calculation of Optical Spectra of TCF-Chromophores." In: *J. Chem. Theory Comput.* 5 (2009).

[12] D. H. Bale. "Nonlinear Optical Materials Characterization Studies Employing Photostability, Hyper-Rayleigh Scattering, and Electric Field Induced Second Harmonic Generation Techniques." Thesis. 2007.

[13] D. H. Bale et al. "Dielectric Dependence of the First hyperpolarizability for Electro-Optic Chromophores". In: *J. Phys. Chem. B.* 115 (2011).

[16] A. D. Becke. "A New Mixing of Hartree-Fock and Local Density-Functional Theories". In: *J. Chem. Phys.* 98 (1993), p. 1372.

[17] A. D. Becke. "Density-functional exchange energy approximation with correct asymptotic-behavior". In: *Phys. Rev. A* 38 (1988), pp. 3098–3100.

[26] J. Campo et al. "Practical Model for First Hyperpolarizability Dispersion Accounting for Both Homogeneous and Inhomogeneous Broadening Effects". In: *J. Phys. Chem. Lett.* 3 (2012), pp. 2248–2252.

[28] M. E. Casida. "Time-Dependent Density-Functional Theory for Molecules and Molecular Solids". In: *J. Mol. Struct. (THEOCHEM)* 914 (2009), p. 3.

[29] D.M. Casimier et al. "Demonstration of a Low Vpi-L Modulator with GHz Bandwidth Based on Electro-Optic Polymer-Clad Silicon Slot Waveguides". In: *Proc. SPIE* 5351 (2004), pp. 243–252.

[30] J. Chai and M. Head-Gordon. In: *Phys. Chem. Chem. Phys* 10 (2008).

[32] B. Champagne and M. Wergifosse. "Electron Correlation effects on the first hyperpolarizability of push-pull pi-conjugated systems". In: *J. Chem. Phys* 134 (2011).

[35] B. Champagne et al. "Density functional theory investigation of the polarizability and second hyperpolarizability of polydiacetylene and polybutatriene chains: Treatment of exact and role of correlation". In: *J. Chem. Phys.* 125 (2006), p. 194114.

[38] Y.J. Cheng et al. "Demonstration of a Low Vpi-L Modulator with GHz Bandwidth Based on Electro-Optic Polymer-Clad Silicon Slot Waveguides". In: *Chem. Mater.* 19 (2007), pp. 1154–1163.

[39] Y.J. Cheng et al. “Donor-Acceptor thiolated polyenic chromophores exhibiting large optical nonlinearity and excellent photostability”. In: *Chem. Mater.* 20.15 (2008), pp. 5047–5054.

[45] C. J. Cramer. *Essentials of computational chemistry: theories and models*. Chinchester, UK: Wiley and Sons, 2004.

[46] S. J. Cyvin, J. E. Rauch, and J. C. Decius. “Theory of Hyper-Raman Effects (Nonlinear Inelastic Light Scattering): Selection Rules and Depolarization Ratios for the Second-Order Polarizability”. In: *J. Chem. Phys.* 43 (1965).

[60] J. A. Davies et al. “Rational Enhancement of Second-Order Nonlinearity: Bis-(4-methoxyphenyl)hetero-aryl-amino Donor-Based Chromophores: Design, Synthesis, and Electrooptic Activity”. In: *J. Am. Chem. Soc* 130 (2008), pp. 10565–10575.

[63] F. Ding et al. “An efficient method for calculating dynamic hyperpolarizabilities using real-time time-dependent density functional theory”. In: *J. Chem. Phys.* 138 (2013), p. 064104.

[66] A. Dreuw and M. Head-Gordon. “Failure of Time-Dependent Density Functional Theory for Long-Range Charge-Transfer Excited States: The Zincbacteriochlorin-Bacteriochlorin and Bacteriochlorophyll-Spheroidene Complexes”. In: *J. Am. Chem. Soc.* 126 (2004), pp. 4007–4016.

[67] A. Dreuw and M. Head-Gordon. “Single-Reference ab Initio Methods for the Calculation of Excited States of Large Molecules”. In: *Chem. Rev.* 105 (2005), pp. 4009–4037.

[69] A. Elangovan and J. Davies. “Rational Enhancement of Second-Order Nonlinearity: Bis-(4-methoxyphenyl)hetero-aryl-amino Donor-Based Chromophores: Design, Synthesis, and Electrooptic Activity”. In: *J. Am. Chem. Soc* 130 (2008), pp. 10565–10575.

[73] K. Firestone. “Frequency-agile hyper-Rayleigh scattering studies of nonlinear optical chromophores”. Thesis. 2005.

[77] M. J. Frisch et al. *Gaussian 09, Revision D.01.* Computer Program. 2013.

[79] K. Garrett et al. “Optimum Exchange for Calculation of Excitation Energies and Hyperpolarizabilities of Organic Electro-optic Chromophores”. In: *Journal of Chemical Theory and Computation* 10.9 (2014), pp. 3821–3831.

[84] D.C. Graham et al. “Optimization and Basis-Set Dependence of a Restricted-Open-Shell Form of B2-PLYP Double-Hybrid Density Functional Theory”. In: *J. Phys. Chem. A* 113 (2009), pp. 9861–9873.

[85] S. Grimme. “Semiempirical hybrid density functional with perturbative second-order correlation”. In: *J. Chem. Phys.* 124 (2006), pp. 034108–16.

[86] S. Grimme, F. Neese, and T. Schwabe. “Analytic derivatives for perturbatively corrected “double hybrid” density functionals: Theory, implementation, and applications”. In: *J. Chem. Phys.* 126 (2006), pp. 124115–15.

[102] H. Iikura et al. “Long-range correction scheme for generalized-gradient-approximation exchange functionals”. In: *J. Chem. Phys.* 115 (2001), pp. 3540–44.

[105] C. M. Isborn et al. “Comparison of Static First Hyperpolarizabilities Calculated with Various Quantum Mechanical Methods.” In: *J. Phys. Chem. A.* 111 (2007).

[106] Tomasi J., Mennucci B., and Cammi R. “Quantum Mechanical Continuum Solvation Models”. In: *Chem. Rev.* 105 (2005), p. 2999.

[109] D. Jacquemin et al. “Extensive TD-DFT Benchmark: Singlet-Excited States of Organic Molecules”. In: *J. Chem. Theory Comput.* 5 (2009), p. 2420.

[111] D. Jacquemin et al. “TD-DFT Performance for the Visible Absorption Spectra of Organic Dyes: Conventional versus Long-Range Hybrids”. In: *J. Chem. Theory Comput.* 4 (2008), p. 123.

[112] S.-H. Jang et al. In: *Chem. Mater.* 18 (2006), pp. 2982–2988.

[114] F. Jensen. *Introduction to Computational Chemistry*. West Sussex, England: Wiley and Sons, 2006.

[118] P. Johnston. Univ. of Washington, Seattle, WA. Unpublished work. 2011.

[124] M. Kamiya et al. "Nonlinear optical property calculations by the long-range-corrected coupled-perturbed Kohn-Sham method." In: *J. Chem. Phys.* 122 (2005).

[129] A. Karton et al. "Highly Accurate First-Principles Benchmark Data Sets for the Parametrization and Validation of Density Functional and Other Approximate Methods. Derivation of a Robust, Generally Applicable, Double-Hybrid Functional for Thermochemistry and Thermochemical Kinetics". In: *J. Phys. Chem. A* 112 (2008), pp. 12868–12886.

[131] T. Kinnibrugh et al. "Influence of isomerization on nonlinear optical properties of molecules." In: *J. Phys. Chem. B.* 110.27 (2006), pp. 13512–22.

[133] B. Kirtman et al. "Calculation of electric dipole (hyper)polarizabilities by long-range-correction scheme in density functional theory: a systematic assessment for polydiacetylene and polybutatriene oligomers." In: *J. Chem. Phys.* 128.11 (2008), p. 114108.

[150] A. Laurent and D. Jacquemin. "TD-DFT Benchmarks: A Review". In: *Int. J. Quantum Chem.* 113 (2013), p. 2019.

[152] A. Lee and S. Colwell. "The determination of hyperpolarizabilities using density functional theory with nonlocal functionals". In: *The Journal of Chemical Physics* 101 (1994), p. 9704.

[153] C. Lee, W. Yang, and R.G. Parr. "Development of the Colle-Salvetti correlation-energy formula into a functional of the electron density". In: *Phys. Rev. B* 37 (1988), pp. 785–789.

[157] Y. Liao. Univ. of Central Florida, Orlando, FL. Unpublished work. 2008.

[161] D. Lingerfelt et al. “Dynamical Investigations of Inhomogeneous Vibrational Broadening in Diluted Magnetic Semiconductor Nanocrystals”. In: *The Journal of Physical Chemistry C* 118.6 (2014), pp. 3266–3273.

[164] K. Lopata et al. “Excited-State Studies of Polyacenes: A Comparative Picture Using EOMCCSD, CR-EOMCCSD(T), Range-Separated (LR/RT)-TDDFT, TD-PM3, and TD-ZINDO”. In: *Journal of Chemical Theory and Computation* 7.11 (2011), pp. 3686–3693.

[169] S. Marder et al. “Relation Between Bond-Length Alternation and Second Electronic Hyperpolarizability of Conjugated Organic Molecules.” In: *Science* 261 (1993), pp. 186–189.

[190] P. Petelenz and B. Pac. “Is Dipole Moment a Valid Descriptor of Excited State’s Charge-Transfer Character?” In: *Journal of the American Chemical Society* 135.46 (2013), pp. 17379–17386.

[195] M.A. Rohrdanz and J.M. Herbert. “Simultaneous benchmarking of ground- and excited-state properties with long-range-corrected density functional theory.” In: *J. Chem. Phys.* 129 (2008).

[196] M.A. Rohrdanz, K.M. Martins, and J.M. Herbert. “A long-range-corrected density functional that performs well for both ground-state properties and time-dependent density functional theory excitation energies, including charge-transfer excited states.” In: *J. Chem. Phys.* 130 (2009).

[216] S. Sok et al. “Solvent Induced Shift of the Lowest Singlet pi to pi* Charge-Transfer Excited State of p Nitroaniline in Water: An Application of the TDDFT/EFP1 Method”. In: *The Journal of Physical Chemistry A* 115.35 (2011), pp. 9801–9809.

[220] P. J. Stephens and N. Harada. *Plotting UV-vis Spectra from oscillator and dipole strengths*. Gaussian Technical Notes. 2014. URL: `www.gaussian.com/g_whitepap/tn_uvvisplot.htm`.

[224] K. Y. Suponitsky, Y. Liao, and A. E. Masunov. "Electronic Hyperpolarizabilities for Donor Acceptor Molecules with Long Conjugated Bridges: Calculations versus Experiment." In: *J. Phys. Chem. A.* 113 (2009).

[225] K. Y. Suponitsky, S. Tafur, and A. E. Masunov. "Applicability of Hybrid Density Functional Theory Methods to Calculation of Molecular Hyperpolarizability". In: *J. Chem. Phys.* 129 (2008), p. 044109.

[227] A. Szabo and N. Ostlund. *Modern Quantum Chemistry.* New York: McGraw-Hill, 1982.

[228] A. Tarnopolsky et al. "Double-Hybrid Functionals for Thermochemical Kinetics". In: *J. Phys. Chem. A* 112 (2008), pp. 3–8.

[229] Y. Tawada et al. "A long range corrected time-dependent density functional theory." In: *J. Chem. Phys.* 120 (2004).

[240] O. A. Vydrov et al. "Importance of short-range versus long-range Hartree Fock exchange for the performance of hybrid density functionals". In: *J. Chem. Phys.* 125 (2006).

[243] E.W. Weisstein. *Gaussian Function.* From MathWorld–A Wolfram Web Resource; Accessed via www.mathworld.wolfram.com/GaussianFunction.html. 2015.

[249] T. Yanai, D.P. Tew, and N.C. Handy. "A new hybrid exchange-correlation functional using the Coulomb-attenuating method (CAM-B3LYP)." In: *Chem. Phys. Lett.* 393.51 (2004).

[251] R. Zalesny et al. "Toward Fully Nonempirical Simulations of Optical Band Shapes of Molecules in Solution: A Case Study of Heterocyclic Ketoimine Difluoroborates". In: *The Journal of Physical Chemistry A* 119.21 (2015), pp. 5145–5152.

Chapter 3

TUNING EXACT EXCHANGE IN DFT USING KOOPMANS' THEOREM TO ACCURATELY PREDICT λ_{MAX} AND β: COMPARISONS BETWEEN THEORY AND MEASUREMENT

Some parts of this chapter were adapted with permission from *The Journal of Chemical Theory and Computation*, **2014** *10* (9), pp. 3821-3831.

Long-range corrected (LC) and range-separated hybrid (RSH) density functionals have been reported to perform better than conventional functionals for a myriad of molecular properties that are sensitive to long-range interactions, including Rydberg excitations and charge-transfer, as well as polarizabilities and nonlinear optical properties in large π-conjugated molecules [14], [82], [83], [95], [240], [207], [107], [218]. The optimal value of the range-separation parameter, ω (introduced in Chapter 2), is strongly dependent on the nature of a particular D-π-A system since it controls the transition between SR and LR scales depending on the electron correlation of the system [143]. Various optimal-tuning strategies have been developed to combat this issue, such that ω can be chosen in a "system-specific but non-empirical way" [127]. Such tuning strategies are based on a choice of ω that satisfies a known exact property. One property that the true, exact density functional should possess is that the computed ionization potential (IP) of a molecule should be equal to the negative of the energy of the highest occupied molecular orbital, ϵ_{HOMO}, i.e. it should obey Koopmans theorem [140], [9], [7], [11]. Because of the delocalization error of DFT, the energy of the HOMO is generally predicted to be too high in energy relative to the IP. This can be remedied by mixing some exact exchange into the DFT energy, but the amount of exchange necessary to enforce Koopmans theorem is system dependent. By *tuning* ω to the value at which the $IP = -\epsilon_{HOMO}$, the delocalization error is minimized, which has been shown to improve the accuracy of some computed molecular properties, such as IP, EA, and fundamental energy gaps [143]. The 'optimal' ω for an N-electron molecule is determined where the energy difference, J_{IP},

equals zero:

$$J_{IP} = \epsilon_{HOMO}(N) + [E_{gs}(N-1) - E_{gs}(N)], \tag{3.1}$$

where $\epsilon_{HOMO}(N)$ is the highest-occupied molecular orbital (HOMO) energy for the N-electron system and $E_{gs}(N)$ is the corresponding SCF energy (i.e., total ground-state energy). For charge transfer systems, we also consider the electron affinity (EA) of the molecule. However, unlike the connection between the ϵ_{HOMO} and IP employed in Equation 3.1, there is no rigorous theoretical basis for an analogous connection between the energy, ϵ_{LUMO}, of the lowest unoccupied molecular orbital and EA. A convenient remedy for this is to apply the IP tuning to the anion, $N+1$, electron system. This leads to the second tuning condition to be met for the optimal ω value where J_{EA} equals zero energy difference:

$$J_{EA} = \epsilon_{HOMO}(N+1) + [E_{gs}(N) - E_{gs}(N+1)], \tag{3.2}$$

thus, for each system in its optimized geometry, the optimal ω value is that at which both J_{IP} and J_{EA} achieve zero difference between the neutral and anionic HOMO energies and neutral and anionic ionization potentials, respectively. We examine the simple approach of achieving zero difference with their sum:

$$J_{GAP} = J_{IP} + J_{EA} \tag{3.3}$$

The 'J_{GAP}-optimal tuning method', as I will call it here, has recently been reported to outperform default-parameterized LC functionals for predicting optical aborption spectra, particularly those transitions attributed to charge-transfer excitations [187], [146], [110]. Few studies outside of this work have explored this tuning method applied to first-order hyperpolarizabilities [80], [81]. Based on these previous findings, we explore the effectiveness of the J_{GAP}-optimal tuning method in predicting optical properties of interest to organic electro-optic materials.

In this chapter, we examine how different values of ω affect the accuracy of the computed λ_{max} and hyperpolarizabilty β for a benchmark set of NLO charge transfer molecules using three LC/RSH density functionals: LC-BLYP, LC-ω-PBE, and CAM-B3LYP [102], [240], [249]. We determine if tuning ω using Koopmans' theorem improves the accuracy of these computed properties compared to the default ω of each of these functionals. In Section 1 we describe a subset of 14 molecules from

Table 2.1 chosen for this study. Section 2 gives the computational details. In Section 3 we present the optimally tuned ω values for the benchmarking set with the three functionals and carefully analyze the role that exact exchange plays in our results. In Sections 4 and 5 we compute the excitation energies and hyperpolarizabilties, respectively, over the range of ω and compare the best fit with experimental measurement to the tuned ω values from Section 3. In Section 5, we conclude by sharing our recommendations for optimal exchange in DFT for computing optical properties based on the results in Sections 4 and 5.

3.1 The FTC-CLD Benchmark Set and Donor-Acceptor Length Metric

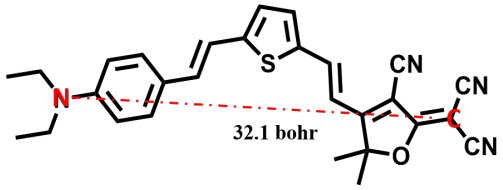

Figure 3.1: **Description of Donor-Acceptor (D-A) length** Distance between donor nitrogen (highlighted blue 'N') and malononitrile carbon (highlighted blue 'C') of the acceptor as a simple metric of the chromophore length, labeled D-A length in Table 3.1.

Structures and experimental properties for the 14-molecule test set used in this study are shown in Table 3.1. Each of the molecules in this test set were chosen from Table 2.1 because they each contain similar donor and acceptor groups; namely, a tricyanofuran (TCF) acceptor linked through a π-conjugated bridge to a N,N-diethylaniline donor. The main variation is the bridge character, which was already classified in Chapter 2 as either thienylenevinylene (FTC-type), polyene (CLD-type) [5], or short-bridge type. Here, we add YLD130 as a 'hybrid' because its bridge contains both the prototypical FTC (thiophene group) and CLD (isophorone ring) groups. In this benchmark set, the donors and acceptors are similar, but not all identical. There are two different aniline donors, the standard N,N-diethyl-aniline donor and the diethyl-amino-phenyl-thienyl (APT) donor; and three different acceptors, the standard dimethyl-TCF acceptor, the CF_3-phenyl-substituted TCF acceptor, and the CF_3-substituted TCF acceptor , belonging only to the SHJ2 (TCF1-CF3) system. However, unlike the larger benchmark set in Table 2.1, this subset of molecules are structurally

similar enough to define a dependable metric for donor-acceptor (D-A) length. Figure 3.1 illustrates the length metric which is measured for each of the optimized molecular geometries according to the distance between the nitrogen (N) atom on the diethyl-aniline donor and the malononitrile carbon (C) atom of the TCF acceptor. This metric will be used as an approximate measure of molecular size. D-A lengths are reported in Table 3.1.

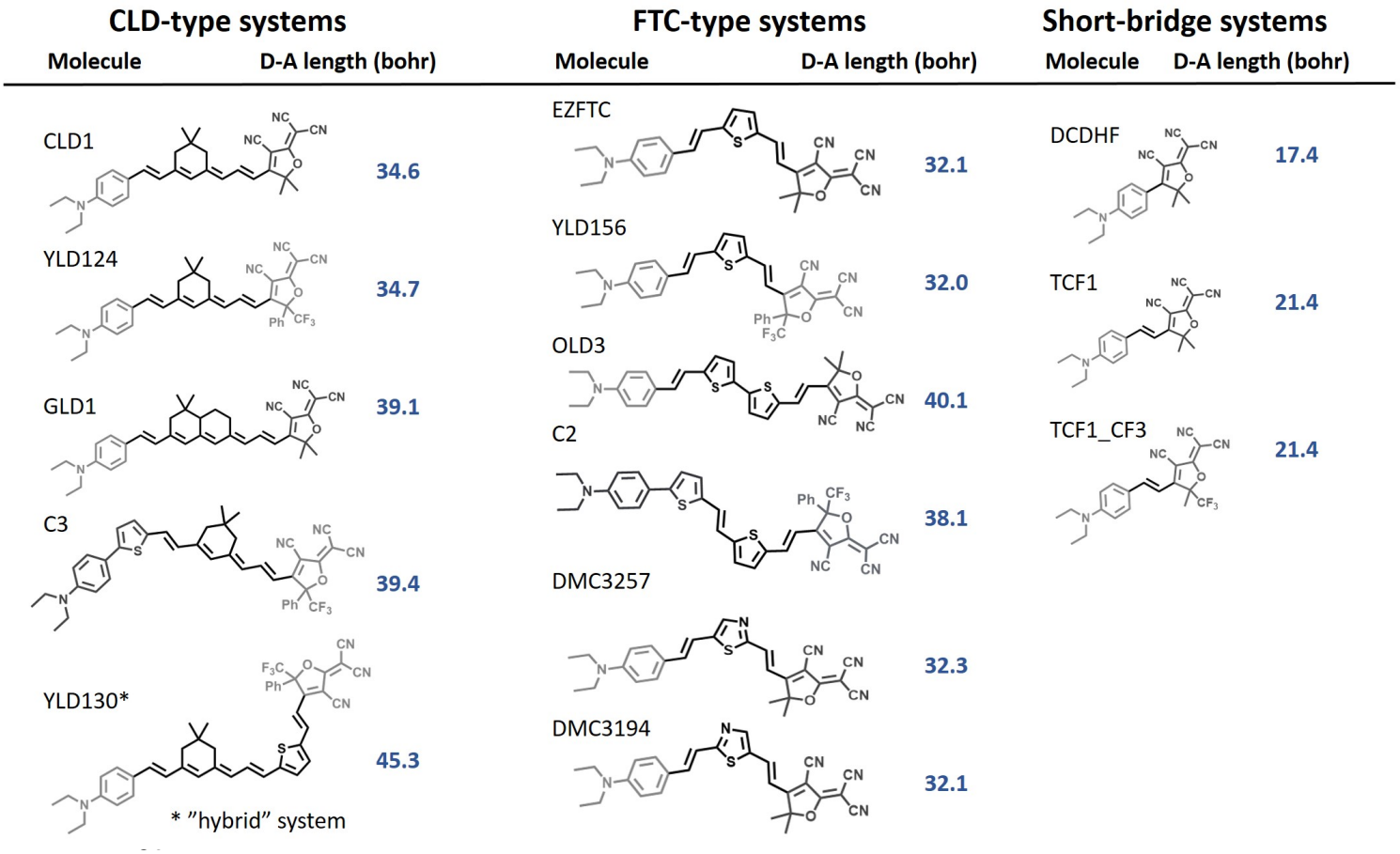

Table 3.1: **D-A lengths and Optimized Geometries of 14-benchmark set.** Structures and corresponding D-A lengths (bohr) are organized according to bridge character. Measured HRS and UV-vis data are given in Table 2.1.

3.2 Computational Details

All calculations were performed with the Gaussian-09 Rev D.01 electronic structure package [77]. Using the same computational method from Section 2.2, the geometry of the molecules was optimized at the B3LYP/6-31+G* level of theory with PCM to account for solvent effects. Properties were computed with three long-range corrected (LC) functional LC-BLYP [102], LC-ωPBE [240] and the range-separated hybrid (RSH) functional CAM-B3LYP [249], each of which varies the ω parameter that determines the ratio of DFT and exact exchange included at a particular r_{12} distance.

Excitation energies were computed using the linear response time-dependent DFT formalism. The excitation energy of the state with the largest oscillator strength, which was the lowest energy transition in all cases, was compared to the experimental one-photon absorption energy, λ_{max}.

The frequency-dependent hyperpolarizabilities consistent with hyper-Rayleigh Scattering (HRS) measurements, $\beta_{HRS}(2\omega)$, were computed at 1906nm from analytical derivatives obtained via the coupled-perturbed Kohn-Sham (CPKS) method [124]. In order to complete each ω-tuning calculation, i.e. to compute each value of Equations 3.1-3.3 the energies of the ground N-electron (charge=0, spin=0), cation (N-1)-electron (charge=+1, spin=1/2), and anion (N+1)-electron (charge=-1, spin=1/2) systems must each be calculated. Each of the energy calculations were performed in vacuo. Although performed separately, the optimized geometry of the neutral state was used for all open- and closed-shell energy calculations. The single-point computations of the open-shell cation and anion states were performed using the unrestricted Kohn-Sham formalism. The SCF energies, E_{gs}, and alpha electron orbital energy eigenvalues corresponding to the HOMO, ϵ_{HOMO}, were carefully selected from each output and evaluated.

3.3 J_{GAP}-optimal tuning method

In order to compute Equation 3.3, ground state energies, E_{gs}, as well as HOMO and LUMO energies (ϵ_{HOMO} and ϵ_{LUMO}, respectively) were computed in vacuum for neutral and charged species of each of the benchmarks (Table 3.1) using long-range corrected (LC) and range-separated hybrid (RSH) DFT. Plots of the orbital energies with varying long-range Hartree-Fock exchange are shown in the Supporting Information.

Figure 3.2 shows the results for the optimally-tuned range-separation parameter, ω, according to the J_{GAP}-tuning method (Equation 3.3) for each of the functionals studied. The plotted results for Equations 3.1 and 3.2 are given in Figures B.5, B.6, and B.7 in the Supporting Information. Henceforth, ω^* denotes the ideal range-separation parameter determined by the J_{GAP}-tuning method. The computed energies, J_{IP}, J_{EA}, and J_{GAP}, change considerably over the range 0.10-0.20 $bohr^{-1}$ for LC-ωPBE and LC-BLYP and 0.25-0.70 $bohr^{-1}$ for CAM-B3LYP. The results of the ω-tuning calculations show a general correlation between molecular length (D-A length) and ω^* for each of the functionals used. The longer the conjugation length of the bridge, the more ω^* shifts closer to 0.0 $bohr^{-1}$; a trend that has been previously reported by Baer and others [9], [145], [187], [8]. To corroborate these findings, a subset of the benchmark set four CLD-type systems which have identical donor (N,N-diethyl-aniline) and acceptor (TCF) units but varying conjugation length (n-units) of the polyene bridge, namely DCDHF (n=0), TCF1 (n=1, monoene), CLD1 (n=4, tetraene), and GLD1 (n=5, pentaene), shows a linear trend in ω^* with D-A length, as shown in Figure B.8 in the Supporting Information.

There is also correlation between ω^* and structural trends in bridge-character; namely, the J_{GAP} energy curves are partitioned according to each of the different bridge types in Table 2.1. The short bridge systems have largest predicted optimal ω^* ($\sim$0.18 $bohr^{-1}$, LC-BLYP); the FTC-type systems have moderate values, followed closely by the CLD-type systems ($\sim$0.16 and $\sim$0.14 $bohr^{-1}$, respectively, for LC-BLYP); and the longest system, the "hybrid" bridge YLD130 has the smallest predicted ω^* $\sim$0.13 bohr^{-1}, for LC-BLYP. The results are shown in Figure B.9, also in the Supporting Information.

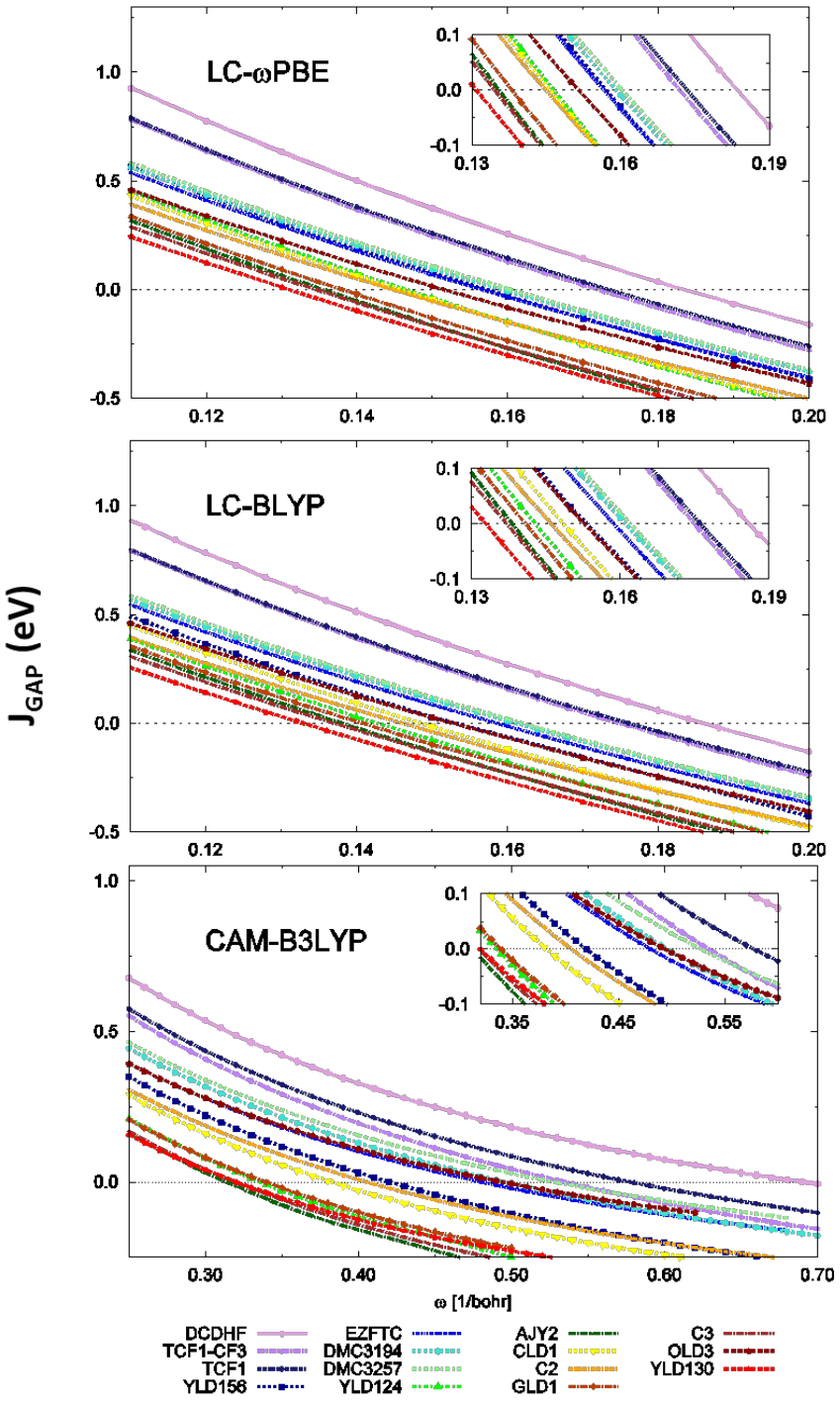

Figure 3.2: J_{GAP}**-tuning results.** Results for the optimally-tuned range-separation parameter, ω, according to the J_{GAP}-tuning method for each of the LC/RSH functionals.

3.4 *Calculated Transition Energy with Comparison to Experimental Data*

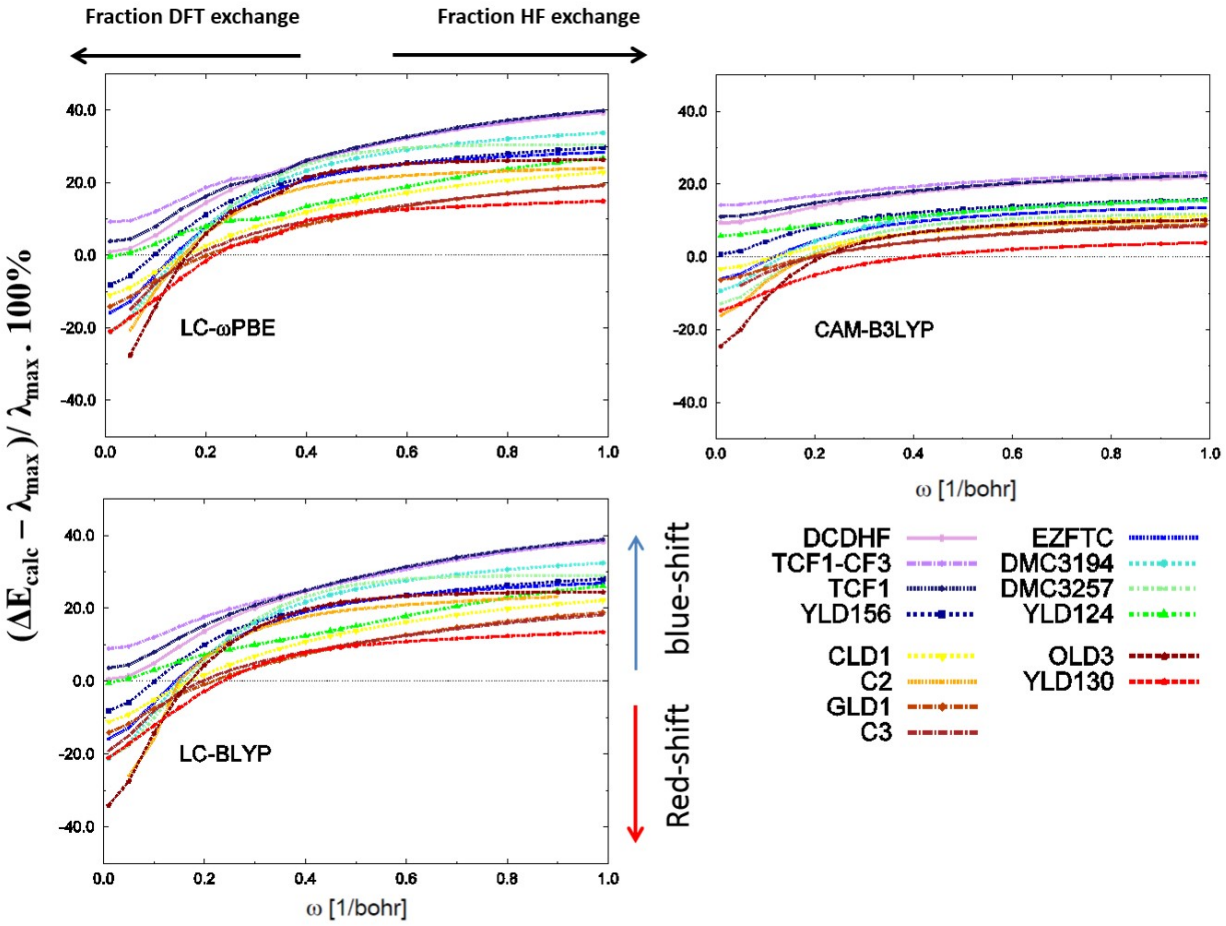

Figure 3.3: **Transition energies (eV) for the linear-response TD-DFT calculations for the functionals LC-wPBE, LC-BLYP, and CAM-B3LYP with PCM (chloroform) and 6-31+G* basis.** PCM-B3LYP/6-31+G* geometry was used for all calculations. Color scheme is organized according to D-A length (i.e., donor-acceptor length) as given in Table 3.1, from shortest (violet, DCDHF) to longest (red, YLD130).

Relative percent error between calculated transition energies (ΔE_{calc}) and experimental transition energies (corresponding to values in Table 2.1) are shown in Figure 3.3 over the range of $\omega \in (0, 1)$. Calculated transition energies (ΔE_{calc}) were computed using linear-response TD-DFT

for the functionals LC-ωPBE, LC-BLYP, and CAM-B3LYP with PCM (chloroform) and 6-31+G* basis. Henceforth, ω' denotes the ideal range-separation parameter determined by empirical fitting to UV-vis data. As is evident from Figure 3.3, the relative errors between LC-BLYP and LC-ωPBE are similar within less than 5% error. Henceforth, we focus on comparing the distinct trends of LC-BLYP and CAM-B3LYP for this analysis. The optimal amount of LR HF exchange needed to predict λ_{max}, referred to as ω', varies for each molecular system; however, for both LC-BLYP and CAM-B3LYP methods, moderate values of ω' (in range 0.1-0.25 $bohr^{-1}$) match well with experimental measurement of λ_{max} for most of the benchmark chromophores. (These results are similar for the 35-molecule benchmark set discussed in Chapter 2; see Figure A.5.) There are a few notable outliers. For the short-bridge systems (DCDHF, TCF1, TCF1-CF3), both DFT methods have lower relative percent error with diminished LR HF exchange ($\omega' \sim 0.0$ $bohr^{-1}$). In fact, zero error is never achieved for the short-bridge systems and only improves (approaches zero) with reduced LR HF exchange. For LC-BLYP, the limit $\omega' \rightarrow 0.0$ $bohr^{-1}$ essentially defaults to the pure DFT functional, BLYP; whereas, for CAM-B3LYP, this limit corresponds to the mild hybrid, B3LYP, which includes a 'cushion' of 20% short-range HF exchange. Interestingly, for both functionals, YLD124 behaves similarly to the short-bridge systems in that the prediction of λ_{max} is optimal when LR HF exchange is essentially removed (ω'=0.01 $bohr^{-1}$). Given that YLD124 has a D-A length that is at least 10 $\mathring{A}$ longer than any of the short-bridge systems, this indicates that other factors beyond molecular size are contributing to the trend in ω'. As a further example of this, the largest molecular system of the benchmark set, YLD130, has a lowest relative percent error when $\omega' = 0.40$ bohr^{-1} (for CAM-B3LYP). Since the structure of YLD130 is bent at the thiophene, thereby limiting overlaps of ground and excited state molecular orbitals, the other important factor determining ω' is the change in transition dipole moment corresponding to the primary CT transition with varying LR HF exchange.

3.5 Calculated Hyperpolarizabilities with Comparison to Experimental Data

TD-DFT relaxed density calculations cannot be done if the functional analytic third derivatives are not available. These methods are not currently available in Gaussian09 for the "wPBEh" functional

(e.g., LC-ωPBE), therefore in the following sections we focus on comparing the trends of LC-BLYP and CAM-B3LYP for which analytic third derivatives can be computed.

3.5.1 Static Molecular Hyperpolarizability

For methods, LC-BLYP and CAM-B3LYP, in Figure 3.4 show a correlation between D-A length and the computed static hyperpolarizability aligned with the dipole axis, $\beta_{zzz}(0)$, with solvent effects included using SCRF with PCM. The hyperpolarizability values are reported according to the perturbation convention. Since the dipole is correlated with D-A length, it follows that $\beta_{zzz}(0)$ is well-correlated with the length of the molecule. Shorter molecules (DCDHF, TCF1, TCF1-CF3) have small $\beta_{zzz}(0)$ values with less than 0.1 standard deviation over the range of ω, whereas the largest molecule (YLD130) has the largest $\beta_{zzz}(0)$.

Both acceptor strength and bridge character also play significant roles in the ranking of $\beta_{zzz}(0)$. For instance, the inclusion of nitrogen group in thiophene-bridge systems DMC3194 and DMC3257, causes a slight reduction in intrinsic hyperpolarizability with comparison to EZFTC, a factor of about 0.70 and 0.90, respectively. Furthermore, YLD156 and CLD1, both having different bridges and acceptors, are predicted to have a similar trend over the full range of ω. The pentaene bridge, GLD1, with standard TCF acceptor follows a similar trend as the tetraene system, YLD124, that has a stronger substituted-TCF acceptor. The similar trends among these structurally different pairs shows a balancing act of the bridge and acceptor on hyperpolarizability. To further highlight the importance of the bridge, the di-thienyl bridge system, OLD3, with TCF acceptor is predicted to have a considerably smaller $\beta_{zzz}(0)$ (about a factor of 3) than the C3, which has a shorter D-A length but a stronger acceptor (TCF-Ph,CF_3) and a polyene bridge. Consistent with previous studies, these results show that polyene-bridge systems with the substituted TCF acceptor (e.g., YLD124) have larger instrinsic hyperpolarizability than thiophene-bridge systems (e.g., EZFTC) [13].

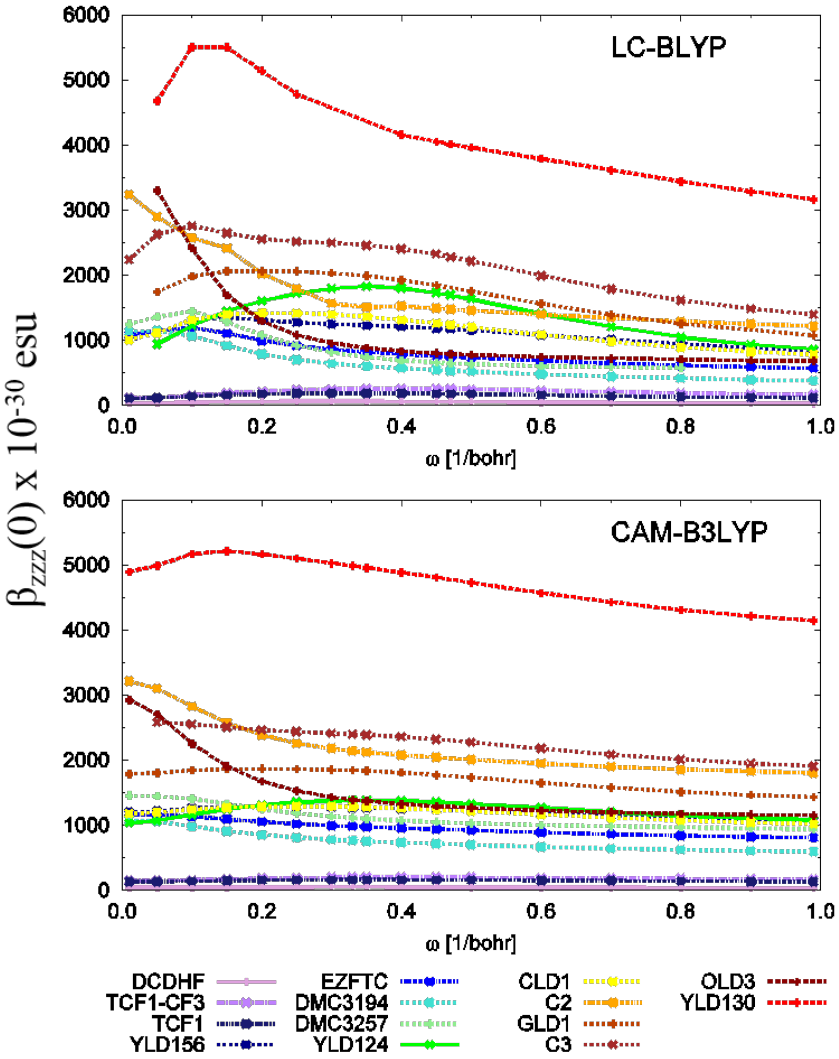

Figure 3.4: **Computed static hyperpolarizability aligned with the dipole axis, β_{zzz}(0).** β in units of 10^{-30} esu, computed using LC-BLYP and CAM-B3LYP with solvent effects (chloroform) included using SCRF with PCM and 6-31+g* basis. PCM-B3LYP/6-31+G* geometry was used for all calculations. The hyperpolarizability values are reported according to the perturbation convention. Color scheme is organized according to D-A length, as given in Table 1, from shortest (violet, DCDHF) to longest (red, YLD130).

3.5.2 Frequency-dependent Molecular Hyperpolarizability

The experimental HRS taken at a frequency of 1907 nm is compared with computed frequency-dependent second-harmonic hyperpolarizabilities, $\beta_{HRS}(-2\omega;\omega,\omega)$. The default parameterizations of LC-BLYP and CAM-B3LYP (ω = 0.47 $bohr^{-1}$ for LC-BLYP and 0.33 $bohr^{-1}$ CAM-B3LYP)

work well for computed frequency-dependent second-harmonic hyperpolarizability, as shown in Figure 3.5. One reason that default LC-BLYP works well is that $\omega = 0.47\ bohr^{-1}$ was chosen such that it was optimal for computing polarizabilities of π-conjugated polyene chains [249], a known issue with functionals that do not include any long-range correction (e.g., BLYP, B3LYP). Regardless of the molecular system or long-range corrected functional, a moderate amount of LR HF exchange ($\sim 40\%$) appears ideal. These results extend to the 35-molecule benchmark set discussed in Chapter 2 (see Figure A.7).

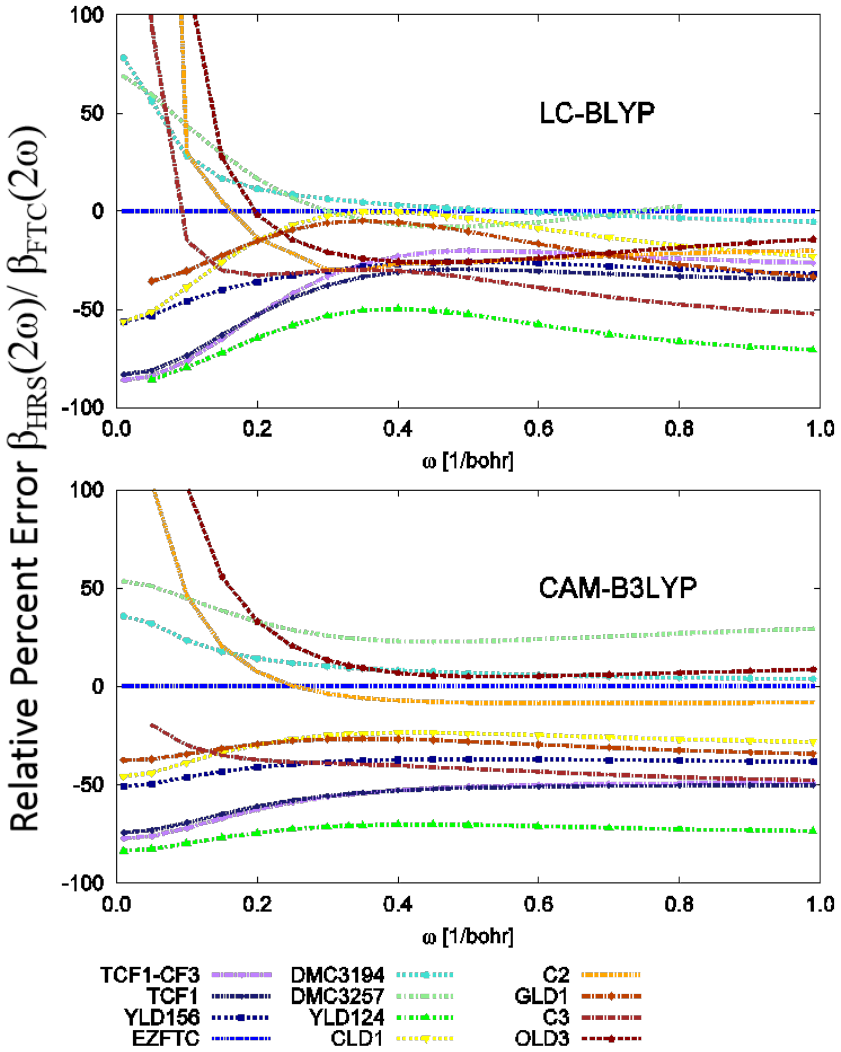

Figure 3.5: **Computed frequency-dependent hyperpolarizability, $\beta_{HRS}(-2\omega;\omega,\omega)/\beta_{HRS}^{FTC}$, at 1907 nm using analytic derivatives via coupled-perturbed Kohn-Sham (CPKS) theory with LC-BLYP (top) and CAM-B3LYP (bottom) and 6-31+G* basis.** Solvent effects (chloroform) included using SCRF with PCM. The abbreviated notation is meant as a ratio with respect to EZFTC, $\beta_{calc} = \beta_{HRS}^{sys,calc}/\beta_{HRS}^{EZFTC,calc}$ and $\beta_{expt} = \beta_{HRS}^{sys,expt}/\beta_{HRS}^{EZFTC,expt.}$.

3.6 Summary of Results

Linear regression fits for optimally-tuned ω versus Donor-Acceptor (D-A) length according to ω-tuning for Koopmans' theorem, ω^* (labeled 'J_{GAP}' in Figures 3.6-3.8), and empirical fit for λ_{max}, ω', are shown in Figure 3.6. There is a strong correlation between D-A length and ω^* for LC-BLYP

(and LC-ωPBE, not shown). R-squared fits according to these methods reveal that 87-91 % of the variation in the choice of ω^* can be described by D-A length, where the remaining 9-13% can be attributed to other factors. CAM-B3LYP is not as well correlated with $R^2 = 0.72$, which is the same as its correlation between D-A length and ω'. The linear regression fits between D-A length and ω' for LC-BLYP and LC-ωPBE each give $R^2 \approx 0.62$, thus the amount of LR HF exchange needed to accurately compute λ_{max} is only weakly correlated with molecular size. For example, YLD124 and CLD1 which have similar structure and D-A length have significantly different ω' values (YLD124, $\omega' \approx 0.01\ bohr^{-1}$; CLD1, $\omega' \approx 0.15\ bohr^{-1}$). This can be explained by the greater acceptor strength of the substituted TCF belonging to YLD124, as this would affect the primary transition dipole moment as well as the difference in ground to excited state dipole moment. Despite deviations due to these other factors, based on the D-A lengths of the 14 molecule test set and their trends in ω', one may conclude that smaller π-conjugated molecules require less LR HF exchange for the accurate computation of λ_{max}; whereas, larger π-conjugated molecules require more LR HF exchange.

Notably, the positive correlation between D-A length versus ω' is opposite of the negative correlation predicted for ω^*. In other words, tuning for Koopmans' theorem is trending in the opposite direction of the experimental data of λ_{max}. However, in agreement with studies by Baer and others [8], [146], [176], [145], these results show that ω^* can be better for predicting λ_{max} than default settings ($\omega_{Default}$), when using LC-BLYP. For CAM-B3LYP, ω^* generally performs worse in predicting λ_{max} than $\omega_{Default}$. The ω-tuning results are, therefore, inconsistent between the two methods. (Note that the BNL functional developed by Baer and coworkers and extensively tested for tuning via Koopmans' theorem varies exchange more similar to LC-BLYP than CAM-B3LYP [10], [163].) In fact, neither the tuned nor default settings for exact exchange are ideal for computing λ_{max}; based on smallest mean absolute error (MAE), the best method overall uses a fraction of exact exchange (ω=0.15 $bohr^{-}1$) smaller than predicted by default settings ($\omega_{Default}$) or ω-tuning via Koopmans theorem (ω^*). However, over the range of ω values, CAM-B3LYP presents smaller MAE in the computation of λ_{max} than either LC-BLYP or LC-wPBE, as shown in Figure 3.7. Therefore, the inclusion of SR HF exchange in CAM-B3LYP ensures stability in the computation of λ_{max}.

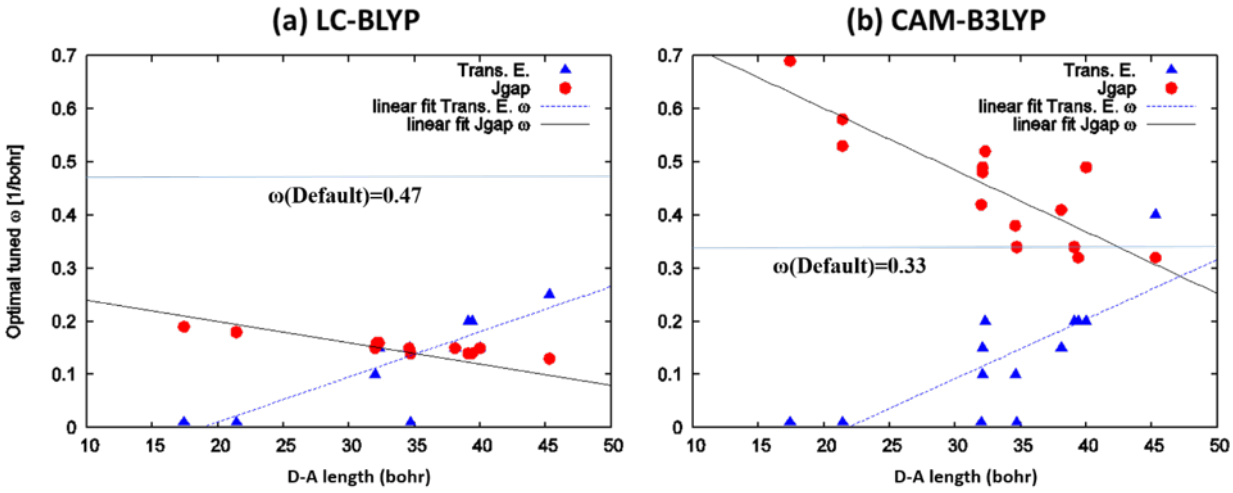

Figure 3.6: **Linear regression fits according to either ω-tuning to Koopmans' theorem or Empirical Fit for λ_{max} versus Donor-Acceptor Length.** Transition energies were calculated with PCM (chloroform) and 6-31+G* basis set. PCM-B3LYP/6-31+G* geometry was used for all calculations. Default settings for the fraction of exact exchange, $\omega_{Default}$, for each functional are shown. (a) LC-BLYP, Variance = 3.4×10^{-3}; (b) CAM-B3LYP, Variance = 3.8×10^{-2}.

Figure 3.8 shows linear regression fits for ω-tuned computed frequency-dependent hyperpolarizabilities, $\beta_{HRS}(2\omega)$, according to optimal ω for Koopmans' theorem, ω^* (i.e., 'J_{GAP}'); transition energy, ω' (Trans. E.); and default settings, $\omega_{Default}$; with each resulting β plotted versus experimental β_{HRS} values. The results show that for LC-BLYP, the computed $\beta_{HRS}(2\omega)$ values according to Koopmans' theorem, ω^*, and transition energy, ω', correlate poorly with experimental β_{HRS} data ($R^2 < 0.4$). However, computed $\beta_{HRS}(2\omega)$ with $\omega_{Default} = 0.47\ bohr^{-1}$ for LC-BLYP correlates strongly with experimental β_{HRS} data ($R^2 \approx 0.9$). For CAM-B3LYP, tuning via Koopmans theorem, ω^*, and default settings, $\omega_{Default}$, yield nearly the same results in computed $\beta_{HRS}(2\omega)$ ($R^2 \approx 0.6$). Similar to LC-BLYP, the CAM-B3LYP results for transition energy, ω', correlate poorly with experimental β_{HRS} data. The minimum MAE is achieved by LC-BLYP using ω=0.40 bohr^{-1}, as illustrated in Figure 3.9. The hyperpolarizabilities computed with CAM-B3LYP are nearly constant for ω >0.20 bohr^{-1}, with the absolute lowest MAE at ω=0.45 bohr^{-1}.

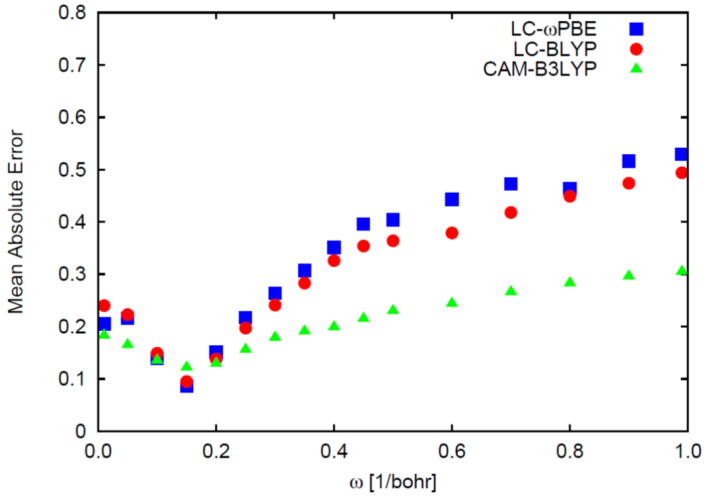

Figure 3.7: **Mean Absolute Error (MAE) for λ_{max} with respect to experimental data for 14 molecule test set.** The MAE for CAM-B3LYP varies the least over the range of % long-range HF exchange used in the functional. Its MAE is minimal (MAE$\approx$ 0.12) when ω is 0.15 bohr^{-1} and increases to roughly 0.31 when $\omega \to 1$. LC-wPBE and LC-BLYP have MAE that achieves a minimum (MAE$\approx$ 0.09) for ω=0.15 bohr^{-1}, but then increases to a maximum of about 0.50 when $\omega \to 1$.

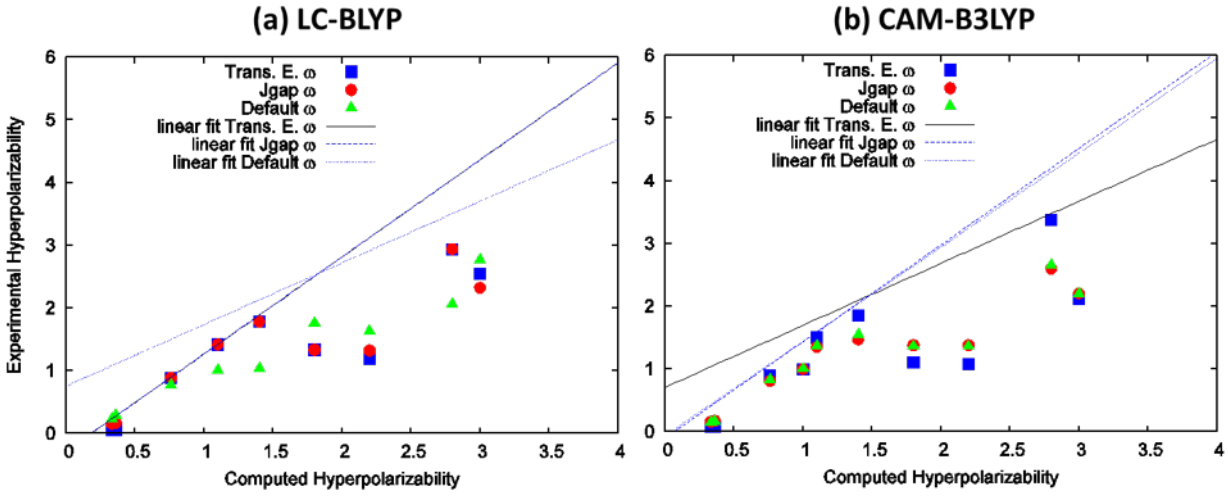

Figure 3.8: **Linear regression fits for tuned computed frequency-dependent hyperpolarizability and experimental HRS values.** The computed values are according to $\beta_{HRS}(2\omega)/\beta_{HRS}^{FTC}$, at 1907 nm by tuning ω according to optimal parameterization for i) computed transition energy and ii) ω-tuning method (J_{GAP}), with comparison to iii) default ω. **(a) LCBLYP**, $R^2(J_{GAP}) = R^2$(Trans. E.) = 0.3917; R^2(Default) = 0.8781. **(b) CAMB3LYP**, $R^2(J_{GAP})$ = 0.6297; R^2(Trans. E.) = 0.3719; R^2(Default) = 0.6457. Note that DCDHF and YLD130 are excluded because they do not have experimental HRS data available at 1907 nm.

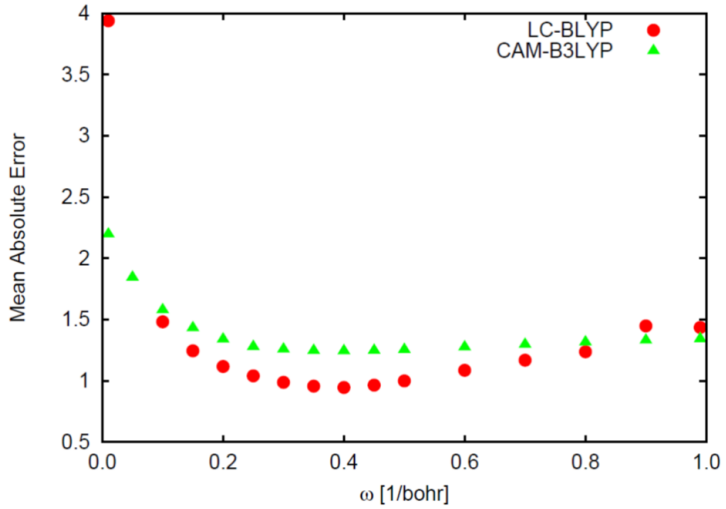

Figure 3.9: **Mean Absolute Error (MAE) for $\beta_{HRS}(2\omega)/\beta_{HRS}^{FTC}$ with respect to experimental HRS data for 14 molecule test set.** Similar to the transition energies, the MAE for CAM-B3LYP varies less than LC-BLYP over the range of % long-range HF exchange used in the functional. Its MAE is nearly constant at about 1.3 for $\omega \geq$0.20 bohr^{-1}, with the absolute lowest MAE$\approx$1.24 at ω=0.45. LC-BLYP has a minimum MAE$\approx$ 0.94 for ω=0.40 bohr^{-1}, but then increases to a maximum of 3.9 when $\omega \to 0$.

3.7 Conclusions

We found that of the DFT methods investigated here, that LC-BLYP and LC-wPBE yielded nearly identical results, thus the analysis was reduced to comparisons between LC-BLYP and CAM-B3LYP. For these methods, we found that the size dependence (determined by D-A length) according to the optimally tuned ω for Koopmans' theorem (ω^*) has the opposite trend for the amount of exact exchange needed to match with experimental λ_{max} (ω'). These findings suggest that tuning for the ionization potential to predict optical transitions according to molecular size is unreliable. We conclude that ω-tuning via Koopmans' theorem, ω^*, is slightly better than $\omega_{Default}$ for predicting λ_{max} using LC-BLYP, but is worse when using CAM-B3LYP. However, ω^* in LC-BLYP does not perform any better in predicting λ_{max} than simply choosing ω=0.15 $bohr^{-1}$. As a general critique of this method, caution is advised in 'tuning out' the LR HF exchange in functionals like LC-BLYP which have no cushion of SR HF exchange, thus defaulting to pure DFT when ω=0. In the case of LC-BLYP, this results in BLYP which is notoriously unreliable for computing electronic

transition energies [67] as well as hyperpolarizabilities (shown previously in Chapter 2). CAM-B3LYP with ω=0.15 $bohr^{-1}$ also has small MAE for computing λ_{max}; however, at the limit ω=0, CAM-B3LYP becomes B3LYP which is a more reliable method than BLYP. A study by Govind, et al. recommends reducing the amount of LR HF exchange in CAM-B3LYP for accurately computing electronic transition energies in D-π-A molecules [5]. Thus, the results presented here concur with the findings of Ref. [5] such that CAM-B3LYP with reduced HF exchange (ω $\sim$0.15 $bohr^{-1}$) is a reasonable choice for the computation of electronic excitation energies of single molecules.

As for predicting hyperpolarizabilities, we found that using either tuning for Koopmans' theorem, ω^*, or transition energy, ω', in LC-BLYP was unreliable. We instead recommend $\omega_{Default}$ using LC-BLYP for the most accurate prediction of β. Indeed, the choice of $\omega_{Default}$=0.47 $bohr^{-1}$ using LC-BLYP is in agreement with conclusions made previously by Champagne and co-workers for accurately computing the polarizability and second hyperpolarizability of extended conjugated systems [32]. In general, moderate amounts of LR HF exchange (at least 40%) in LC functionals provide more accurate predictions of molecular hyperpolarizability. This conclusion is in agreement with findings made by Johnson et al. [116].

In summary, we found that setting the amount of exchange in LC-BLYP to enforce Koopmans' theorem offered some improvement in the prediction of λ_{max}, but was unreliable for predicting NLO properties. Conversely, for CAM-B3LYP, ω-tuning was worse in predicting λ_{max} than default settings; however, had nearly equivalent accuracy as the default for predicting β. The user is cautioned against tuning out the LR HF exchange in functionals such as LC-BLYP since this approaches pure DFT, which is known to report spurious CT states in systems with significant CT character [67], [66]. Rather, for the computation of λ_{max}, we recommend a method which includes both LR and SR HF exchange, such as CAM-B3LYP, so that when the amount of LR HF exchange is reduced there is still some SR exact exchange to help prevent serious self-interaction error (SIE). Finally, we found that for both LC/RSH functionals that the fraction of exchange needed to accurately compute excitation energies (λ_{max}) is not optimal for computing hyperpolarizabilities; rather, we recommend a larger fraction of exact exchange for computing β. LC-BLYP with default parameterization is recommended for this purpose.

3.7.1 Supporting Information

Additional figures and tables are located in Appendix B.

Appendix B includes, in order:

1. Orbital Energies Computed in Vacuum using LC-BLYP, LC-ωPBE and CAM-B3LYP
2. Results of J_{IP}, J_{EA}, and J_{GAP} for LC-BLYP, LC-ωPBE, and CAM-B3LYP
3. J_{GAP}-tuning method results with respect to extended polyene conjugation length.
4. Structural Trends in J_{GAP}-tuning results.
5. Orbital Energies Computed with Solvent Effects using LC-BLYP, LC-ωPBE and CAM-B3LYP
6. Electronic Vertical Excitation Energy plotted versus HOMO-LUMO energy gap
7. Comparison of using $\epsilon_{LUMO}(N)$ in place of $\epsilon_{HOMO}(N+1)$ in Equation 3.2 for the molecule DCDHF.

Additional information including cartesian coordinates of all the B3LYP/6-31+G* optimized structures and tables of the data plotted in this work can be found in the Supporting Information in Ref [79].

3.7.2 Acknowledgements

This work was done in collaboration with Prof. Christine Isborn's group at the University of California Merced whose work was funded by startup funds. Work at University of Washington was partially supported by the National Science Foundation (STC- MDITR DMR-0120967, DMR-1303080, and DMR-0905686) and the Air Force Office of Scientific Research (FA9550-09-1- 0589) and the University of Washington Student Technology Fund (STF). Special thanks goes to Prof. Christine Isborn who worked with me at every stage of this study. I also thank Professors Larry Dalton and Bruce Robinson for revising this work. I thank Dr. Delwin Elder, Dr. Lewis Johnson, and Dr. Bruce Eichinger for valuable discussions. I also appreciate the hard work done by numerous synthetic chemists who made these molecules and the spectroscopists who characterized them. I especially thank Dr. Denise Bale for providing experimental HRS and raw UV-vis data for this study.

References

[5] J. Andzelm et al. "Performance of DFT Methods in the Calculation of Optical Spectra of TCF-Chromophores." In: *J. Chem. Theory Comput.* 5 (2009).

[7] J. Autschbach and M. Srebro. "Delocalization Error and "Functional Tuning" in Kohn-Sham Calculations of Molecular Properties". In: *Accounts of Chemical Research* 47.8 (2014), pp. 2592–2602.

[8] R. Baer, L. Kronik, and T. Stein. "Reliable Prediction of Charge Transfer Excitations in Molecular Complexes Using Time-Dependent Density Functional Theory". In: *J. Am. Chem. Soc.* 131.8 (2009), pp. 2818–2820.

[9] R. Baer, E. Livshits, and U. Salzner. "Tuned Range-Separated Hybrids in Density Functional Theory". In: *Annual Review of Physical Chemistry* 61 (2010), pp. 85–109.

[10] R. Baer and D. Neuhauser. In: *Phys. Rev. Lett.* 94 (2005), p. 043002.

[11] O. V. Baerends and E. J. Gritsenko. “The spin-unrestricted molecular Kohn-Sham solution and the analogue of Koopmans theorem for open-shell molecules”. In: *J. Chem. Phys* 120 (2004).

[13] D. H. Bale et al. “Dielectric Dependence of the First hyperpolarizability for Electro-Optic Chromophores”. In: *J. Phys. Chem. B.* 115 (2011).

[14] H. Bartlett and R. J. Sekino. “Frequency-Dependent Nonlinear Optical-Properties of Molecules”. In: *J. Chem. Phys* 85 (1986), pp. 976–89.

[32] B. Champagne and M. Wergifosse. “Electron Correlation effects on the first hyperpolarizability of push-pull pi-conjugated systems”. In: *J. Chem. Phys* 134 (2011).

[66] A. Dreuw and M. Head-Gordon. “Failure of Time-Dependent Density Functional Theory for Long-Range Charge-Transfer Excited States: The Zincbacteriochlorin-Bacteriochlorin and Bacteriochlorophyll-Spheroidene Complexes”. In: *J. Am. Chem. Soc.* 126 (2004), pp. 4007–4016.

[67] A. Dreuw and M. Head-Gordon. “Single-Reference ab Initio Methods for the Calculation of Excited States of Large Molecules”. In: *Chem. Rev.* 105 (2005), pp. 4009–4037.

[77] M. J. Frisch et al. *Gaussian 09, Revision D.01.* Computer Program. 2013.

[79] K. Garrett et al. “Optimum Exchange for Calculation of Excitation Energies and Hyperpolarizabilities of Organic Electro-optic Chromophores”. In: *Journal of Chemical Theory and Computation* 10.9 (2014), pp. 3821–3831.

[80] A.J. Garza et al. “Can Gap Tuning Schemes of Long-Range Corrected Hybrid Functionals Improve the Description of Hyperpolarizabilities?” In: *The Journal of Physical Chemistry B* 119.3 (2015), pp. 1202–1212.

[81] A.J. Garza et al. “Can Short and Middle Range Hybrids Describe the Hyperpolarizabilities of Long-Range Charge Transfer Compounds?” In: *The Journal of Physical Chemistry A* 118.50 (2014), pp. 11787–11796.

[82] S. J. A. van Gisbergen, J. G. Snijders, and E. J. Baerends. "A density functional theory study of frequency dependent polarizabilities and Van der Waals dispersion coefficients for polyatomic molecules". In: *J. Chem. Phys.* 103 (1995).

[83] S. J. A. van Gisbergen, J. G. Snijders, and E. J. Baerends. "Accurate density functional calculations on frequency-dependent hyperpolarizabilities of small molecules". In: *J. Chem. Phys* 109 (1998).

[95] H.H. Heinze, F. Della Sala, and A. Gorling. "Efficient methods to calculate dynamic hyperpolarizability tensors by time-dependent density-functional theory". In: *J. Chem. Phys.* 116 (2002), p. 9624.

[102] H. Iikura et al. "Long-range correction scheme for generalized-gradient-approximation exchange functionals". In: *J. Chem. Phys.* 115 (2001), pp. 3540–44.

[107] D. Jacquemin, C. Adamo, and et al. "First hyperpolarizability of polymethineimine with long-range corrected functionals." In: *J. Chem. Phys.* 126 (2007).

[110] D. Jacquemin et al. "Performance of an Optimally Tuned Range-Separated Hybrid Functional for 0-0 Electronic Excitation Energies". In: *J. Chem. Theory Comput.* 10 (2014), p. 1677.

[116] L. E. v.d.L. Johnson. "Multi-Scale Modeling of Organic Electro-Optic Materials". Thesis. 2012.

[124] M. Kamiya et al. "Nonlinear optical property calculations by the long-range-corrected coupled-perturbed Kohn-Sham method." In: *J. Chem. Phys.* 122 (2005).

[127] A. Karolewski, L. Kronik, and S. Kummel. "Using optimally tuned range separated hybrid functionals in ground-state calculations: Consequences and caveats". In: *J. Chem. Phys* 138 (2013).

[140] T. Koopmans. In: *Physica (Elsevier)* 1.1-6 (1934), pp. 104–113.

[143] T. Körzdörfer et al. “Long-range corrected hybrid functionals for pi-conjugated systems: Dependence of the range-separation parameter on conjugation length”. In: *J. Chem. Phys* 135 (2011).

[145] L. Kronik et al. “Excitation Gaps of Finite-Sized Systems from Optimally Tuned Range-Separated Hybrid Functionals”. In: *J. Chem. Theory Comput.* 8 (2012), pp. 1515–1531.

[146] N. Kuritz et al. “Charge-Transfer-Like $\pi- > \pi^*$ Excitations in Time-Dependent Density Functional Theory: A Conundrum and Its Solution”. In: *Journal of Chemical Theory and Computation* 7.8 (2011), pp. 2408–2415.

[163] E. Livshits and R. Baer. In: *Phys. Chem. Chem. Phys.* 9 (2007), p. 2932.

[176] P. Mori-Sanchez, A. J. Cohen, and W. Yang. “Localization and Delocalization Errors in Density Functional Theory and Implications for Band-Gap Prediction”. In: *Phys. Rev. Lett.* 100 (2008).

[187] L. Pandey et al. “Lowest excited states and optical absorption spectra of donor-acceptor copolymers for organic photovoltaics: a new picture emerging from tuned long-range corrected density functionals”. In: *Phys. Chem. Chem. Phys.* (2012). DOI: 10.1039/c2cp41724c.

[207] H. Sekino et al. “Polarizability and second hyperpolarizability evaluation of long molecules by the density functional theory with long range correction”. In: *J. Chem. Phys* 126 (2007).

[218] J. W. Song et al. “Nonlinear optical property calculations of polyynes with long range corrected hybrid exchange correlation functionals”. In: *J. Chem. Phys* 129 (2008).

[240] O. A. Vydrov et al. “Importance of short-range versus long-range Hartree Fock exchange for the performance of hybrid density functionals”. In: *J. Chem. Phys.* 125 (2006).

[249] T. Yanai, D.P. Tew, and N.C. Handy. “A new hybrid exchange-correlation functional using the Coulomb-attenuating method (CAM-B3LYP).” In: *Chem. Phys. Lett.* 393.51 (2004).

Chapter 4

UNDERSTANDING SELF-AGGREGATION OF ORGANIC ELECTRO-OPTIC (OEO) CHROMOPHORES USING DENSITY FUNCTIONAL THEORY

There are two main causes of optical loss in organic NLO materials; either due to significant absorption at telecommunication frequencies ($\sim$1.3 or 1.5 μm), absorption of aggregates, or scattering of light due to crystallites [58]. When in bulk, organic NLO chromophores must align in an overall noncentrosymmetric manner to produce an electro-optic response [211], [23]. Achieving a noncentrosymmetric arrangement at high-concentration is a major challenge for many high-β chromophores due to the dipole-dipole interactions between monomers which influence the molecules to assume centrosymmetric order [55], [50]. To overcome this challenge, organic electro-optic (OEO) chromophores are typically diluted into polymers, also known as 'guest-host' materials [236], [222], [19], [115]. Efficient poling may be achieved in this manner due to the polymer matrix exerting a spacer effect, thereby reducing the strength of dipolar coupling [231]. However, the EO coefficient, r_{33} (Equation 1.15), is proportional to chromophore concentration, thus there is strong impetus for increasing chromophore loading. In fact, some of the best performing chromophore systems have been with 100% chromophore loading [115], [236], and there is a continued drive to investigate neat or high density chromophore systems [70], [59]. At these high concentrations, potential problems from aggregation become more of an issue.

Aggregation occurs due to electrostatic attractions between molecules, commonly in the form of π-stacking [189], which is generally deleterious to the performance of second-order NLO materials [223], [58], [56]. Aggregation is commonly classified as either 'H' or 'J' type aggregation [27], [246], [203], [113]. In H-aggregates, the molecules stack on top of each other but have repulsive polar interactions [231]. J-aggregates typically result from attractive dipolar interactions that align the primary transition dipoles of the molecules [170]. Conveniently, these different types of aggregation correspond to distinct shifts in the electronic absorption spectra of these materials. The presence of

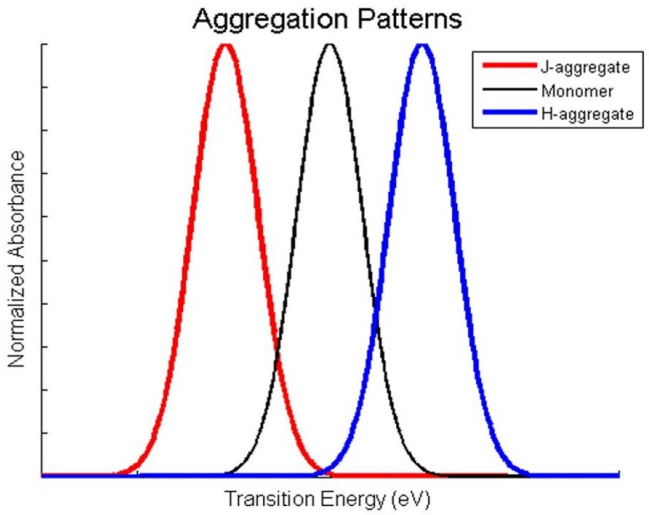

Figure 4.1: **Trends in Electronic Spectra for H- and J-aggregates.** H-aggregates stack vertically on the top of each other; whereas J-aggregates include head-to-tail configurations and 'stair-like' displacement with respect to each monomer. H-aggregates tend to be blue-shifted and J-aggregates are red-shifted from the main CT peak of the monomer absorption spectrum.

H-aggregates results in a blue-shift with respect to the main CT peak of the monomer absorbance spectrum; whereas, J-aggregates cause a red-shift relative to the monomer CT peak [189]. More specifically, these shifts are a result of coupling between monomers in the aggregates which induce delocalized excited states, also known as Frenkel excitons [212], [174], [186], [61].

Shifts in electronic absorption spectra due to the splitting of excited states upon dimerization may be rationalized by the Frenkel exciton model. According to this model, if the interacting molecules are separated by sufficiently large distance, the molecular orbital overlap between the molecules can be ignored [226]. The resonance interaction, which is responsible for the existence of delocalized exciton states in aggregates and molecular crystals, may then be approximated at first-order by the *dipole-dipole approximation* [125]. It follows that the excited state of monomer in the dimer is split in two, according to a splitting energy

$$\Delta E = 2\left[\frac{\vec{\mu}_{ge}^{(1)}\vec{\mu}_{ge}^{(2)}}{R^3} - \frac{3\vec{\mu}_{ge}^{(1)}\vec{R}\vec{\mu}_{ge}^{(2)}\vec{R}}{R^5}\right], \tag{4.1}$$

where $\vec{\mu}_{ge}^{(1)}$ and $\vec{\mu}_{ge}^{(2)}$ are the transition dipole moments of monomer 1 and 2, respectively, and R is the intermolecular separation. In the case that the molecules are acentric, illustrated in Figure 4.2

[253], this equation is simplified [226]

$$\Delta E = 2\mu_{ge}^2 \frac{(1 - 3cos^2\Phi)}{R^3}, \tag{4.2}$$

where angle Φ is illustrated in Figure 4.2. Relating this equation to Equation 1.6, it is clear that changes in μ_{ge}^2 and excited state transition energy affect hyperpolarizability. Note that this is a simple approximation which ignores electronic exchange between chromophores and other important factors which affect intermolecular interaction [201]; thus, the dipole-dipole approximation model (at best) provides only a qualitative description of the relationship between molecular orientation, splitting energy, and molecular hyperpolarizability for monomers separated at large enough distance. These relationships will be investigated in more detail later in this chapter.

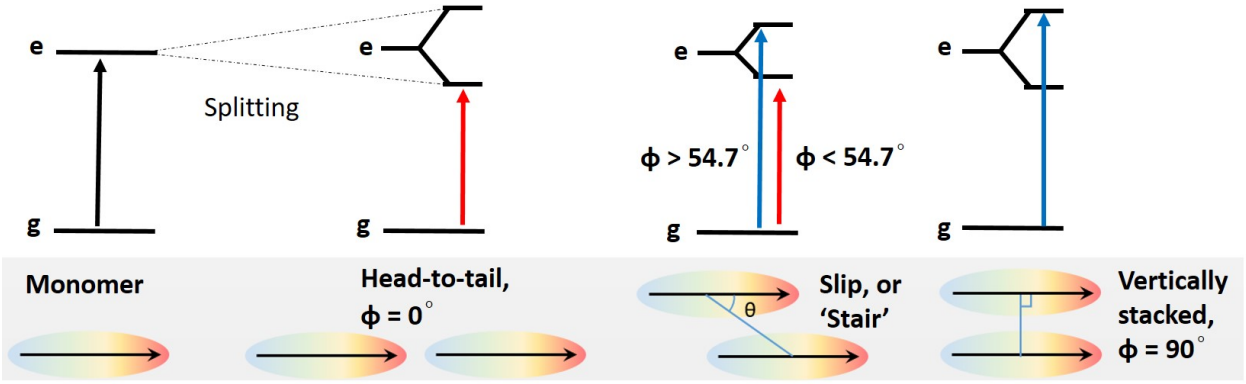

Figure 4.2: **Splitting of excited states due to dimerization based on mutual orientation of molecules in an aggregate, i.e. orientation of transition dipoles.**

Previous work in the Dalton lab by Dr. Ilya Kosilkin focused on understanding aggregation in OEO materials by measuring changes in absorption spectra of dye-doped polymers with respect to increasing concentrations of dye and dielectric environment (ϵ) of the host [144]. A work horse for OEO applications, YLD124, was doped into a polymethyl methacrylate (PMMA) host ($\epsilon \approx 3$) [24] at concentrations ranging between 0.05$-$ 100% (w./w.) in PMMA. These studies showed that the absorption band behaves as it would for a dilute solution ($\sim 1 \times 10^{-5}$M) up to concentrations of 1%, but begins to grow in a red-shifted shoulder with increasing weight percent of YLD124, shown

in Figure 4.3. This behavior is consistent with J-aggregation, however, such broad classification is neither verifiable nor conclusive evidence of how the molecules are assembling on a microscopic level. In order to better understand what is causing this shoulder, theory can be used to determine a correlation between aggregation on a microscopic level and changes in calculated absorption spectra, as well as investigate the effect that intermolecular interactions between closely paired monomers have on overall NLO response.

For this study, we focus on determining the nature of the low-energy shoulder in the YLD124 spectra by exploring the distinct optical properties between monomers and oligomers of YLD124. Based on the crystallographic data, various configurations of dimers of YLD124 were used for calculating differences in absorption spectra and hyperpolarizabilities of single molecules and aggregates. In particular, the effects of intermolecular distance and stacking arrangement on the Pockels hyperpolarizability, $\beta_{zzz}(-\omega;\omega,0)$ and the lowest electronic transiton energy, ΔE_{red}, were studied. In addition to these dimer studies, various configurations of dimers and trimers were extracted from a Monte Carlo simulation of an ensemble of over 100 YLD124 molecules. By averaging over these configurations, we describe the origins of the low energy shoulder on a microscopic level, as well as determine the reduction in overall hyperpolarizability due to intermolecular interactions and pockets of centrosymmetric aggregation in the population.

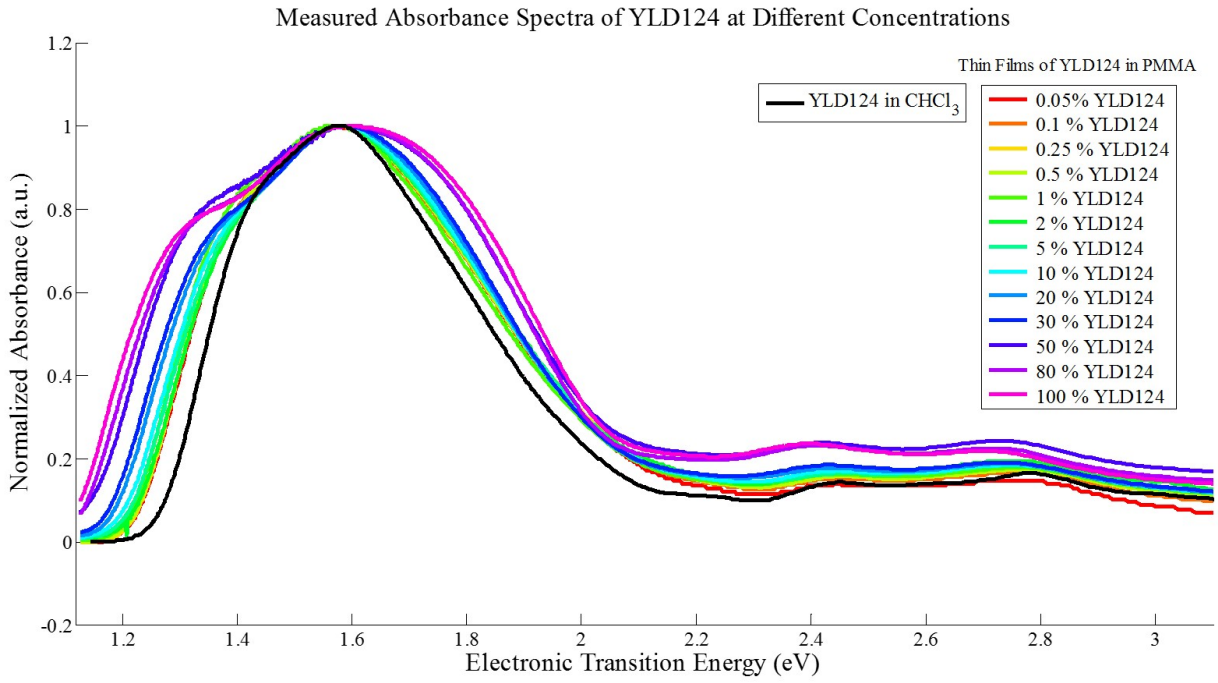

Figure 4.3: **Measured Absorbance Spectra of Thin Films of YLD124/PMMA at Different Concentrations.** Dilute solution of YLD124 in chloroform is shown for comparison. (Data collected by Dr. Ilya Kosilkin.)

4.1 Crystal Data Studies

4.1.1 Crystal Structure for YLD124

Crystallographic data for YLD124 was collected by Peter Johnston of the Dalton lab and Dr. Werner Kaminsky, both at the University of Washington [122]. The crystal is triclinic with space group P-1. There are two molecules per unit cell with parameters a=7.906$\mathring{A}$, b=13.915$\mathring{A}$, and c=22.51$\mathring{A}$. Due to the highly dipolar nature of YLD124, the molecules crystallize in a centrosymmetric fashion, as shown in Figure 4.4. The overall second-order NLO response is, therefore, expected to be near zero.

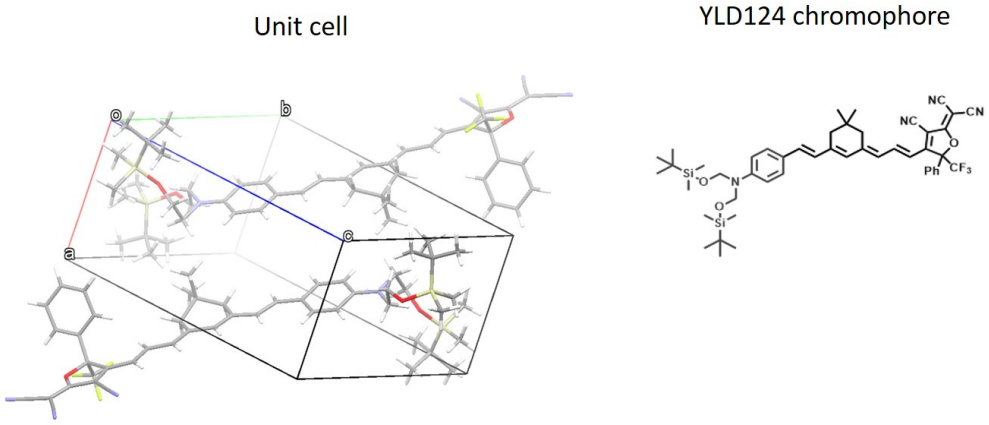

Figure 4.4: **Unit Cell of YLD124.** The YLD124 crystal sample was synthesized by Peter Johnston and crystallographic data was measured by Werner Kaminsky. The crystal is triclinic with space group P-1. There are two molecules per unit cell with parameters a=7.906$\mathring{A}$, b=13.915$\mathring{A}$, and c=22.51$\mathring{A}$.

4.1.2 Comparison of Relative Chromophore Number Densities in Different Media

It is important to address the relative chromophore densities of the YLD124 crystal, thin films, and solutions in our analysis. Based on the dimensions of the unit cell of the YLD124 crystal, the density of the crystal is 1.23 g/cm^3 using the cell volume, which corresponds to a number density $N \approx 8.4 \times 10^{20}$ molecules/cm^3. Compare this with $N \approx 6 \times 10^{15}$molecules/cm^3 for a concentration of C=1×10^{-5} M YLD124 in chloroform solution. The average distance between molecules in this concentration of solution is about 550 $\mathring{A}$ apart (based on $C \times N_A^{-1/3}$, for N_A=Avogadro's number), such that the molecules are essentially independent of each other [1]; whereas, the distance between molecules in the crystal is about 6 $\mathring{A}$ by comparison (a factor of a 10^2 difference in estimated intermolecular distance). Now we relate these concentrations to N needed for successful EO applications. For example, maximum EO response for poled dye-doped polymers has been observed for FTC and CLD-type chromophores at about $N \approx 2 \times 10^{20}$ $\mathring{A}$. EO response was observed to decrease when the number density reached 4×10^{20} and above [56].Similar studies showed that optimum chromophore loading ranged from 30% to 40%, where increasing the weight percent of dye in the polymer above 40% reduced EO response [58]. This reduction in EO response with greater

[1] Assuming dipolar interactions are not so strong that chromophores aggregate in solution, which is thought to occur in YLD124

chromophore number density is likely due to centrosymmetric aggregation caused by strong electrostatic interactions between chromophores. Even in the presence of a poling field, dipole-dipole interactions between chromophores can be strong enough to defeat re-organization from an applied field. Thus, self-aggregation of chromophores complicates poling efforts.

4.1.3 Hyperpolarizability Calculations using the YLD124 Crystal Structure

As mentioned earlier, due to the centrosymmetry of the YLD124 crystal, the overall hyperpolarizability is expected to be practically zero. In order to study stacking types of YLD124 that give non-trival β, the centrosymmetry of the unit cell was broken by adding one neighboring molecule along the a, b, and c crystal axes. Furthermore, of these different trimer stacking arrangments, the centrosymmetric partner from the unit cell was removed to examine long-range interactions between the different acentric neighboring pairs, as shown in Figure 4.5.

Gaussian-09 Rev D.01 was used to compute the desired electronic and optical properties of oligomers of YLD124. Frequency-dependent hyperpolarizabilities consistent the linear electro-optic effect, $\beta_{zzz}(-\omega;\omega,0)$, were computed in vacuum at 1310 nm from analytical derivatives obtained via the coupled-perturbed Kohn-Sham (CPKS) method using long-range corrected methods LC-BLYP [229] and wB97xD [30]. The functional LC-BLYP was selected based on its favorable results for computing hyperpolarizabilities of single molecules (discussed in Chapters 2 and 3). Furthermore, an accurate description of dispersion is critical for electronic properties of π-stacked molecular systems, thus the dispersion-corrected wB97xD was also used. (For a thorough review of dispersion-corrected methods in DFT, see Ref [135].) All of the calculations were performed using 6-31+G* basis set and are according to the perturbation convention [244].

The results of the computed dipoles, polarizabilities, and hyperpolarizabilities are shown in Tables 4.1 and 4.2. Total hyperpolarizabilities for each oligomer computed with LCBLYP and wB97xD relative to the β of the isolated molecule are shown in Figure 4.6. The dipole moments (μ) and polarizabilities (α) computed using LC-BLYP are slightly smaller than those computed using wB97xD; however, the absolute hyperpolarizabilities (β) from LC-BLYP are consistently $\sim 20\%$ larger than wB97xD. Consequently, the relative hyperpolarizabilities of dimers or oligomers with

respect to the monomer, $\beta_{zzz}(-\omega;\omega,0)/\beta_{monomer}$, for LC-BLYP and wB97xD are nearly identical.

The dimer in the unit cell by itself gives $\beta \approx 0$, as expected. However, upon adding a third molecule, it is clear that none of the trimer configurations have β values larger than the isolated molecule hyperpolarizability. In fact, the semi-eclipsed trimer configuration along Crystal Axis a (i.e., 'YLD124 trimer, a') has β_{trimer} that is only ∼30% the $\beta_{monomer}$ value. This gives substantial evidence of intermolecular interactions between the monomers that, for these configurations, causes an overall reduction in β. Accordingly, when the centrosymmetric partner of the unit cell is deleted, none of the resulting dimers have a hyperpolarizability that is $2 \times \beta_{monomer}$ or greater. Considering that these dimer configurations assume acentric order, they are expected to deliver a bulk NLO response that is proportional to the product of number density and molecular hyperpolarizability, i.e. $r_{33} \propto N\beta_{monomer}$, according to Equation 1.15 where in this case $\langle cos^3\theta\rangle$=1. Local field factors in Equation 1.15 should partially correct for these intermolecular interactions, however, as noted in Ref [18], in this regime the local field factor is only weakly dependent on number density, N, which assumes intermolecular interactions to be negligible. In effect, Equation 1.15 essentially assumes that the monomer hyperpolarizabilities are additive when acentric order is achieved, which these results and others [88], [18], [226] have shown to be untrue, at least when intermolecular interactions play a significant role.

It is apparent from these results that sigificant π-orbital overlap between monomers (e.g., 'Crystal axis a' dimer) causes a reduction in β. The arrangement along 'Crystal axis b' produces the largest hyperpolarizability of the three crystal arrangements, likely because the donor on one molecule is overlapped with the acceptor of its neighbor. The configuration along 'Crystal axis c' does not put its monomers in a favorable D-A arrangement, however, its hyperpolarizability is similar to that of 'Crystal axis b'. This may explained by the relatively large intermolecular distance between the monomers ($\sim 22\mathring{A}$) in 'Crystal axis c', which would suggest that β increases when the monomers are farther apart.

A thorough review of methods to connect microscopic and macroscopic nonlinearities up to the year 2003 is given by B. Champagne and D. Bishop in Advances in Chemical Physics, Vol. 126 [31]. Cited in this review are computational studies of intermolecular interactions between monomers and its effect on hyperpolarizability based on small systems such as para-nitroaniline

(pNA) using semiempirical methods like INDO and AM1 and sum-over-states (SOS) to compute β [18], [250]. Of these, a 1992 computational study by Marks and Ratner found that β increased with intermolecular separation between cofacial eclipsed (here, referred to as 'π-stacked') dimers of pNA, but also featured a minimum occurring near $\sim 3.5\mathring{A}$ and sharply increases for distances smaller than $3.0\mathring{A}$. They hypothesized this increase was due to strong intermolecular dipole-dipole interactions. Furthermore, their studies on a different molecule with a relatively small dipole moment (3-methyl-4-nitropyridine 1-oxide, POM), showed results that were markedly different than pNA in that no minimum (no sharp increase at small distances) was observed. Based on sensitivity of the results to both molecular structure and electronic properties, as well as the computational methods used in these studies (based on hardware and algorithms available two decades ago), the work presented here for YLD124 cannot be assumed to necessarily arrive at the same conclusions. Also, an investigation of bulk electronic and NLO effects based on molecular clusters which contain chromophores with significantly *greater* molecular hyperpolarizability than small molecules like pNA would be useful to the scientific community. The well-characterized, high-β chromophore YLD124 is an excellent candidate for this purpose. Thus, we develop a study on YLD124 using both the crystal geometry as well as various hypothetical arrangements to explore the effect that relative position between the molecules has on both linear and nonlinear optical properties of this high-β chromophore.

It is worth noting that a recent study by Suponitsky and Masunov [226] on pNA and structurally similar systems, including 4-nitro-4′-aminostilbene (ANS), concluded that positive and negative contributions to the overall aggregate hyperpolarizability is due to electrostatic repulsions felt between neighboring molecular dipoles and not the total interaction energy, which falls in line with the simplified Frenkel exciton model given by Equation 4.2. They also suggested that stacks of at least 6-8 molecules must be included in the supramolecular approach to properly account for the effects of intermolecular surroundings on hyperpolarizability. Unfortunately, larger molecules such as YLD124 (81 atoms and 326 electrons per molecule if TBDMSO groups are removed) are too expensive for this size oligomer. In this study, the limit is three YLD124 molecules per DFT calculation (with 6-31+G* basis).

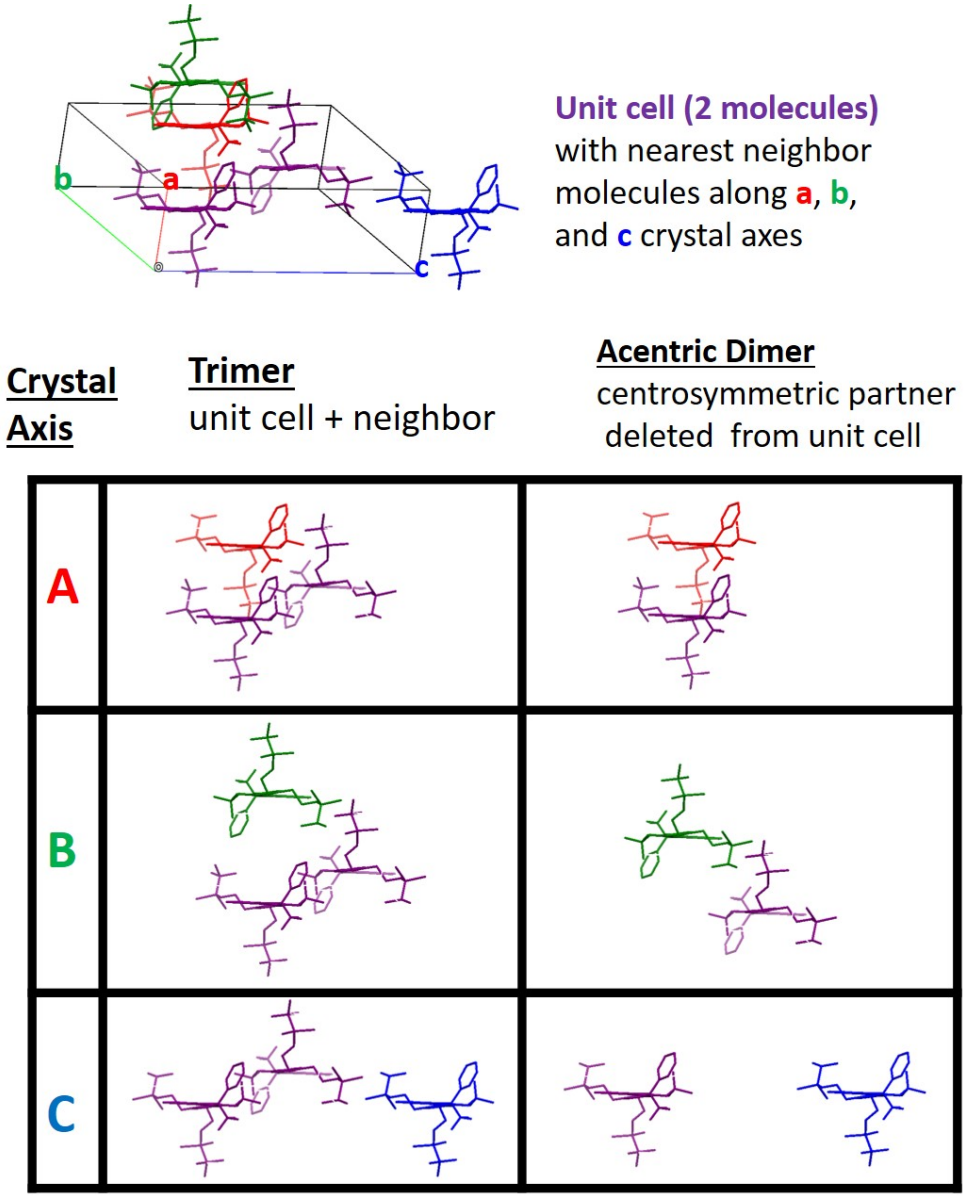

Figure 4.5: **Different Stacking Arrangements along the Different Crystal Axes.** The YLD124 crystal is centrosymmetric, thus its overall second-order NLO response is expected to be near zero. In order to study stacking types of YLD124 that give non-trival β, the centrosymmetry of the unit cell (containing molecules shown in purple) was broken by considering the neighboring molecules along the a, b, and c crystal axes. Note the color coding. Furthermore, of these different trimer stacking arrangments, the centrosymmetric partner from the unit cell was removed to examine long-range interactions between the different acentric neighboring pairs, as shown above. Hydrogen atoms have been omitted for clarity.

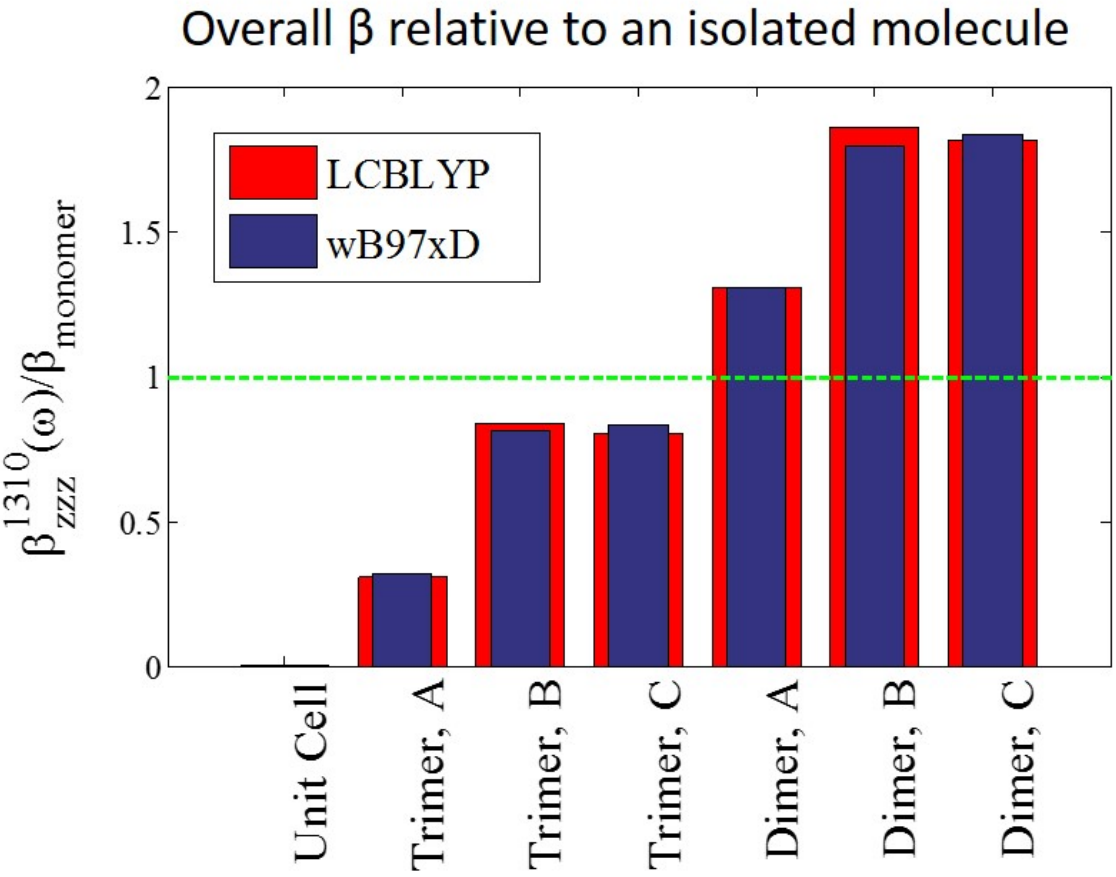

Figure 4.6: **Pockels Hyperpolarizability, $\beta(-\omega;\omega,0)\times10^{-30}$ esu, for each oligomer computed at 1310-nm in vacuum using LCBLYP and wB97xD with 6-31+G* basis set.** For the YLD124 unit cell, $\beta\approx0$. For all trimers (a,b,c), $\beta_{zzz}(\omega)/\beta_{monomer}<1$, where $\beta_{monomer}$ is the hyperpolarizability of the isolated molecule. For each of the acentric dimers, $\beta_{zzz}(\omega)/\beta monomer<2$. These results demonstrate that, even for oligomers with perfect acentric order, it does not necessarily follow that $\beta_{total}\neq n\times\beta_{monomer}$, n being the number of monomers.

Molecular System	μ **(D)**	$\alpha_{zzz}(0)$	$\alpha_{zzz}(-\omega;\omega)$	$\beta_{zzz}(0)$	$\beta_{HRS}(0)$	$\beta_{zzz}(-\omega;\omega,0)$	$\frac{\beta_{zzz}(-\omega;\omega,0)}{\beta_{monomer}}$
YLD124, monomer	27.9	81.1	84.2	552	301	835	1
YLD-124, dimer (unit cell)	0.0114	240.6	263.4	0.4140	0.2047	0.8914	1.07×10^{-3}
YLD-124 a, trimer	24.5	477	531	211	125	259	0.31
YLD-124 b, trimer	27.0	363	370	469	252	702	0.84
YLD-124 c, trimer	26.6	493	555	458	257	671	0.80
YLD-124 a , dimer	52.7	320	353	757	420	1093	1.31
YLD-124 b , dimer	55.5	240	263	1022	556	1548	1.85
YLD-124 c, dimer	54.9	326	365	1013	560	1517	1.82

Table 4.1: **Results of Electronic and Optical Properties of Monomer and Cluster Geometries using LC-BLYP/6-31+G* in vacuum.** α is in units of 10^{-24} esu and β is in units of 10^{-30} esu. (Hyper-)polarizabilites are reported according to the perturbation convention.

Molecular System	μ **(D)**	$\alpha_{zzz}(0)$	$\alpha_{zzz}(-\omega;\omega)$	$\beta_{zzz}(0)$	$\beta_{HRS}(0)$	$\beta_{zzz}(-\omega;\omega,0)$	$\frac{\beta_{zzz}(-\omega;\omega,0)}{\beta_{monomer}}$
YLD124, monomer	28.9	85.6	89.7	452	255	710	1
YLD-124, dimer (unit cell)	0.01	282	0.0508	0.0562	0.0865	2.93	4.12×10^{-3}
YLD-124 a, trimer	25.1	523	594	182	111	227	0.32
YLD-124 b, trimer	27.9	377	417	374	209	578	0.81
YLD-124 c, trimer	27.5	545	626	388	225	593	0.83
YLD-124 a , dimer	54.2	350	392	622	358	928	1.31
YLD-124 b , dimer	57.4	249	276	813	460	1276	1.80
YLD-124 c, dimer	56.8	358	409	835	479	1299	1.83

Table 4.2: **Results of Electronic and Optical Properties of Monomer and Cluster Geometries using wB97xD/6-31+G* in vacuum.** α is in units of 10^{-24} esu and β is in units of 10^{-30} esu. (Hyper-)polarizabilites are reported according to the perturbation convention.

4.1.4 Effect of Different Stacking Arrangements on β.

We first explore the effect of different stacking interactions on hyperpolarizability. For this study, we examine β of different dimers and trimers of YLD124 relative to the single-molecule hyperpolarizability, $\beta_{monomer}$. Since the relative hyperpolarizabilities with respect to the monomer, $\frac{\beta_{zzz}(-\omega;\omega,0)}{\beta_{monomer}}$, for LC-BLYP and wB97xD were nearly identical, we limit the methods to wB97xD which includes

dispersion correction. Otherwise, the hyperpolarizabilities were computed using the same methods (6-31+G* basis set in vacuum, analytical differentiation via CPKS method, reported in the perturbation convention, etc.) described in Section 4.1.3.

Figure 4.7 shows stacking along the crystal axes extending over three unit cells in which the centrosymmetric partner is deleted from each unit cell. In addition to the crystal geometries, Figure 4.8 shows generated geometries that describe stacking arrangements of particular interest, including the 'head-to-tail' configuration which effectively extends the π-conjugated pathway, the vertically 'π-stacked' arrangement (each monomer separated by 9 $\mathring{A}$ vertically), and the 'stair' which allows for overlap of separate donor and acceptor moieties by offseting the vertical stacking distance by 37° along the molecular axis (the magic angle, 54.7 °, is where dipolar coupling is expected to vanish, based on Equation 4.2). The intermonomeric distance (center of coordinates of molecule 1 to molecule 2) along the same plane in the head-to-tail arrangement is 27 $\mathring{A}$; whereas, the center-to-center distance between molecules for the π-stacked and stair arrangements are 9 and 15 $\mathring{A}$, respectively. These kinds of configurations, particularly the head-to-tail and side-by-side (crystal axis c) configurations, can occur in organic electro-optical dendrimers [180], [222], [19] which provides further motivation for studying the impact that intermolecular interactions have on overall hyperpolarizability.

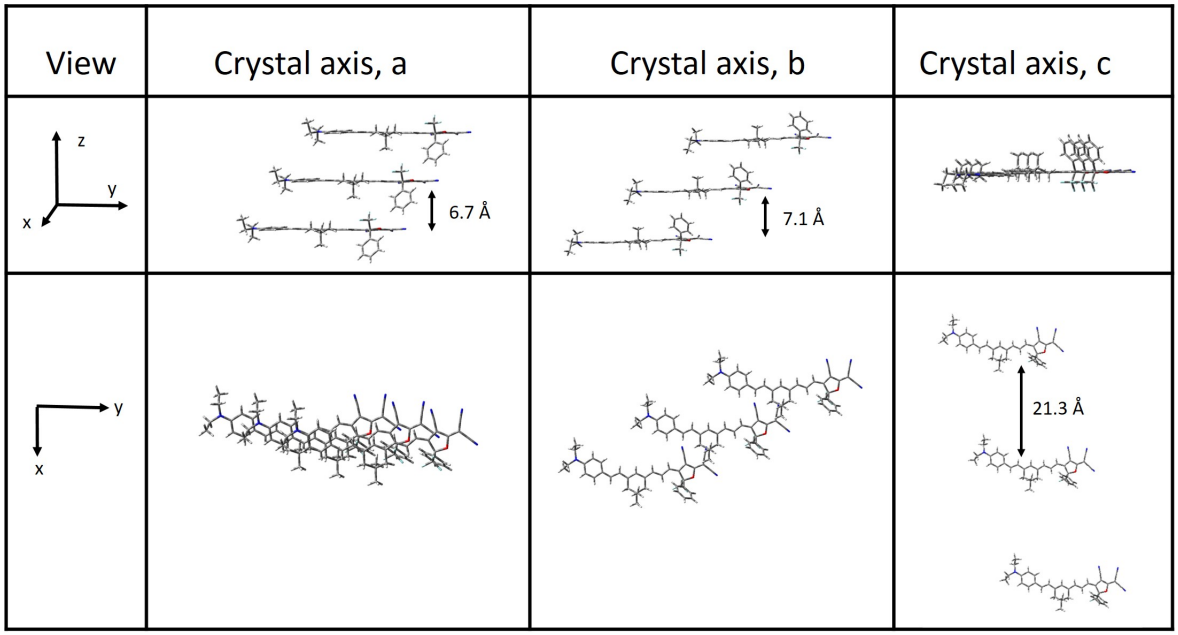

Figure 4.7: **Different Perspectives of Stacking Arrangements of YLD124 Monomers along Crystal Axes.** The trimers representing the stacking along the a, b, and c axes cover three unit cells. The centrosymmetric partner of each unit cell is deleted. The distance between monomer centers is roughly 7-22 $\mathring{A}$, depending on the arrangment.

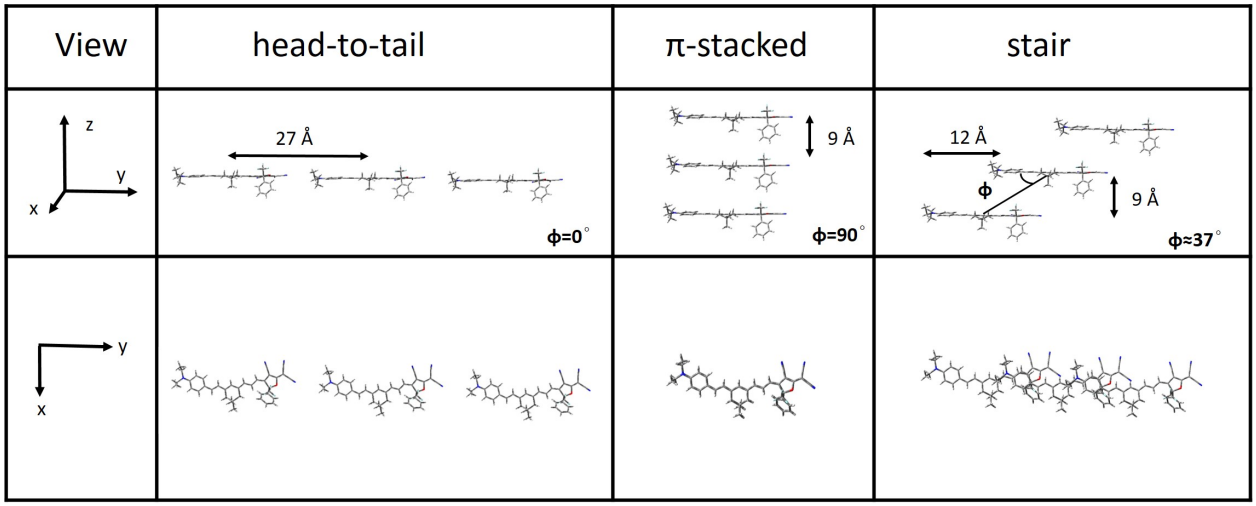

Figure 4.8: **Generated Stacking Configurations of Interest.** The distance between monomer centers is 9-27 $\mathring{A}$ for the different stacking arrangements.

Figure 4.9 shows the comparison of hyperpolarizabilities for different assemblies of YLD124 dimers and trimers relative to the isolated molecule, $\beta monomer$. The majority of stacking arrangements investigated here are less than an *additive effect* in β modeled by the black line $n \times \beta_{monomer}$, where n is the number of molecules. Similar to the results for the stacking along the crystal axis a, the π-stacked dimer hyperpolarizability is only about 36% larger than the single molecule hyperpolarizability.

The results so far suggest that reduction in π-orbital overlap and/or in electrostatic repulsions between neighboring donor and acceptor groups leads to an increase in β. We note that these arrangements are purely hypothetical and due to their significant polar repulsions, would be unlikely to naturally occur on a large scale. However, instances of such arrangements may still occur in isotropic media or poled polymers. For these arrangements, the overlap of electron clouds of neighboring molecules can be significant [88]. The stacking along crystal axis b but has a staggered arrangement with roughly 8 $\mathring{A}$ horizontal separation (along x axis) between each chromohpore which helps further reduce repulsions felt from nearby donor and acceptor groups. Following the above trend, this more energetically stable configuration (crystal axis b) improves β compared with the π-stacked dimer and is about 83% larger than the single molecule hyperpolarizability.

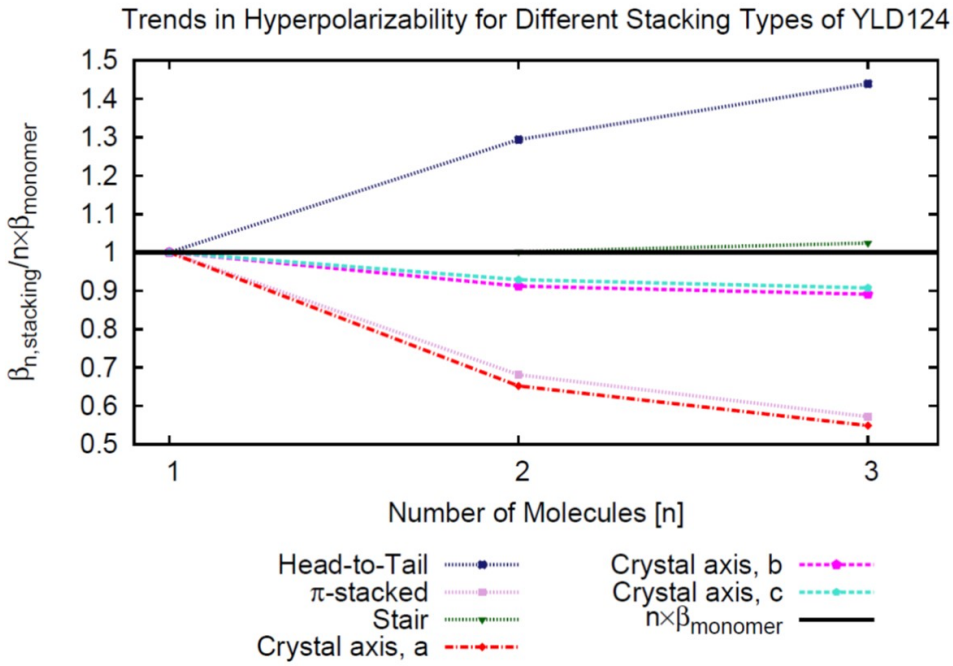

Figure 4.9: **Ratio of $\beta_{zzz}(-\omega;\omega,0)$ of the dimer and trimer configurations with $n \times \beta monomer$.** Comparison of different assemblies of YLD124 dimers and trimers with the additive model, $n \times \beta monomer$, represented by the black line where n is the number of molecules. The average contribution to the total hyperpolarizability from each monomer in an assembly is shown.

Number of Molecules, n	$n \times \beta_{monomer}$	**Head-to-tail**	**π-stacked**	**Stair**	**Crystal axis, a**	**Crystal axis, b**	**Crystal axis, c**
1	681						
2	1363	1763	929	1365	889	1245	1266
3	2044	2942	1169	2094	1122	1821	1855

Table 4.3: **The Pockels hyperpolarizability, $\beta_{zzz}(-\omega;\omega,0)$, for different oligomer configurations of YLD124.**

The arrangment that most closely matches the additive effect, $n \times \beta_{monomer}$, is that of the 'stair' configuration which was generated to test the effect of vertically overlapping the donor of

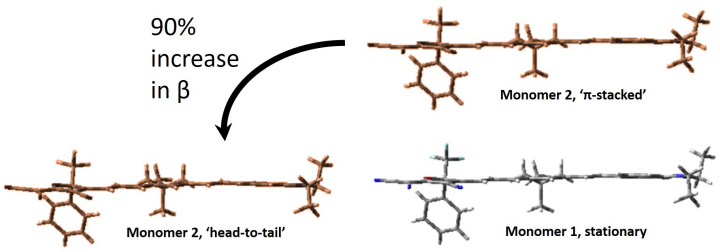

Figure 4.10: **Significant increase in β dependent upon relative position of acentric monomers.** An increase of ∼90% is shown according to wB97xD/6-31+G* calculations for vertically stacked versus planar head-to-tail arrangements of monomers.

one molecule with the acceptor of its neighbor while maintaining co-aligned dipoles. The trendline fit is $\beta_n^{stair} \approx 1.037 \times n\beta_{monomer}$ - 33. In this case, the effect of placing the donor and acceptor near each other is favorable, however, the conjugation path is 'broken' by the step between monomers. So far, these results can be qualitatively described by Equation 4.2.

Oudar and Chemla's two-level model (TLM) [183], described in Equation 1.4, predicts that extended π-conjugation along a planar backbone that allows for maximum overlap between donor and acceptor will increase β, thus it is expected that the 'head-to-tail' arrangement in which the molecules lie in the same plane will be more favorable than the displaced 'stair' arrangement. Indeed, the head-to-tail arrangement leads to considerable increase in β with increasing n, such that each molecule in the head-to-tail dimer has 30% larger hyperpolarizability than the isolated molecule. This effect continues to increase, each monomer hyperpolarizability is on average 44% larger than the isolated molecule in the head-to-tail trimer. The considerable enhancement in β for this arrangement is worth contrasting with the diminishing effects seen for the eclipsed (π-stacked) scenarios. These results, in particular the π-stacked, stair, and head-to-tail configurations, show that the average unit β in the dimer configurations gradually goes from ∼30% *less than* to 30% *greater than* the hyperpolarizability of the isolated molecule, as illustrated in Figure 4.10. The nearly 90% increase in β_{dimer} going from the vertically stacked dimer to planar head-to-tail arrangement may be qualitatively rationalized by the TLM. In the vertically stacked arrangement, the dimer molecular orbtials (MO) are heavily distorted and as a result the charge transfer band shifts to higher energies. This behavior is typical of H-aggregation in which the polar repulsions

experienced by the vertically π-stacked arrangement result in a blue-shift in CT excitation energy. This is accompanied by a small decrease in the shift in ground to excited state dipole moments, $\Delta\mu$, and primary CT transition dipole moment, μ_{ge} [18], thus the "allowedness" or charge-transfer corresponding to this transition is weakened. According to the TLM, these effects cooperatively lead to reduction in β.

To further test the TLM on the YLD124 dimers, $\beta_{zzz}(-\omega;\omega,0)$, the primary charge-transfer excitation energy, ΔE_{CT}, $\Delta\mu$, and approximated $|\mu_{ge}|^2$ [33] were computed according to varying the position between two co-aligned YLD124 monomers along a translation axis, x, and orbital angle, θ, as illustrated in Figure 4.11. The contour plots of each of these quantities is shown in Figure 4.12. Excitation energies were computed in vacuum using the linear response time-dependent DFT formalism applied to wB97xD. At least 8 excited states were requested for each calculation. Both hyperpolarizabilities, excitation energies, and ground and excited state dipole moments were computed using wB97xD/6-31+G* in vacuum.

Studying the contour plots for hyperpolarizability and CT transition energy with respect to relative intermonomeric position (Figure 4.12), we first note that β changes over a range of 160 units, whereas, transition energy covers a range of 0.07 eV ($\sim$18 nm). Neither of these ranges are large in relation to the mean values, however, these results clearly show a correlation between the vertically π-stacked configuration (x=0, θ=$\pi/2$, and intermolecular distance 10 $\mathring{A}$) and reduction in β coinciding with increase in CT transition energy, consistent with the TLM. Furthermore, the shift in ground to excited state dipole moment, $\Delta\mu$, decreases when the monomers are overlapped with minima occurring when $x \in (-4,0)$ for $\theta \approx 3\pi/4$ and $x \in (0,4)$ for $\theta \approx 1\pi/4$. The transition dipole moment, μ_{ge}, also reaches a minimum when $x \approx 0$. The configuration that is optimal for β, and likewise $\Delta\mu$ and $|\mu_{eg}|^2$, is when the monomers are spaced farthest apart from each other ($x > 7\mathring{A}$) and also lie in the same plane ($\theta = 0, \pi$). Comparing these results with the 'head-to-tail' dimer, in which $\beta_{zzz}(-\omega;\omega,0)$=1763$\times 10^{-30}$ esu, suggests that the 'head-to-tail' configuration is the best possible arrangement for increasing bulk-level hyperpolarizability.

For the YLD124 molecule which is composed of 81 atoms and 326 electrons (with TBDMSO groups removed), the computational expense of running wB97xD calculations with 6-31+G* is un-

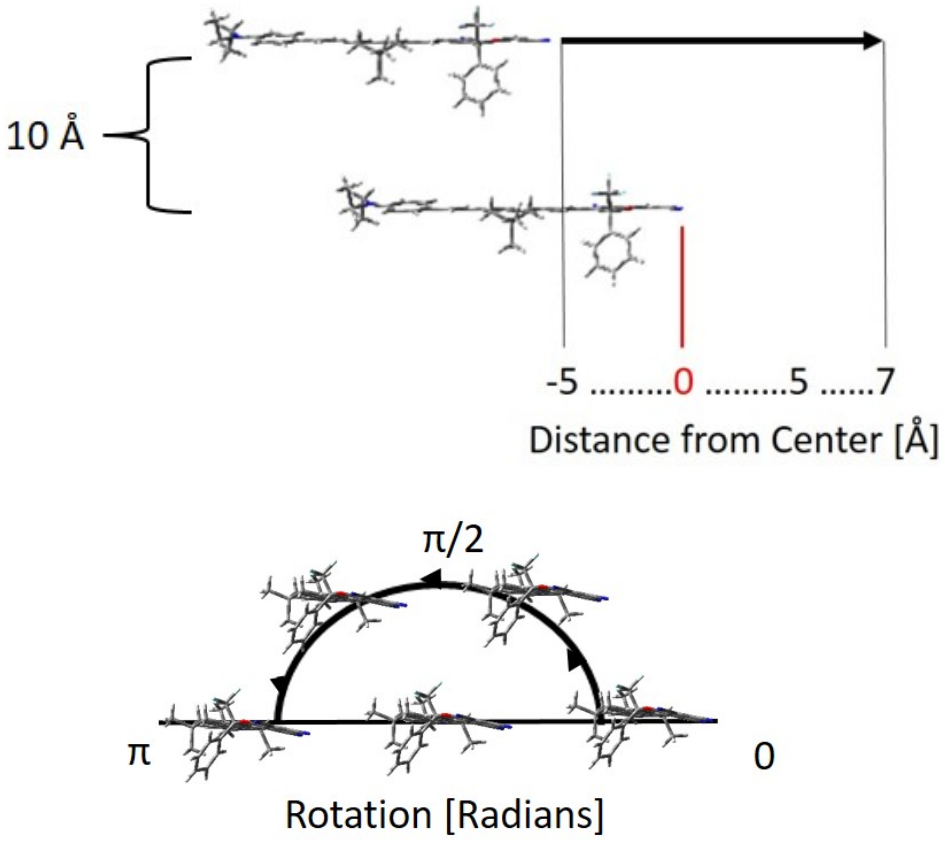

Figure 4.11: **Positioning Monomer 1 with Monomer 2.** Top: Monomer 1 remains stationary while Monomer 2 traverses along the molecular axis; Bottom: Monomer 2 orbits Monomer 1 along an angle from 0 to π. The illustrations are not necessarily drawn to scale. The YLD124 monomers are separated by 14 $\mathring{A}$ horizontally in plane and 10 $\mathring{A}$ directly vertical, the positions in between smoothly follow the resulting arc.

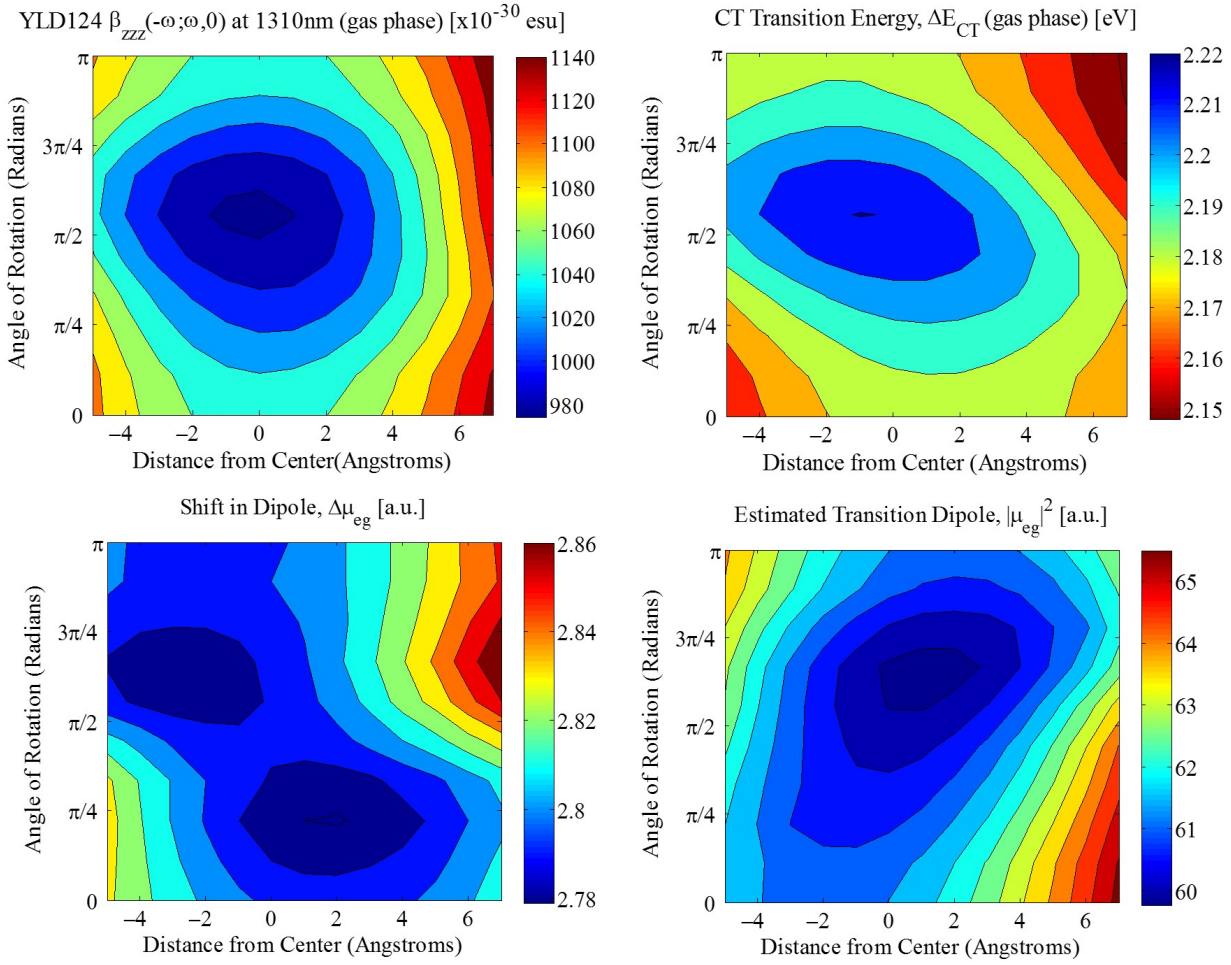

Figure 4.12: **Effect of Relative Position of Non-centrosymmetric Monomers of YLD124 on Linear and Nonlinear Optical Response** Top Left: First dipole hyperpolarizability consistent with the linear Pockels effect, $\beta_{zzz}(-\omega;\omega,0)$; Top Right: CT transition energy corresponding to the peak oscillator strength. (Note that a decrease in transition energy corresponds to a red-shift, so the colorbar is flipped.) Bottom Left: Shift in ground to excited state dipole moment, given in atomic units (conversion is 2.5418 Debye/a.u.). Bottom Right: CT transition dipole, $|\mu_{ge}|^2$, approximated by $\beta_{zzz}(0) \sim 6\frac{|\mu_{ge}|^2\Delta\mu}{\Delta E_{eg}^2}$, [33] where static β, $\Delta\mu$, and transition energy, ΔE are all converted to atomic units.

fortunately too costly for oligomers larger than trimers. For this reason, a larger set of oligomer calculations was performed on a small molecule, DCDHF (see Table 2.1), which has 45 atoms and 176 electrons per molecule. With this monomer size, frequency-dependent β calculations using wB97xD/6-31+G* could be run on octamers of DCDHF. The results of stacking trends and contour plots similar to Figures 4.9 and 4.12 are shown in the Supporting Information, illustrated in Figure C.2 and corresponding data contained in Table C.1. In brief, the results for DCDHF extended to 8 monomers are qualitatively similar to the results for YLD124 for some stacking arrangements. For example, as the number of molecules increases, the hyperpolarizability of each DCDHF molecule in the head-to-tail arrangement (at 8 units) approaches a constant of 1.8× the hyperpolarizability of the isolated molecule.

4.1.5 Effect of Intermolecular Distance on β and Transition Energy

In addition to stacking behavior between molecules, we also examine the effect that intermolecular distance has on hyperpolarizability and transition energies. For this study, we examine the stacking arrangements of noncentrosymmetric monomers along the three YLD124 crystal axes with comparison to the 'head-to-tail' arrangement, as shown in Figure 4.13. All calculations were performed in vacuo using wB97xD/6-31+G* basis set.

The closest interplanar distance between the monomers along 'Crystal axis, a' and 'Crystal axis, b' are based on the geometries from the crystallographic data shown in Figure 4.13, which are roughly 6.7 $\mathring{A}$ and 7.1 $\mathring{A}$, respectively. For 'Crystal axis, c', the intermonomeric separation based on crystallographic data was reduced from ∼22 $\mathring{A}$ to ∼11 $\mathring{A}$ to be comparable with the other geometries. When the monomers along the c axis are moved closer together, the β reduces to a value similar to the 'Crystal axis, a' value, as shown in Figure 4.14. In fact, the hyperpolarizability curves for 'Crystal axis, a' and 'Crystal axis, c' with respect to intermonomeric distance are practically identical. In either of these scenarios, as the monomers approach each other, they experience significant electrostatic repulsion due to minimal off-set ($< 5\mathring{A}$) of their acceptor groups. The hyperpolarizability for 'Crystal axis, a' decreases as much as 35% compared to $2 \times \beta_{monomer}$ based on its default crystallographic geometry (interplanar distance ~ 6.7 $\mathring{A}$) and it is assumed that 'Crystal

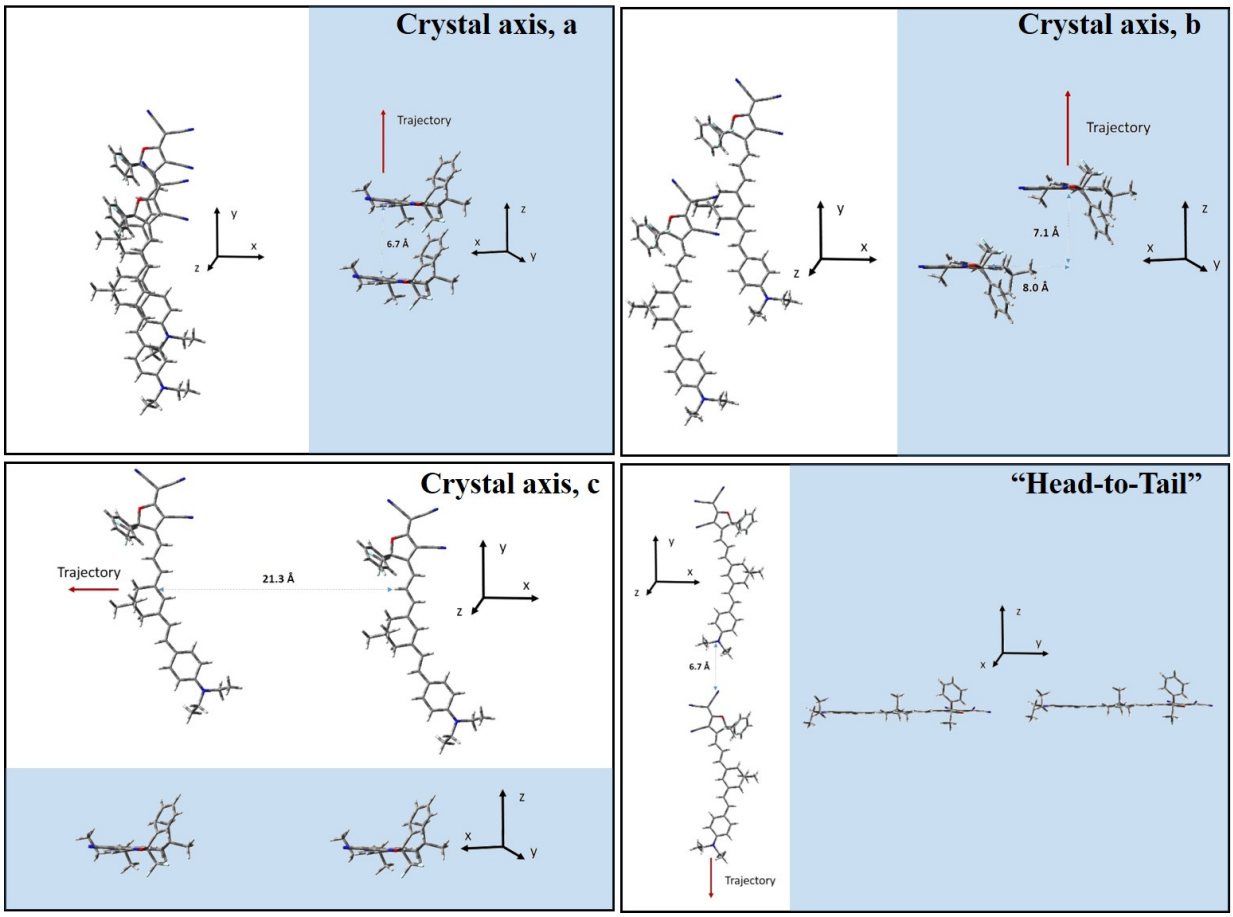

Figure 4.13: **Geometries and Trajectories for the Intermolecular Distance Study.** The stacking arrangements along the a, b, and c crystal axes, as well as the 'head-to-tail' arrangement, are shown according to two perspectives. The relative distance between monomers at their initial* positions were determined in GaussView. The more precise unit cell dimensions are a=7.9, b=13.9, and c=22.5 $\mathring{A}$. The trajectories for the distance study are illustrated by red arrows. (*For crystal axis c the actual separation based on crystallographic data is shown; however, for the calculations this separation was reduced from $\sim 22\mathring{A}$ to $\sim 11\mathring{A}$ to be comparable with the other distance ranges.)

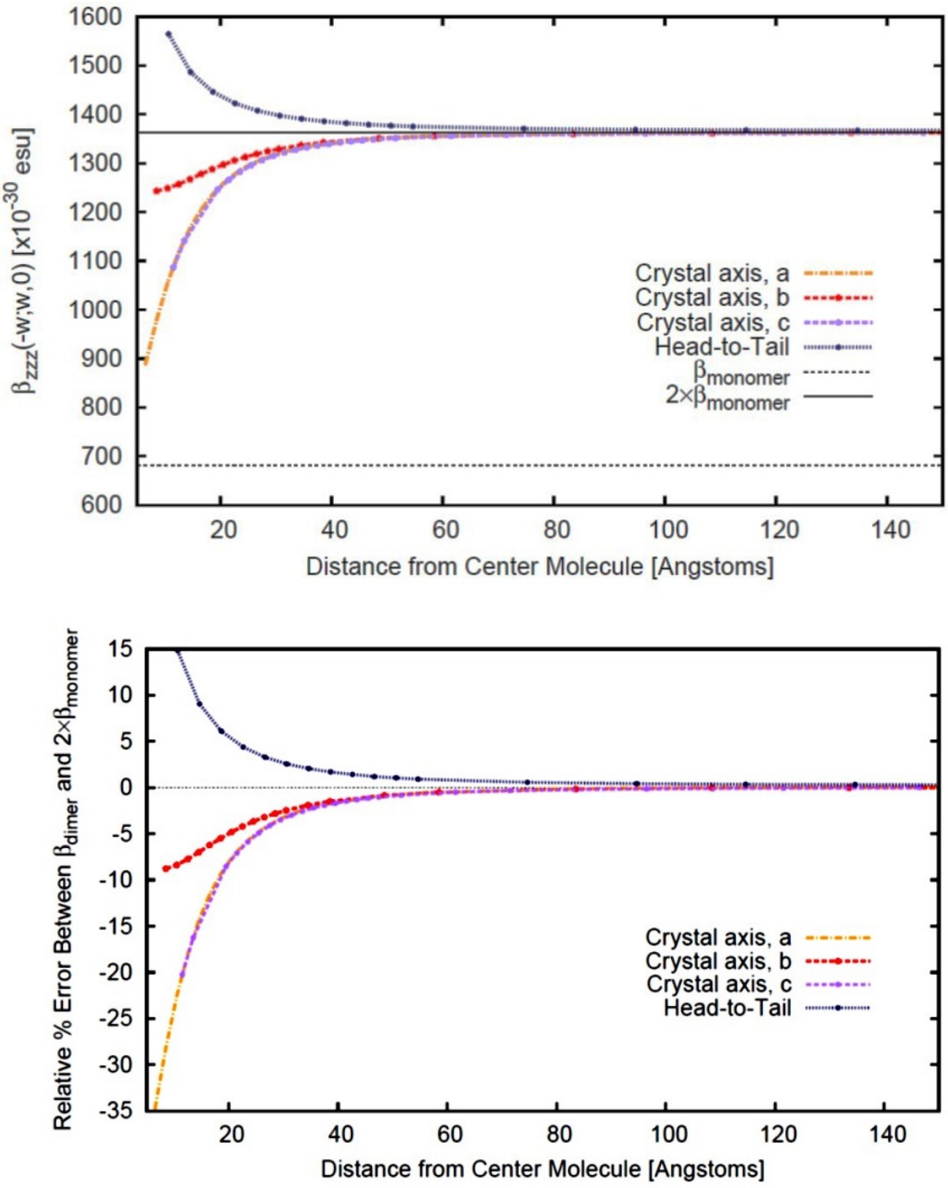

Figure 4.14: **Computed Hyperpolarizability as a function of Intermolecular Distance. Top:** Hyperpolarizability computed in vacuum using wB97xD/6-31+G*. **Bottom:** Relative percentage error between computed β_{dimer} and the limiting value, $2 \times \beta_{monomer}$. For clarification, the error is taken as $\left(\frac{\beta_{dimer}-2\beta_{monomer}}{2\beta_{monomer}}\right) \times 100\%$. At greater than 20 $\mathring{A}$ apart, the hyperpolarizabilities become additive within 10%, thus approaching $2 \times \beta_{monomer} \sim 1363 \times 10^{-30}$ esu, where $\beta_{monomer}$ is the hyperpolarizability of the isolated molecule in vacuum. At this distance, the molecules are independent of each other.

axis, c' would follow a similar trend < 10 $\mathring{A}$. The hyperpolarizability for 'Crystal axis, b', on the other hand, is 30% larger than either 'a' or 'c' at short interplanar distances, likely because each monomer is off-set by roughly 10 $\mathring{A}$ such that the acceptor of one overlaps with the center (bridge) of the other. This off-set improves hyperpolarizability of the dimer at short distance, however, there is still a notable decrease as they approach each other. The only arrangement that shows improvement in β at small intermolecular distance is the 'head-to-tail' arrangement which increases at about the same rate that 'Crystal axis, a' (or 'c') decreases with decreasing distance. It is clear that the hyperpolarizability of the dimer is largely affected by the direction along which the monomers approach each other; however, as the molecules pull apart, regardless of their behavior at short distance, their collective hyperpolarizability approaches an additive limit. Specifically, at distances greater than 20 $\mathring{A}$, the curves increase asymptotically to a value that is within 10% of $2 \times \beta_{monomer}$. Thus, these results suggest that the additive hyperpolarizability assumption, $N \times \beta_{monomer}$, that is the basis for r_{33} calculations is valid at low concentrations in which intermolecular interactions may be considered negligible. Once the molecules are within $\sim 20\mathring{A}$ of each other, the overall β of the dimer strongly deviates from this additivity assumption and it dependent on concentration.

Figure 4.15 shows the change in the lowest (most red-shifted) transition energy, ΔE_{red}, with respect to intermolecular distance, according to the models shown in Figure 4.13. Also shown is the difference between this lowest energy transition and the peak charge-transfer (CT) transition, $\Delta E_{CT} - \Delta E_{red}$. In some cases, such as for the isolated molecule of YLD124, the lowest energy transition is also the primary CT transition, so this difference is zero. ΔE_{red} does not change drastically over the distance investigated here ($> 5\mathring{A}$); the range in energy covers only about 0.1 eV, or roughly 30 nm. However, the trends for all of the models, except for 'Crystal axis, b', show growth ('Crystal axis, c') or decay ('Crystal axis, a' and 'head-to-tail') for distances less than 10 $\mathring{A}$. Decreasing intermolecular distance induces a blue-shift of the main CT peak in 'Crystal axis, c' and a red-shift in 'head-to-tail'. Examining the $\Delta E_{CT} - \Delta E_{red}$ curves, it is clear that there no additional low-lying states arise from the 'Crystal axis, c' or 'Head-to-Tail' (the curves are constant at zero). On the other hand, 'Crystal axis, a' and 'b' do exhibit a red shoulder; both of the $\Delta E_{CT} - \Delta E_{red}$ curves increase at faster rate than the change in ΔE_{red} over the same distance interval, thus ΔE_{CT} is also simultaneously blue-shifting thereby widening the gap. Also, as the gap widens the ΔE_{red}

oscillator strength grows slightly stronger. Nevertheless, these changes are small compared with $\Delta E_{CT} - \Delta E_{red}$ of the measured absorption spectrum of YLD124/PMMA which is 110-120 nm, or about 0.25 eV. Thus, to see any appreciable change in computed ΔE for the oligomer populations to compare with measurement will require very small intermonomeric distances ($< 10\mathring{A}$).

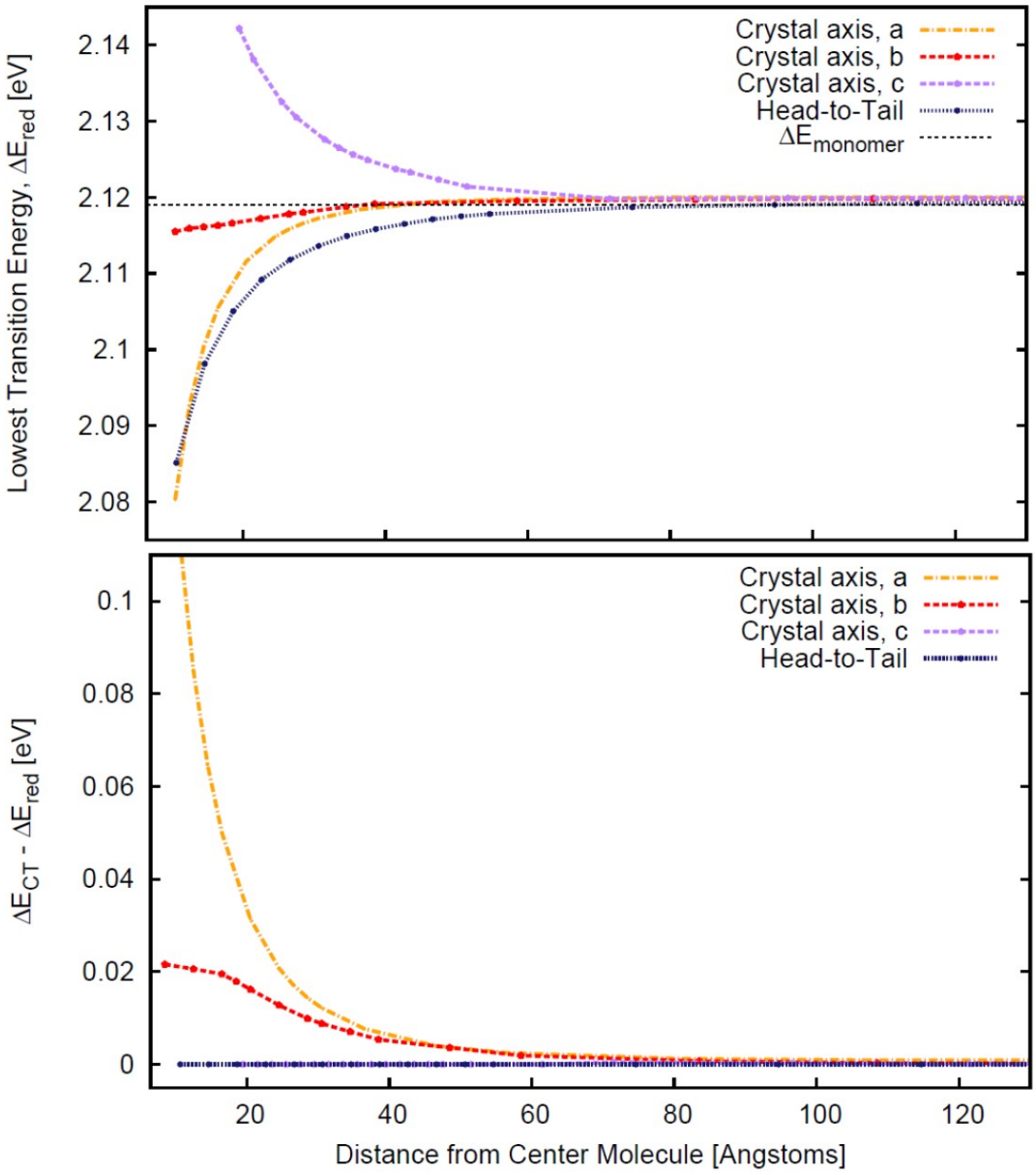

Figure 4.15: **Changes in Transition Energy as a function of Intermolecular Distance.** At 30$\mathring{A}$ apart, the transition energies are within the monomer value ± 0.01 eV. These results suggest that very small intermolecular distances (< 10 $\mathring{A}$) are required to observe any significant deviations between monomer and oligomer populations using DFT.

4.1.6 Monomers, Dimers, and...Yaw, Pitch and Roll!

The relative orientation of a rigid object can be described by Euler angles, often called the 'roll', 'pitch', and 'yaw' [42]. As illustrated in Figure 4.16, the roll angle rotates the molecule along the y-z plane, analogous to a rotisserie on a scewer (that is the x axis); the yaw moves the "head" of the molecule (for this work, the acceptor end) from side to side by rotating it in the x-y plane and pitch moves the head up and down by rotating it in the x-z plane. To understand the effect of relative orientation of two monomers on β and lowest transition energy, each of the roll, pitch and yaw angles of Monomer 2 were each varied with respect to Monomer 1 at a controlled interplanar distance (see right pane of Figure 4.16). For each of the controls, the distance was held constant at 18 $\mathring{A}$ apart (chosen to make room for the change in pitch) while the roll, pitch, and yaw were rotated from -180° to 180°. (At its initial position, Monomer 2 has the same x and y coordinates as Monomer 1 with only its z coordinate shifted by 18 $\mathring{A}$.) Based on this configuration, rotating Monomer 2 about the roll axis has the least effect on β; whereas, yaw and pitch shift β to zero as they approach ±180° (antiparallel configuration between monomers). The effect of changing roll and pitch on the most red-shifted transition energy, ΔE_{red}, is practically undetectable ($\sim$ 0.01 eV which is equivalent to about a few nanometers in wavelength). The changing yaw reveals some variation, ΔE_{shift} = 0.07 eV (18 nm), such that when yaw=±90°, the electronic properties are like the isolated molecule ($\Delta E_{red} = \Delta E_{CT}$=2.12 eV). At yaw=±180°, in which the dipoles of the respective monomers are antiparallel to each other, the spectrum red-shifts. Based on the results in Section 4.1.5, if the intermonomeric distance was reduced from 18$\mathring{A}$ to less than 10$\mathring{A}$, ΔE_{red} would be expected to shift to even lower energy. Also, if the initial position of Monomer 2 was shifted so to allow overlap of its donor with the acceptor of Monomer 1, the chance of excitonic coupling would be more likely. With the cofacial eclipsed configuration discussed here, little change in transition energy is expected.

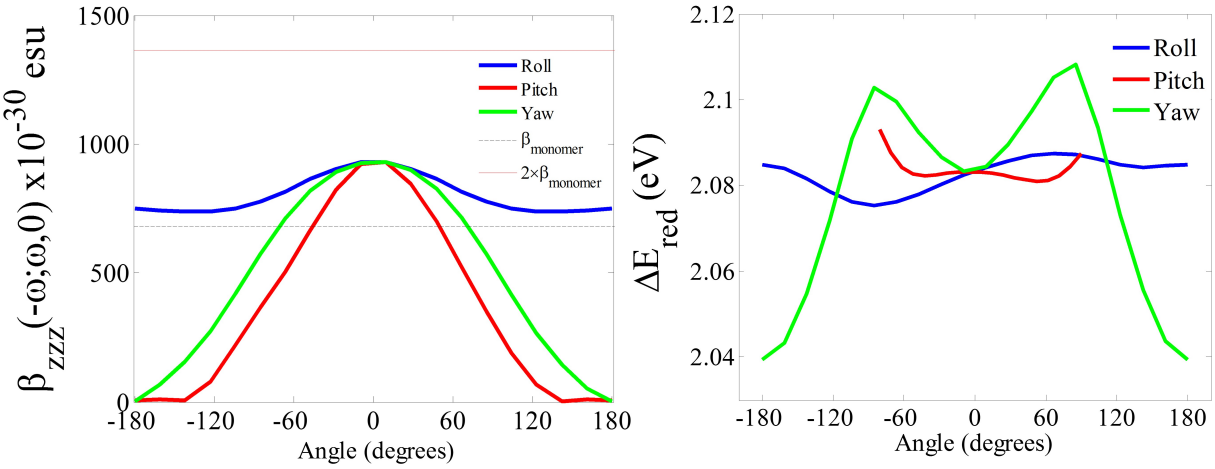

Figure 4.17: **Effect of Relative Orientation on β and lowest transition energy computed with wB97xD/6-31+G* in vacuum.** As expected, when the dipoles are oriented opposite to each other, $\beta = 0$ (yaw, pitch=$\pm$180°). The roll angle has little affect on either β or transition energies for the eclipsed dimer.

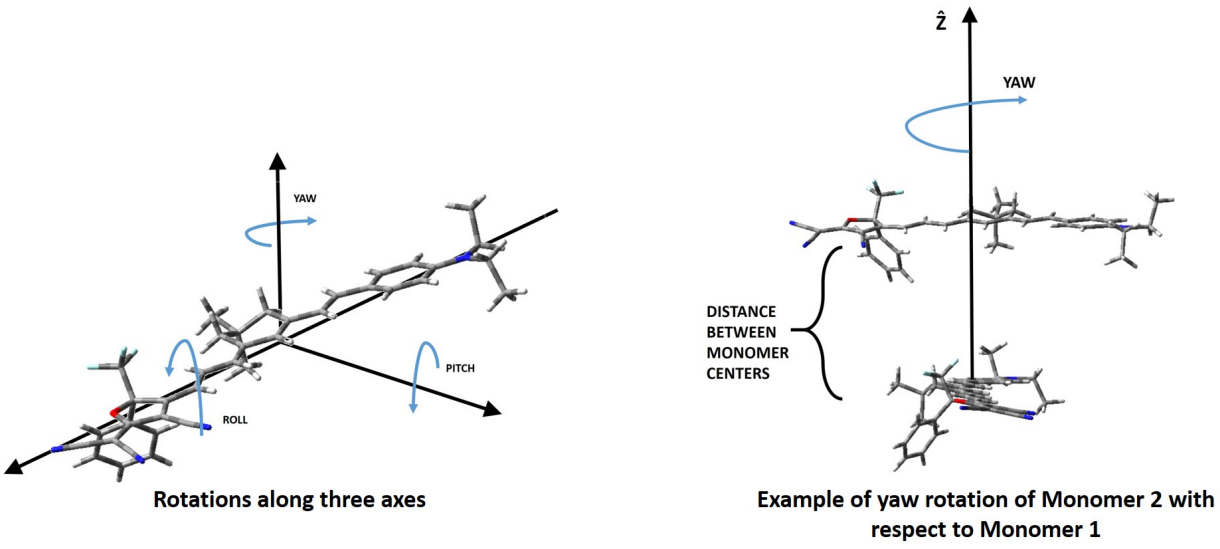

Figure 4.16: **Roll, Pitch, and Yaw.** Left: Illustration of the Roll, Pitch, and Yaw. Right: Example of rotating the yaw of Monomer 2 with respect to Monomer 1 (which is held static).

The intermolecular distance and Euler angles do not completely describe the relative position of monomers in an oligomer. To build a complete transformation matrix, both the rotation matrix (i.e., Euler angles) and translation vector (position in x, y, z) between monomers are needed. The concept of the translation vector was implicitly modeled in Figure 4.11 in which Monomer 2 is translated along an axis parallel to Monomer 1, as well as along an arc orbiting Monomer 1. The translation vector helps to distinguish various forms of aggregation. For example, consider the case in which two acentric monomers are in a vertically π-stacked arrangement which allows for the donor on monomer 1 ('D1') and acceptor on monomer 2 ('A2') to overlap. In this case, the relative roll, pitch, and yaw angles are 0°. Now, compare this with the case when D1 and A2 are still overlapped but instead the monomers are stacked in a 'stair' arrangement. Again, the relative roll, pitch, and yaw angles are 0°. As shown previously in Figure 4.10, the 'π-stacked', 'stair', and 'head-to-tail' dimers have the same relative yaw, pitch, and roll angles but yield distinctly different hyperpolarizabilities. Adding information from a translation vector would help distinguish these different arrangements by specifying the shifts between monomers along the x, y, and z axes.

Recall that the goal is to determine how relative orientation of monomers in a cluster affects the overall electronic and nonlinear optical response. The only problem is trying to plot a property, such as β, versus the cluster geometry that now depends on at least six dimensions: yaw, pitch, and roll, as well as x, y, and z translations between monomers. Due to the inherent complexity of the cluster geometry, it is useful to instead control most of these parameters while only varying one or two and then probing a given property of interest. The results thus far have shown that the first hyperpolarizability, β, is very sensitive to changes in yaw and pitch angles, as well as intermonomeric distance. We will examine disordered molecular orientations in Section 4.2, but first we consider a few test cases.

As illustrated in Figure 4.1.6, Monomer 2 is rotated 90° separately about each of the yaw, pitch, and roll axes, and then orbited along an arc with respect to Monomer 1 while simultaneously traversing the x axis (parallel to the molecular axis of Monomer 1). In agreement with Figure 4.17, the roll angle has little affect on β, thus, the results for roll=90° are similar to roll=0°. These results suggest that the relative roll angle between molecules of YLD124 does not significantly matter. Therefore, these results are similar to the hyperpolarizability contour plot shown in Figure 4.12 in

which the relative roll, pitch and yaw are all 0°. Similarly, the largest hyperpolarizability is achieved when the monomers are farthest apart and lie in the same plane (orbit angle=0, π). Also shown on the right hand side in Figure 4.1.6 is the difference in excited state energies in $\Delta E_{CT} - \Delta E_{red}$. Clearly, the largest energy gap ($\sim$ 0.2 eV) occurs when the monomers are nearly vertically overlapped (x$\approx$ 0 $\mathring{A}$, orbit angle$\approx \pi/2$) and gradually becomes zero as the monomers are moved apart along the translation axis, x.

The middle panel in Figure 4.1.6 shows what happens when the yaw is rotated 90°. The result is a β similar to the monomer value ($\sim 680 \times 10^{-30}$ esu), indicating that the sums and differences of the separate β tensor contributions effectively cancel each other in this arrangement. This result is consistent with the additivity model. The hyperpolarizability is largest, at approximately $\beta_{monomer}$+100 (see Figure C.4 for more details), when the monomers are coplanar and either A2 is directed at D1 (x=-10 $\mathring{A}$, orbit angle=0) or A1 is directed at D2 (x=10 $\mathring{A}$, orbit angle=π). The smallest hyperpolarizability, approximately $\beta_{monomer}-100$, occurs when A2 is directed at A1 (x=5 $\mathring{A}$, orbit angle=0). The bottom panel shows what happens when the pitch is rotated 90° with the acceptor pointing downward. This configuration yields hyperpolarizabilities that are 25-50% below the $\beta_{monomer}$ value. Based on the yaw 90° results, this reduction in β may be due to the acceptor on Monomer 2 being directed at Monomer 1, therefore causing significant electrostatic repulsion effects. Indeed, as Monomer 2 is moved away from Monomer 1 at x=-10 $\mathring{A}$, the hyperpolarizability increases slightly ($\sim 500 \times 10^{-30}$ esu). Over the entire grid of positions for both Yaw 90° and Pitch 90°, $\Delta E_{CT} - \Delta E_{red} \approx 0$. Thus, these kinds of configurations do not contribute significantly to a "red shoulder".

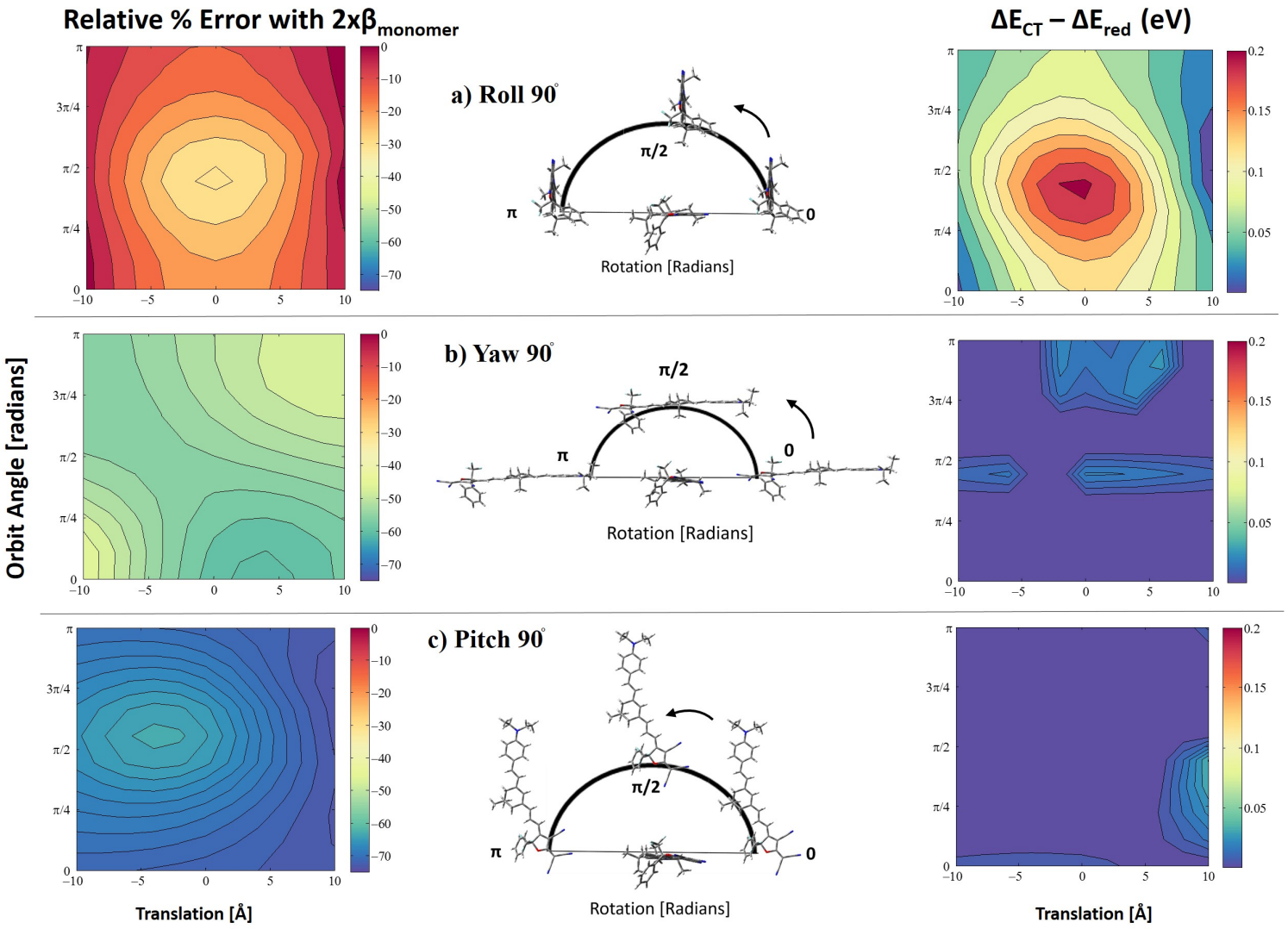

Figure 4.18: **Change in Frequency-dependent Hyperpolarizability and Lowest Excited State Energies with Relative Orientation of YLD124 Monomers.** The linear Pockels hyperpolarizability, $\beta_{zzz}(-\omega;\omega,0) \times 10^{-30}$ esu, and electronic transition energies, ΔE, were computed in vacuum using wB97xD/6-31+G* for various YLD124 dimers. The orbital angle is illustrated, as well as Monomer 1 (stationary) with respect to Monomer 2 (transient), the latter which has been re-oriented according to a 90° shift along the roll, yaw, or pitch axis. Monomer 2 is simultaneously traversed along 'x' which is the molecular axis of Monomer 1, as illustrated in Figure 4.11. Panel a) shows changes in β and splitting of the lowest electronic excited states, $\Delta E_{CT} - \Delta E_{red}$, when Monomer 2 is rolled 90°; Panel b) shows Monomer 2 rotated 90° about the yaw axis; and Panel c) shows Monomer 2 pitched downward by 90°.

Based on the results so far, it is clear that intermolecular distance and relative yaw angle are two principal geometric factors that strongly determine the magnitudes of β and transition energy. The question arises, does reduction in overall hyperpolarizability due to intermolecular interactions in acentric-order systems matter when in practice it is so difficult to achieve net asymmetric order in the first place? (Most high-β chromophore ensembles have predicted order less than $cos^3(\theta) \approx 0.3$ [232].) Recall that this is the basic assumption of the oriented gas model. Studies comparing the oriented gas model to supermolecular calculations of stacking interactions in molecular crystals have shown that the accuracy of the oriented gas model is highly dependent on crystal packing [247], [226]. The overall consensus is that intermolecular interactions are non-negligible in the determination of $\chi^{(2)}$. For the stacking interactions investigated here, recall the case shown in Table 4.3 in which a cofacial eclipsed YLD124 dimer arrangement results in 32% reduction in average hyperpolarizability per monomer compared to the isolated molecule. As the more monomers are stacked vertically in this arrangement, the reduction in average hyperpolarizability per monomer becomes more severe: 43% reduction based on the stacked trimer case. It is likely that this reduction would gradually increase before reaching an asymptote at sufficient oligomer size (based on small molecule studies, see Figure C.2). For the head-to-tail case, the trend is opposite: the unit hyperpolarizability in the chain increases with increasing oligomer size. Of course, in a poled polymer material the chromophores are slightly (sometimes very) disordered, certainly not ordered in a perfectly acentric manner. Since a significant percentage of YLD124 chromophores are expected to assume quasi-antiparallel orientation relative to neighboring molecules in an high-density isotropic ensemble, it is important to examine how relative yaw angle combined with intermolecular distance affects changes in computed excited state energies and correlate this to changes in β.

Combining these factors (yaw angle and distance), we examine our last case in which Monomer 2 is moved up the z axis away from the static position of Monomer 1 and at discrete steps along its trajectory (2 $\mathring{A}$ increments), Monomer 2 is spun about its yaw angle like a disc from 0 to 180°. At each angle, the frequency-dependent hyperpolarizability consistent with the linear Pockels effect, $\beta_{zzz}(-\omega;\omega,0)$, as well as transition energies and oscillator strengths were computed using wB97xD/6-31+G* in vacuum. The results are plotted in Figure 4.19. The right-hand side plot shows the difference between the primary charge transfer (CT) transition energy (corresponding to

the maximum oscillator strength) and the lowest transition energy, $\Delta E_{CT} - \Delta E_{red}$. The left-hand side plot shows the change in linear Pockels hyperpolarizability, $\beta_{zzz}(-\omega;\omega,0)$.

A red shoulder in the absorption spectrum grows in when the monomers approach each other (z <10 $\mathring{A}$) except for yaw angles equal to $\pm\pi/2$, in which the interacting dimer MOs cancel to yield an electronic absorption spectrum similar to the monomer. Accordingly, $\beta_{dimer} \approx \beta_{monomer}$ at $\pm\pi/2$ (plotted in percentage as $\left(\frac{\beta_{dimer}-2\beta_{monomer}}{2\beta_{monomer}}\right) \times 100\% \approx -50\%$). Otherwise, as Monomer 2 is trajected away, the low-energy transition, ΔE_{red}, diminishes and β increases. Otherwise, $\beta \rightarrow 0$ (plotted as -100%) as yaw$\rightarrow \pm 180°$. These results confirm that the presence of a red shoulder, $\Delta E_{CT} - \Delta E_{red}$, coincides with a decrease in β. However, the shoulder appears for both centrosymmetric (yaw $\rightarrow \pm\pi$) and non-centrosymmetric (yaw=0) configurations. In the following section, we quantify the relative contributions of these different types of aggregation by computing β and $\Delta E_{CT} - \Delta E_{red}$ of various YLD124 dimer and trimer snapshots from an isotropic ensemble.

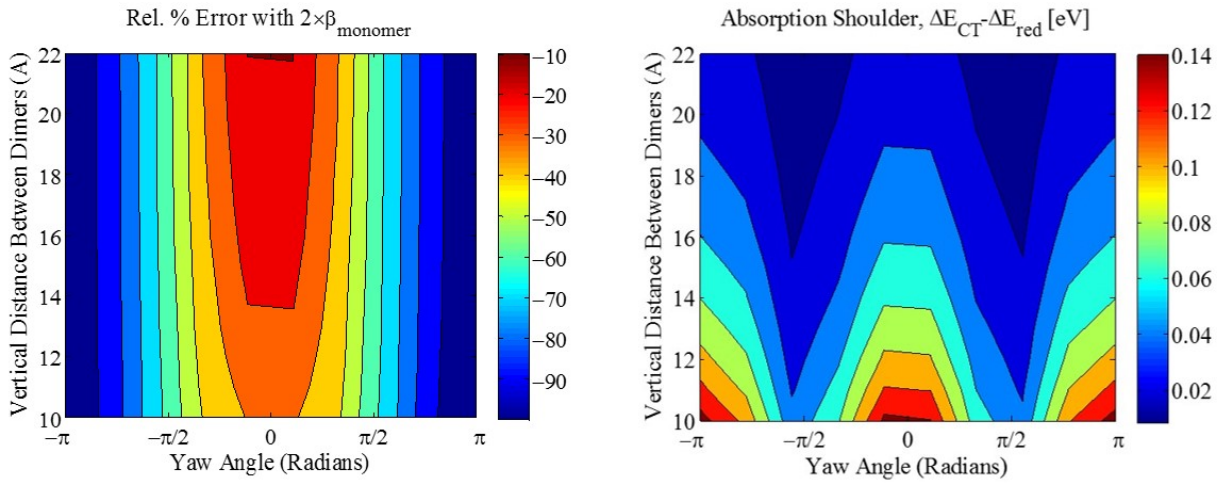

Figure 4.19: **Correlating frequency-dependent β and appearance of a red shoulder in the electronic absorption as a function of chromophore density and order.** The LHS shows relative percentage error between computed β_{dimer} and the limiting value, $2\times\beta_{monomer}$. The contour plots correspond to changes in Monomer 2 with respect to Monomer 1 as shown in the red-hand side of Figure 4.16, where Monomer 1 is held stationary while Monomer 2 is trajected vertically along the z axis and spun in the xy-plane at discrete steps. The intermolecular distance serves as a proxy for chromophore density and the yaw angle describes centrosymmetric vs. noncentrosymmetric order. All β calculations were done using wB97xD/6-31+G* in vacuum. For clarification, the error is taken as $\left(\frac{\beta_{dimer}-2\beta_{monomer}}{2\beta_{monomer}}\right)\times 100\%$.

4.2 A QM/MM Analysis of Electronic and NLO Response of an Isotropic Ensemble

We wish to connect the features of the electronic absorbance spectrum of a thin film doped with YLD124 to aggregation and, henceforth, the impact that aggregation and intermolecular interactions has on macroscopic nonlinear optical (NLO) response. One approach is to first model a large ensemble ($>$ 100 molecules) that reflects the order and density of chromophores in an unpoled film. This step can be performed using molecular mechanics (MM) methods [151], [45]. Once the ensemble has achieved an optimized configuration using MM, oligomers that are appropriately-sized for QM calculations may be extracted to determine properties such as electronic transition energy and hyperpolarizability. This procedure of treating the ensemble at different levels of theory to

combine speed and accuracy is known as the QM/MM (quantum mechanics/molecular mechanics) approach [241].

For this study, a Monte-Carlo (MC) [177], [193] program designed and run by Dr. Andreas Tillack [232] was used to determine the overall order of an unpoled racemic mixture of YLD124. In order to run the simulation for this large ensemble ($> 10,000$ atoms), the MC program decomposes the YLD124 molecule from a fully-atomistic description to a coarse-grained model of 24 ellipsoids tailored to match the shape and size of the bridge and substituents. A total of 108 YLD124 molecules (an even number of each enantiomer) was placed in a fixed volume and the simulation was run. The simulation includes the reaction field of surrounding YLD124 molecules such that each molecule is placed in a polarizable continuum with ϵ_∞=2.89. Upon completion, the resulting, average self-consistent dielectric for the 108-molecule cluster is 4.09, with a density that is approximately 0.8 g/cm^3 and overall isotropic order, $\langle cos^3\theta \rangle$=0$\pm$0.02 [1]. The 108-molecule snapshot is shown in Figure 4.20.

Various dimer and trimer configurations were extracted from the 108-molecule snaphot by scanning intermonomeric distances within 5$-$22 $\mathring{A}$. Of these scans, 260 dimer configurations and 100 trimer configurations were used for QM calculations of frequency-dependent hyperpolarizability and electronic excitation energies. All QM calculations were performed in vacuum using wB97xD with 6-31+G* basis set. Static and frequency-dependent hyperpolarizabilities were calculated from analytic derivatives using the coupled-perturbed Kohn Sham (CPKS) method in wB97xD. The linear Pockels hyperpolarizabilities, $\beta_{zzz}(-\omega;\omega,0)$, were calculated at a common telecomm wavelength, 1310 nm. Absolute hyperpolarizabilities are in units of 10^{-30} esu and are given according to the perturbation convention [244]. Electronic excitation energies were computed using the linear response time-dependent DFT (TDDFT) formalism with wB97xD. At least 8 excited states were requested for each of the dimer and trimer calculations. Of particular interest to this study are the lowest-lying excited state transitions, namely the primary intramolecular charge-transfer (CT) excitation energy and any additional low-lying energies below this transition that may be attributed to intermolecular CT. The goal is to identify a relationship between molecular assembly, β, and the appearance of low-lying excited state transitions, i.e. a "red shoulder", in the simulated electronic absorbance spectra.

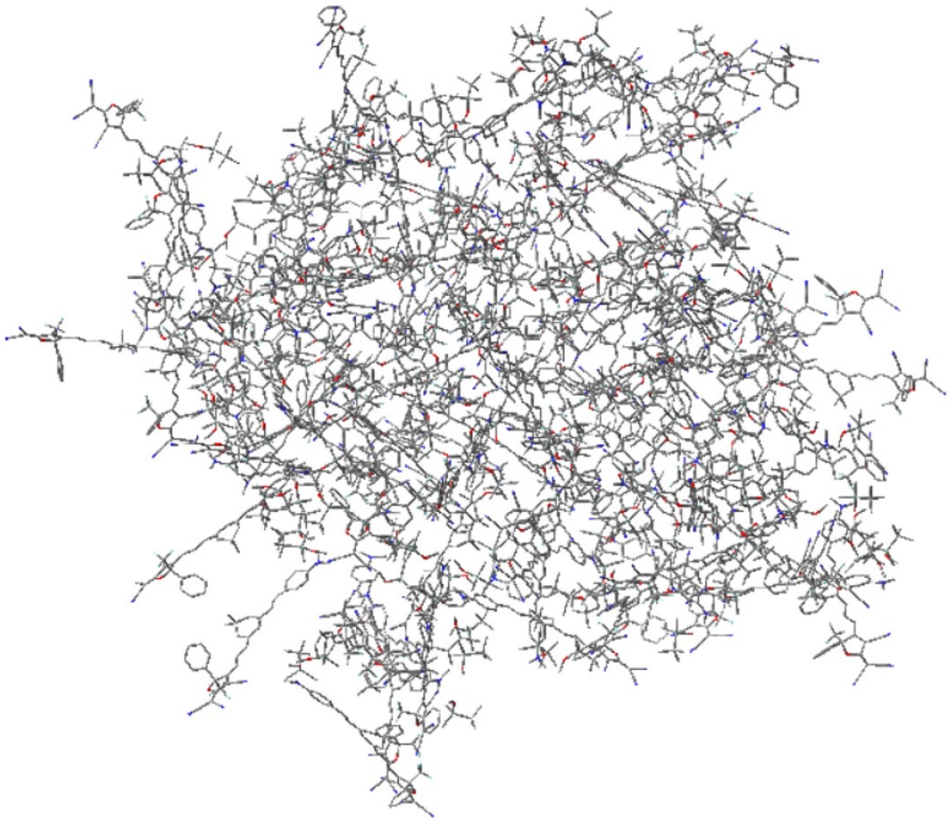

Figure 4.20: **Unpoled Racemic Mixture of 108 YLD124 molecules.** The geometry of the 108-molecule cluster was provided by Dr. Andreas Tillack using a Monte-Carlo (MC) code he developed. The ensemble has density 0.8 g/cm^3 and overall isotropic order, $\langle cos^3\theta \rangle$=0$\pm$0.02. Hydrogen atoms have been omitted from this illustration for clarity.

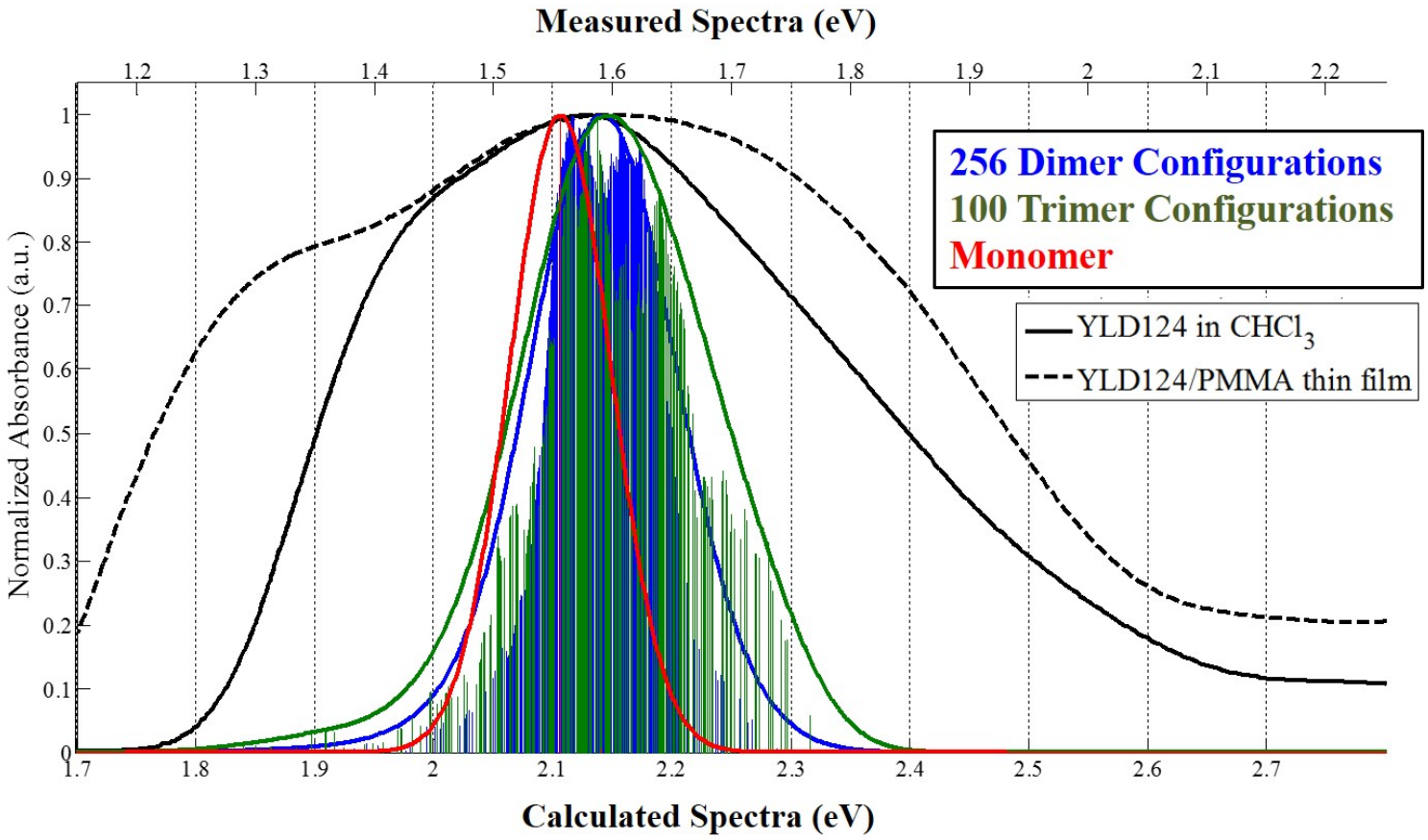

Figure 4.21: **Computed and Measured Spectra of YLD124.** Measurements provided by I. Kosilkin are of YLD124 in chloroform solution (solid black curve) and 100% doped into a PMMA thin film (dotted black curve). The calculations are grouped and color coded according to monomer, dimer, and trimer configurations. The monomer curve is a single monomer calculation; the dimer curve represents 256 unique dimer configurations; and the trimer curve is made of 100 unique trimer configurations. The sticks are oscillator strengths. The calculated data is shifted by roughly 0.5 eV to compare with the measured data. The measured and computed energy ranges are shown on separate (top and bottom) axes.

The calculated electronic transition energies and oscillator strengths for each of the monomer, dimer, and trimer populations are plotted in Figure 4.21. The ranges of the measured UV-vis spectra and the calculated spectra are superimposed such that the energies of the measured spectra are on the top axis. Note that the vacuum wB97xD calculations, shown on the bottom axis, are blue shifted by ∼0.5 eV with respect to measurement. The sticks represent the oscillator strengths for

each transition of a given monomer, dimer, or trimer calculation. If a transition is within ~ 0.03 eV (5 nm) of any other calculation in its category, the transition is counted once and their corresponding oscillator strengths are summed. For example, if two dimer calculations have transition energies at 2.0 eV, both with oscillator strength f=1.0, the plot will show a stick at 2.0 eV with f=2.0, and so on. This effectively illustrates the relative contribution of a given transition energy over the full ensemble of configurations. The curves blanketing each of the profiles are tightened (FWHM=0.1 eV) Gaussian fits. There are no rotamers of YLD124 in the simulation (systems have all-transoid backbone) and the coarse-grained description of each monomer results in very minimal change in geometry in the π-backbone from monomer to monomer. Thus, one monomer from the simulation was chosen to represent the typical absorbance spectrum of an isolated molecule ($\Delta E_{CT} \sim 2.1$ eV). Of the dimer and trimer spectra, each profile is described by 256 unique dimers [1] and 100 unique trimers, respectively.

For the dimer spectra, 39% of the lowest energy transitions, ΔE_{red}, are identical to the largest oscillator strength transition energy, ΔE_{CT}, as shown in Figure 4.22. Furthermore, 58% have ΔE_{red} within 0.05 eV of ΔE_{CT}. In fact, the the median dimer ΔE_{CT} energy is equivalent to that of the isolated molecule, roughly 2.1 eV. Nevertheless, the dimer spectra clearly show evidence of red and blue shifts with respect to the monomer spectrum based on Figure 4.21. We wish to correlate the red shifts in the oligomer spectra with particular forms of aggregation and determine its impact on the overall hyperpolarizability. Conveniently, the hyperpolarizability serves a dual purpose, as a measure of EO response as well as a proxy for the relative orientations of the monomers in the ensemble. In order to connect all of the factors of interest, Figure 4.23 shows the results of β, intermonomeric distance ($\mathring{A}$), and the appearance of additional low-lying transition energies, $\Delta E_{CT} - \Delta E_{red}$ (eV), for each dimer. For brevity, $\Delta E_{CT} - \Delta E_{red}$ will henceforth be denoted as $\Delta\mathscr{E}$; $\beta_{monomer}$ will be called β_M and β_{dimer} will be called β_D.

---

[1] Of the 260 dimer calculations submitted for both ΔE and β calculations, 4 TDDFT and 7 CPKS calculations did not finish. As a result, there are 251 of the 260 dimers that have both computed ΔE and β values.

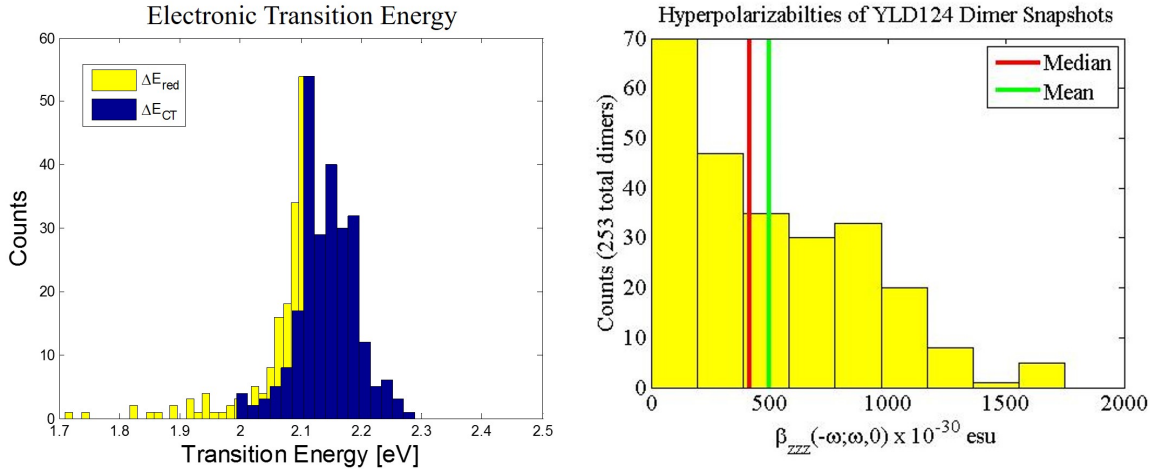

Figure 4.22: **Electronic Transition Energies and Pockels Hyperpolarizabilities for Various Dimer Configurations.** Left: The majority of the lowest lying transition energies, ΔE_{red} (yellow), are the same as the intramolecular charge-transfer energy, ΔE_{CT} (blue). Furthermore, the median ΔE is 2.1 eV, same as the monomer. Right: The median $\beta_{zzz}(-\omega;\omega,0)$ value from the various dimer configurations is 419×10^{-30} esu, 38% less than $\beta_{monomer}$. Dividing this value by the number of molecules per oligomer, in this case 2, gives an estimate of the average hyperpolarizability of each molecule in the ensemble.

As intermonomeric distance decreases, the gap between the primary CT peak and the red shoulder, $\Delta\mathscr{E}$, increases, indicating that the monomer centers (centroids of each monomers' coordinates) need to be within roughly 12 $\mathring{A}$ for mixing of the optical transitions with intermolecular CT states to occur. The majority of configurations which meet these criteria have β_D values less than β_M. Less than 2% of the population of dimers have hyperpolarizabilities larger than two times the monomer value. The different cases of β versus $\Delta\mathscr{E}$ are broken into 6 categories based on β_D greater and/or less than β_M and/or $2\times\beta_M$ and $\Delta\mathscr{E}$ less or greater than 0.1 eV, as shown in Figure 4.23. The separate categories are listed in the following, with percentage of the total population given in parentheses:

I. (1.6% total): $\beta_D > 2\times\beta_M$ and $\Delta\mathscr{E}$ <0.1 eV,

II. (22% total): $\beta_M < \beta_D < 2\times\beta_M$ and $\Delta\mathscr{E}$ <0.1 eV,

III. (57% total): $\beta_D < \beta_M$ and $\Delta\mathscr{E}$ <0.1 eV,

IV. (0.8% total): $\beta_D > 2 \times \beta_M$ and $\Delta\mathscr{E}$ >0.1 eV,

V. (7% total): $\beta_M < \beta_D < 2 \times \beta_M$ and $\Delta\mathscr{E}$ >0.1 eV,

VI. (12% total): $\beta_D < \beta_M$ and $\Delta\mathscr{E}$ >0.1 eV

Categories **I** and **IV** have the most favorable dimer configurations for hyperpolarizability with β_D ranging from 1450×10^{-30} esu to 1751×10^{-30} esu (approx. 2.13 to 2.57 greater than β_M). Unfortunately, these configurations also represent the smallest percentage of the population: only 2.4% combined. The **I** and **IV** configurations all have similar intermolecular distance (11.4-13.9 $\mathring{A}$) and have a similar stair-like geometry in which the monomers have co-aligned dipoles and the donor of one monomer is partially overlapped with the acceptor of the other. These categories are distinguished by $\Delta\mathscr{E}$ less or greater than 0.1 eV. Dimers in category **I** exhibit some mixing of the first excited state (lowest energy) transition with intermolecular charge transfer states, usually as a less than 10% contribution from HOMO→LUMO. (Orbital energies and MO visualizations for dimers exemplary of each category are shown in Figures C.7-C.12.)[2] For most of the systems, the first two excited states are split between *intra*molecular CT on monomer 1 and *intra*molecular CT on monomer 2. The orbitals are slightly distorted which induces small ±0.05 eV shifts in the transitions relative to 2.1 eV that is the primary CT transition of the isolated molecule. One of the **I** dimers has $\Delta\mathscr{E}$ ∼0.073 eV and, thus, its excited state description is qualitatively more similar to that of the category **IV** configurations. Unlike the majority of the category **I** dimers, this and the **IV** configurations have nearly co-planar monomers thus allowing for considerable overlap between the donor and acceptor of neighboring monomers. (The category **I** systems have monomers that are shifted or rotated away from each other thereby minimizing intermolecular orbital overlap between donor and acceptor.) This results in significant intermolecular CT character in the first two excited states. The first excited state of dimers in category **IV** includes $40 - 60\%$ contributions from intermolecular CT states (HOMO→LUMO). These ΔE_{red} transitions are relatively weak, with only 10-33% the oscillator strength of the next excited state (and largest oscillator strength) transition, ΔE_{CT}.

Categories **II** and **V** have moderate hyperpolarizabilities ranging from 696×10^{-30} esu to 1278×10^{-30}

[2]The percentage of single particle contributions to the vertical excited states was determined using the same method as Ref [237].

esu (1.02 to 1.88 greater than β_M). Combined these categories make up 29% of the total dimer population. The mean intermolecular distance for configurations belonging to category **II** is 13.7 $\mathring{A}$; whereas, for **V** it is 10.0 $\mathring{A}$. The closer monomers in category **V** allows for more intermolecular orbital overlap to occur which partially explains the greater $\Delta\mathscr{E}$ values. The smaller intermolecular distance also results in the average total energy for category **V** being 2.3 kcal/mol larger than category **II**. The median ΔE_{CT} values for each of these categories are at least 0.07 eV greater than the the median value of the total dimer spectrum ($\sim$ 2.1 eV). It is clear based on the different spectra shown in Figure 4.24 that the ΔE_{CT} values for category **II** (2.00−2.20 eV) are not as strongly blue-shifted as for category **V** (2.19−2.29 eV). Some examples of dimers in these categories are shown in Figures C.8 and C.11. In general, the dimers in category **V** have roughly co-aligned dipoles and are non-centrosymmetric. Electrostatic repulsions experienced between adjacent acceptor groups for some of these dimers may explain the relatively strong blue shift in ΔE_{CT}, which is consistent with H-aggregation. Three of the 18 dimers in category **V** have intermolecular CT mixing (13-49% contribution) occurring in the first excited state transition corresponding to ΔE_{red}. It is these same three dimers which also include intermolecular CT contributions to the next excited state transition corresponding to ΔE_{CT}. Only one of the 55 dimers in category **II** features any intermolecular CT contribution to its lowest-lying excited states. Otherwise, all other systems in category **II** have lowest-energy optical transitions primarily described by mixed intramolecular CT states.

Categories **III** and **VI** have hyperpolarizabilities smaller than β_M which range from zero hyperpolarizability to basically the isolated molecule value at 679×10^{-30} esu, i.e. $\beta_D \in (0, \beta_M)$. These categories make up 69% of the total dimer population. As shown in Figure 4.22, the median hyperpolarizability of the total dimer population is 419×10^{-30} esu which is 38% less than β_M. Dividing this value by the number of molecules per oligomer, in this case 2, gives an estimate of the average hyperpolarizability of each molecule in the ensemble. Thus, as a result of intermolecular interactions and symmetry, the average hyperpolarizability of each YLD124 molecule in the unpoled ensemble is roughly 210×10^{-30} esu, based on this analysis. Compare this with the isolated molecule which has nearly 3.25× larger hyperpolarizability. Due to some systems in these categories having nearly zero hyperpolarizability, it makes sense that many of the dimers are generally centrosymmetric (i.e., have oppositely aligned dipoles). The main distinguishing geometric parameter between category

III and **VI** is intermolecular distance. The mean intermolecular distance in **III** is 15.2 $\mathring{A}$ and it is about half that for **VI** at 7.6 $\mathring{A}$. Due to minimal intermolecular interactions for dimers in category **III** (which are 57% of the total), the absorbance spectrum for **III** shown in Figure 4.24 is similar to the monomer spectrum. The median ΔE_{CT} of category **III** dimers is 2.13 eV. In this category, nine of the 142 dimers has mixing of optical transitions with intermolecular CT states (ranging from 10-85% contribution to the first excited state transition) compared with 11 out of 30 dimers in category **VI** (ranging from 2-63% contribution to the first excited state transition). Of all of the categories, **VI** features the largest $\Delta\mathscr{E}$ values ranging from $0.10-0.46$ eV. The energy difference between the primary CT peak and shoulder in the measured spectra is at least 0.2 eV; therefore, the shoulder featured in the **VI** spectrum in Figure 4.24 is the most comparable to the shoulder in the measured spectrum based on $\Delta\mathscr{E}$. Otherwise, this analysis of dimer configurations is largely qualitative in its comparisons between measurement and theory. For instance, the shoulder in the measured spectrum is roughly 75% the intensity of the primary charge-transfer peak. As for the calculations, the few dimer configurations which do reveal a shoulder in their optical spectra via the occurrence of additional low-lying excited states have corresponding oscillator strengths that are relatively weak (f=0.08-1.8, compared to f ~2-5 for the strongest transitions) and do not add up to 3/4 of the largest peak in the total dimer spectrum.

Overall, there is noticeable correlation between computed frequency-dependent hyperpolarizabilities of the dimers and their computed optical spectra. Based on Figures 4.23-4.24, the categories with the same range of hyperpolarizabilities have optical spectra that are qualitatively similar. For example, dimers with large hyperpolarizabilities in categories **I** and **IV** have spectra that are about 0.1 eV red-shifted from the monomer spectrum and feature an additional weak transition near 2.2 eV. Furthermore, dimers with moderate hyperpolarizabilities in categories **II** and **V** have spectra with median ΔE_{CT} values that are at least 0.07 eV blue shifted with respect to the monomer spectrum. Dimers with hyperpolarizabilities smaller than that of the isolated molecule in categories **III** and **VI** represent the largest populations. The largest category, **III**, has an optical spectrum similar to the monomer (median ΔE_{CT} is 2.13 eV). The category **VI** spectrum features a slightly blue-shifted ΔE_{CT} peak (2.18 eV) and additional low-lying CT states (ranging from 1.71-2.08 eV) that are characterized by significant intermolecular CT. It is the features of the category **VI** spectrum

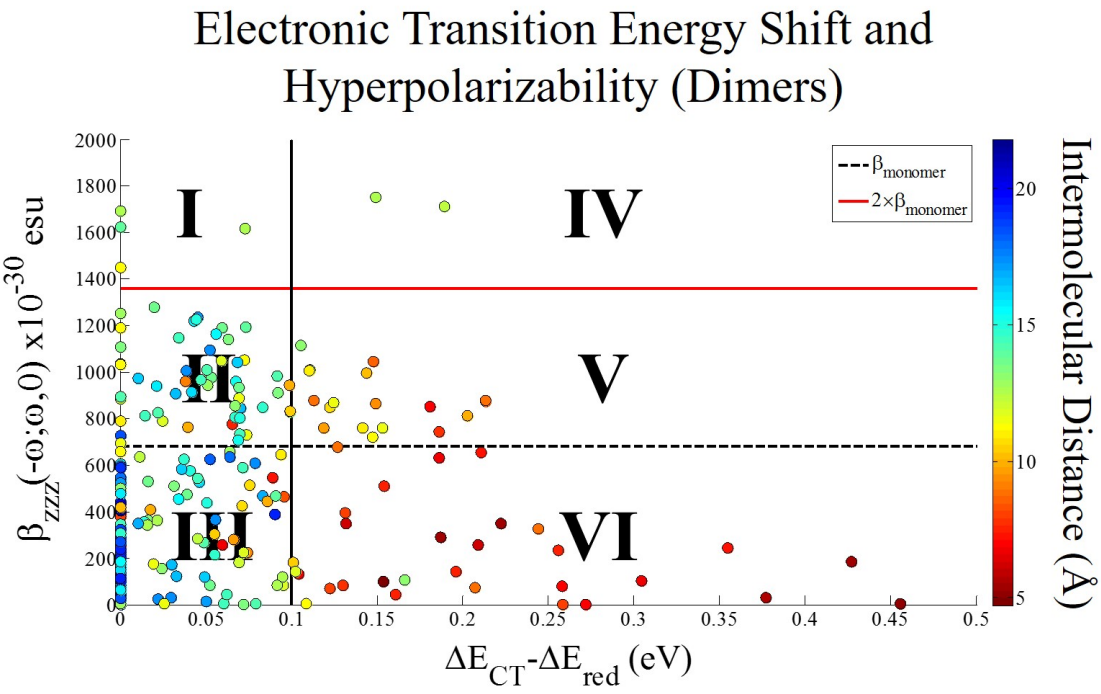

Figure 4.23: **Hyperpolarizability versus the appearance of low-lying CT states in simulated electronic absorption spectra for various dimer configurations.** The different cases of β versus transition energies are broken into 6 categories based on β_{dimer} greater and/or less than $\beta_{monomer}$ and/or $2 \times \beta_{monomer}$ and the difference between the lowest energy transition, ΔE_{red} and largest oscillator transition, ΔE_{CT} less or greater than 0.1 eV

that are most qualitatively similar to the features of the measured UV-vis spectrum of YLD124 in PMMA shown in Figure 4.21.

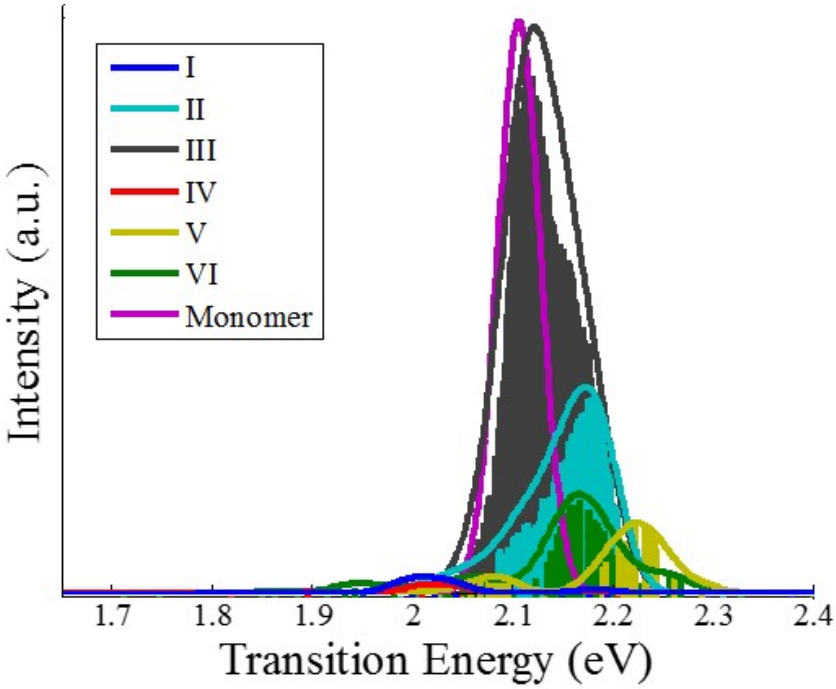

Figure 4.24: **Computed spectra for dimers in categories I-VI.** The relative intensities are not normalized. The typical monomer spectrum centered at 2.1 eV is shown for comparison.

The previous analysis done on the various dimer configurations determined that shoulders in the computed dimer spectrum (Figure 4.21) were a result of excitonic coupling occurring in configurations with considerable D/A overlap between monomer units. As a result of this excitonic coupling, the lowest-energy electronic transition of the monomer splits into a band of states which result in shoulders appearing in the simulated electronic absorption spectra in the 1.6-2.4 eV region. With increasing oligomer size, this band is split into even more excited states. Indeed, this is the case comparing the computed spectra of monomer to dimer to trimer in Figure 4.21. Compared with the dimer spectra, the lowest transition energies, ΔE_{red}, of the trimer configurations are distinct from the largest oscillator strength transitions, ΔE_{CT}, as shown in Figure 4.25. The median ΔE_{CT} of all of the trimer configurations is at 2.17 eV, whereas, the median ΔE_{red} value is 2.05 eV. To help further analyze the relationship between β and optical transitions of the trimer population, the same categories **I**−**VI** used in Figure 4.23 were applied to the data of 91 [3] unique trimer con-

[3] 100 TDDFT calculations successfully completed; whereas, only 91 β calculations succeeded

figurations. The results are shown in Figure 4.26 with the calculated spectra for each category plotted in Figure 4.27. The relative populations in order of each category of trimers are 0%, 12%, 23%, 2%, 20%, and 43%. As evidenced here, the majority (65%) of trimers have $\Delta\mathscr{E} > 0.1$ eV. The same percentage of trimers have hyperpolarizabilities between 200 to 800×10^{-30} esu. Compared with the dimer configurations, the range in hyperpolarizabilities for the trimers are less varied due to the additional disorder introduced by the third molecule. This causes the mean and median hyperpolarizability values of the trimer configurations to be the same, both equal to 604×10^{-30} esu, as shown in Figure 4.25. This value is larger than the median for the dimer configurations because there are an odd number of chromophores for each sampling which breaks most occurrences of centrosymmetry and effectively increases the average. Dividing this value by 3, however, gives 201×10^{-30} esu which is similar to the average hyperpolarizability of each monomer in the dimer ensemble (210×10^{-30} esu).

It is clear from Figure 4.26, that the categories applied to the trimers are not as clearly distinguished as they were for the dimers. The intermolecular distance which here is defined as the minimum distance between two monomers in a trimer configuration correlates poorly with both β and $\Delta\mathscr{E}$ data. Still, from this plot it is clear that all trimers which have $\Delta\mathscr{E} \approx 0$ have monomers that are separated by at least 11 $\mathring{A}$.

The majority (78%) of trimers fall in one of three categories: **III**, **V**, and **VI**. The category **III** spectrum shown in Figure 4.27 has a peak transition energy similar to the monomer spectrum. It also has higher energy transitions which notably occur at 2.2 and a little under 2.3 eV. Category **V** has two peak transitions of similar intensity that are respectively 0.05 eV and 0.18 eV blue-shifted from the monomer spectrum. The category with the largest percentage of the trimer population, **IV**, peaks at around 2.2 eV and has lower energy shoulders each occurring around 2.15, 2.05, and 1.9 eV.

For all categories of trimers, the largest oscillator strength transition corresponding to ΔE_{CT} occurs within the first three excited state transitions. Over 76% of trimers feature mixing of HOMO-2→LUMO and HOMO→LUMO+2 in the optical transitions of the first three excited states. These states correspond to a mixture of inter- and *intra*-molecular CT transitions. Orbital energies and MO visualizations for trimers selected from the most populated categories, **III**, **V**, and **VI**, are

shown in Figures C.13-C.15.

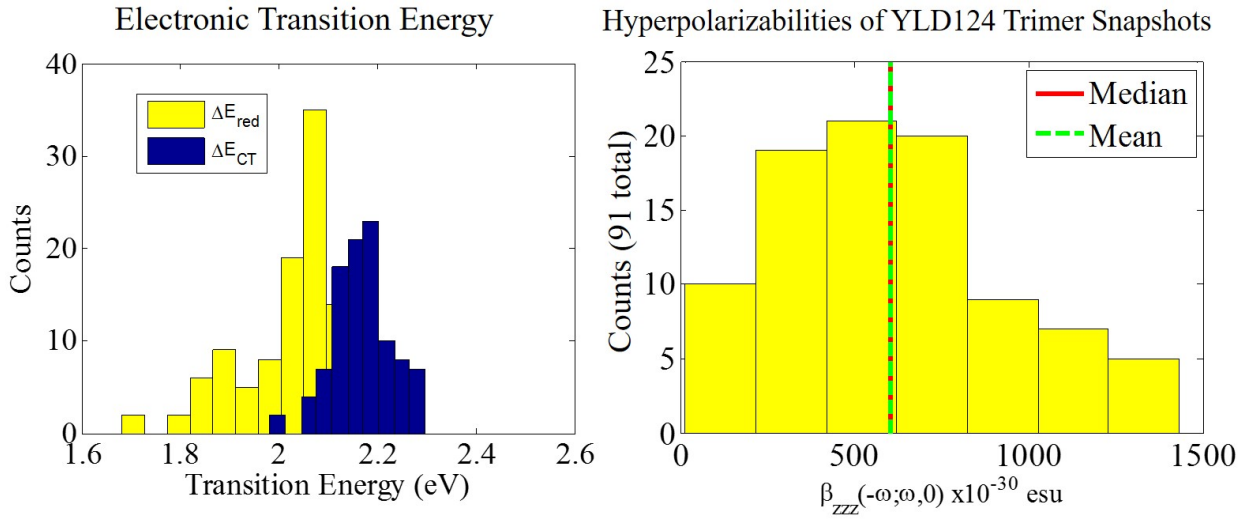

Figure 4.25: **Electronic Transition Energies and Pockels Hyperpolarizabilities for Various Dimer Configurations.** Left: The lowest lying transition energies, ΔE_{red} (yellow), are now diverging from the primary intramolecular charge-transfer energies, ΔE_{CT} (blue). Compared with the monomer spectrum, the median ΔE_{CT} is blue-shifted by 0.07 eV and the median ΔE_{red} is red-shifted by 0.05 eV. Right: The median $\beta_{zzz}(-\omega;\omega,0)$ value from the various trimer configurations is 604×10^{-30} esu, still less than $\beta_{monomer}$.

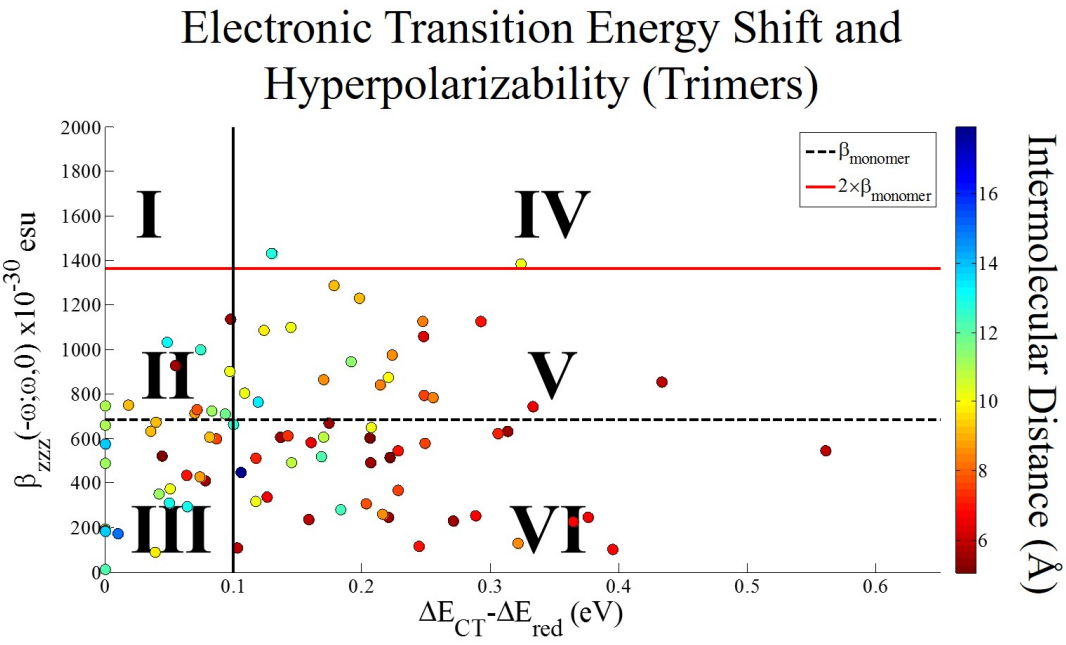

Figure 4.26: **Hyperpolarizability versus the appearance of low-lying CT states in simulated electronic absorption spectra for various trimer configurations.** The different cases of β versus transition energies are broken into 6 categories based on β_{trimer} greater and/or less than $\beta_{monomer}$ and/or $2 \times \beta_{monomer}$ and the difference between the lowest energy transition, ΔE_{red} and largest oscillator strength transition, ΔE_{CT} less or greater than 0.1 eV

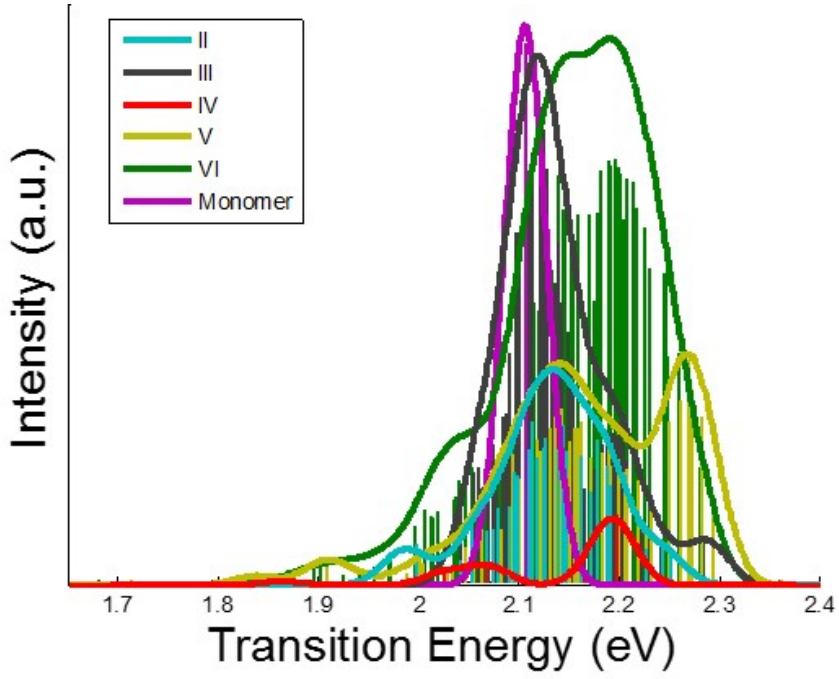

Figure 4.27: **Computed spectra for trimers in categories II-VI.** The relative intensities are not normalized. The typical monomer spectrum centered at 2.1 eV is shown for comparison. There are no values for category I.

In summary, dimer and trimer configurations which yield small computed hyperpolarizabilities (less than the isolated molecule) coincide with calculated spectral features that are qualitatively similar to the measured UV-vis spectrum of YLD124 at high concentration. Namely, the category **VI** spectra, for both dimers and trimers, feature a slightly blue-shifted primary CT peak and additional low-lying CT states that are characterized by significant intermolecular CT between the monomer units. The dimers in this category are generally centrosymmetric, which explains the modest hyperpolarizabilities; likewise, the trimer configurations typically include a centrosymmetric pair and a third molecule that does not appreciably add to the overall β. Also, the intensity of the lowest energy transitions occurring in the trimer spectrum are generally much stronger than those occurring in the dimer spectrum. For instance, the median oscillator strength of lowest transition energy, ΔE_{red}, of the trimer population is f=0.9989 $\approx$ 1; whereas, for the dimer population

it is 0.072. [4] Based on the trend from monomer to dimer to trimer, it is expected that the intensity of the shoulder will increase if TDDFT calculations are run on larger oligomers. Thus, it is possible that QM sampling of large enough clusters will give results that are quantitatively comparable to the features in the measured electronic absorption spectrum.

It should be noted that the theme of this study is to identify qualitative trends between aggregation types and features in the computed optical spectra and overall hyperpolarizability. In keeping with this theme whilst reducing the computational cost, solvent effects were neglected and the geometries provided by the coarse-grained description in the MC simulation were used directly without subsequent fully-atomistic geometry optimization. Despite these simplifications, the results presented here on dimers and trimers provide intriguing evidence that pockets of centrosymmetric aggregation are responsible for the appearance of a low-energy shoulder in the spectra of YLD124 with increasing concentration.

4.3 Conclusions

In order to achieve macroscopic electro-optic response, it is necessary to have overall noncentrosymmetric order of the organic nonlinear optical material [74]. Molecules with large molecular hyperpolarizabilties tend to be highly dipolar and thus prefer to align in a centrosymmetric manner to reduce electrostatic repulsions between neighboring dipoles [19]. For these systems it is necessary to induce acentric order. One method known as electric field poling re-orients the chromophore dipoles by application of a large DC field [50]. For poling measurements, the organic electro-optic dye is prepared by doping it into a polymer film with typical number densities around 2-4$\times 10^{20}$ molecules/cm^3 [56]. Unfortunately, centrosymmetric aggregation which competes with the poling field can sometimes occur at these concentrations [58]. The good news is that aggregation can be conveniently identified in the electronic absorption spectrum of some materials by increasing the concentration of dye [231], [78], [181], [248], [132], [91], [203], [113]. This study focuses on a high-β chromophore, YLD124, that when doped at high concentrations (>30 weight percent) in PMMA reveals a noticeable low-energy shoulder in its UV-vis spectrum [144]. To investigate if aggrega-

[4] Note that these statistics include only the lowest energy transitions that are not equal to ΔE_{CT}, which corresponds to the largest oscillator strength.

tion is the cause of this shoulder, gas-phase time-dependent density functional theory (TDDFT) calculations were run on various oligomers of YLD124. Gas-phase frequency-dependent hyperpolarizabilities consistent with the Pockel effect, $\beta_{zzz}(-\omega;\omega,0)$, at 1310nm, were also calculated using DFT to connect features in the computed optical spectra of the oligomers to changes in nonlinear optical response. Long-range corrected DFTs, LC-BLYP [229] and wB97xD [30], with 6-31+G* basis set were used for this purpose.

The study was divided into two parts, based on ordered versus disordered geometries of the YLD124 oligomers. The ordered geometries were derived from measured crystallographic data for YLD124 [122]. The unit cell of the YLD124 crystal is centrosymmetric, so the co-aligned (acentric) YLD124 molecules from neighboring unit cells were extracted for theoretical investigation. For these pairs of molecules, the acentric order is nearly perfect, $\langle cos^3\theta\rangle \approx 1$, which helps in isolating the effect of intermolecular interactions on β. As evidence of coupling between YLD124 monomers, the results showed that none of the acentric dimers from the crystal had β equal to or greater than the value of twice the isolated molecule ($2\times\beta_{monomer}$=1362×10^{-30} esu, for wB97xD). Additional hypothetical geometries were generated for comparison with these results. Notably, a cofacially eclipsed ("π-stacked") dimer resulted in a hyperpolarizability that was only 35% $2\times\beta_{monomer}$; whereas, a planar head-to-tail arrangment (i.e., chain of co-aligned monomers) resulted in a 70% enhancement in β compared with the isolated molecule. Regardless of the behavior at short intermolecular distances, the hyperpolarizabilities of the different dimers approach the same independent-molecule limit as the monomers are pulled farther apart resulting in $\beta_{dimer} = 2\times\beta_{monomer}$ for intermolecular distances greater than 40 $\mathring{A}$. In addition, to observe noticeable changes in computed optical spectra due to coupling between monomers, the intermolecular distance must be less than 10 $\mathring{A}$.

Disordered geometries were derived by extracting various dimer and trimer configurations from a Monte-Carlo (MC) simulation [232], [193] of an unpoled racemic mixture of 108 YLD124 molecules. It was determined that dimer and trimer configurations which yield modest hyperpolarizabilities ($< \beta_{monomer}$) and have intermonomeric distances less than 10 $\mathring{A}$ coincide with computed optical transitions that are qualitatively similar to the measured UV-vis spectrum of YLD124 in PMMA. Like the measured data, these configurations feature a slightly blue-shifted primary CT peak and additional low-lying CT states. The dimers and trimers in this category typically include a cen-

trosymmetric pair of monomers which explains the small hyperpolarizabilities for these oligomers. Also, it was determined that the intensities of the additional low-energy electronic transitions that appear in the trimer spectra are considerably stronger than those which appear in the dimer spectra. Based on this trend from monomer to dimer to trimer, it is expected that the intensity of the low-energy shoulder that is composed of these low-lying electronic states will grow with increasing oligomer size, thus more closely resembling the features of the measured YLD124 spectrum.

4.3.1 Supporting Information

Additional figures and tables are located in Appendix C.

Appendix C includes, in order:

1. Hyperpolarizability trends for the various oligomers of the small molecule, DCDHF
2. Data Tables for the Roll, Pitch, and Yaw Contour Plots in Figure 4.1.6
3. Closer Look: Dimer and Trimer Spectra separately plotted
4. Molecular Orbitals and Orbital Energies of Selected Dimers in Categories **I**-**VI**
5. Molecular Orbitals and Orbital Energies of Selected Trimers in Categories **III**, **V**, and **VI**

4.3.2 Acknowledgements

Work at University of Washington was partially supported by the National Science Foundation (STC- MDITR DMR-0120967 and DMR-0905686) and the Air Force Office of Scientific Research (FA9550-09-1-0682, FA9550-10-1-0558, and FA9550-15-1-0319) and the University of Washington Student Technology Fund (STF). I thank Prof. Larry Dalton, Dr. Delwin Elder and other members of the Dalton group for helpful discussions. This work was facilitated though the use of the AFRL Spirit supercomputer system at the DoD supercomputing resource center and Hyak supercomputer system at the University of Washington. I would like to thank Dr. Joshua Hendrickson who is the principal investigator for the Nanobeam Nanophotonics subproject on Spirit that I am very fortunate to be a part of. I would like to also thank Patrick Lestrange and the HPC club at University of Washington for helping me gain access to the Hyak supercomputer for which I used to run many of the memory-intensive TDDFT dimer and trimer calculations in this study. I would also like to thank Dr. Andreas Tillack for helpful discussions and for providing the Monte-Carlo snapshot of YLD124. Much gratitude is given to Dr. Ilya Kosilkin for providing UV-vis spectra of YLD124 from his dissertation. I also enthusiastically thank Peter Johnston and Dr. Werner Kaminsky for crystallographic data of YLD124 and DCDHF.

References

[1] Based on discussions with Andreas Tillack, c. 2015.

[18] S. D. Bella, M. Ratner, and T. Marks. "Design of Chromophoric Molecular Assemblies with Large Second-Order Optical Nonlinearities. A Theoretical Analysis of the Role of Intermolecular Interactions." In: *J. Am. Chem. Soc.* 114 (1992), pp. 5842–5849.

[19] S. Benight et al. "Reduced Dimensionality in Organic Electro-Optic Materials: Theory and Defined Order". In: *J. Phys. Chem. B.* 114 (2010), pp. 11949–11956.

[23] R. Boyd. *Nonlinear Optics*. San Diego, CA, USA: Academic Press, Inc., 1992.

[24] J. Brandrup et al. *Polymer Handbook*. New York, New York: Wiley and Sons, 1999.

[27] C.R. Cantor and P.R. Schimmel. *Techniques for the Study of Biological Structure and Function*. San Francisco, CA, USA: W.H. Freeman and Company, 1980, p. 349.

[30] J. Chai and M. Head-Gordon. In: *Phys. Chem. Chem. Phys* 10 (2008).

[31] B. Champagne and D. Bishop. "Calculations of Nonlinear Optical Properties for the Solid State". In: *Advances in Chemical Physics (Vol 126)*. Ed. by I. Prigogine and S. Rice. 2003. Chap. 2, pp. 41–92.

[33] B. Champagne et al. "Ab Initio Coupled Hartree-Fock Investigation of the Static First Hyperpolarizability of Model all-trans-Polymethineimine Oligomers of Increasing Size". In: *The Journal of Physical Chemistry A* 101.17 (1997), pp. 3158–3165.

[42] L.J. Clancy. *Aerodynamics*. Section 16.6. London, UK: Pitman Publishing Limited, 1975.

[45] C. J. Cramer. *Essentials of computational chemistry: theories and models*. Chinchester, UK: Wiley and Sons, 2004.

[50] L. R. Dalton, P. A. Sullivan, and D. H. Bale. "Electric Field Poled Organic Electro-optic Materials: State of the Art and Future Prospects". In: *Chem. Rev.* 110 (2010), pp. 25–55.

[55] L.R. Dalton. "Organic electro-optic materials." In: *Pure Appl. Chem.* 76.7-8 (2004), pp. 1421–1433.

[56] L.R. Dalton et al. "Low (Sub-Volt) Halfwave Voltage Polymeric Electro-optic Modulators Achieved by Controlling Chromophore Shape". In: *Science* 288 (2000), p. 119.

[58] L.R. Dalton et al. "Progress toward Device-Quality Second-Order Nonlinear Optical Materials. 1. Influence of Composition and Processing Conditions on Nonlinearity, Temporal Stability, and Optical Loss". In: *Chem. Mater.* 10 (1998), pp. 146–155.

[59] L.R. Dalton et al. "Systematic Nanoengineering of Soft Matter Organic Electro-optic Materials". In: *Chemistry of Materials* 23.3 (2011), pp. 430–445.

[61] A. Davydov. *Theory of molecular excitons.* New York: Plenum Press, 1971.

[70] D.L. Elder et al. "Matrix-Assisted Poling of Monolithic Bridge-Disubstituted Organic NLO Chromophores". In: *Chemistry of Materials* 26.2 (2014), pp. 872–874.

[74] K. A. Firestone et al. "Frequency-Agile Hyper-Rayleigh Scattering Studies of Electro-Optic Chromophores". In: *Proc. SPIE* 5395 (2005), 0P1.

[78] A. Furube et al. "Effect of Aggregation on the Excited-State Electronic Structure of Perylene Studied by Transient Absorption Spectroscopy". In: *The Journal of Physical Chemistry A* 110.20 (2006), pp. 6465–6471.

[88] M. Guillame, E. Botek, and B. Champagne. "Theoretical investigations of the linear and second-order nonlinear susceptibilities of the 3-methyl-4-nitropyridine-1-oxyde (POM) crystal". In: *J. Chem. Phys.* 121 (2004), pp. 7390–7400.

[91] F. Haverkort, A. Stradomska, and J. Knoester. "First-Principles Simulations of the Initial Phase of Self-Aggregation of a Cyanine Dye: Structure and Optical Spectra". In: *The Journal of Physical Chemistry B* 118.29 (2014), pp. 8877–8890.

[113] E.E. Jelley. In: *Nature* 138 (1936), p. 1009.

[115] W. Jin et al. "Benzocyclobutene barrier layer for suppressing conductance in nonlinear optical devices during electric field poling". In: *Appl. Phys. Lett.* 104 (2014), p. 243304.

[122] W. Kaminsky. *Report: Crystal Structure Report for Dalton-Reid, ID-YLD124*. Sample Submitted by Peter Johnston. 2012. URL: `cad4.cpac.washington.edu/structures`.

[125] I. Kaplan. *Intermolecular interactions : Physical picture, computational methods, model potentials.* Hoboken, NJ: Wiley and Sons, Inc., 2006, pp. 39–41.

[132] S. Kirstein and S. Daehne. "J-Aggregates of Amphiphilic Cyanine Dyes: Self-Organization of Artificial Light Harvesting Complexes". In: *Int. J. Photoenergy* 2006 (2006), p. 1.

[135] J. Klimes and A. Michaelides. "Perspective: Advances and challenges in treating van der Waals dispersion forces in density functional theory". In: *J. Chem. Phys.* 137 (2012), p. 120901.

[144] I. Kosilkin. "Organic Materials for Electro-Optic and Optoelectronic Applications: Understanding Structure - Property Relationships". Thesis. 2012.

[151] A. Leach. *Molecular Modelling: Principles and Applications*. Harlow (UK): Prentice Hall, 2001.

[170] B. McCarthy et al. "Charge Transfer or J-Coupling? Assignment of an Unexpected Red-Shifted Absorption Band in a Naphthalenediimide-Based Metal-Organic Framework". In: *J. Phys. Chem. Lett.* 4 (2013), pp. 453–458.

[174] P. Millie, F. Momicchioli, and D. Vanossi. "Exciton Effects in the Dimer and Higher Aggregates of a Simple Merocyanine Dye. A CS INDO CI Based Theoretical Study". In: *The Journal of Physical Chemistry B* 104.41 (2000), pp. 9621–9629.

[177] Metropolis N. et al. In: *J. Chem. Phys.* 21 (1953), p. 1087.

[180] Y. Okuno, S. Yokoyama, and S. Mashiko. "Interaction between Monomeric Units of Donor-Acceptor functionalized Azobenzene Dendrimers: Effects on Macroscopic Configuration and First Hyperpolarizability". In: *J. Phys. Chem. B.* 105 (2001), pp. 2163–2169.

[181] D. Ostrowski et al. "The Effects of Aggregation on Electronic and Optical Properties of Oligothiophene Particles". In: *ACS Nano* 6.6 (2012), pp. 5507–5513.

[183] J. L. Oudar and D. S. Chemla. "Hyperpolarizabilities of the Nitroanilines and their Relations to the Excited State Dipole Moment". In: *J. Chem. Phys.* 66 (1977), p. 2664.

[186] F. Pan et al. "Nature of Low-Lying Excited States in H-Aggregated Perylene Bisimide Dyes: Results of TD-LRC-DFT and the Mixed Exciton Model". In: *J. Phys. Chem. B.* 113 (2009), pp. 14581–14587.

[189] G. Pescitelli, L. Di Bari, and N. Berova. "Application of electronic circular dichroism in the study of supramolecular systems". In: *Chem. Soc. Rev.* 43 (2014), p. 5211.

[193] B. Robinson and L.R. Dalton. "Monte Carlo Statistical Mechanical Simulations of the Competition of Intermolecular Electrostatic and Poling-Field Interactions in Defining Macroscopic Electro-Optic Activity for Organic Chromophore/Polymer Materials". In: *J. Phys. Chem. A* 104 (2000), pp. 4785–4795.

[201] M. Sarovar et al. "Ab-initio calculation of molecular aggregation effects: A Coumarin-343 case study". In: *J. Phys. Chem. B* 117 (2013), p. 11072.

[203] G. Scheibe. In: *Angew. Chem.* 49 (1936), p. 563.

[211] Y. R. Shen. *The Principles of Nonlinear Optics*. New York, New York: Wiley, Inc., 1984.

[212] D. Silva et al. "Self Aggregation and Optical Absorption of Stilbazolium Merocyanine in Chloroform". In: *J. Phys. Chem. B* 118 (2014).

[222] P. Sullivan et al. "Modeling the Optical Behavior of Complex Organic Media: From Molecules to Materials". In: *J. Phys. Chem. B* 113 (2009).

[223] S.S. Sun et al. "1,3-Bis(dicyanomethylidene)indane-Based Second-Order NLO Materials". In: *Chemistry of Materials* 8.11 (1996), pp. 2539–2541.

[226] K. Suponitsky and A. Masunov. "Supramolecular step in design of nonlinear optical materials: Effect of π...π stacking aggregation on hyperpolarizability". In: *J. Chem. Phys.* 139 (2013), p. 094310.

[229] Y. Tawada et al. “A long range corrected time-dependent density functional theory.” In: *J. Chem. Phys.* 120 (2004).

[231] A. Teshome et al. “Strategies for optimising the second-order nonlinear optical response in zwitterionic merocyanine dyes”. In: *Opt. Mat.* 31 (2009).

[232] A. Tillack. “Electro-Optic Material Design Criteria Derived from Condensed Matter Simulations Using the Level-of-Detail Coarse-Graining Approach.” Thesis. 2015.

[236] Pereverzev Y. V. et al. “Guest-host cooperativity in organic materials greatly enhances the nonlinear optical response”. In: *J. Phys. Chem. C* 112 (2008), p. 4355.

[237] R. Aaron Vogt, Thomas G. Gray, and Carlos E. Crespo-Hernandez. “Subpicosecond Intersystem Crossing in Mono- and Di(organophosphine)gold(I) Naphthalene Derivatives in Solution”. In: *Journal of the American Chemical Society* 134.36 (2012), pp. 14808–14817.

[241] A Warshel and M. Levitt. “Theoretical studies of enzymic reactions: Dielectric, electrostatic and steric stabilization of the carbonium ion in the reaction of lysozyme”. In: *Journal of Molecular Biology* 103.2 (1976), pp. 227–249.

[244] A. Willetts et al. In: *J. Chem. Phys.* 97.10 (1992), pp. 7590–7599.

[246] O. Worz and G. Scheibe. In: *Z. Naturforsch.* 146 (1969), p. 381.

[247] K. Wu, J. Snijders, and C. Lin. “Reinvestigation of Hydrogen Bond Effects on the Polarizability an Hyperpolarizability of Urea Molecular Clusters”. In: *J. Chem. Phys. B.* 106 (2002), pp. 8954–8958.

[248] F. Wurthner, T. E. Kaiser, and C. R. Saha-Möller. “J-Aggregates: From Serendipitous Discovery to Supramolecular Engineering of Functional Dye Materials”. In: *Angew. Chem., Int. Ed.* 50 (2011), p. 3376.

[250] T. Yasukawa, T. Kimura, and M. Uda. “A AM1 Study of the effects of intermolecular interactions on hyperpolarizabilities of p-nitroanilines”. In: *Chem. Phys. Lett.* 169.3 (1990).

[253] X.-F. Zhang, Q. Xi, and J. Zhao. “Fluorescent and triplet state photoactive J-type phthalocyanine nano assemblies: controlled formation and photosensitizing properties”. In: *J. Mater. Chem.* 20 (2010), p. 6726.

Appendix A

CHAPTER 2 SUPPORTING INFORMATION

A.1 Conformational Analysis of FTC and CLD-type systems

Previous conformational analysis studies based on FTC and CLD structures have suggested that several rotamers of this type can coexist in low-viscosity solution [131], [5]. The prototype FTC and CLD conjugated bridges, EZFTC and CLD1 as shown in Figure 2.1, contain three rotatable single bonds that can exist in the cisoid (c) or transoid (t) conformation resulting in eight possible conformers: *ttt*, *ttc*, *ctt*, *ctc*, *tct*, *tcc*, *cct*, and *ccc*. The geometry of the eight conformers were optimized and the resulting structures used to compute the excitation energy and hyperpolarizability (see Tables A.1 and A.2). The reported energies are computed at the PCM-B3LYP/6-31+G* level of theory, while the properties are computed with LC-BLYP/6-31+G* with the default range tuning parameter of $\omega = 0.47\ bohr^{-1}$. The Boltzmann populations at 298 K, labeled as statistical weights, reveal that only the *ttc* and *ttt* conformers of CLD1 have a statistical probability above 1%. For these two conformers, the computed properties of interest are quite similar; the respective dipole moments vary minimally from 24.1 to 25.2 D, the excitation energies are 2.01 and 2.03 eV, and likewise, $\beta_{HRS}(0)$ varies slightly from 193×10^{-30} to 205×10^{-30} esu, and the difference in $\beta_{zzz}(0)$ is similarly negligible. For chromophores in the benchmarking set with the CLD-type bridge (CLD1, GLD1, YLD124, and C3), we use the *ttc* conformer for all subsequent computation. The *ttt* and *ttc* conformers of EZFTC are also the most likely (37% and 34% statistical weights, respectively), while the *ctc* and *ctt* conformers both have weights of 11%. For the two dominant conformers, the excitation energy and β_{HRS} values are quite similar, but, upon rotation of the TCF group from transoid to cisoid, the computed dipole moment increases by approximately 3D and the $\beta_{zzz}(0)$ value also increases. The static hyperpolarizability varies substantially for the four conformers; $\beta_{zzz}(0)$ nearly doubles from 167×10^{-30} esu for *ctt* to 291×10^{-30} esu for *ttc* and *ctc*. Since β_{HRS} is computed as an orientational average of the tensor components of β, it is not surprising that

$\beta_{HRS}(0)$ varies less than the single tensor component $\beta_{zzz}(0)$ which is aligned in the direction of the dipole (z-) axis [46]. Although not the lowest energy conformer, for consistency with the CLD-type structures, we have chosen to use the *ttc* conformer for the FTC-type structures (EZFTC, YLD156, etc.) unless otherwise noted. Also, the short-bridge systems (DCDHF, TCF1, TCF1-CF3, etc.) as well as the hybrid system, YLD130, obey the ttc (transoid-bridge, cisoid TCF) convention.

ΔE_{gs} (kcal/mol)	Stat. Weight (298K)	Excitation Energy (eV)	μ (D)	$\beta_{zzz}(0)$	$\beta_{HRS}(0)$	$\beta_{HRS}(2\omega)$ at 1906-nm	Conformers
0.00	0.55	2.01	24.4	419	193	321	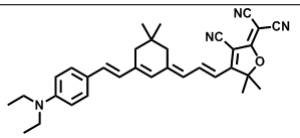 ttc
0.13	0.44	2.03	25.2	403	205	424	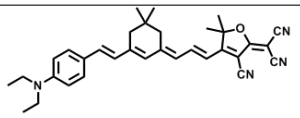 ttt
2.40	9.5e-03	1.99	25.3	337	188	328	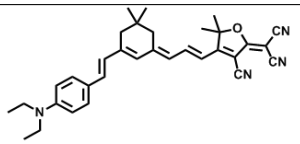 ctt
4.11	5.3e-04	1.98	25.4	394	172	272	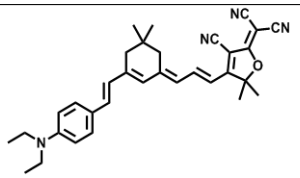 ctc
4.76	1.8e-04	2.00	24.1	420	201	340	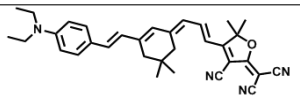 tct
5.47	5.3e-05	1.98	25.3	397	198	324	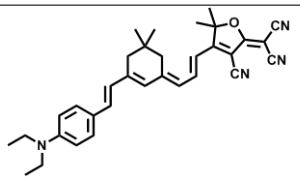 tcc
7.07	3.6e-05	1.98	25.1	418	189	310	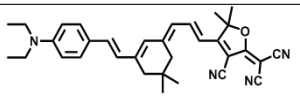 cct
7.69	1.3e-06	1.95	25.6	346	186	330	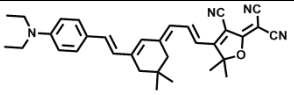 ccc

Table A.1: **Conformational Analysis for CLD1.** Units of hyperpolarizability, β, are $10^{-30} esu$ and are reported in the perturbation convention. The reported g.s. energies are computed at the PCM-B3LYP/6-31+G* level of theory, while the properties (excitation energy and β) are computed with LC-BLYP/6-31+G* with the default range tuning parameter of ω=0.47 $bohr^{-1}$.

ΔE_{gs} (kcal/mol)	Stat. Weight (298K)	Excitation Energy (eV)	μ (D)	$\beta_{zzz}(0)$	$\beta_{HRS}(0)$	$\beta_{HRS}(2\omega)$ at 1906-nm	Conformers
0.00	0.37	2.08	20.3	185	124	195	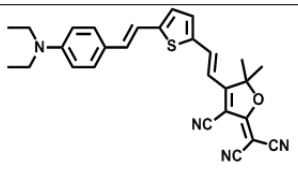 ttt
0.05	0.34	2.08	22.9	291	125	205	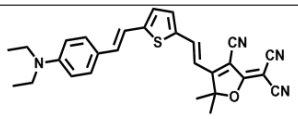 ttc
0.72	0.11	2.13	22.8	291	131	234	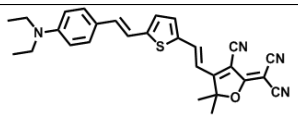 ctc
0.73	0.11	2.25	19.9	167	98	160	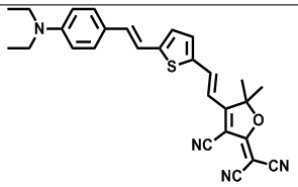 ctt
1.38	0.036	2.08	22.8	330	144	225	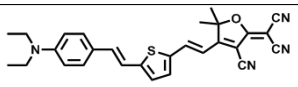 tct
1.71	0.020	2.04	20.9	219	138	223	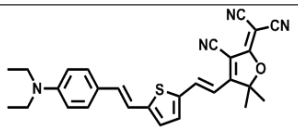 tcc
2.02	0.012	2.13	23.1	326	150	278	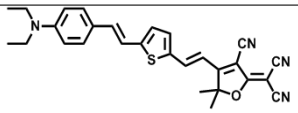 cct
2.38	6.7e-03	2.08	22.6	277	151	237	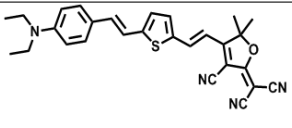 ccc

Table A.2: **Conformational Analysis for EZFTC.** Units of hyperpolarizability, β, are $10^{-30} esu$ and are reported in the perturbation convention. The reported g.s. energies are computed at the PCM-B3LYP/6-31+G* level of theory, while the properties (excitation energy and β) are computed with LC-BLYP/6-31+G* with the default range tuning parameter of ω=0.47 $bohr^{-1}$.

A.2 Modification of Molecular Structures for Computational Studies

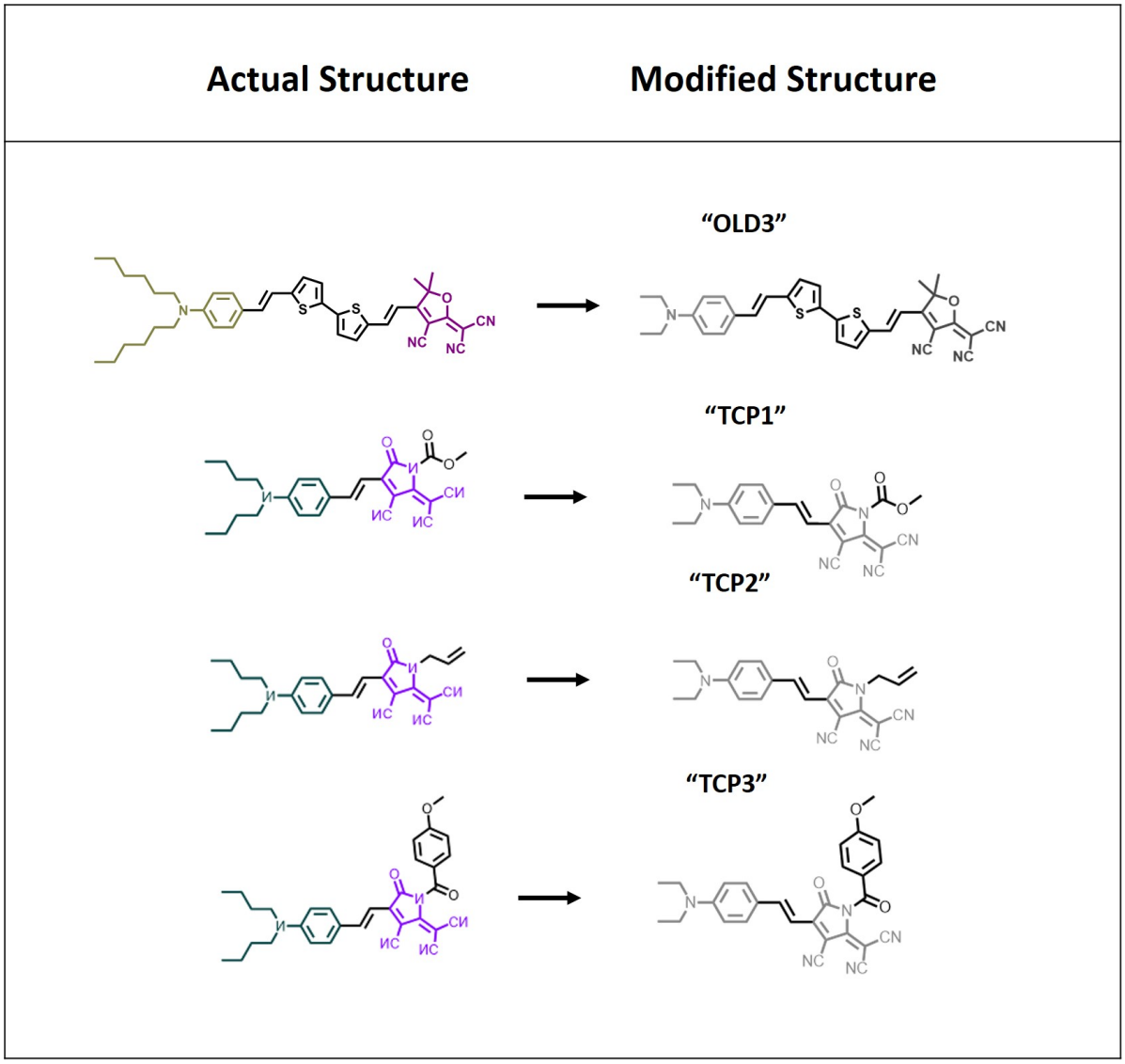

Figure A.1: **Structural Modifications for Computational Efficiency: Removal of TBDMSO groups and Long Alkyl Chains on Donor.** Note that the modified structure of YLD124 is indeed AJY1. The experimental λ_{max} red shifts by $\sim$ 24 nm upon removal of TBDMSO groups and similarly λ_{max} calculated using LC-BLYP/6-31+G* red shifts by $\sim$ 20 nm. Di-hexyl and di-butyl groups were shortened to di-ethyl chains off the aniline donor to save time in geometry optimization by creating a more rigid structure. The BODIPY- series (-H, -F, -CN, -NO2) was also modified by removing TBDMSO groups, but these modifications are not illustrated here.

Actual Structure	Modified Structure
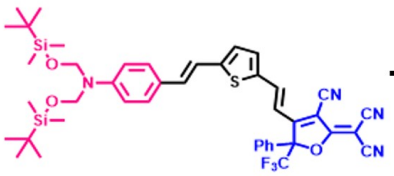	“YLD156” 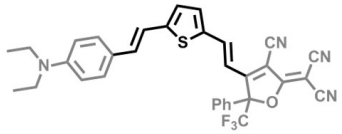
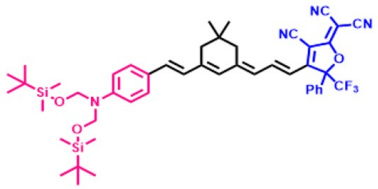	“YLD124” 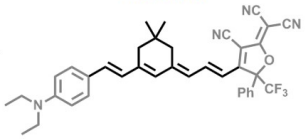
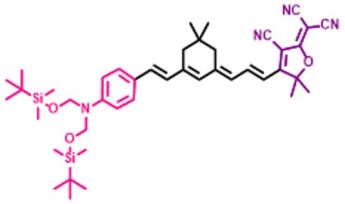	“CLD1” 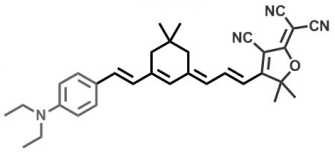
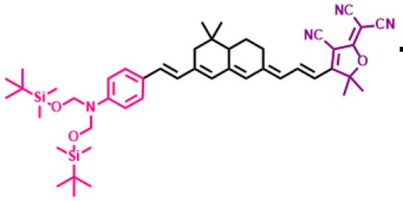	“GLD1” 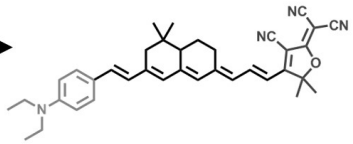
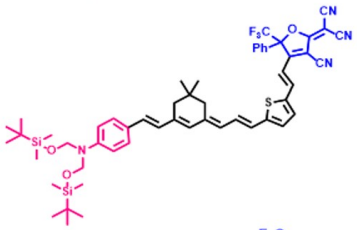	“YLD130” 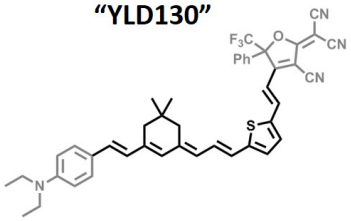
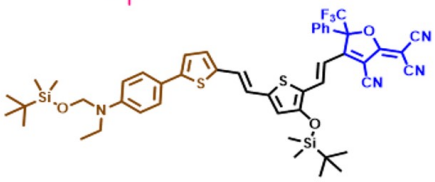	“AALD1158” 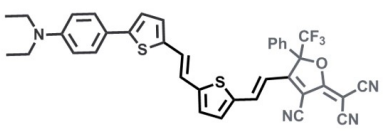
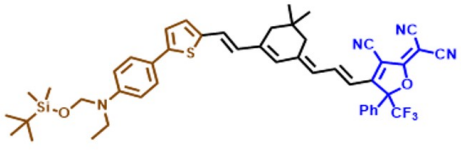	“AALD2023” 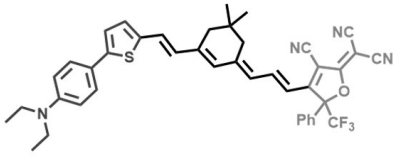

A.3 Average Absorbance Linewidth of 35 molecule benchmark set based on measured UV-vis spectra

The average full-width-half-maximum for the 35 benchmark set was determined using a MATLAB that I wrote which reads wavelengths and absorbance values from .txt files and determines the FWHM of the largest peak. The results are in Table A.3, along with examples of some of the plots that are generated.

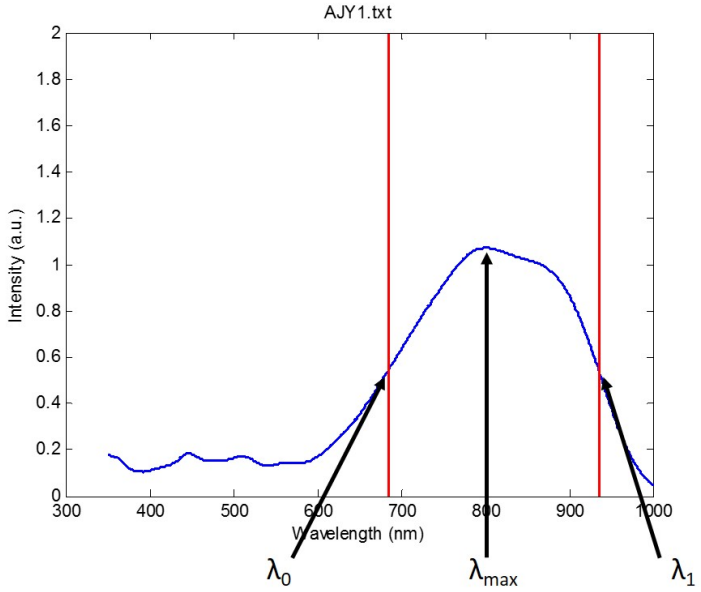

Figure A.2: **Example of Plot from MATLAB code used to find Linewidth.** FWHM in wavelength, $\Delta\lambda$, is $\lambda_1 - \lambda_0$. The peak wavelength is λ_{max}. The MATLAB code finds λ_0 and λ_1 for the spectral data and marks them with the red vertical lines. The FWHM is then computed in wavelength and electrovolts.

The full width half maxima were determined in electrovolts (eV) using the following,

$$FWHM = 1240/\lambda_0 - 1240/\lambda_1, \tag{A.1}$$

where λ_1 and λ_0 are defined in Figure A.2. In other cases when λ_0 and λ_1 are not known, FWHM in wavelength can be converted to eV using the approximation:

$$FWHM = \frac{\Delta\lambda}{\lambda_{max}^2 - \frac{\Delta\lambda^2}{4}} \times 1240 \tag{A.2}$$

where λ_{max} is defined in Figure A.2 and $\Delta\lambda$ is the FWHM in wavelength.

Molecule	**FWHM (nm)**	**FWHM (eV)**, using Equation A.2	**FWHM (eV)**, using Equation A.1
AJY1	254	0.488	0.507
AJY2	256	0.500	0.517
AJY3	259	0.508	0.523
B1	228	0.535	0.566
B2	243	0.541	0.559
B3	250	0.507	0.537
B4	247	0.509	0.535
BODIPYCN	120	0.332	0.323
BODIPYF	135	0.350	0.343
BODIPYH	116	0.328	0.315
BODIPYNO2	146	0.370	0.368

continued on next page

Table A.3: **Full Width Half Maxima (FWHM) Determined from UV-vis Measurement.**

Molecule	**FWHM (nm)**	**FWHM (eV)**, using Equation A.2	**FWHM (eV)**, using Equation A.1
C2	240	0.496	0.564
C3	269	0.547	0.568
CLD1	210	0.544	0.562
DCDHF	53	0.164	0.270
EZFTC	179	0.497	0.493
FTCDAAP1	189	0.480	0.500
FTCDAAP2	196	0.471	0.482
FTCDAAP3	199	0.471	0.487
FTCDAAP4	201	0.454	0.462
JDD1	200	0.460	0.459
JDD2	290	0.509	0.510
JDD3	229	0.414	0.394
TC1_CF3	82	0.310	0.298
TCF1	82	0.310	0.298
TV1101	118	0.283	0.277
YLD124	252	0.492	0.522
YLD156	192	0.437	0.423
YLN144	174	0.572	0.574
Average	193	0.444	0.456

A.4 Additional Plots for Comparing Computed to Measured Hyperpolarizability

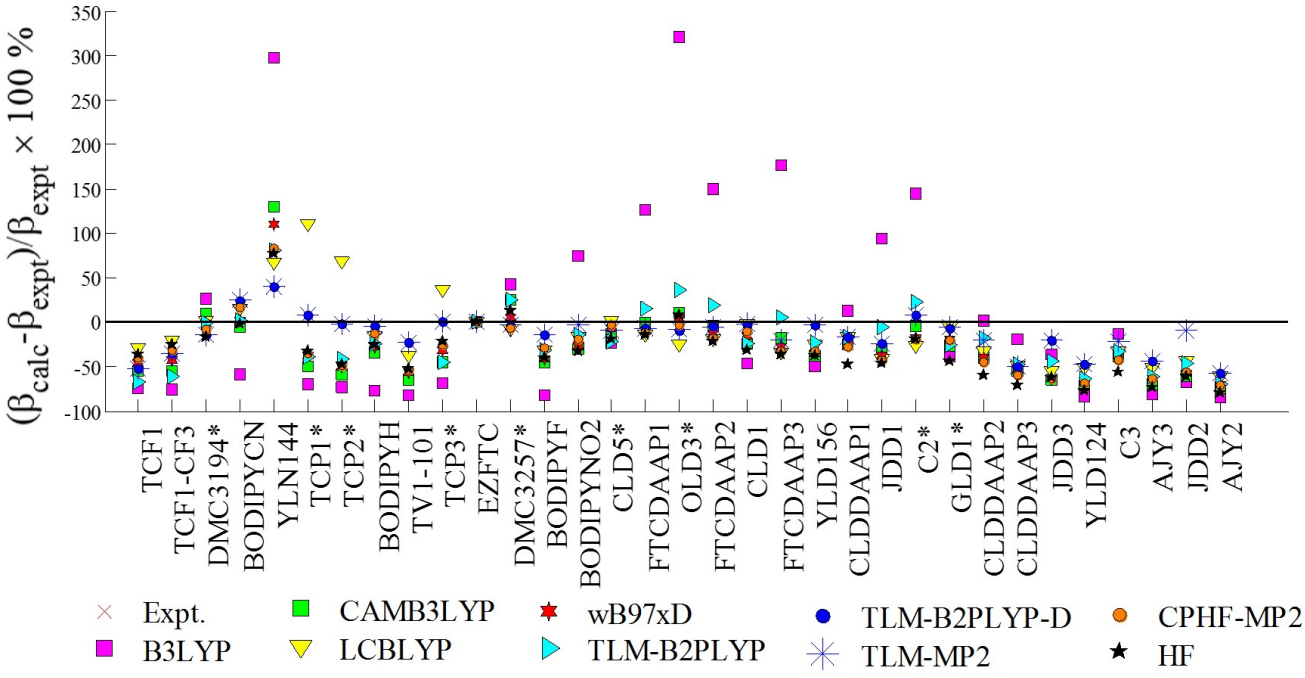

Figure A.3: **Relative Percent Error between Computed $\beta_{HRS}(2\omega)/\beta_{FTC}$ and HRS measurement.** From this plot it is clear which theoretical methods have the largest standard deviation of error (STE). B3LYP alternately underestimates and overestimates β. The best method, TLM-MP2, stays within $\pm 50\%$ relative error.

In order to predict the performance of an organic EO material for device applications based on r_{33}, it is necessary to first obtain an accurate description of the absolute hyperpolarizability, β_{zzz}. Recall that HRS is related to the second harmonic hyperpolarizability, $\beta_{HRS}(-2\omega;\omega,\omega)$, whereas, r_{33} is related to the Pockels (or linear electro-optic) effect hyperpolarizability, $\beta_{zzz}(-\omega;\omega,0)$, in which the refractive index of an electro-optic material is controlled by application of a low-frequency (dc $\sim$ 10 THz) electric field. Unfortunately, $\beta_{zzz}(-\omega;\omega,0)$ cannot be directly measured. For this discussion, we instead compare theory to the measured $\beta_{HRS}(-2\omega;\omega,\omega)$ values. Experimental absolute hy-

perpolarizabilities were determined from ratios by multiplying the experimental $\beta_{sys}/\beta_{FTC} \pm \delta_{ratio}$ values listed in Table 2.1 with $\beta_{FTC} \pm \delta_{FTC} = (1360 \pm 700) \times 10^{-30}$ esu and applying propagation of error according to:

$$(\beta_{sys}/\beta_{FTC} \pm \delta_{ratio}) \times (\beta_{FTC} \pm \delta_{FTC}) = (\beta_{sys}/\beta_{FTC} \times \beta_{FTC}) \left[1 \pm \sqrt{\left(\frac{\delta_{ratio}}{\beta_{sys}/\beta_{FTC}} \right)^2 + \left(\frac{\delta_{FTC}}{\beta_{FTC}} \right)^2} \right],$$

where δ_{ratio} and δ_{FTC} are the errors for the hyperpolarizability ratios and the EZFTC reference, respectively. (Note that converting $\beta_{FTC}/\beta_{CHCl_3} = 2780 \pm 1440$ to absolute hyperpolarizability, $\beta_{FTC} \pm \delta_{FTC} = (1360 \pm 700) \times 10^{-30} esu$, is done by multiplying by $\beta_{CHCl_3} = 0.49 \times 10^{-30} esu$ [119],[12],[73]). The dashed line shown in Figure A.4 is $\beta_{sys}/\beta_{FTC} \times \beta_{FTC}$ and the solid lines are the best line fits to plus and minus the propagated errors. Only the two best performing methods based on MAE and STE, LC-BLYP and TLM-MP2 (see Table 2.2), are shown for comparison to measurement. Clearly, theory greatly underestimates the measured HRS values, thus illustrating the use for comparing theory to relative hyperpolarizabilities for benchmarking.

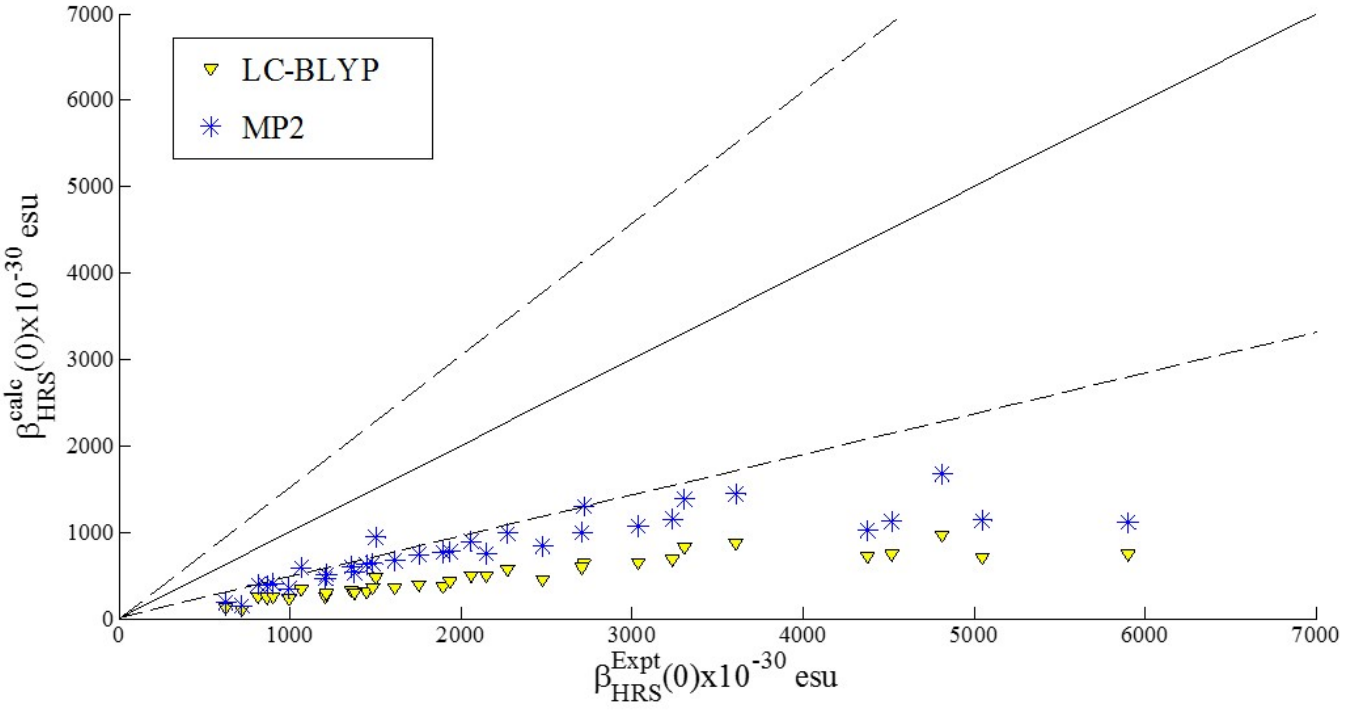

Figure A.4: **Comparison of Theoretical Methods with Experimental Measurements of Absolute Hyperpolarizabilities.** Absolute hyperpolarizabilities were determined by multiplying the experimental $\beta_{sys}/\beta_{FTC} \pm \delta_{ratio}$ values listed in Table 2.1 with $\beta_{FTC} \pm \delta_{FTC} = (1360 \pm 700) \times 10^{-30}$ esu and applying propagation of error.

A.5 Influence of Long-range Hartree-Fock Exchange on Computed Electronic Excitation Energies

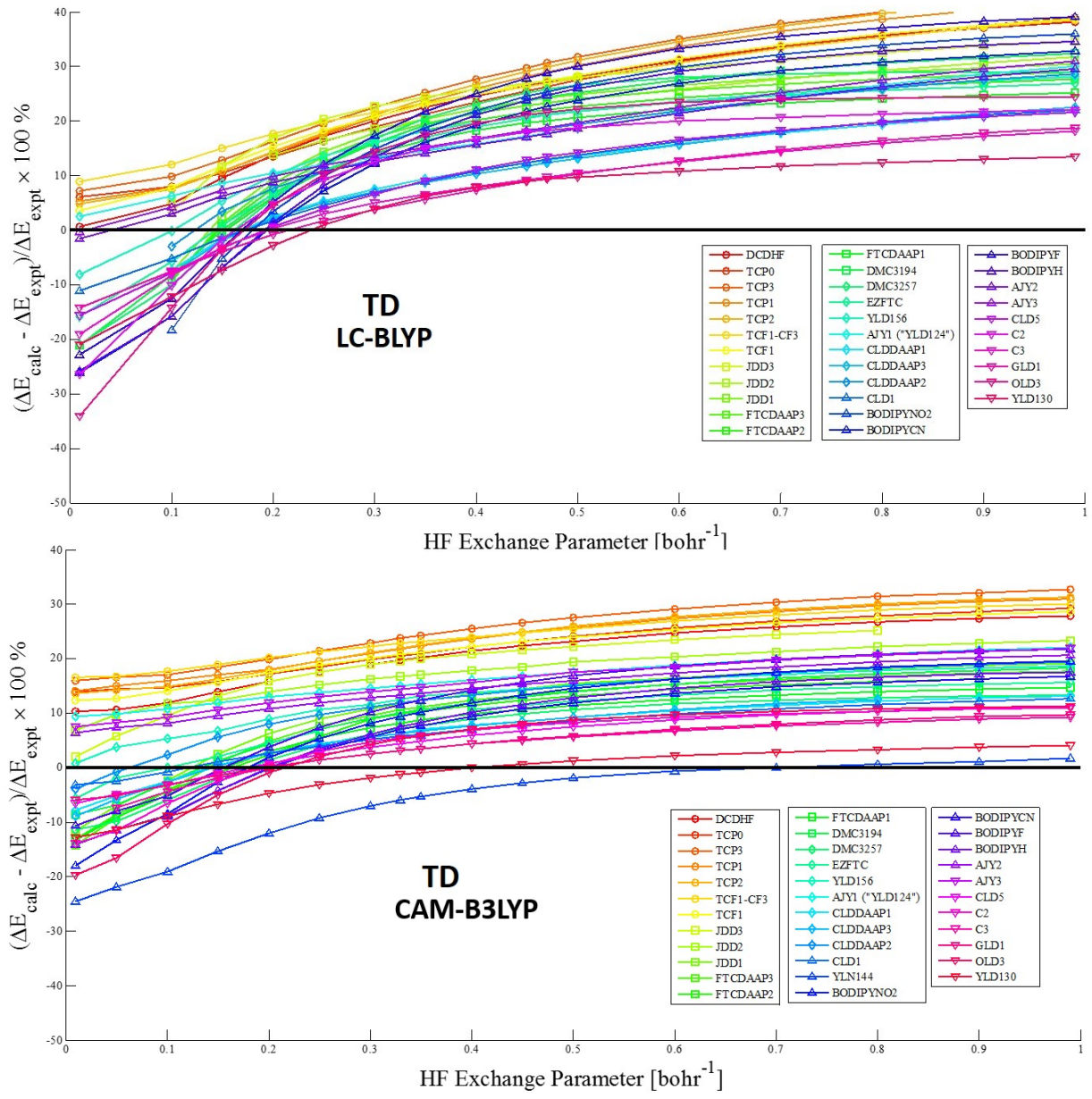

Figure A.5: **Relative Percent Error in Calculated Transition Energy and Measurement.** Computed transition energies were determined using linear-response TD-DFT calculations for the functionals LC-BLYP and CAM-B3LYP with PCM (chloroform) and 6-31+G* basis. PCM-B3LYP/6-31+G* geometry was used for all calculations. Color scheme is organized according to D-A length (i.e., donor-acceptor length) as given in Table 2.1, from shortest (violet, DCDHF) to longest (red, YLD130).

Relative percent error between calculated transition energies (ΔE_{calc}) and experimental transition energies (corresponding to values in Table 2.1) are shown in Figure A.5 for the 34 molecule benchmark set. Calculated transition energies (ΔE_{calc}) were computed using linear-response TD-DFT for long-range corrected functionals LCBLYP and CAMB3LYP with PCM (chloroform) and 6-31+G* basis. The fraction of long-range (LR) HF exchange in these functionals is tuned approximately over a range of 0 (all DFT LR exchange) to 1 (all HF LR exchange). The optimal amount of LR HF exchange needed to predict λ_{max} varies for each molecular system; however, for both LC-BLYP and CAM-B3LYP methods, 10-25% LR HF exchange matches well with experimental measurement for most of the benchmark chromophores. Full simulated and measured spectra are shown in Figures A.10-A.43.

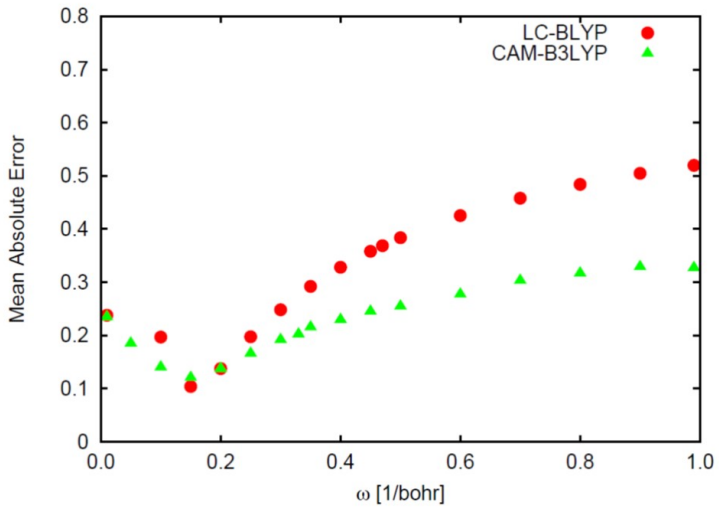

Figure A.6: **Mean Absolute Error (MAE) for λ_{max} with respect to experimental data for 34 molecule test set.** The MAE for CAM-B3LYP varies the least over the range of % long-range HF exchange used in the functional. Its MAE is minimal (MAE$\approx$ 0.12) when ω is 0.15 bohr^{-1} and increases to roughly 0.33 when $\omega \to 1$. LC-BLYP has MAE that achieves a minimum (MAE$\approx$ 0.1) for ω=0.15 bohr^{-1}, but then increases to a maximum of about 0.52 when $\omega \to 1$.

A.6 Influence of Long-range Hartree-Fock Exchange on Computed Frequency-Dependent Hyperpolarizabilities

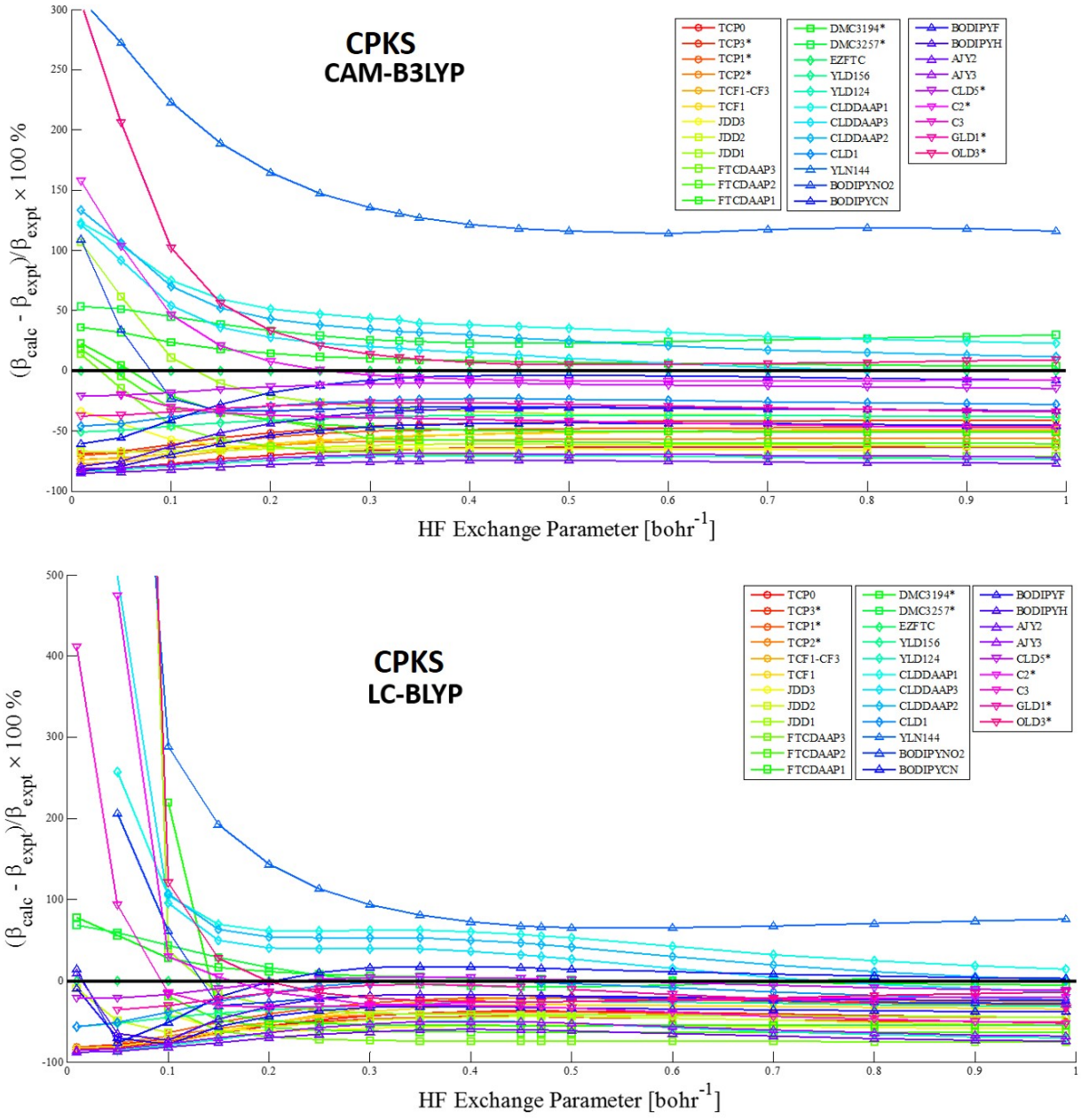

Figure A.7: **Relative Percent Error in Calculated $\beta_{HRS}(2\omega)$ and Measurement**. Computed hyperpolarizabilities using analytic derivatives via coupled-perturbed Kohn-Sham (CPKS) theory for the functionals LC-BLYP and CAM-B3LYP with PCM (chloroform) and 6-31+G* basis. PCM-B3LYP/6-31+G* geometry was used for all calculations. Color scheme is organized according to D-A length (i.e., donor-acceptor length) as given in Table 2.1, from shortest (violet, DCDHF) to longest (red, YLD130).

HRS measurements at 1907 nm in chloroform are compared with computed frequency-dependent second-harmonic hyperpolarizabilities, $\beta_{HRS}(-2\omega;\omega,\omega)$ using coupled-perturbed Kohn-Sham (CPKS) in LC-BLYP and CAM-B3LYP. The relative percent error between theory and measurement are shown in Figure A.7. The fraction of long-range (LR) HF exchange in these functionals is tuned approximately over a range of 0 (all DFT LR exchange) to 1 (all HF LR exchange). The default settings for LR HF exchange in LC-BLYP and CAM-B3LYP ($\omega = 0.47$ $bohr^{-1}$ for LC-BLYP and 0.33 $bohr^{-1}$ CAM-B3LYP) work well for computing β, according to these results. If there is no LR HF exchange, as is the case with BLYP and B3LYP, the computed hyperpolarizabilities become largely overestimated.

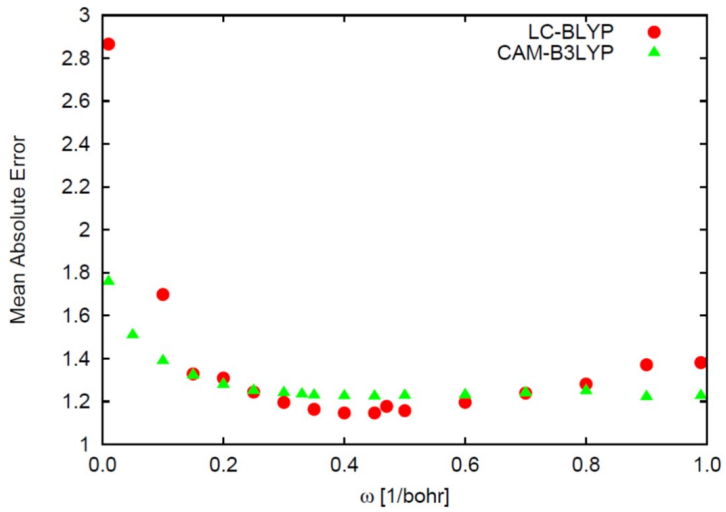

Figure A.8: **Mean Absolute Error (MAE) for $\beta_{HRS}(2\omega)/\beta_{HRS}^{FTC}$ with respect to experimental HRS data for 32 molecule test set.** Similar to the transition energies, the MAE for CAM-B3LYP varies less than LC-BLYP over the range of % long-range HF exchange used in the functional. Its MAE is nearly constant at about 1.2 for $\omega \geq$0.20 bohr^{-1}. LC-BLYP has a minimum MAE$\approx$ 1.15 for ω=0.45 bohr^{-1}, but then increases to a maximum of 2.9 when $\omega \to 0$.

A.7 Results of the damped TLM fit using computed ω_{eg}

The results of the TLM fit can be very sensitive to the choice of transition energy, ω_{eg}. Thus, the empirical data used in the TLM-MP2 results discussed in Section 2.3 were shown to perform better than any other method based on mean absolute error (MAE) and standard deviation of errors

(STE). However, if the purpose is to find a reliable theoretical method to be used on target molecules that have not yet be characterized, one must test the TLM fit using a calculated transition energy. Thus, determining a reliable method for the computation of ω_{eg} is critical. The transition energy generally increases as more HF exchange is added to hybrid and long-range corrected functionals, as shown in Figure A.5. By tuning the amount of LR HF exchange in the functional, we can observe its affect on the TLM-fit at 1907-nm and apply this to $\beta_{HRS}^{MP2}(0)$. The relative error between measured HRS β and these new 'TLM-MP2' fits using computed ω_{eg} are shown in Figure A.7.

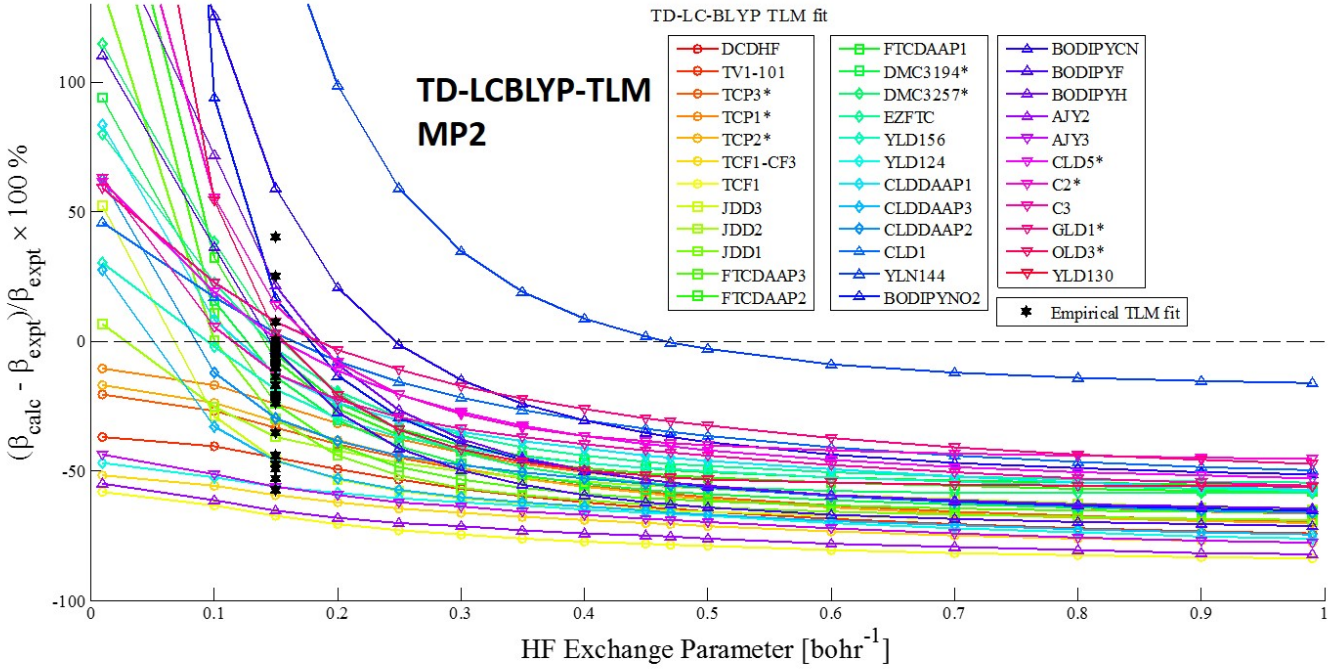

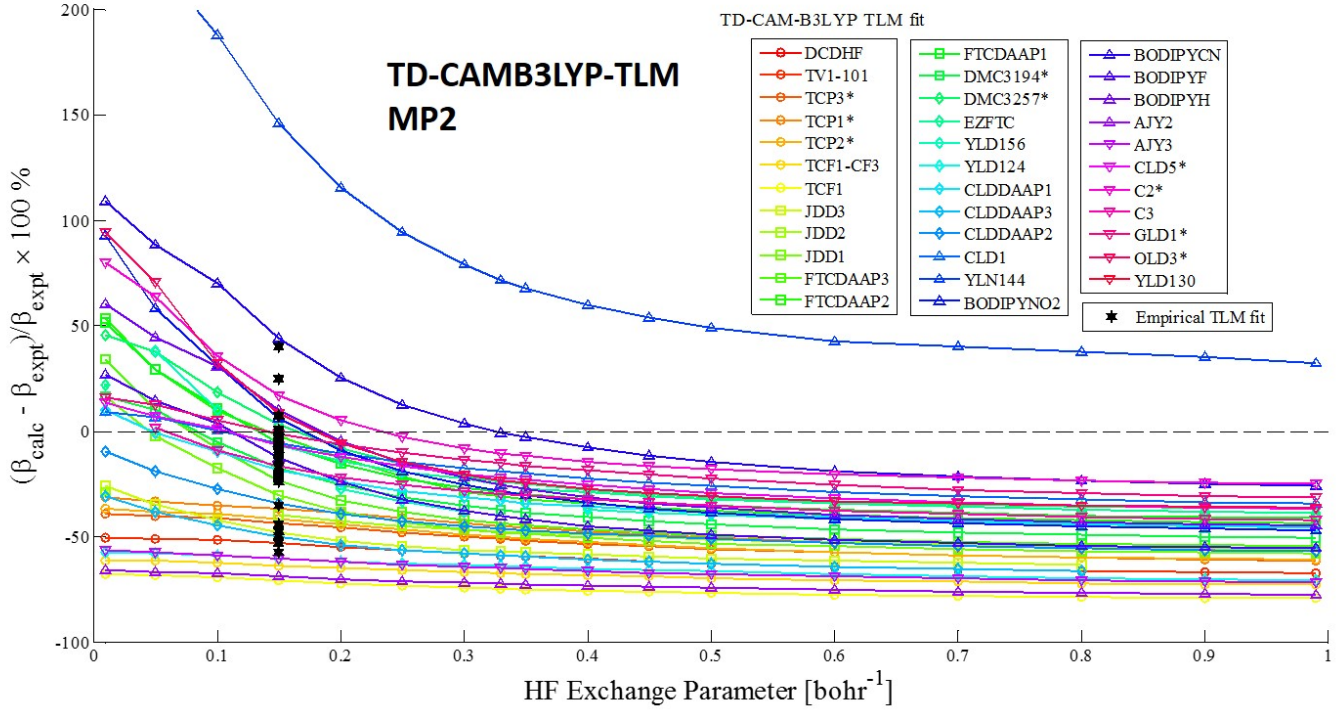

Figure A.9: **Relative Percent Error of Calculated $\beta_{HRS}(2\omega)$ with respect to Experimental HRS data.** Static relative hyperpolarizabilities, $\beta_{HRS}(0)/\beta_{HRS}^{FTC}$, were computed via finite-field method (FFM) in MP2 and extrapolated to 1907nm using a TLM-fit with transition energies provided by TD-DFT, except for the reference EZFTC for which the measured ω_{eg} was used. The DFT methods are LC-BLYP and CAM-B3LYP. The amount of long-range HF exchange in these functionals was tuned from 0 to 1.

A.8 Data Tables for Static and Dynamic Relative Hyperpolarizabilities

Molecule	Expt.	HF	BLYP	B3LYP	CAM-B3LYP	LC-BLYP	wB97xD	MP2	B2PLYP	B2PLYP-D
EZFTC (ref.)	1	1	1	1	1	1	1	1	1	1
TCF1	0.33	0.21	0.05	0.09	0.15	0.23	0.18	0.16	0.11	0.16
TCF1-CF3	0.36	0.27	0.05	0.09	0.16	0.29	0.20	0.23	0.14	0.23
DMC3194	0.76	0.63	1.28	0.96	0.83	0.77	0.75	0.66	0.75	0.65
BODIPYCN	0.81	0.80	0.88	0.34	0.76	0.93	0.82	1.01	0.82	1.01
YLN144	0.82	1.45	3.63	3.26	1.89	1.37	1.73	1.15	1.48	1.15
TCP1	0.84	0.57	0.19	0.25	0.43	1.79	0.53	0.91	0.52	0.91
TCP2	0.89	0.46	0.18	0.23	0.37	1.49	0.45	0.86	0.52	0.86
BODIPYH	0.9	0.67	0.96	0.20	0.60	0.76	0.64	0.86	0.69	0.85
TV1-101	0.95	0.45	0.12	0.17	0.33	0.60	0.42	0.74	–	0.73
TCP3	0.98	0.77	0.23	0.31	0.53	1.33	0.66	0.99	0.54	0.98
DMC3257	1.1	1.24	1.75	1.57	1.37	1.01	1.15	1.06	1.37	1.06
BODIPYF	1.16	0.69	1.02	0.21	0.63	0.80	0.68	1.00	0.80	1.00
BODIPYNO2	1.27	0.86	0.57	2.21	0.88	1.05	0.92	1.23	1.09	–
CLD5	1.3	1.05	1.00	1.00	1.13	1.33	1.21	1.17	1.01	–
FTCDAAP1	1.3	1.11	49.51	2.94	1.30	1.12	1.18	1.21	1.50	1.21
OLD3	1.4	1.50	6.90	5.90	1.55	1.04	1.45	1.28	1.91	1.27
FTCDAAP2	1.58	1.23	8.49	3.94	1.51	1.28	1.37	1.50	1.89	1.50
CLD1	1.8	1.23	0.78	0.98	1.36	1.76	1.51	1.76	1.36	1.75
FTCDAAP3	1.99	1.28	6.83	5.51	1.63	1.32	1.44	1.57	2.10	–

continued on next page

Table A.4: **Relative frequency-dependent hyperpolarizabilities at 1907-nm consistent with HRS, $\beta_{HRS}(2\omega)/\beta_{FTC}$: Comparison between theory and measurement.** The molecules are listed in order of increasing experimental $\beta_{HRS}(2\omega)/\beta_{FTC}$. B2PLYP-D results were practically identical to MP2 and thus for brevity are not shown.

Molecule	Expt.	HF	BLYP	B3LYP	CAM-B3LYP	LC-BLYP	wB97xD	MP2	B2PLYP	B2PLYP-D
YLD156	2.2	1.38	0.96	1.09	1.36	1.63	1.43	2.14	1.71	2.14
CLDDAAP1	2.49	1.31	9.52	2.82	1.85	2.08	1.87	2.07	2.08	2.06
JDD1	2.54	1.36	6.70	4.93	1.74	1.48	1.57	1.93	2.41	1.94
C2	2.8	2.26	6.52	6.86	2.66	2.07	2.29	3.01	3.43	3.02
GLD1	3	1.70	1.91	1.84	2.20	2.82	2.42	2.82	2.24	2.81
CLDDAAP2	3.52	1.39	213.4	3.56	2.10	2.36	2.11	2.79	2.88	–
CLDDAAP3	5.2	1.49	25.5	4.22	2.36	2.68	2.37	2.63	2.73	2.61
JDD3	5.3	1.98	5.91	3.35	1.87	2.39	1.95	4.22	2.97	4.20
YLD124	5.4	1.25	0.63	0.88	1.58	2.63	1.85	2.84	1.98	2.83
C3	5.7	2.51	44.57	4.94	3.46	3.85	3.54	4.46	3.81	–
AJY3	5.9	1.53	0.84	1.09	1.81	2.88	2.13	3.30	2.29	3.30
JDD2	6	2.34	5.41	1.95	2.31	3.37	2.56	5.40	3.19	–
AJY2	7.5	1.57	0.87	1.12	1.85	2.94	2.17	3.20	2.23	3.20

Molecule	Expt.	HF	BLYP	B3LYP	CAM-B3LYP	LC-BLYP	wB97xD	MP2	B2PLYP	B2PLYP-D
EZFTC (ref.)	1	1	1	1	1	1	1	1	1	1
TCF1	0.53	0.26	0.14	0.16	0.22	0.31	0.24	0.25	0.18	0.25
TCF1-CF3	0.46	0.32	0.13	0.15	0.23	0.37	0.27	0.30	0.18	0.29
DMC3194	0.89	0.70	1.10	0.98	1.23	0.78	0.82	0.77	0.88	0.77
BODIPYCN	0.79	0.83	0.74	0.66	0.86	1.03	0.91	0.98	0.80	0.98
YLN144	1.10	1.49	2.28	2.22	1.82	1.46	1.73	1.55	1.99	1.54
TCP1	0.60	0.66	0.31	0.33	0.49	0.76	0.59	0.64	0.37	0.64
TCP2	0.64	0.63	0.32	0.33	0.49	0.73	0.58	0.62	0.37	0.62
BODIPYH	0.89	0.73	0.52	0.54	0.73	0.87	0.77	0.85	0.68	0.85
TV1-101	0.73	0.58	0.24	0.27	0.42	0.69	0.51	0.57	–	0.56
TCP3	0.66	0.70	0.31	0.33	0.50	0.79	0.60	0.67	0.37	0.66
DMC3257	1.07	1.26	1.20	1.32	0.84	0.96	1.16	1.03	1.33	1.02
BODIPYF	1.02	0.74	0.50	0.54	0.75	0.90	0.80	0.88	0.70	0.87
BODIPYNO2	1.09	0.89	3.37	1.11	0.96	1.12	1.00	1.06	0.93	–
CLD5	1.42	1.07	1.11	1.06	1.16	1.33	1.23	1.29	1.11	–
FTCDAAP1	1.19	1.07	2.41	1.80	1.19	1.08	1.12	1.11	1.37	1.11
OLD3	1.39	1.42	3.45	2.65	1.53	1.15	1.36	1.27	1.90	1.27
FTCDAAP2	1.29	1.17	2.81	2.03	1.33	1.20	1.24	1.23	1.55	1.23
CLD1	1.67	1.25	0.96	1.04	1.36	1.76	1.50	1.63	1.26	1.63
FTCDAAP3	1.58	1.19	3.44	2.31	1.38	1.54	1.27	1.25	1.67	–

continued on next page

Table A.5: **Relative static hyperpolarizabilities at 1907-nm consistent with HRS, $\beta_{HRS}(0)/\beta_{FTC}$: Comparison between theory and measurement.** As with Table A.8, the molecules are listed in order of increasing experimental $\beta_{HRS}(2\omega)/\beta_{FTC}$.

Molecule	Expt.	HF	BLYP	B3LYP	CAM-B3LYP	LC-BLYP	wB97xD	MP2	B2PLYP	B2PLYP-D
YLD156	1.51	1.38	0.92	1.03	1.28	1.55	1.35	1.48	1.18	1.47
CLDDAAP1	1.99	1.20	2.32	1.84	1.57	1.81	1.62	1.65	1.67	1.65
JDD1	1.82	1.30	3.14	2.23	1.50	1.38	1.41	1.39	1.73	1.39
C2	2.00	2.15	3.00	2.75	2.17	1.95	2.01	2.15	2.45	2.16
GLD1	2.43	1.61	1.47	1.54	1.90	2.54	2.08	2.29	1.82	2.28
CLDDAAP2	2.23	1.27	2.77	2.05	1.71	1.99	1.77	1.77	1.83	–
CLDDAAP3	3.71	1.33	2.99	2.18	1.85	2.18	1.91	1.88	1.95	1.87
JDD3	2.38	1.92	2.43	1.62	1.55	2.11	1.67	1.90	1.34	1.89
YLD124	3.22	1.24	0.75	0.88	1.38	2.21	1.61	1.70	1.18	1.69
C3	3.54	2.14	2.20	2.19	2.39	2.98	2.50	2.77	2.37	–
AJY3	3.33	1.31	0.83	0.96	1.47	2.30	1.70	1.86	1.29	1.86
JDD2	2.65	2.16	1.52	1.30	1.79	2.69	2.02	2.39	1.41	–
AJY2	4.34	1.31	0.83	0.96	1.47	2.29	1.70	1.85	1.29	1.85

A.9 Measured and Simulated Absorbance Spectra for the 34 molecule benchmark set

The following TD-DFT calculations were performed in chloroform solvation environment using PCM following a B3LYP/6-31+G* geometry optimization of the molecule. Molecules are pictured in alphabetical order.

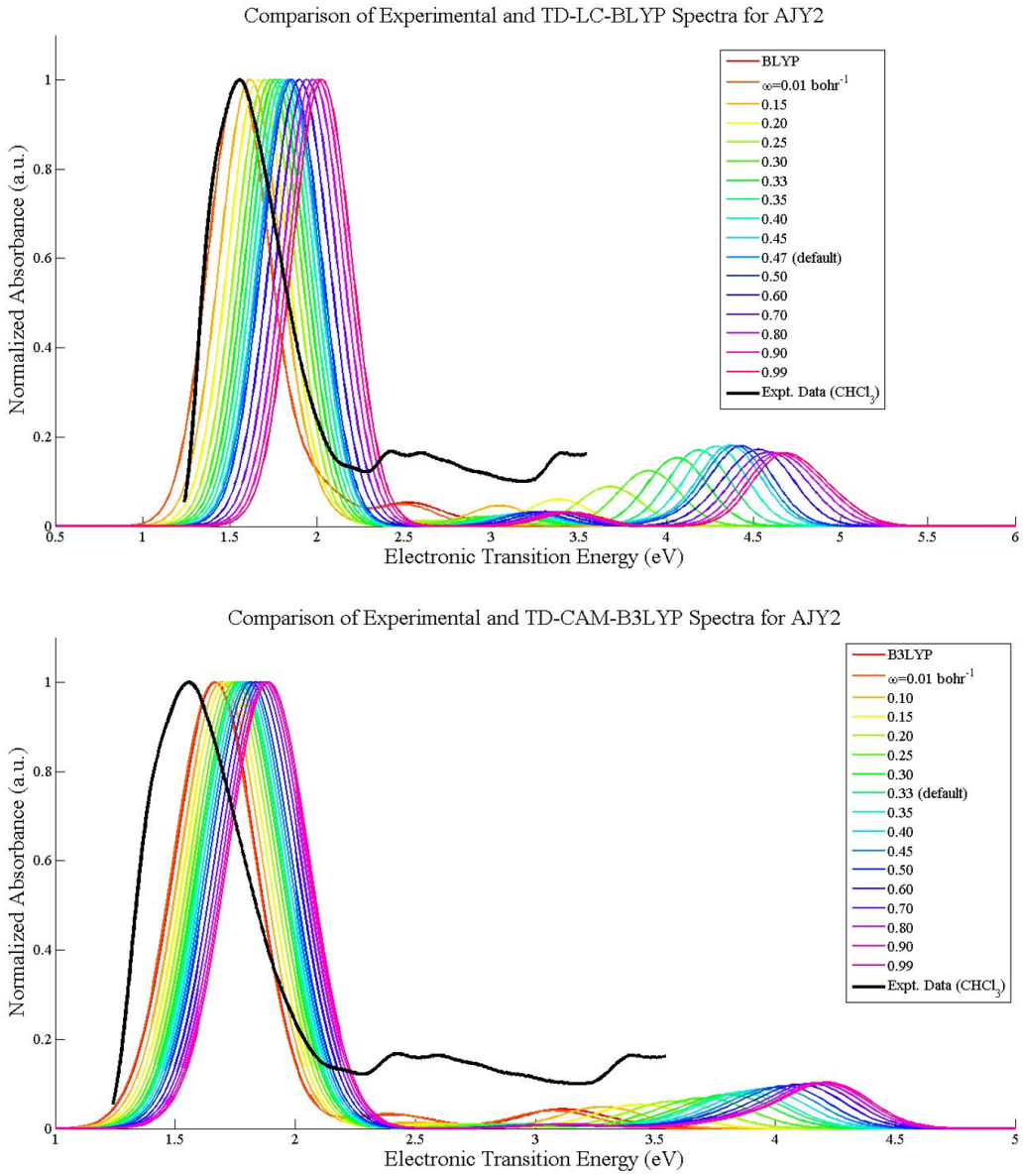

Figure A.10: **Comparison of Absorbance Spectra computed with TD-DFT and experimental UVv-is measurement for molecule AJY2.** Note that diminshing LR HF exchange in LC-BLYP and CAM-B3LYP results in better match between experiment and theory for this molecule. The ideal fraction of LR HF exchange occurs at around $\omega = 0.0 - 0.05\ bohr^{-1}$ in LC-BLYP; B3LYP is also a suitable match. Raw UV-vis data provided by Dr. Denise Bale.

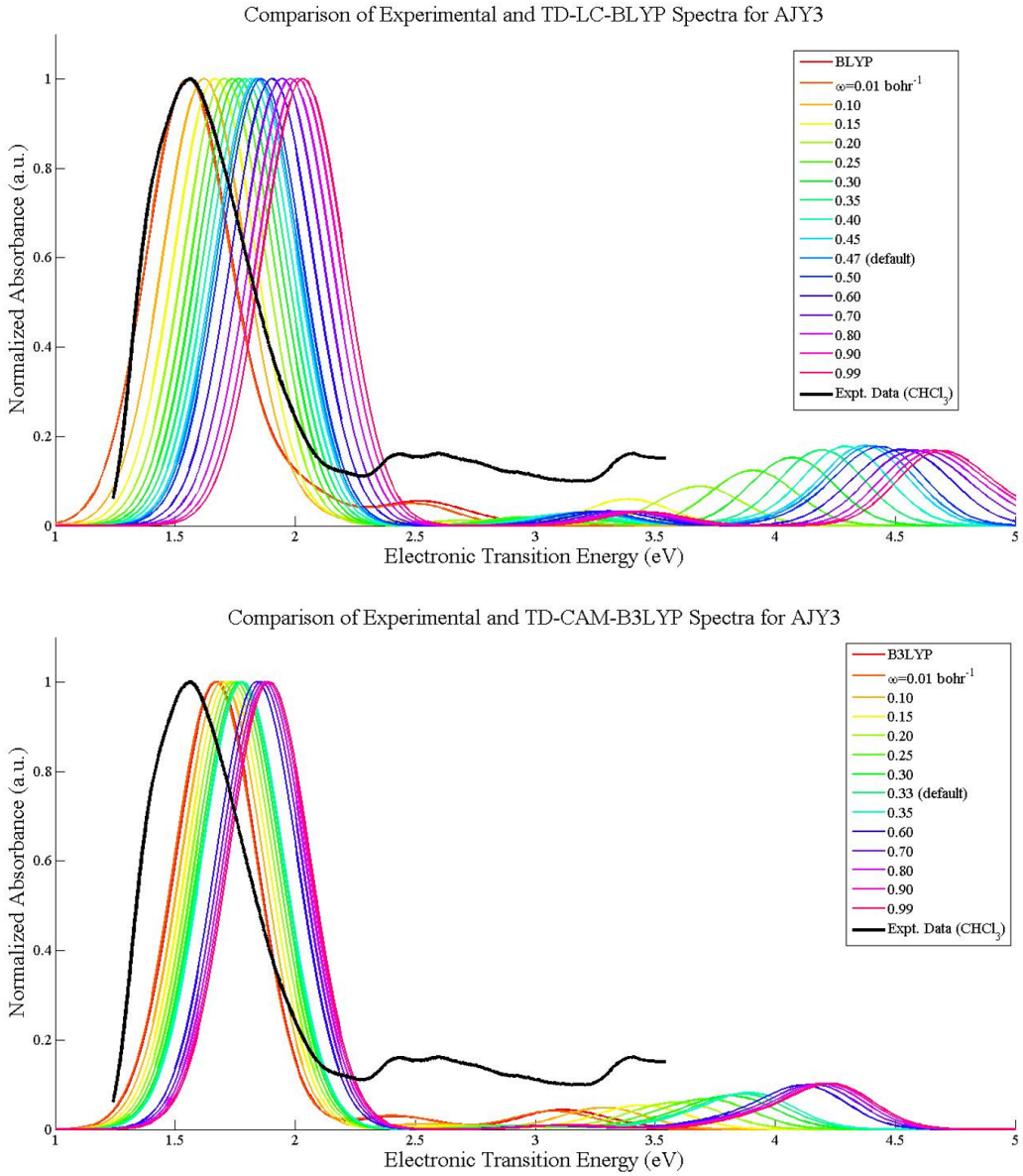

Figure A.11: **Comparison of Absorbance Spectra computed with TD-DFT and experimental UVv-is measurement for molecule AJY3.** Similar to its structural family ('AJY' series and YLD124), diminshing LR HF exchange in LC-BLYP and CAM-B3LYP results in better match between experiment and theory for AJY3. The ideal fraction of LR HF exchange occurs at around $\omega = 0.0 - 0.05\ bohr^{-1}$ in LC-BLYP; B3LYP is also a suitable match. Raw UV-vis data provided by Dr. Denise Bale.

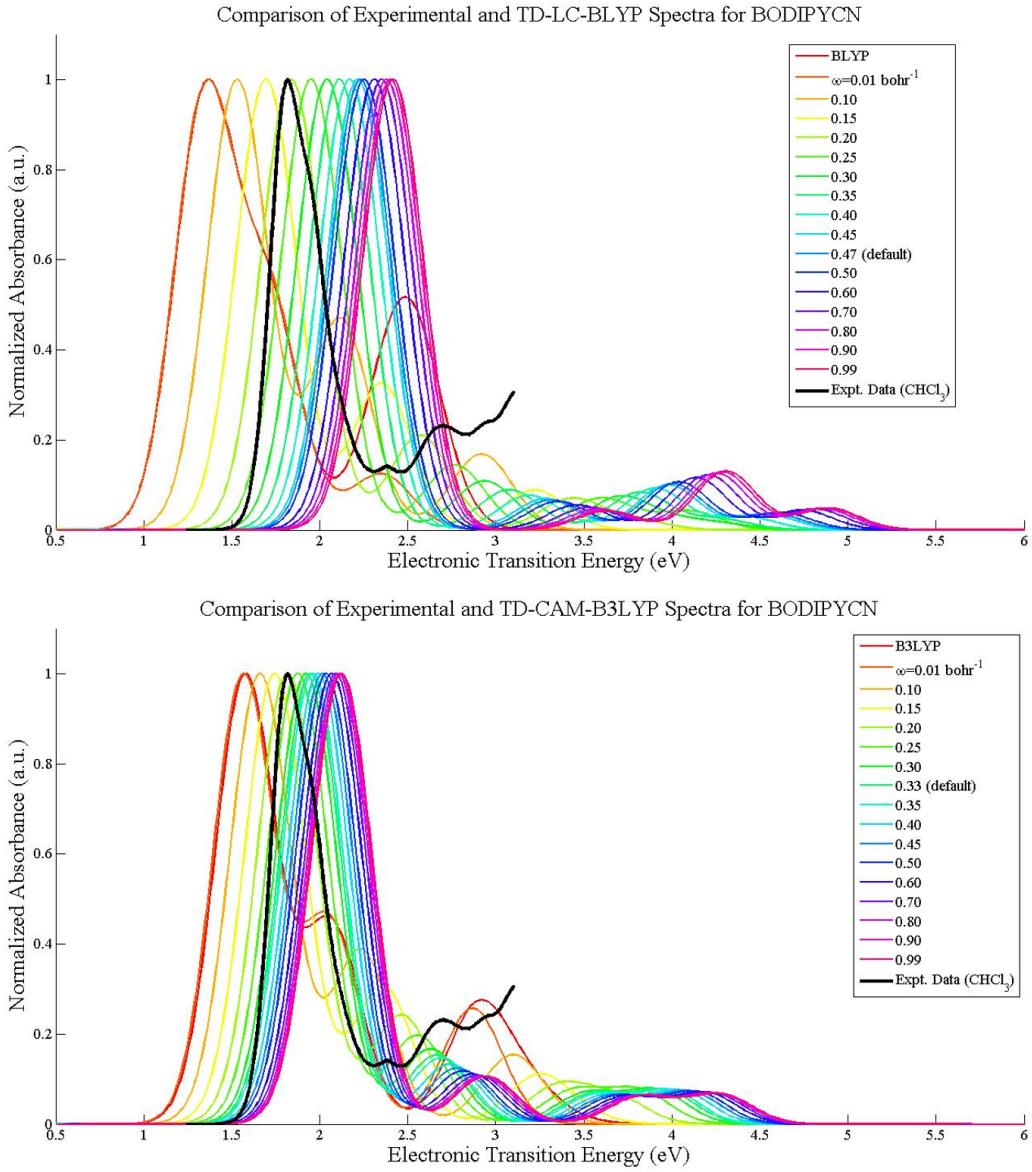

Figure A.12: **Comparison of Absorbance Spectra computed with TD-DFT and experimental UVv-is measurement for molecule BODIPYCN.** For this molecule, BLYP and B3LYP (the limits of reducing LR HF to zero in LC-BLYP and CAM-B3LYP, respectively) grow in strong high-energy transitions near 2.5-3 eV. The ideal fraction of LR HF exchange occurs at around $\omega = 0.16 - 0.20\ bohr^{-1}$ in LC-BLYP or CAM-B3LYP. Raw UV-vis data provided by Dr. Denise Bale.

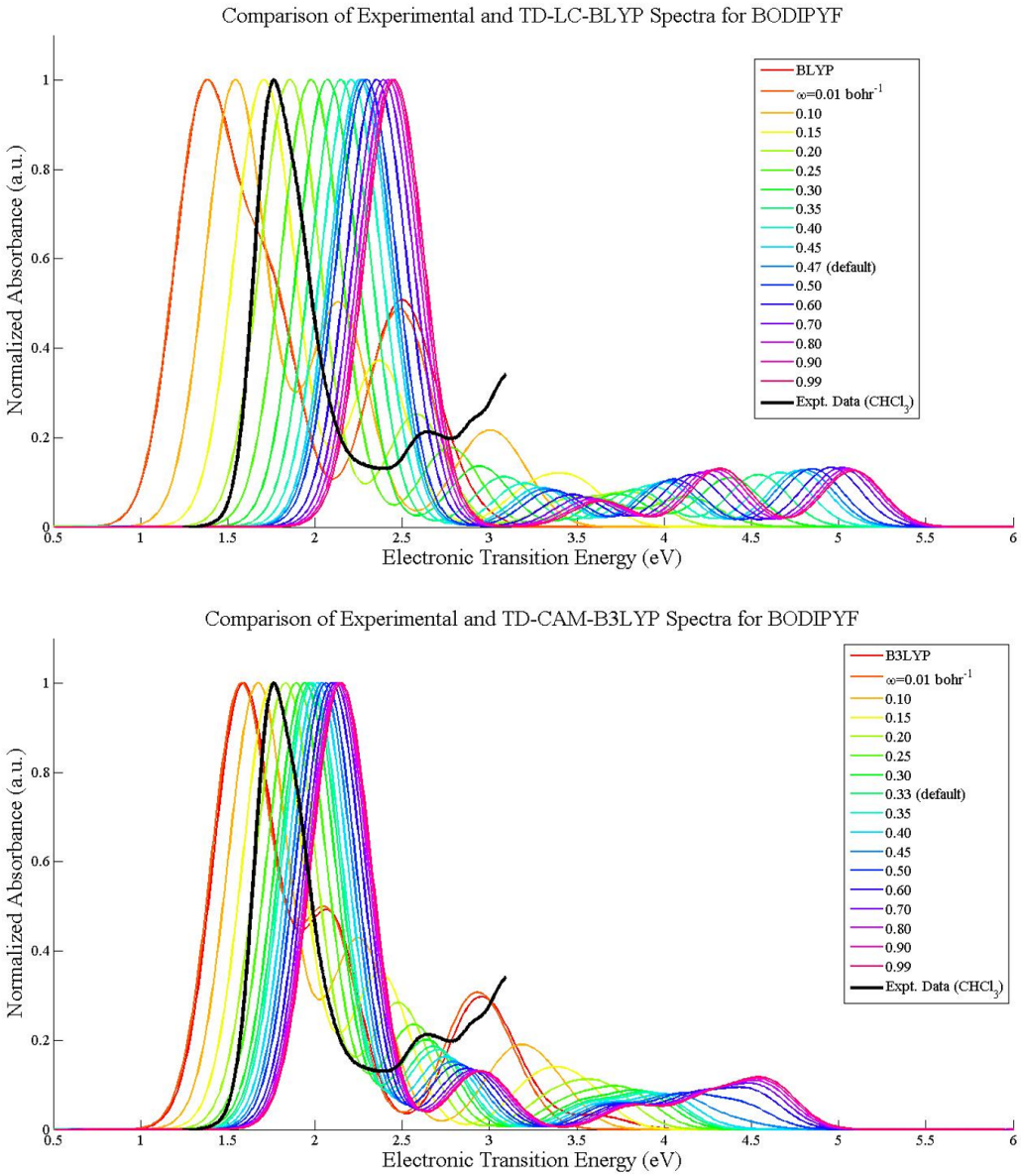

Figure A.13: **Comparison of Absorbance Spectra computed with TD-DFT and experimental UVv-is measurement for molecule BODIPYF.** The results for this system are similar to BODIPYCN. Raw UV-vis data provided by Dr. Denise Bale.

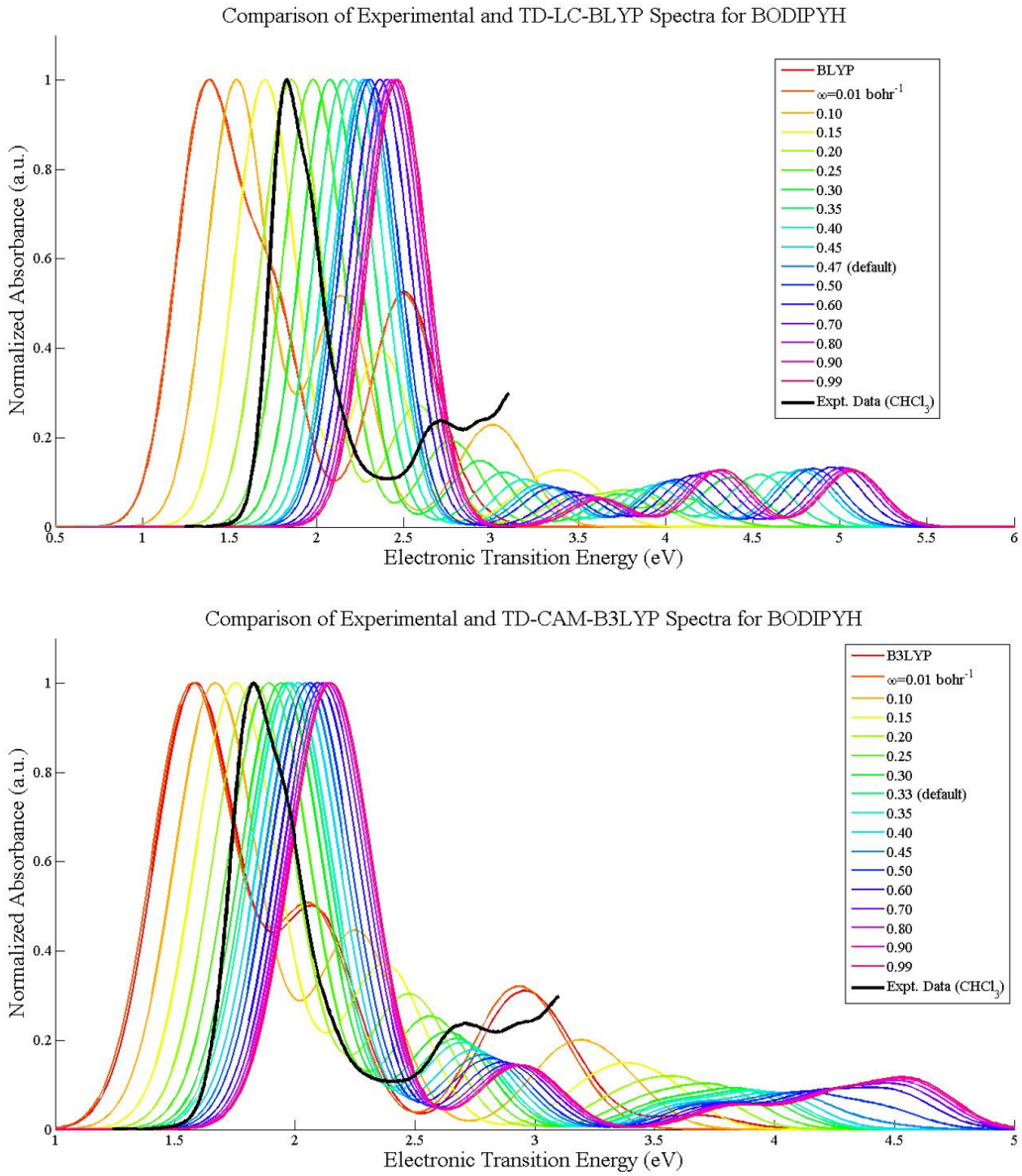

Figure A.14: **Comparison of Absorbance Spectra computed with TD-DFT and experimental UVv-is measurement for molecule BODIPYH.** Similar to other BODIPY molecules, BLYP and B3LYP give strong high-energy transitions near 2.5-3 eV. The ideal fraction of LR HF exchange occurs at around $\omega = 0.19 - 0.20\ bohr^{-1}$ in LC-BLYP or CAM-B3LYP. Raw UV-vis data provided by Dr. Denise Bale.

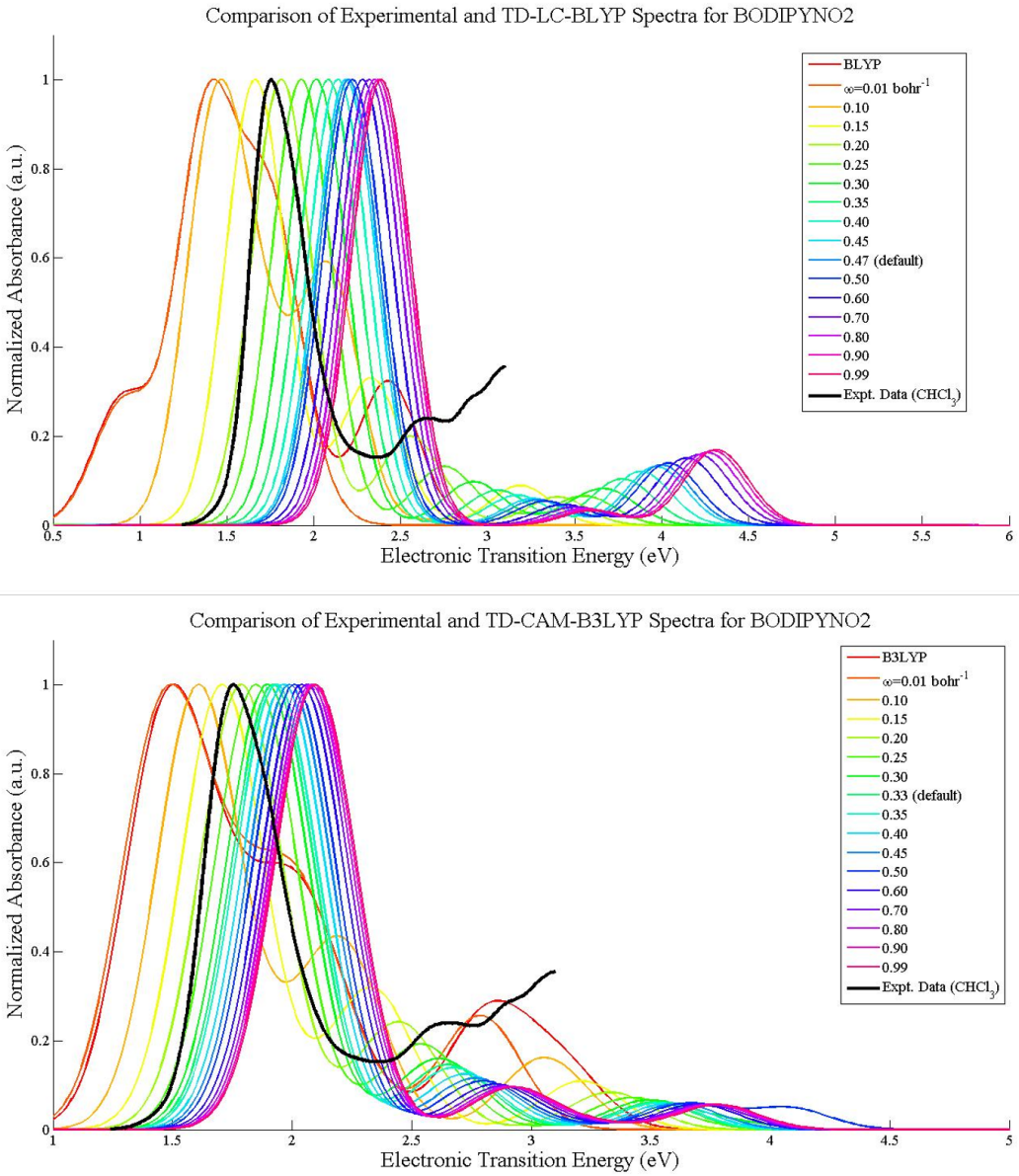

Figure A.15: **Comparison of Absorbance Spectra computed with TD-DFT and experimental UVv-is measurement for molecule BODIPYNO2.** The erratic behavior in computed absorbance spectra of the BODIPY series when approaching BLYP and B3LYP is exemplified by BODIPYNO2. For example, B3LYP reports 3 major peaks at approximately 1.5, 2.2, and 3 eV. However, like others in this series, the ideal fraction of LR HF exchange occurs at around $\omega = 0.17 - 0.20\ bohr^{-1}$ in LC-BLYP or CAM-B3LYP. Raw UV-vis data provided by Dr. Denise Bale.

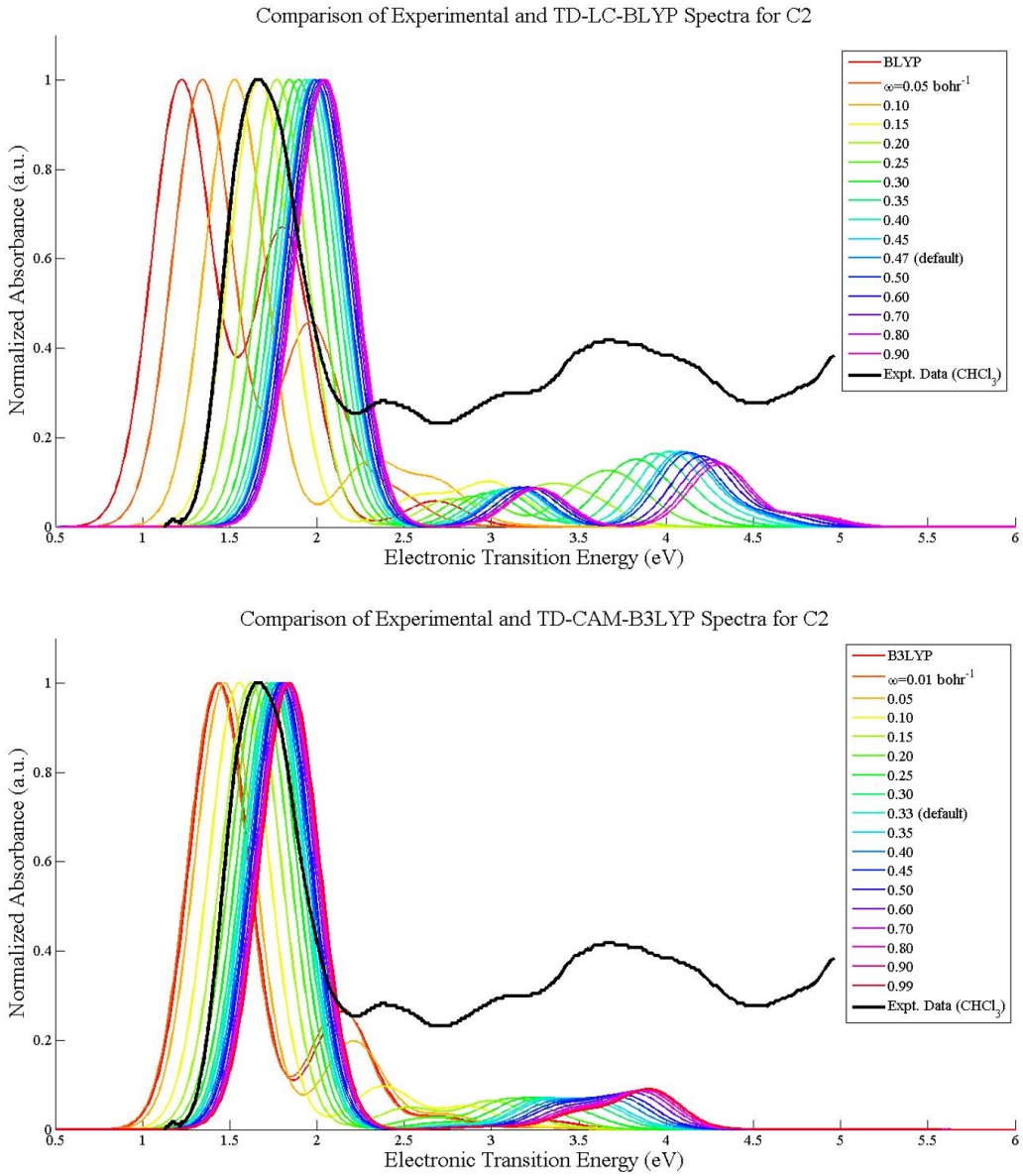

Figure A.16: **Comparison of Absorbance Spectra computed with TD-DFT and experimental UVv-is measurement for molecule 'C2' (AALD1158).** The ideal fraction of LR HF exchange occurs at around $\omega = 0.16 - 0.19\ bohr^{-1}$ in LC-BLYP or CAM-B3LYP. Raw UV-vis data provided by Dr. Denise Bale.

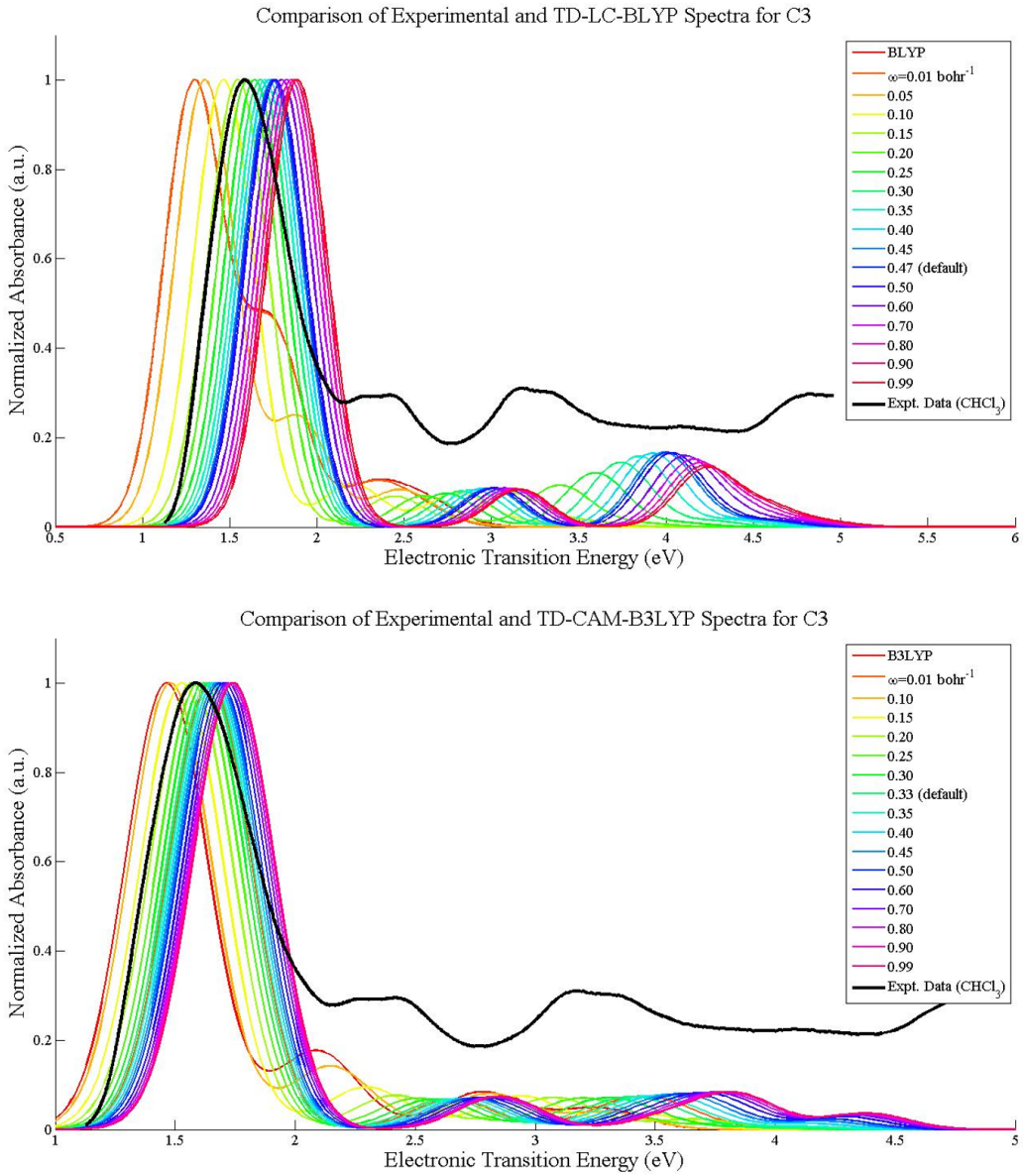

Figure A.17: **Comparison of Absorbance Spectra computed with TD-DFT and experimental UVv-is measurement for molecule 'C3' (AALD2023).** The ideal fraction of LR HF exchange occurs at around $\omega = 0.19 - 0.25 bohr^{-1}$ in LC-BLYP or CAM-B3LYP. Raw UV-vis data provided by Dr. Denise Bale.

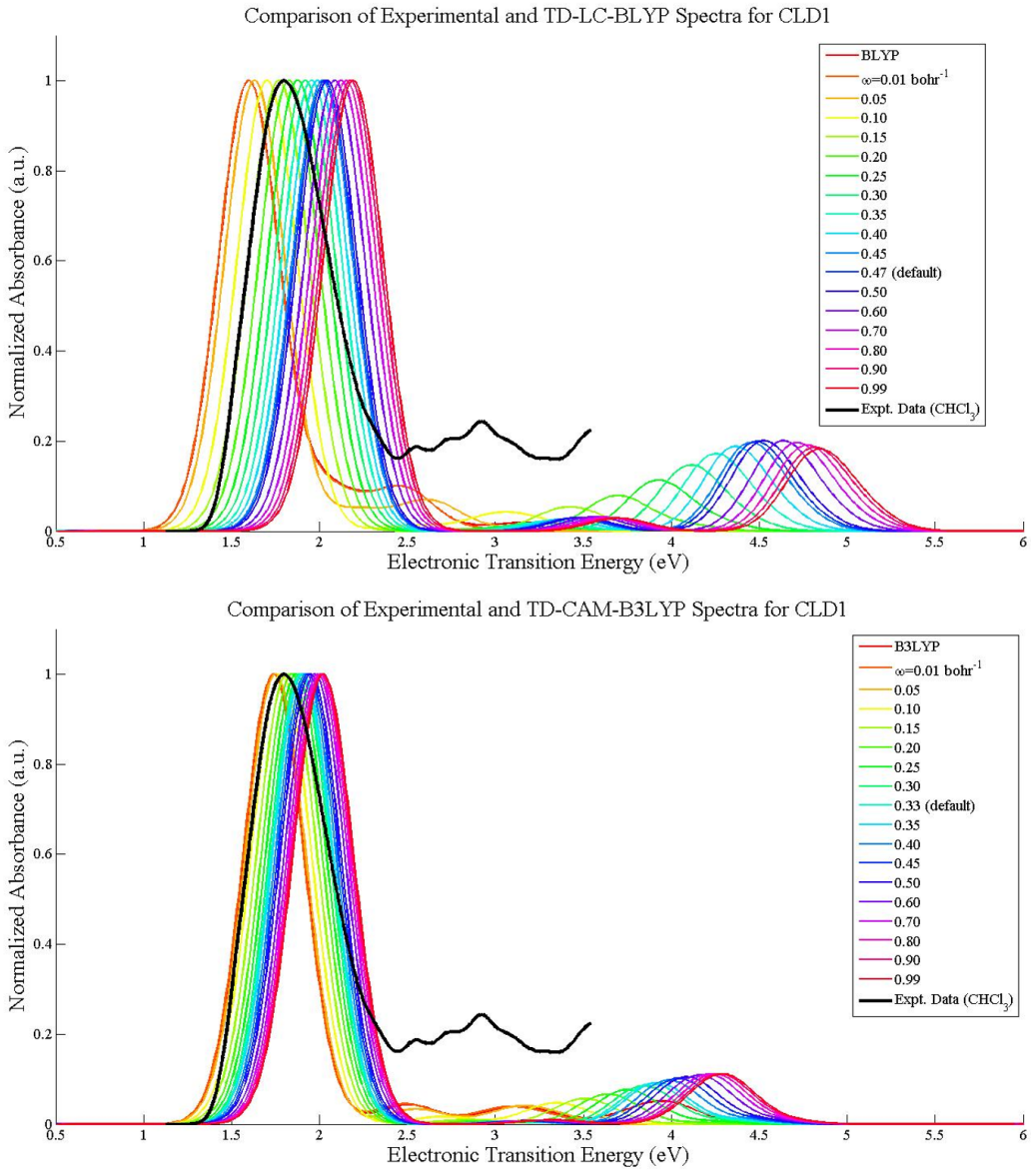

Figure A.18: **Comparison of Absorbance Spectra computed with TD-DFT and experimental UVv-is measurement for molecule CLD1.** Despite the similar structure to the AJY series, LR HF exchange for CLD1 is required for a good match to λ_{max}; the ideal fraction occurs at $\omega = 0.15\ bohr^{-1}$ in LC-BLYP and $\omega = 0.10\ bohr^{-1}$ in CAM-B3LYP. Raw UV-vis data provided by Dr. Denise Bale.

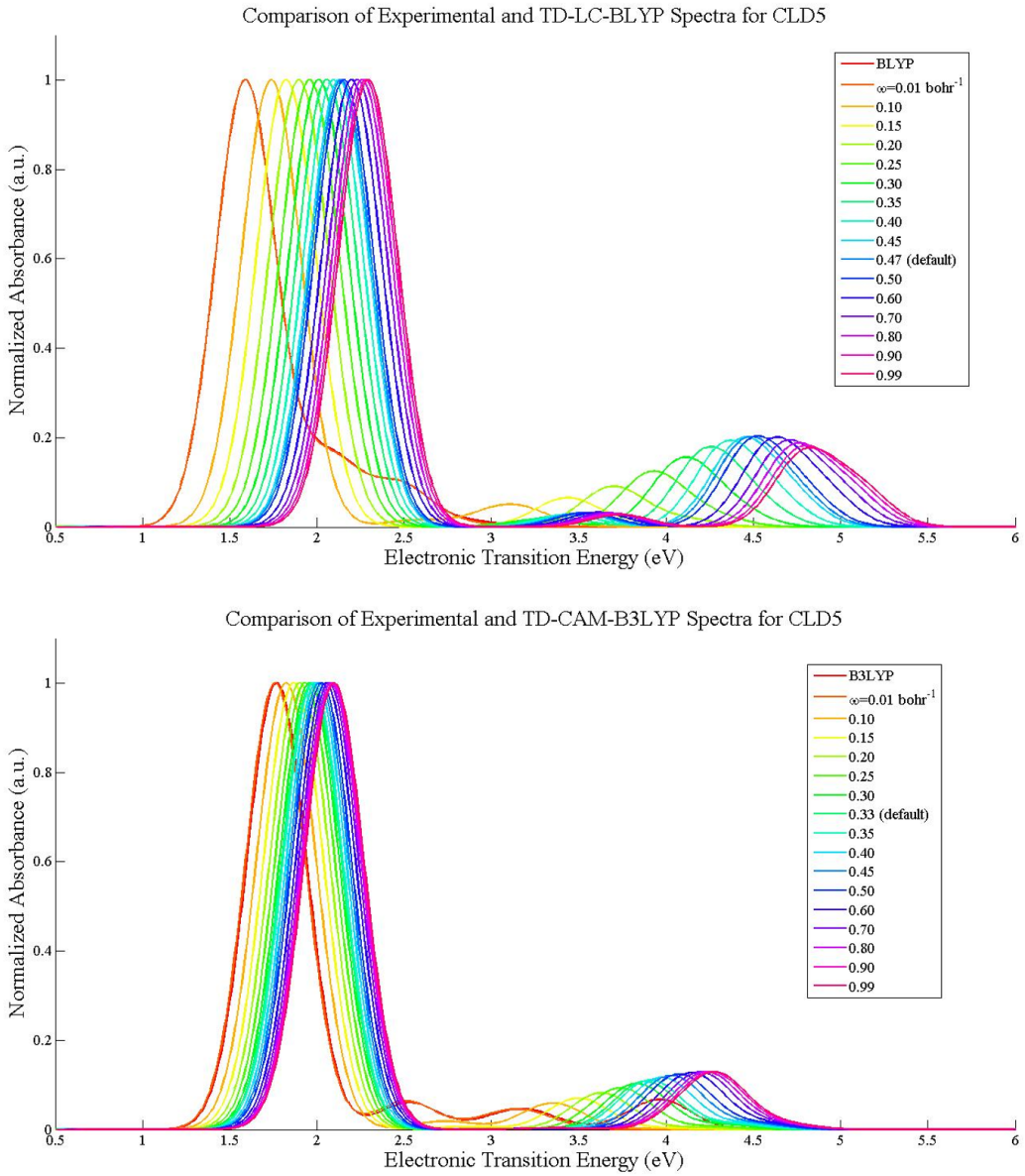

Figure A.19: **Comparison of Absorbance Spectra computed with TD-DFT for molecule CLD5.** Raw UV-vis measurements for CLD-5 are not available. A plot of the measured spectrum can be viewed in Ref. [73]. A suitable match for measured λ_{max} (658 nm $\approx$ 1.884 eV) is $\omega = 0.15 - 0.19\ bohr^{-1}$ in LC-BLYP or CAM-B3LYP.

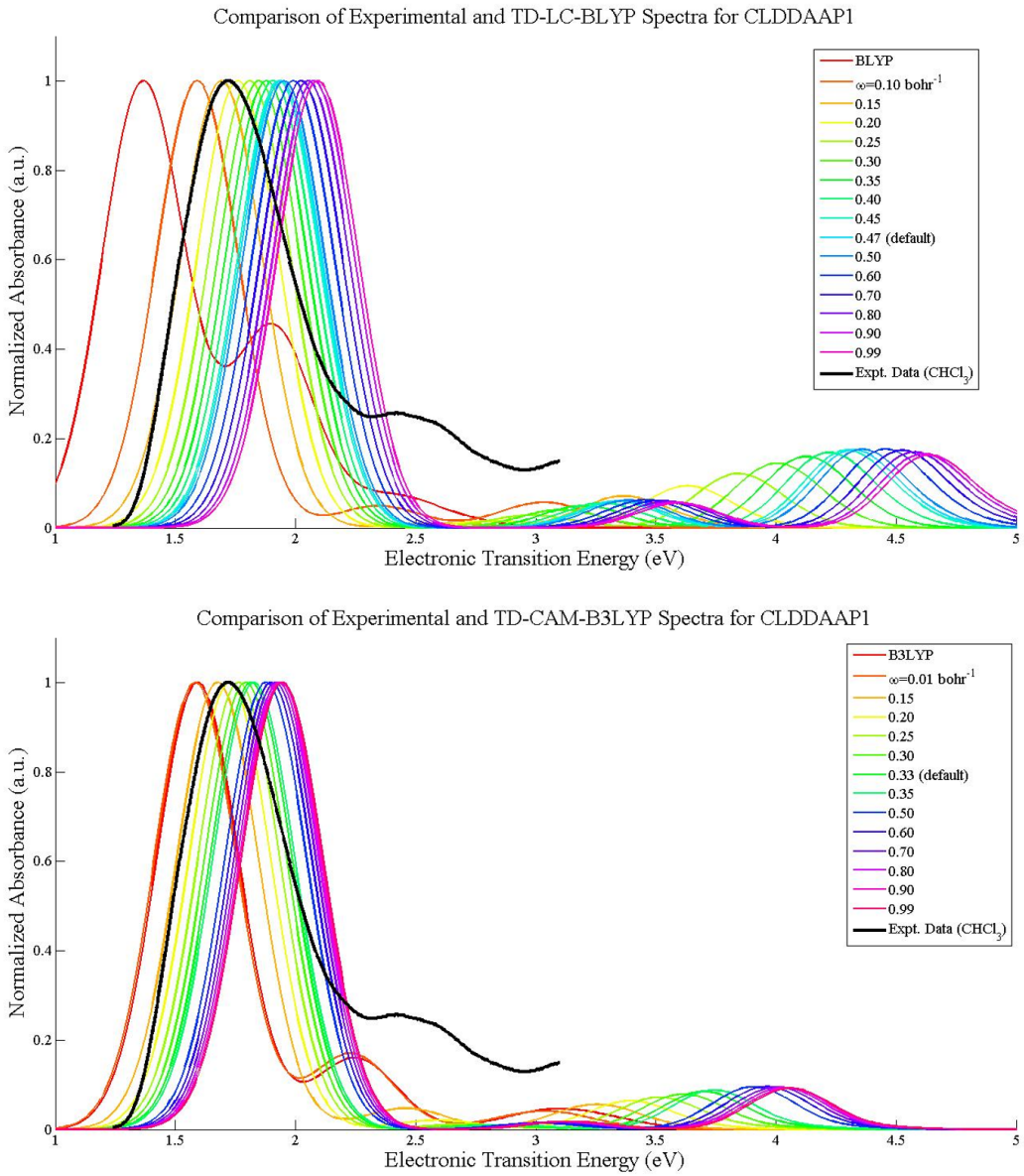

Figure A.20: **Comparison of Absorbance Spectra computed with TD-DFT and experimental UVv-is measurement for molecule 'CLD-DAAP1'.** The ideal fraction occurs at $\omega = 0.15-0.18\, bohr^{-1}$ in LC-BLYP or CAM-B3LYP. Raw UV-vis data provided by Dr. Denise Bale.

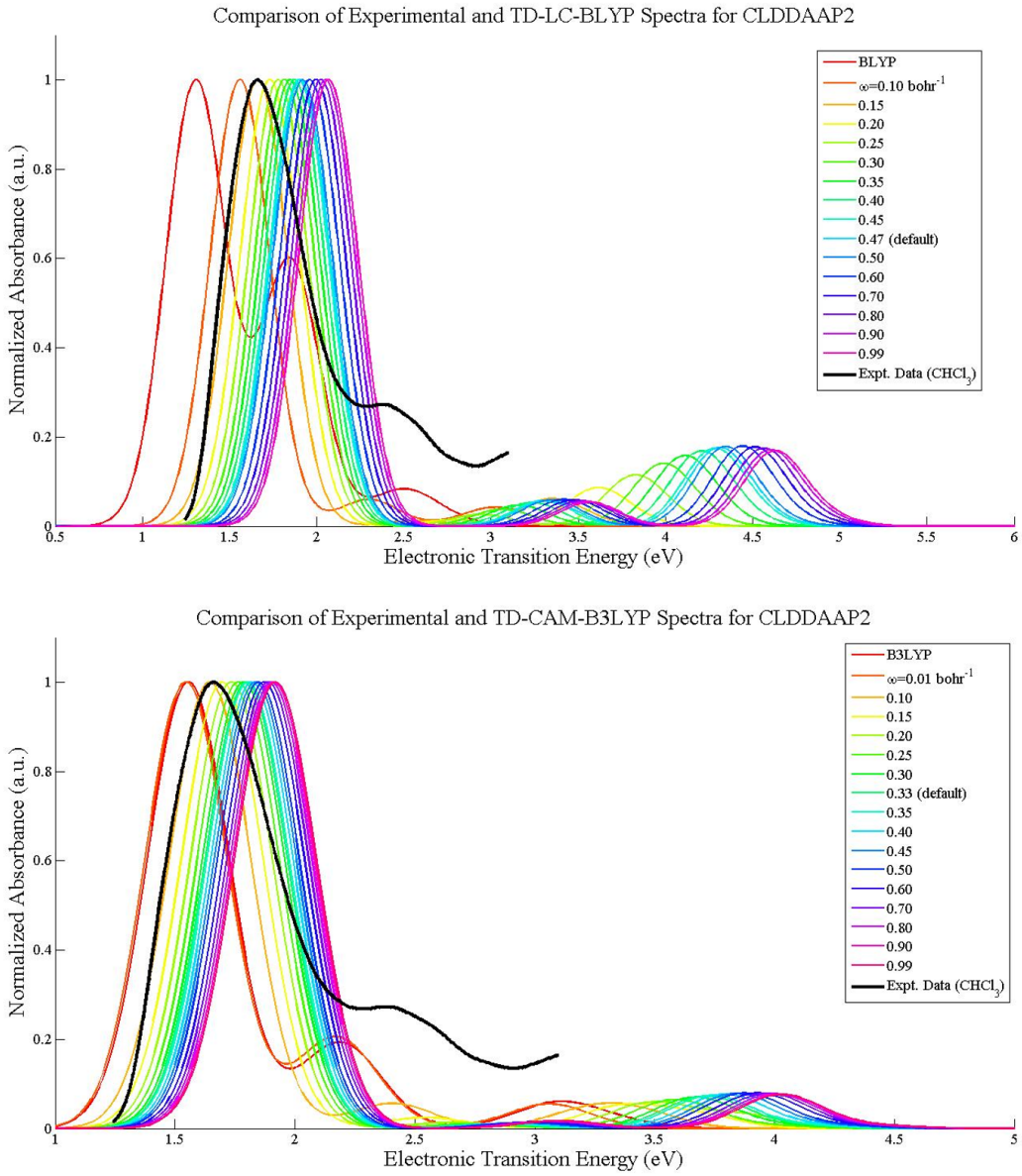

Figure A.21: **Comparison of Absorbance Spectra computed with TD-DFT and experimental UVv-is measurement for molecule 'CLD-DAAP2'.** The ideal fraction occurs at $\omega = 0.12-0.15\ bohr^{-1}$ in LC-BLYP or CAM-B3LYP. Raw UV-vis data provided by Dr. Denise Bale.

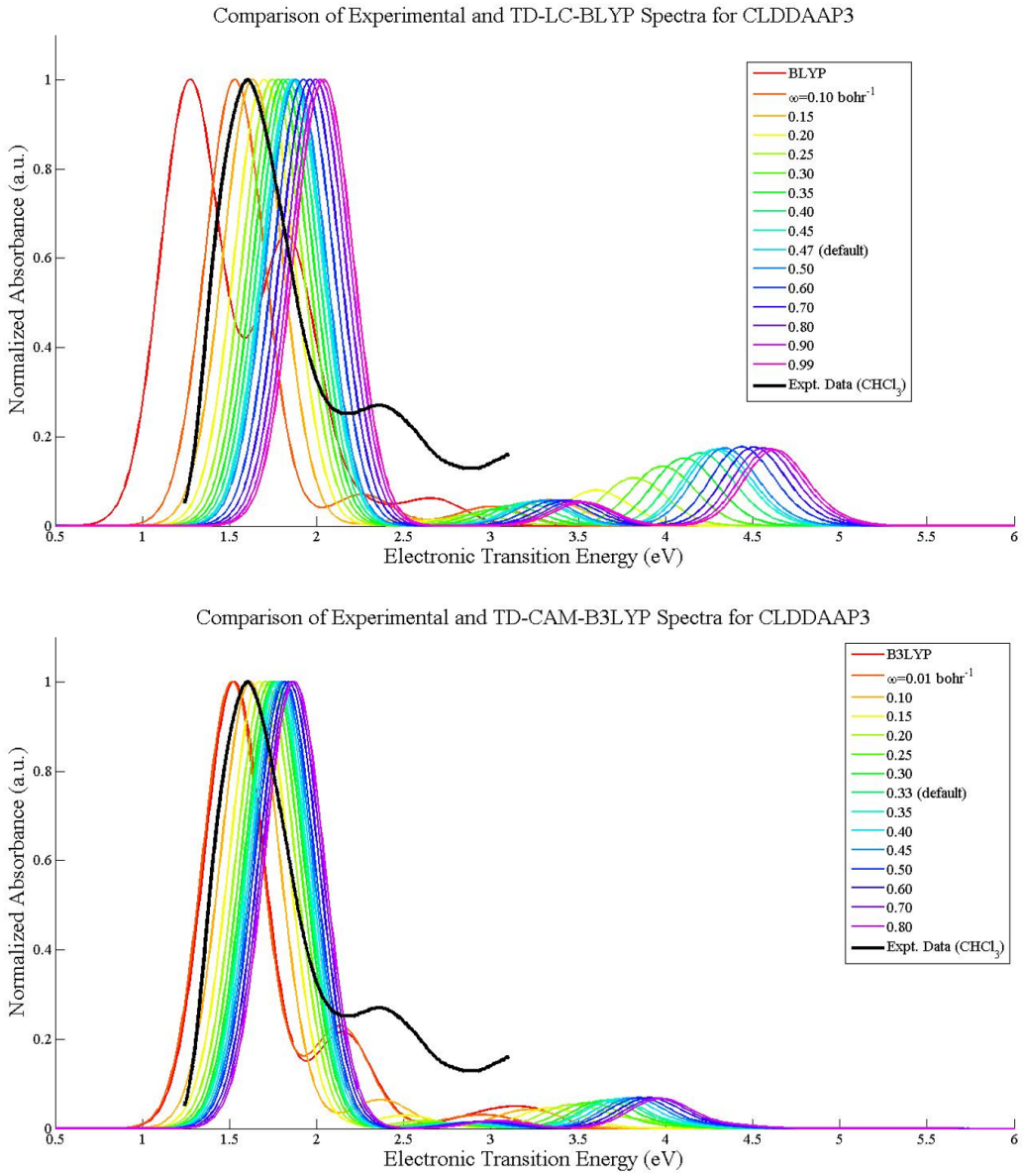

Figure A.22: **Comparison of Absorbance Spectra computed with TD-DFT and experimental UVv-is measurement for molecule 'CLD-DAAP3'.** The ideal fraction occurs at $\omega = 0.15-0.17\, bohr^{-1}$ in LC-BLYP or CAM-B3LYP. Raw UV-vis data provided by Dr. Denise Bale.

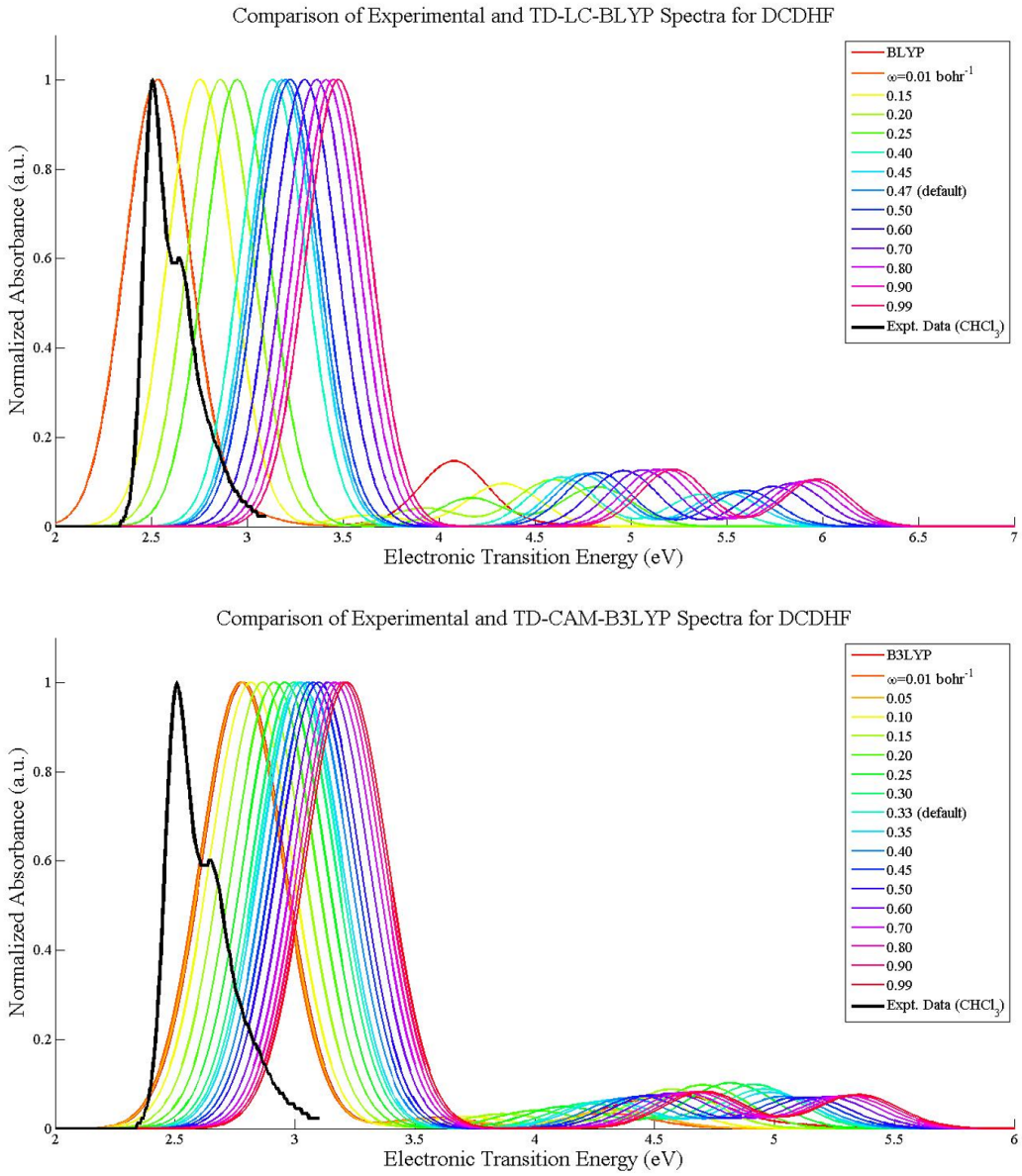

Figure A.23: **Comparison of Absorbance Spectra computed with TD-DFT and experimental UVv-is measurement for molecule DCDHF.** Note that diminshing LR HF exchange in LC-BLYP and CAM-B3LYP results in better match between experiment and theory for this molecule; thus, BLYP and B3LYP are suitable matches. Raw UV-vis data provided by Dr. Denise Bale.

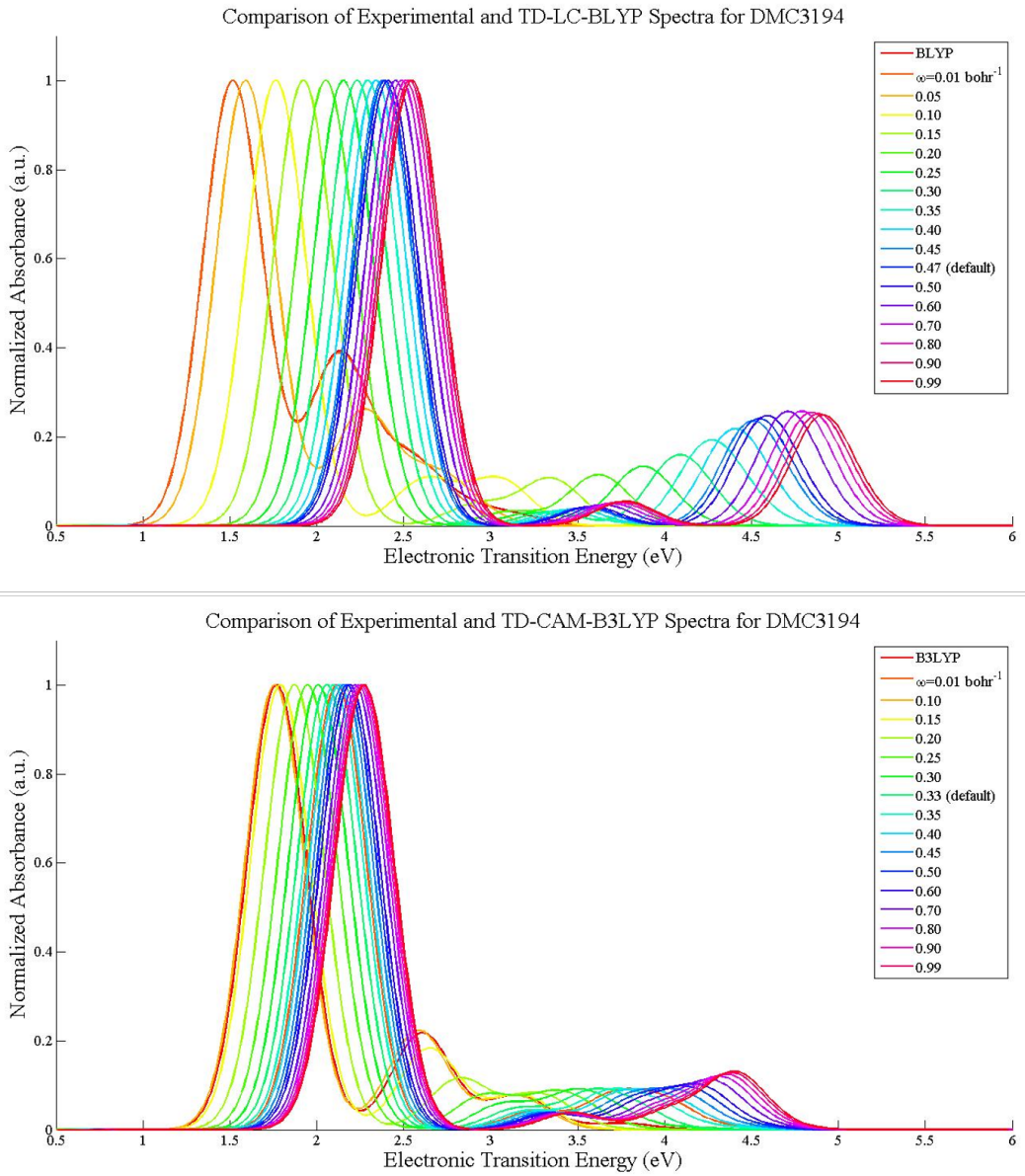

Figure A.24: **Comparison of Absorbance Spectra computed with TD-DFT for molecule DMC3-194.** Raw UV-vis measurement for DMC3194 is not available. A plot of the measured spectra can be viewed in Ref. [73]. A suitable match for both measured λ_{max} of DMC3-194 (645 nm $\approx$ 1.923 eV) is $\omega = 0.15 bohr^{-1}$ in LC-BLYP or CAM-B3LYP.

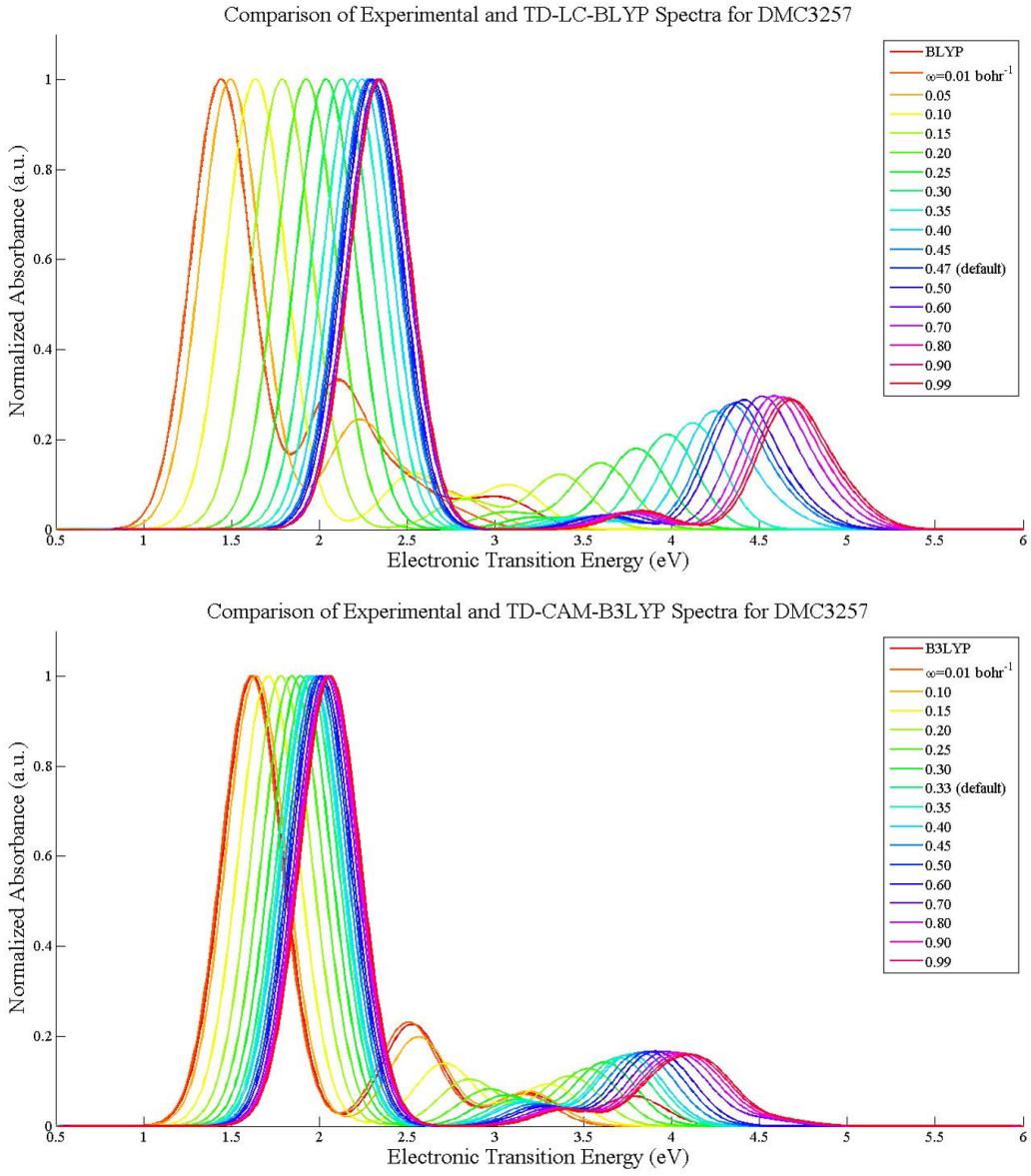

Figure A.25: **Comparison of Absorbance Spectra computed with TD-DFT for molecule DMC3-257.** Raw UV-vis measurement for DMC3257 molecules is not available. A plot of the measured spectra can be viewed in Ref. [73]. A suitable match for both measured λ_{max} of DMC3-257 (682 nm $\approx$ 1.818 eV) is $\omega = 0.15 bohr^{-1}$ in LC-BLYP or CAM-B3LYP.

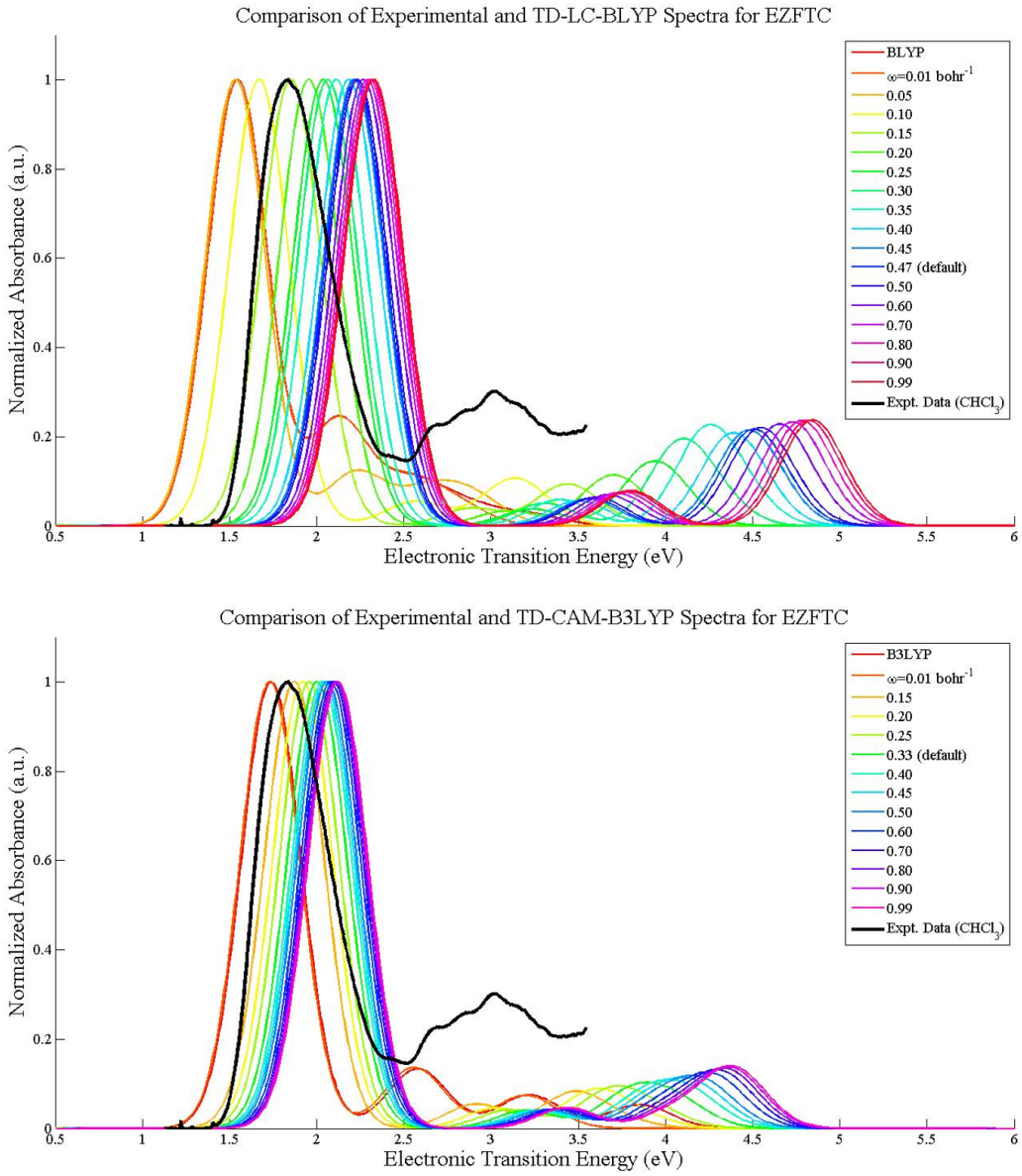

Figure A.26: **Comparison of Absorbance Spectra computed with TD-DFT and experimental UVv-is measurement for molecule EZ-FTC.** The ideal fraction occurs at around $\omega = 0.15-0.20\, bohr^{-1}$ in LC-BLYP or CAM-B3LYP. Raw UV-vis data provided by Dr. Denise Bale.

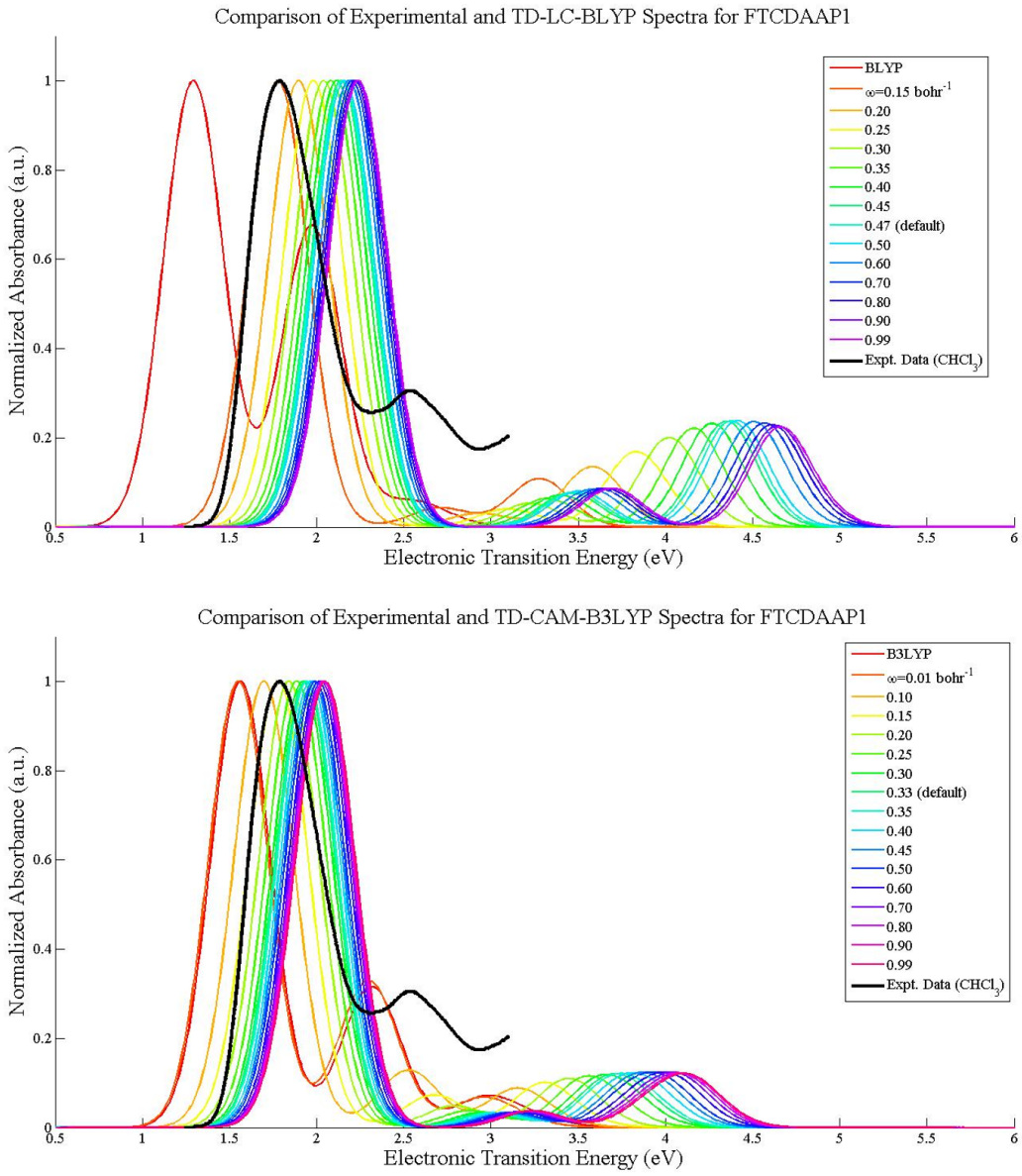

Figure A.27: **Comparison of Absorbance Spectra computed with TD-DFT and experimental UVv-is measurement for molecule 'FTC-DAAP1'.** The ideal fraction occurs at $\omega = 0.16\ bohr^{-1}$ in LC-BLYP or CAM-B3LYP. Raw UV-vis data provided by Dr. Denise Bale.

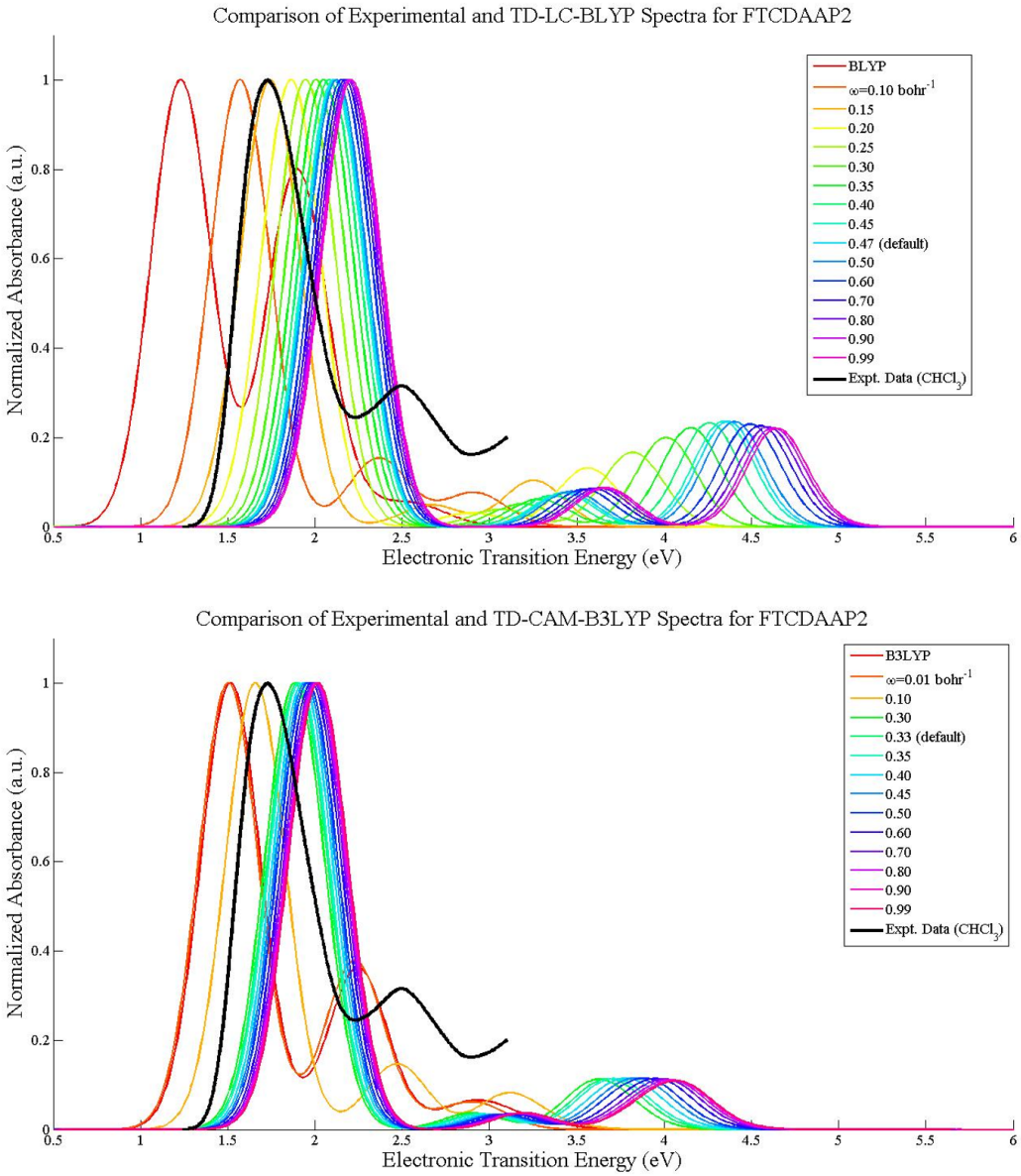

Figure A.28: **Comparison of Absorbance Spectra computed with TD-DFT and experimental UVv-is measurement for molecule 'FTC-DAAP2'.** The ideal fraction occurs at $\omega = 0.15\ bohr^{-1}$ in LC-BLYP or CAM-B3LYP. Raw UV-vis data provided by Dr. Denise Bale.

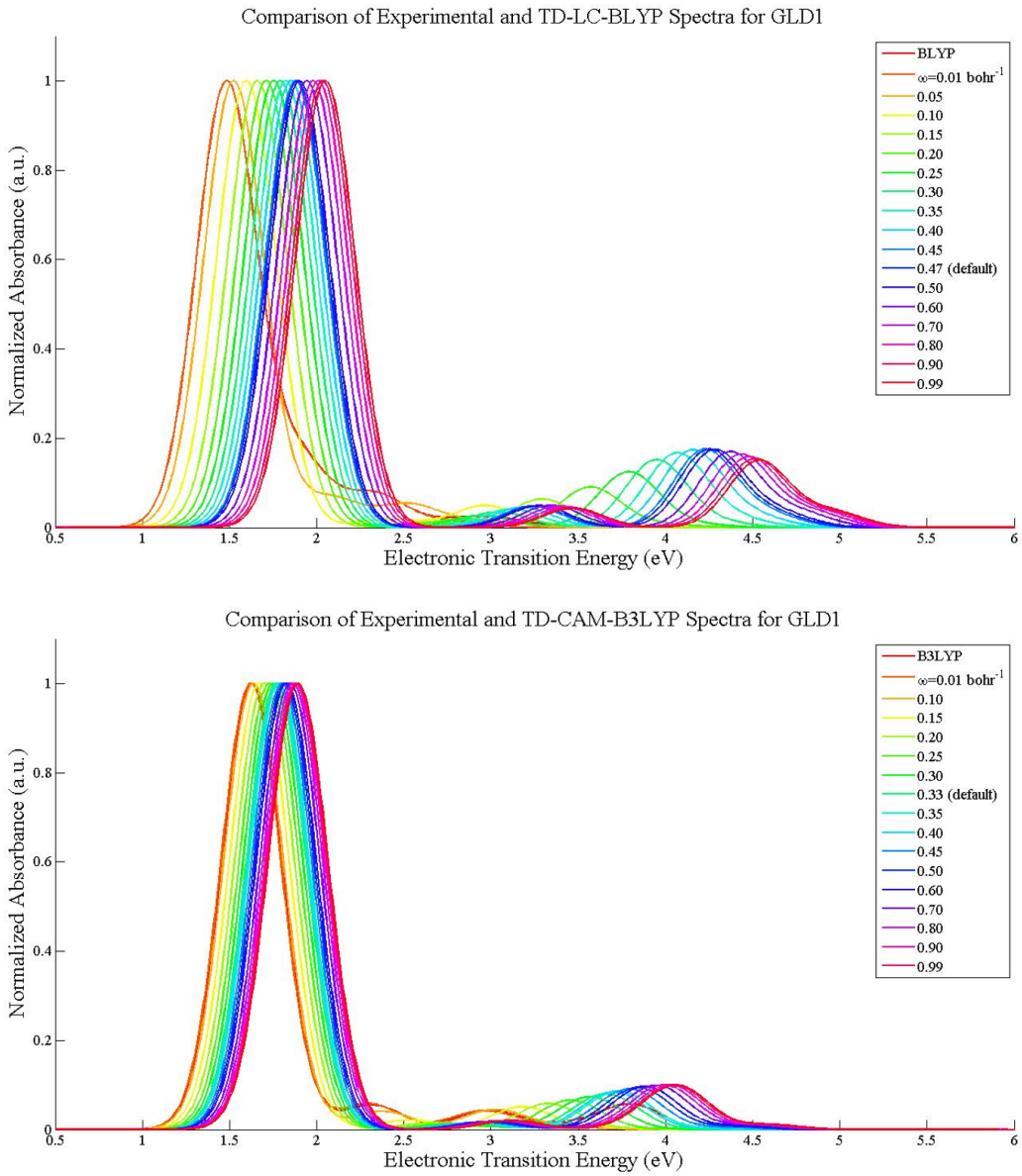

Figure A.29: **Comparison of Absorbance Spectra computed with TD-DFT and experimental UVv-is measurement for molecule GLD1.** Raw UV-vis measurements for GLD1 are not available. A plot of the measured spectrum can be viewed in Ref. [73]. A suitable match for measured λ_{max} (719 nm $\approx$ 1.725 eV) is $\omega = 0.17 - 0.21\ bohr^{-1}$ in LC-BLYP or CAM-B3LYP.

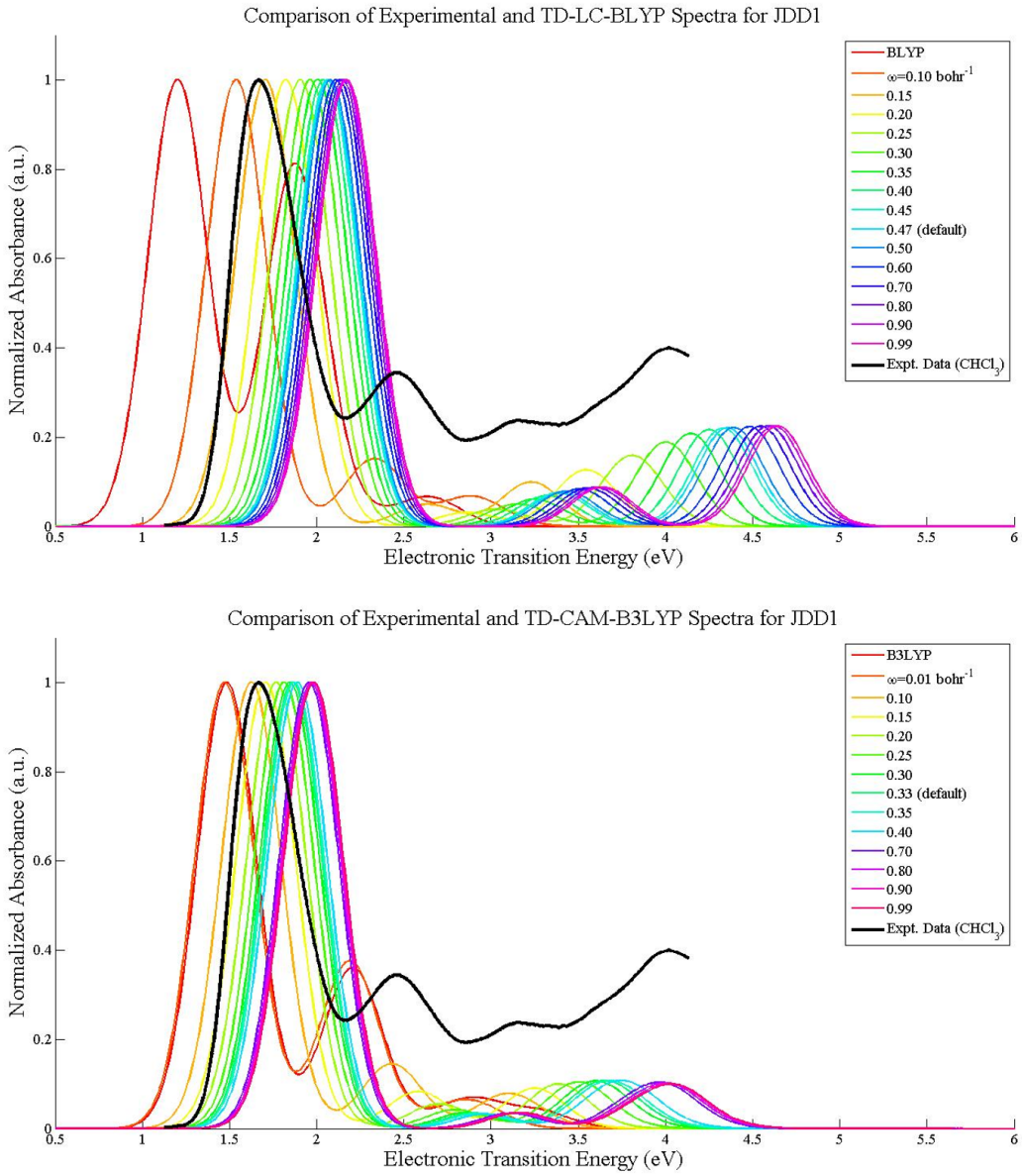

Figure A.30: **Comparison of Absorbance Spectra computed with TD-DFT and experimental UVv-is measurement for molecule JDD1.** The ideal fraction of LR HF exchange occurs at around $\omega = 0.10 - 0.13\ bohr^{-1}$ in LC-BLYP or CAM-B3LYP. Raw UV-vis data provided by Dr. Denise Bale.

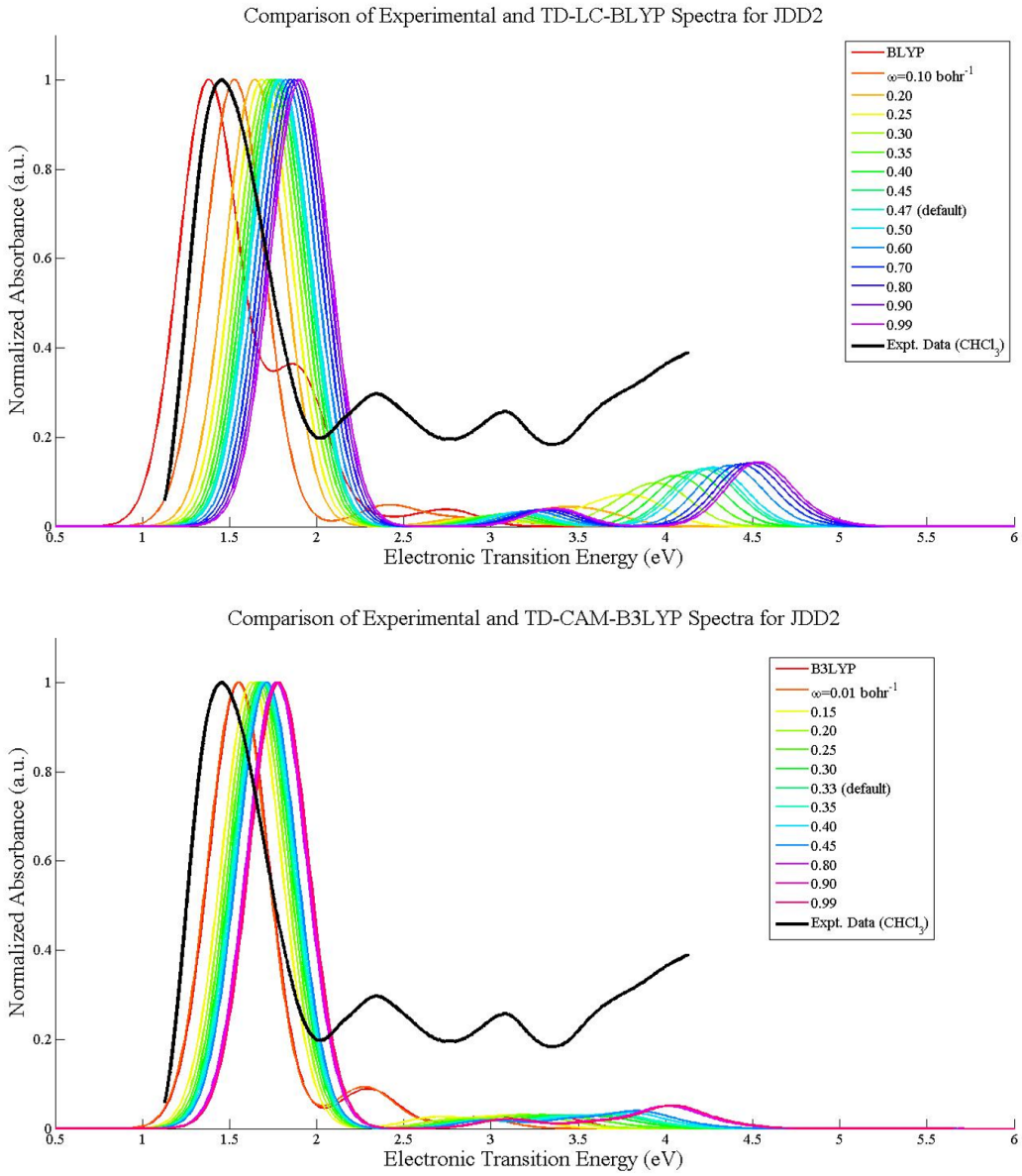

Figure A.31: **Comparison of Absorbance Spectra computed with TD-DFT and experimental UVv-is measurement for molecule JDD2.** The ideal match for λ_{max} is BLYP or B3LYP. Raw UV-vis data provided by Dr. Denise Bale.

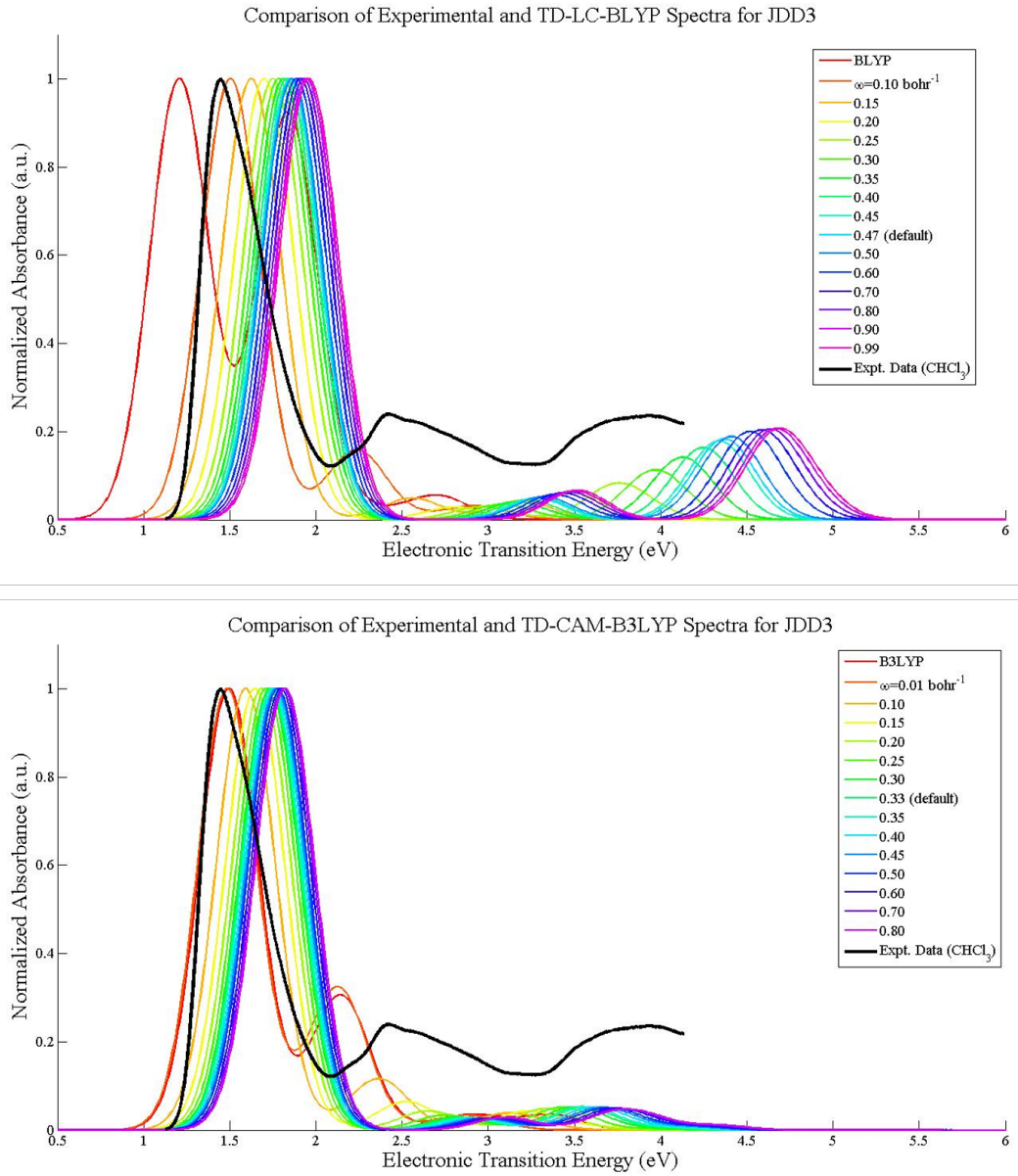

Figure A.32: **Comparison of Absorbance Spectra computed with TD-DFT and experimental UVv-is measurement for molecule JDD3.** The ideal match for λ_{max} is $\omega = 0.10\ bohr^{-1}$ in LC-BLYP or B3LYP. Raw UV-vis data provided by Dr. Denise Bale.

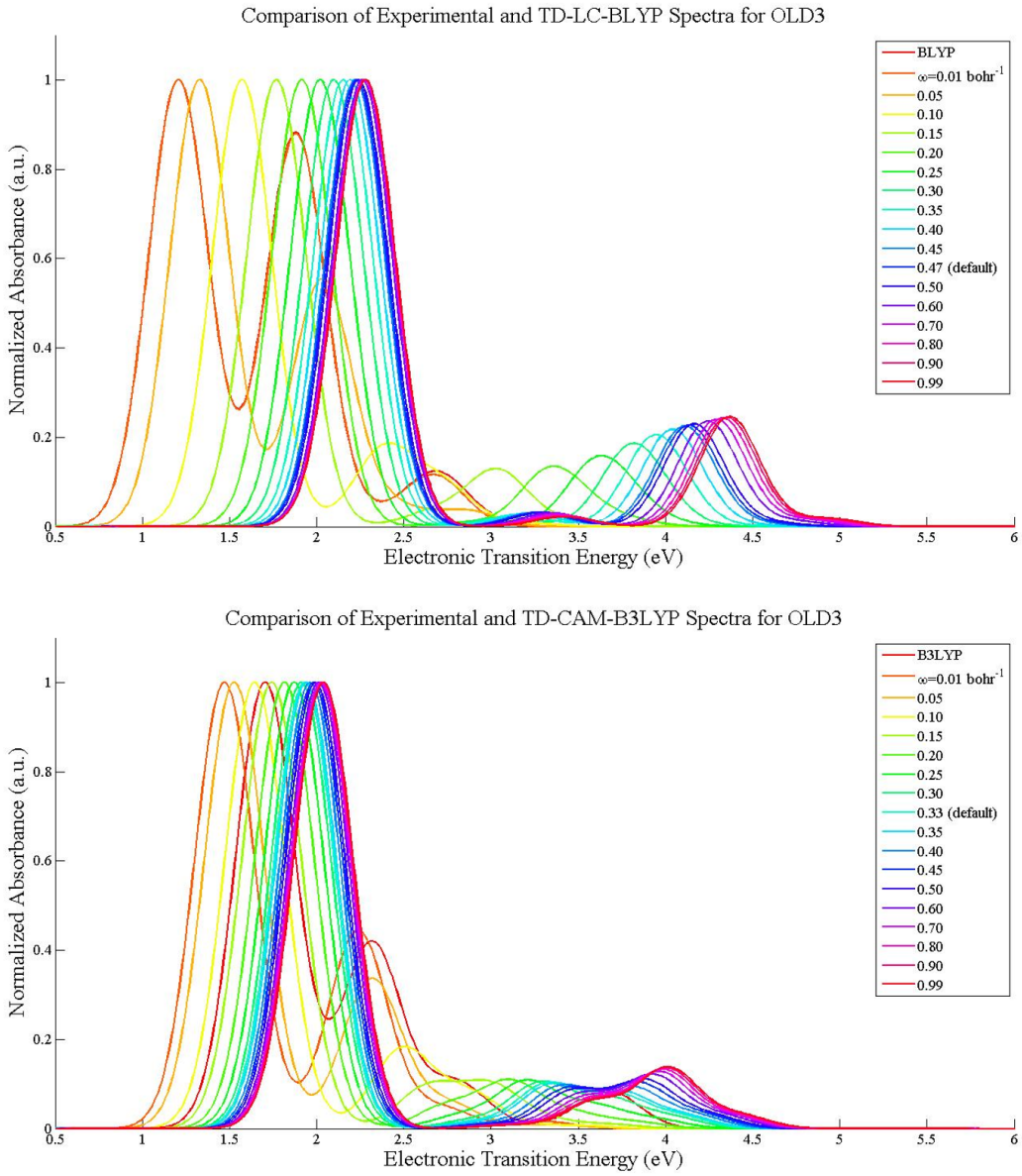

Figure A.33: **Comparison of Absorbance Spectra computed with TD-DFT and experimental UVv-is measurement for molecule OLD3.** The ideal fraction of LR HF exchange occurs at around $\omega = 0.15 - 0.17\ bohr^{-1}$ in LC-BLYP or CAM-B3LYP. Raw UV-vis data provided by Dr. Denise Bale.

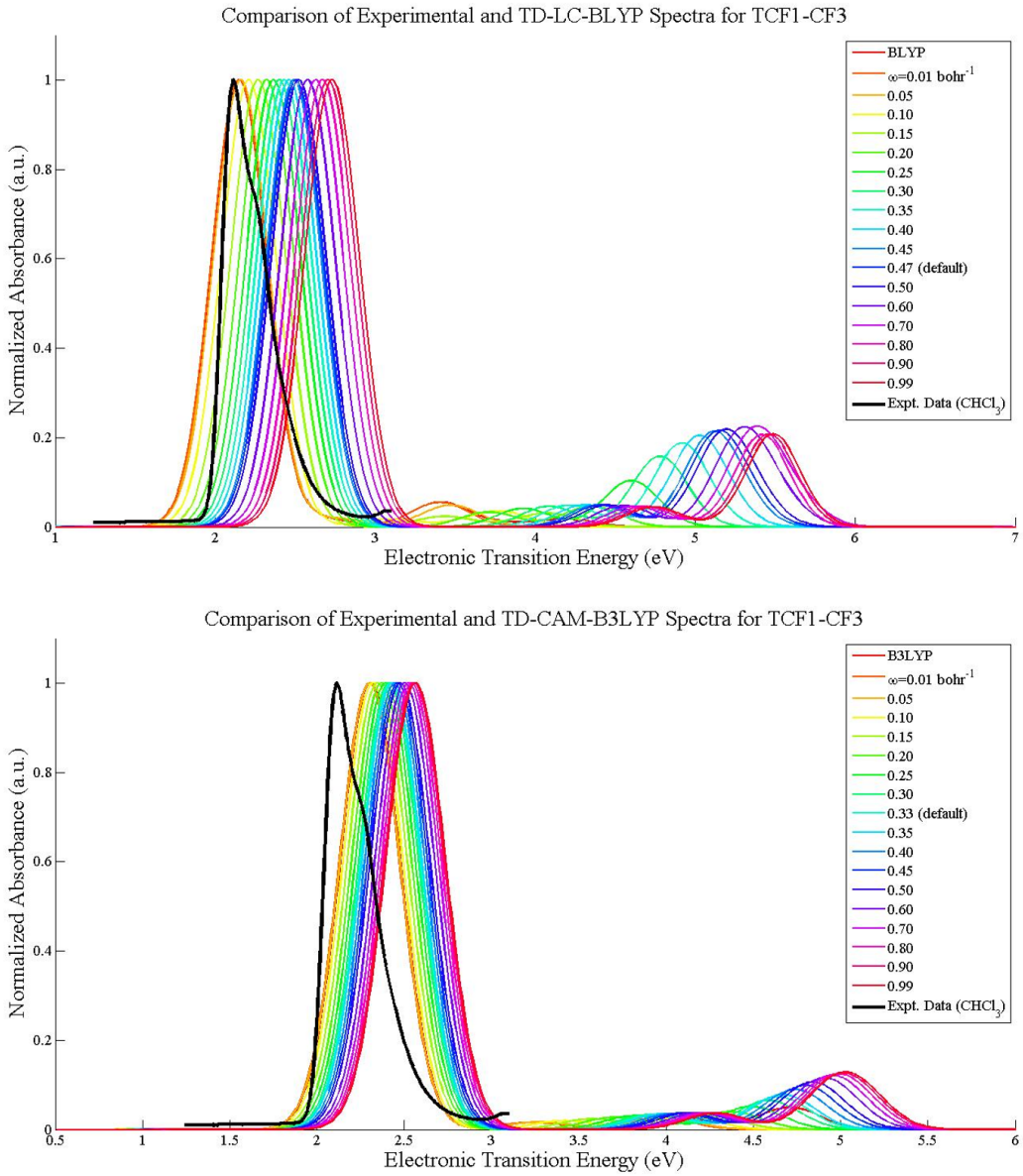

Figure A.34: **Comparison of Absorbance Spectra computed with TD-DFT and experimental UVv-is measurement for molecule TCF1-CF3.** The ideal match for λ_{max} is BLYP or B3LYP. Raw UV-vis data provided by Dr. Denise Bale.

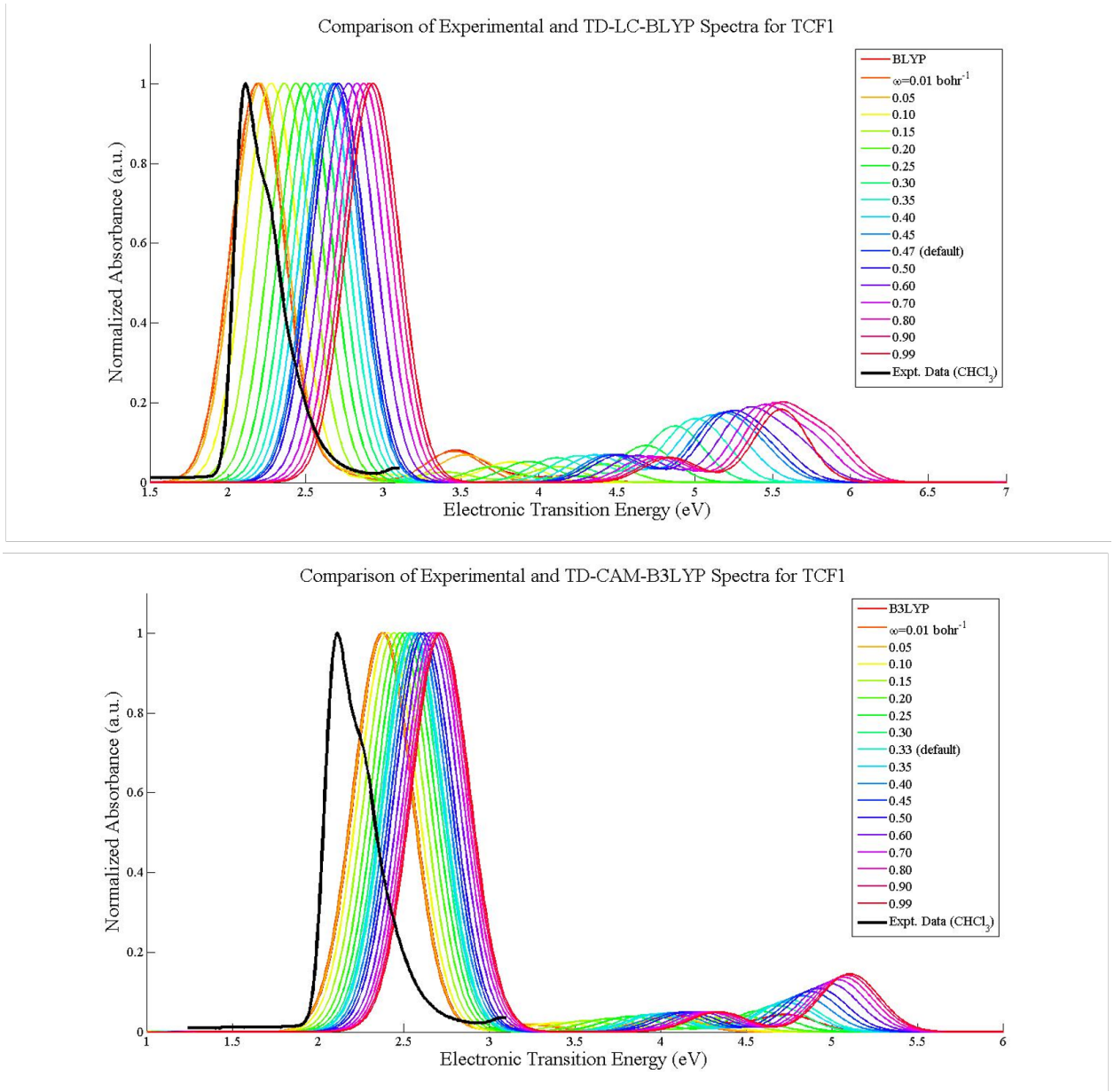

Figure A.35: **Comparison of Absorbance Spectra computed with TD-DFT and experimental UVv-is measurement for molecule TCF1.** The ideal match for λ_{max} is BLYP or B3LYP. Raw UV-vis data provided by Dr. Denise Bale.

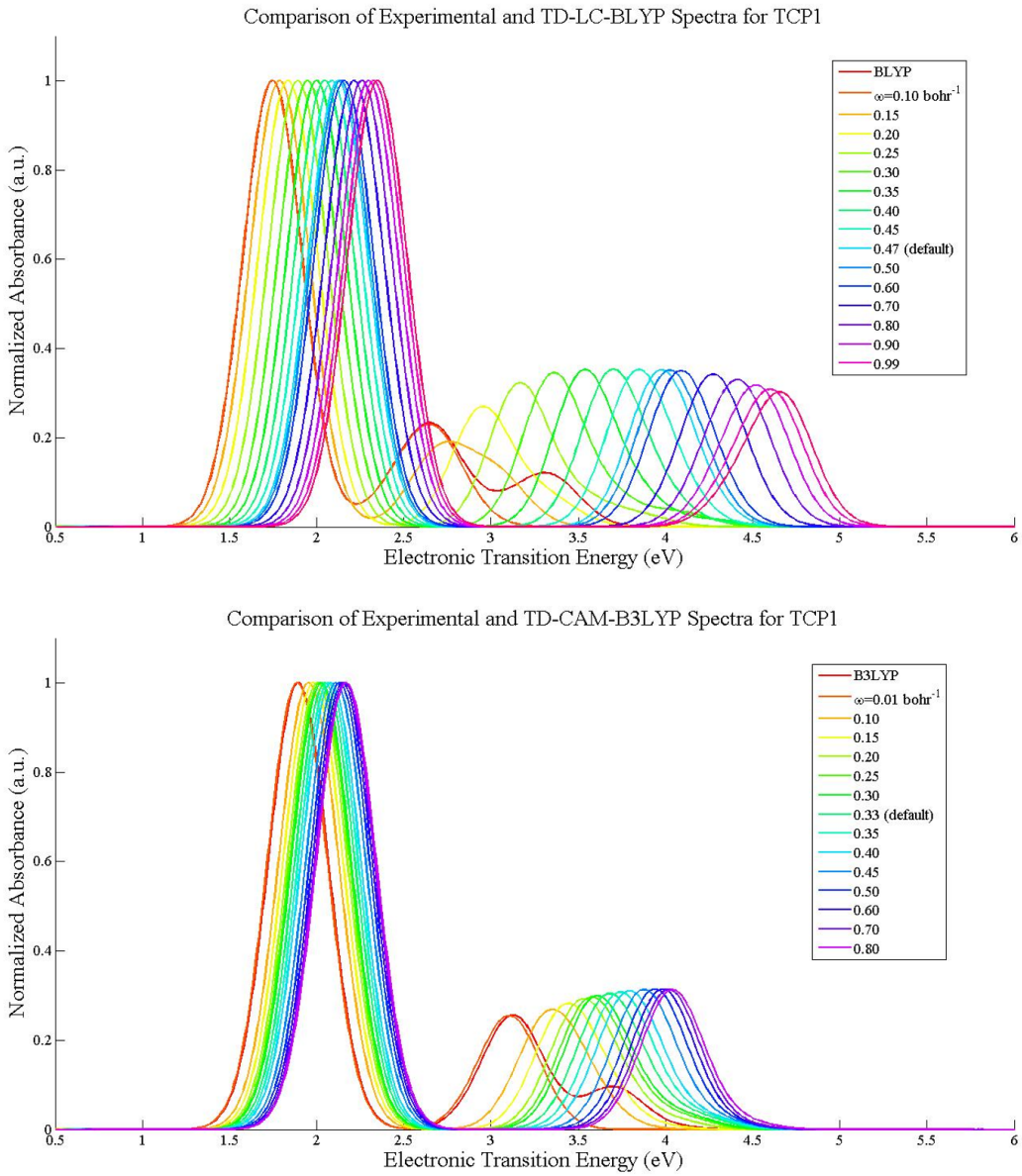

Figure A.36: **Comparison of Absorbance Spectra computed with TD-DFT and experimental UVv-is measurement for molecule TCP1.** Raw UV-vis measurements for TCP1 are not available. A plot of the measured spectrum can be viewed in Ref. [73]. A suitable match for measured λ_{max} (749 nm $\approx$ 1.656 eV) is BLYP or B3LYP.

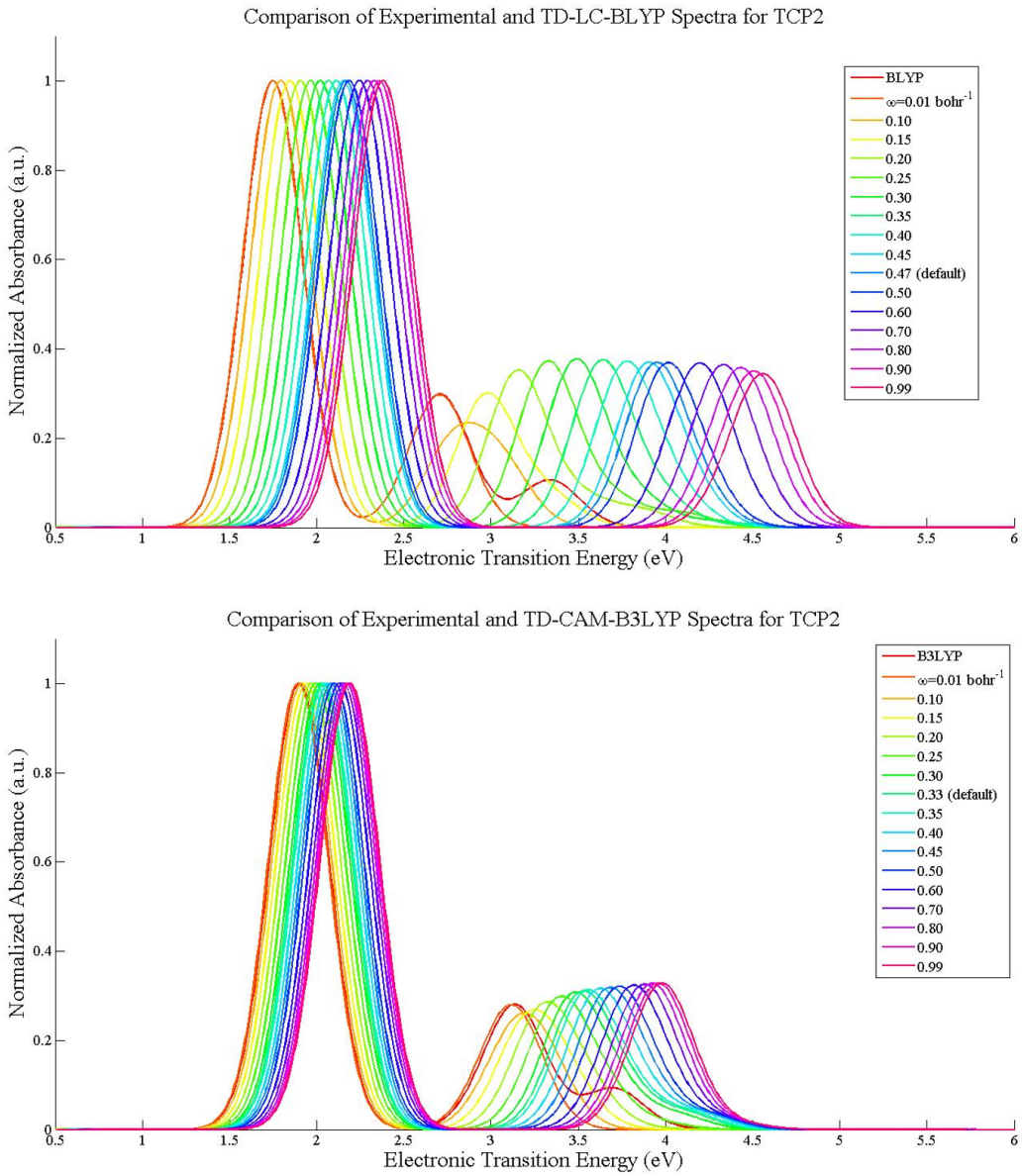

Figure A.37: **Comparison of Absorbance Spectra computed with TD-DFT and experimental UVv-is measurement for molecule TCP2.** Raw UV-vis measurements for TCP2 are not available. A plot of the measured spectrum can be viewed in Ref. [73]. A suitable match for measured λ_{max} (744 nm $\approx$ 1.667 eV) is BLYP or B3LYP.

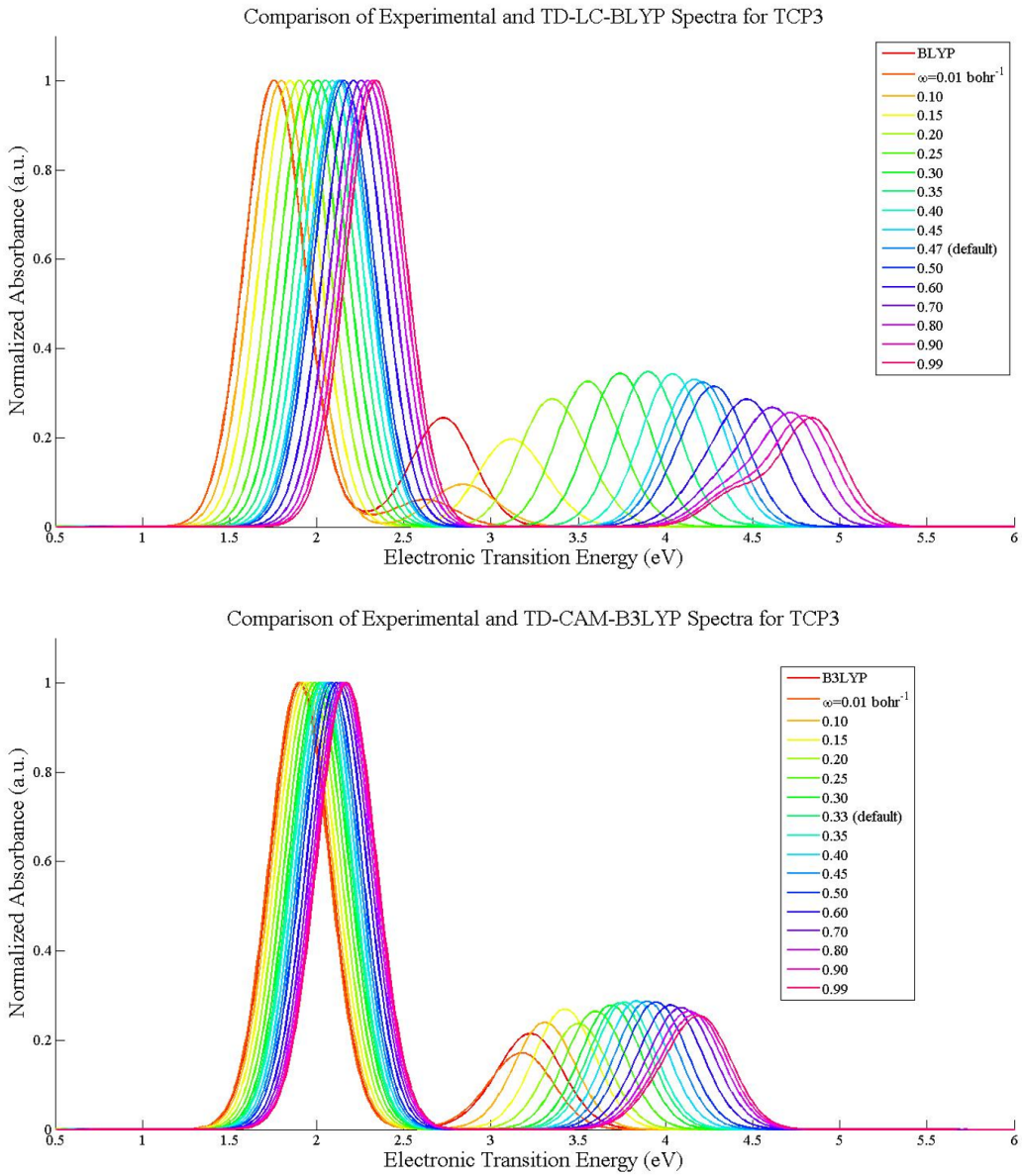

Figure A.38: **Comparison of Absorbance Spectra computed with TD-DFT and experimental UVv-is measurement for molecule TCP3.** Raw UV-vis measurements for TCP3 are not available. A plot of the measured spectrum can be viewed in Ref. [73]. A suitable match for measured λ_{max} (758 nm $\approx$ 1.636 eV) is BLYP or B3LYP.

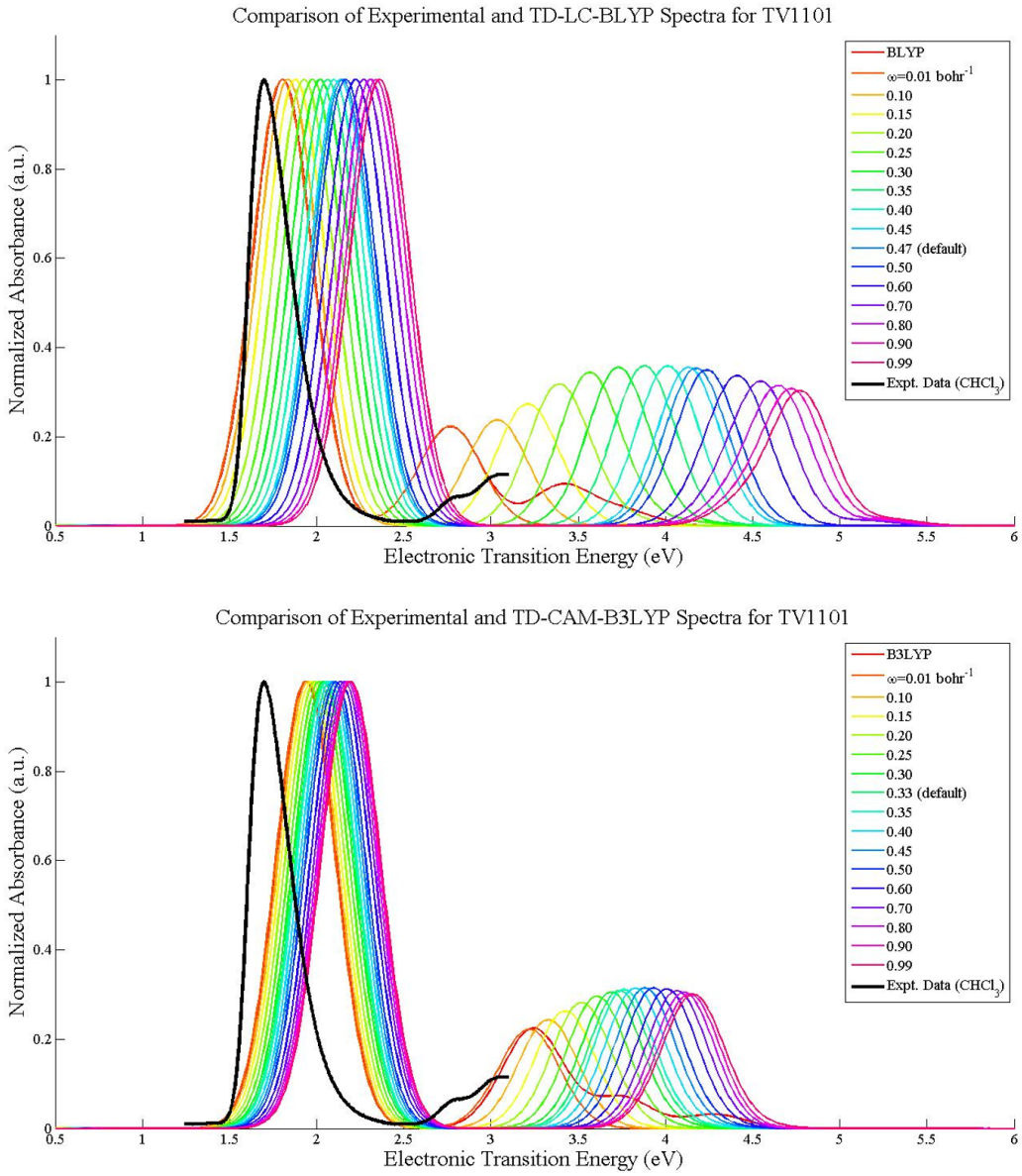

Figure A.39: **Comparison of Absorbance Spectra computed with TD-DFT and experimental UVv-is measurement for molecule TV1-101.** The ideal match for λ_{max} is BLYP or B3LYP. Raw UV-vis data provided by Dr. Denise Bale.

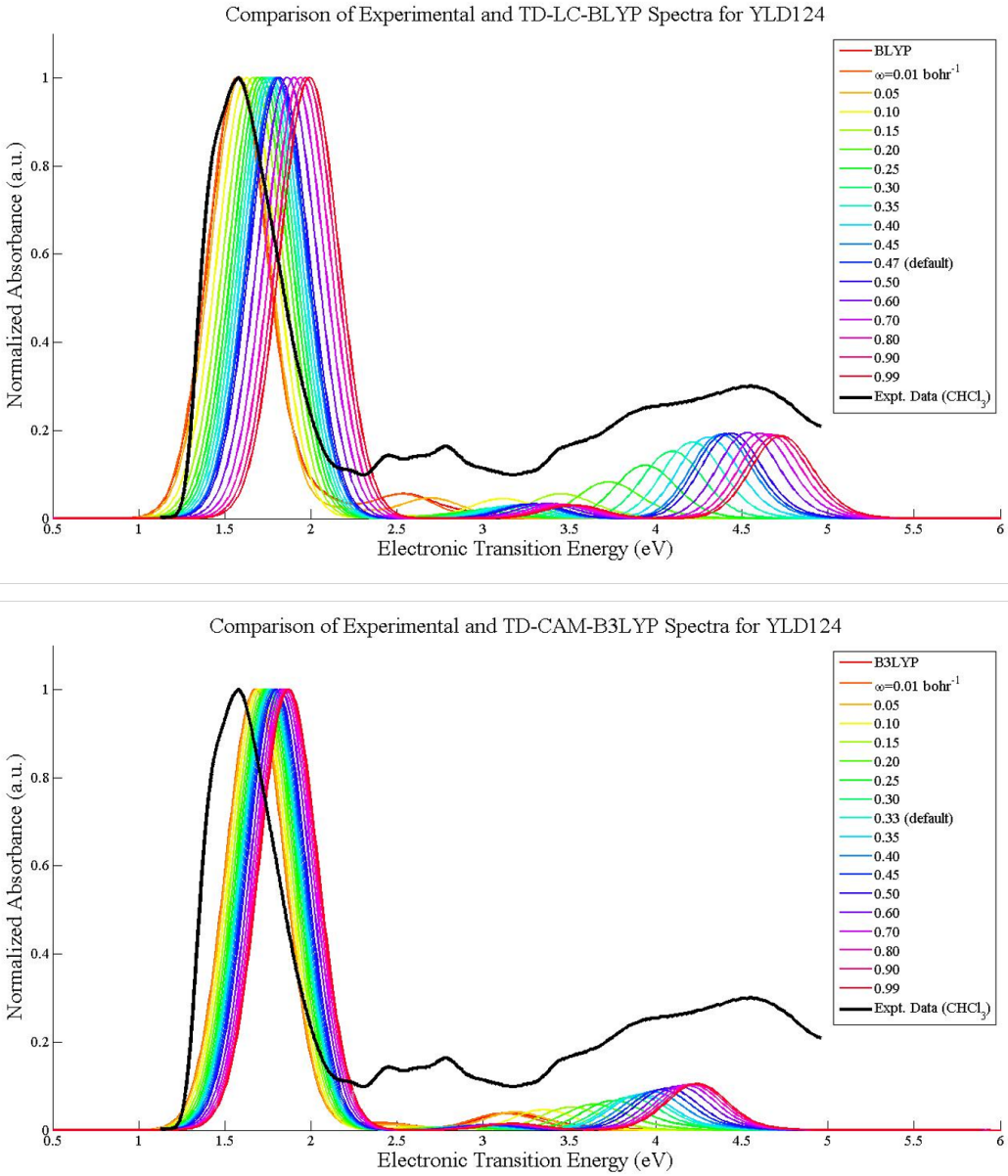

Figure A.40: **Comparison of Absorbance Spectra computed with TD-DFT and experimental UVv-is measurement for molecule YLD124.** The ideal match for λ_{max} is BLYP or B3LYP. Raw UV-vis data provided by Dr. Denise Bale.

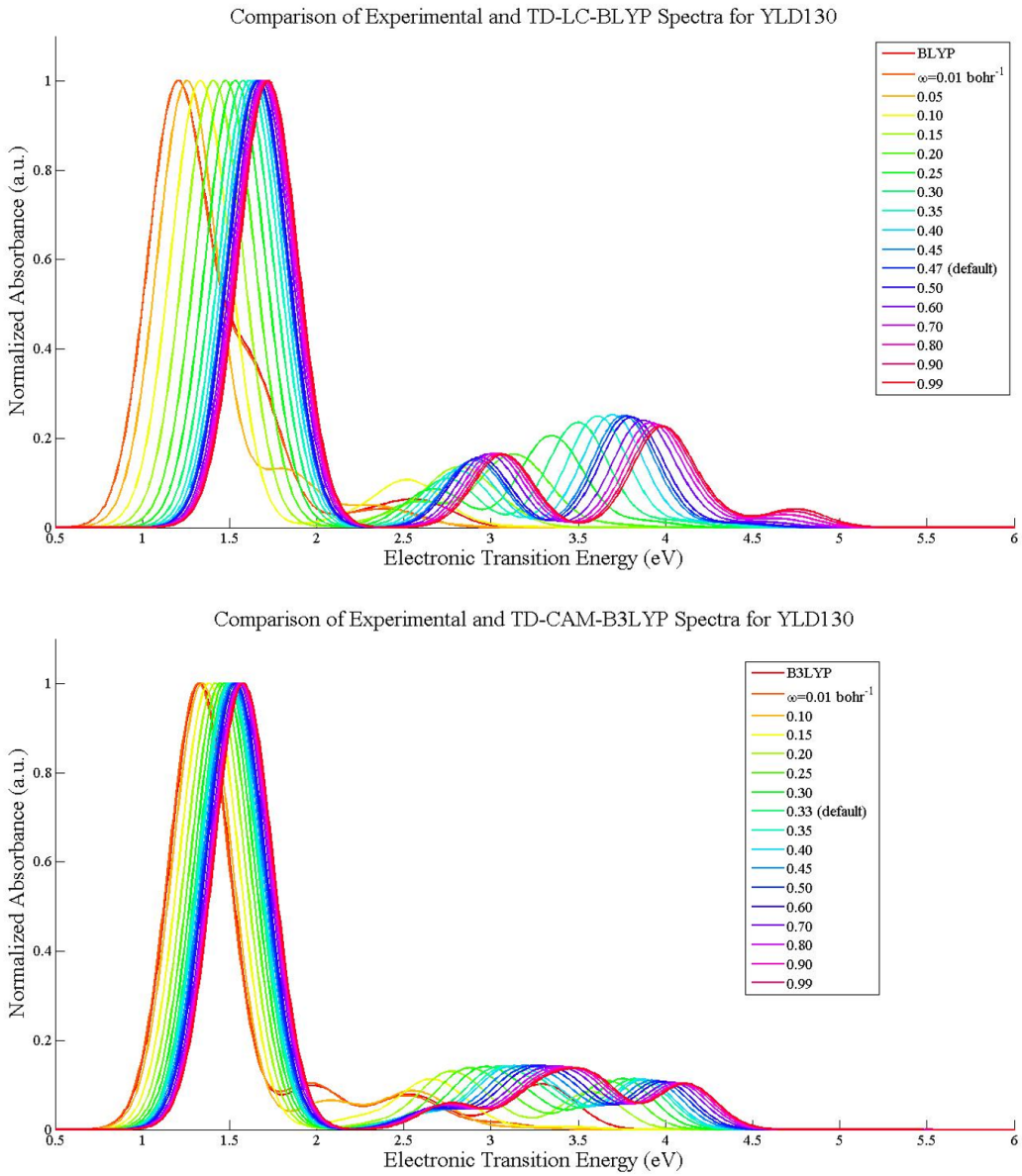

Figure A.41: **Comparison of Absorbance Spectra computed with TD-DFT and experimental UVv-is measurement for molecule YLD130.** Raw UV-vis measurements for TCP2 are not available. A plot of the measured spectrum can be viewed in Ref. [73]. A suitable match for measured λ_{max} (817 nm $\approx$ 1.518 eV) is $\omega = 0.15 - 0.25 bohr^{-1}$ in LC-BLYP or CAM-B3LYP.

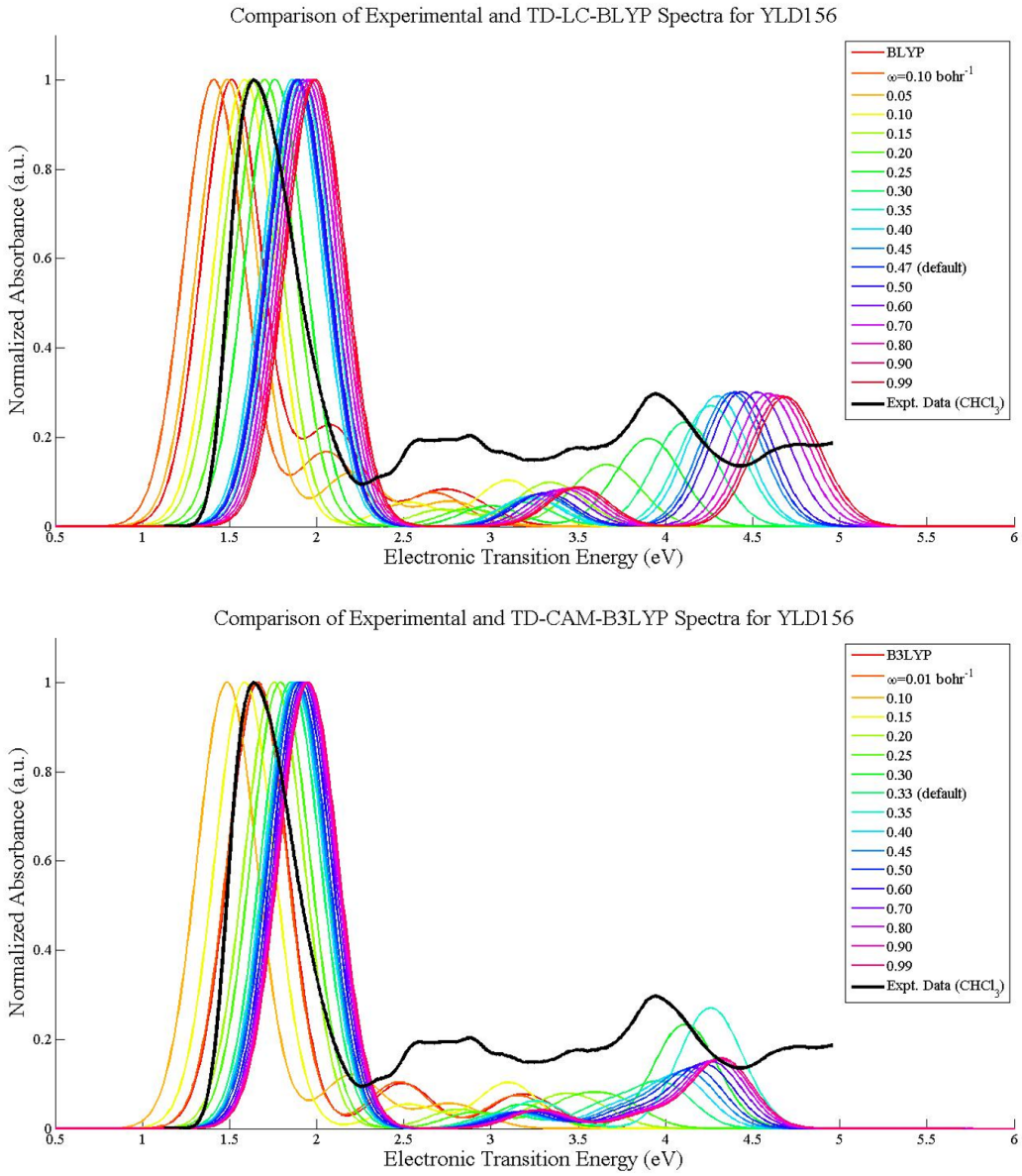

Figure A.42: **Comparison of Absorbance Spectra computed with TD-DFT and experimental UVv-is measurement for molecule YLD156.** The ideal match for λ_{max} is $\omega = 0.10 - 0.15\ bohr^{-1}$ in LC-BLYP or CAM-B3LYP Raw UV-vis data provided by Dr. Denise Bale.

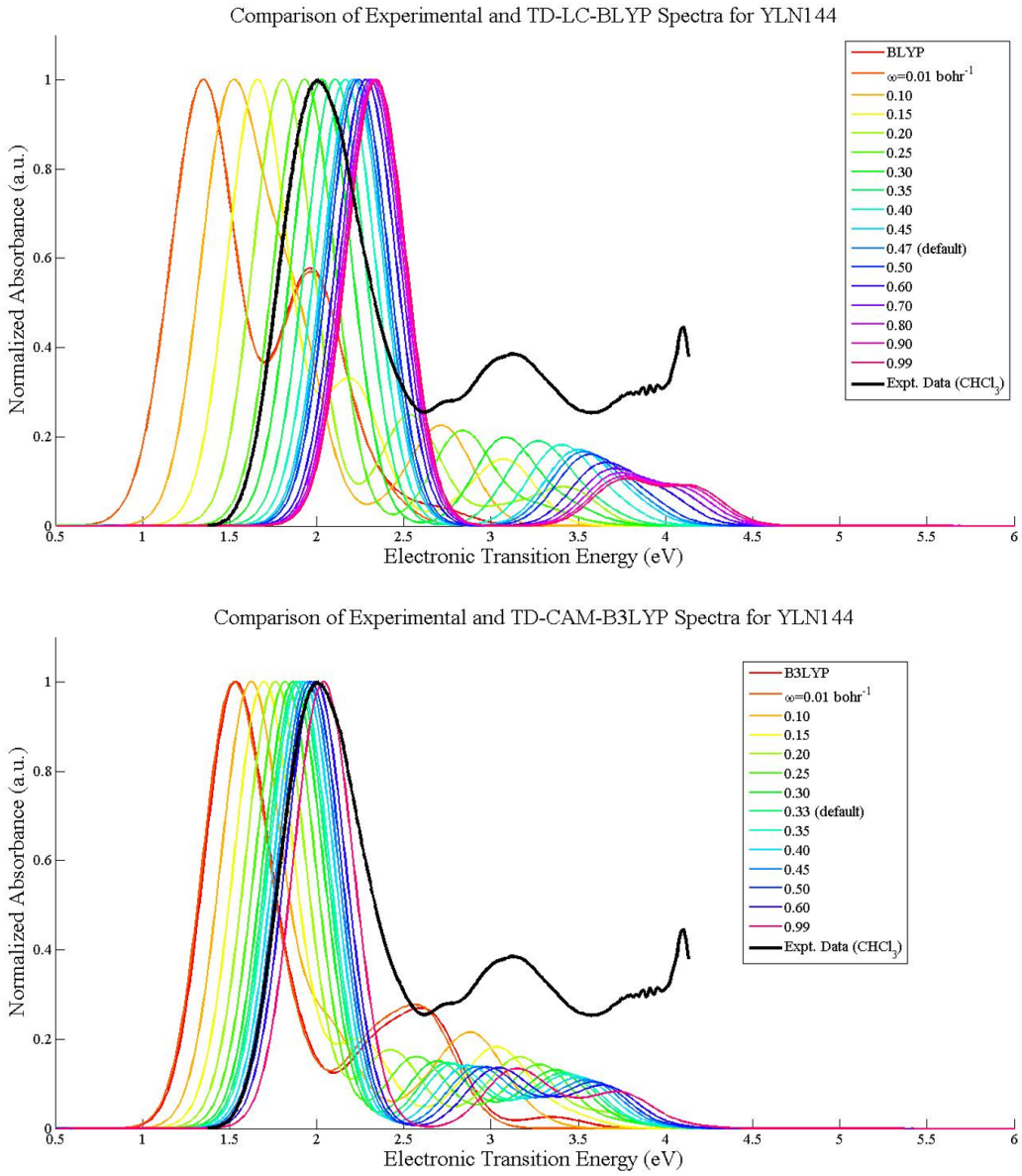

Figure A.43: **Comparison of Absorbance Spectra computed with TD-DFT and experimental UVv-is measurement for molecule YLN144.** The ideal match for λ_{max} is $\omega = 0.25 - 0.30\ bohr^{-1}$ in LC-BLYP or CAM-B3LYP Raw UV-vis data provided by Dr. Denise Bale.

Appendix B

CHAPTER 3 SUPPORTING INFORMATION

B.1 Orbital Energies in Vacuo

Ground state energies, E_{gs}, as well as HOMO and LUMO energies (ϵ_{HOMO} and ϵ_{LUMO}, respectively) were computed in vacuum for neutral and charged species of each of the benchmarks (Table 3.1) using long-range corrected (LC) and range-separated hybrid (RSH) DFT. Plots of the orbital energies with varying long-range Hartree-Fock exchange are shown below.

According to the orbital energies computed using LC-BLYP, shown in Figure B.1, the anion HOMO energy, $\epsilon_{HOMO}(N+1)$, which is used in the calculation of J_{EA} in Equation 3.2, and the neutral LUMO energy, $\epsilon_{LUMO}(N)$, behave very differently over the energy range -0.150 to -0.050 hartrees. The $\epsilon_{LUMO}(N)$ energies span a smaller range than $\epsilon_{HOMO}(N+1)$ and are less discretized with respect to each molecule; also, the $\epsilon_{LUMO}(N)$ energies increase with increasing ω, opposite the trend of $\epsilon_{HOMO}(N+1)$. Depending on the molecular system, the $\epsilon_{HOMO}(N)$ energies are approximately 0.118 - 0.202 hartrees (3.2 - 5.5 eV) lower than the $\epsilon_{HOMO}(N+1)$ energies. Interestingly, this energy gap between neutral and anionic HOMO energies stays generally constant as more HF exchange is added (as ω increases). In comparison, energy gaps based on the difference of neutral HOMO and LUMO energies tend to increase with increasing HF exchange. These general trends in $\epsilon_{HOMO}(N+1)$ and $\epsilon_{LUMO}(N)$ are similar for all of the DFT methods studied here. The results for $\epsilon_{HOMO}(N)$, ϵ_{HOMO}(N+1), and ϵ_{LUMO}(N) for CAM-B3LYP and LC-ωPBE are shown in Figures B.3 and B.2, respectively.

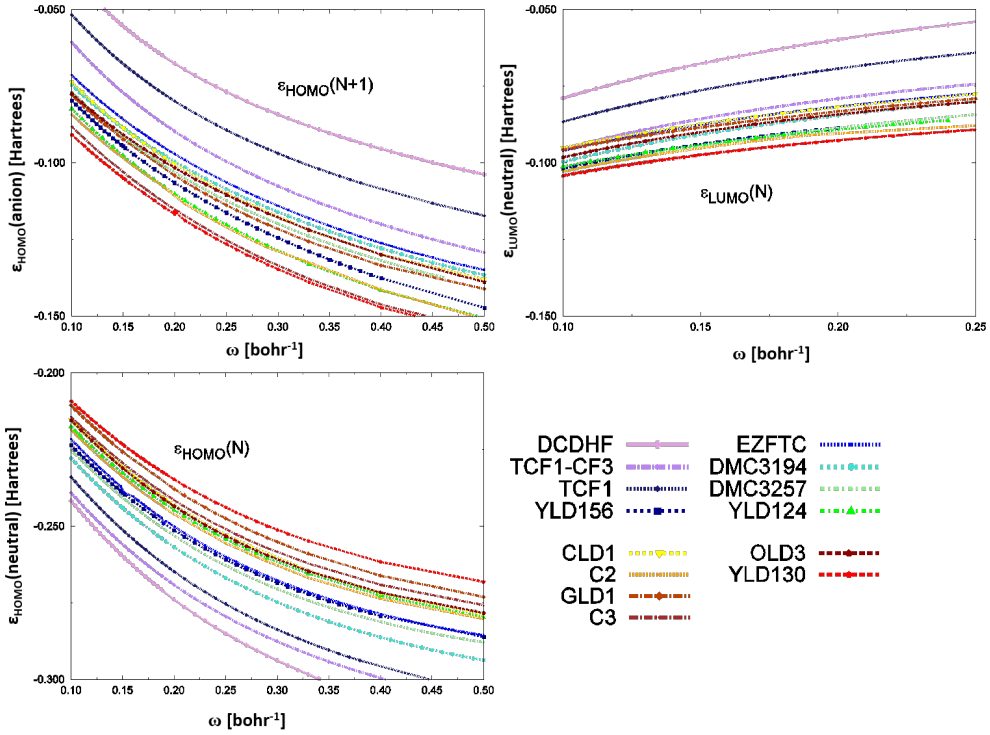

Figure B.1: **Vacuum orbital energies computed using LCBLYP.** Note that ϵ_{HOMO}(N+1) and ϵ_{LUMO}(N) energies span over a similar range, however, the have different trends with respect to ω. Each of the systems of the benchmarking set are colored in order of molecular length, as described in Figure 3.1 and Table 3.1, from shortest D-A length (violet, DCDHF) to longest (bright red, YLD130).

The computed orbital energies in vacuum are similar for LC-BLYP and LC-ωPBE; whereas, the CAM-B3LYP (Equation 2.8) energies are generally larger over the range of LR HF exchange (ω) in comparison with the LC-functionals, as shown in Figure B.4.

As advised in the work by Baer and others [9], $\epsilon_{HOMO}(N+1)$ was used in this work for the calculation of J_{GAP} (Equation 3.3); however, the use of $\epsilon_{LUMO}(N)$ for computing various molecular properties (namely, EA and energy gaps) is more common. We revisit the use of $\epsilon_{HOMO}(N+1)$ versus $\epsilon_{LUMO}(N)$ in the computation of J_{GAP} in Section B.5 later in this Supporting Information for Chapter 3.

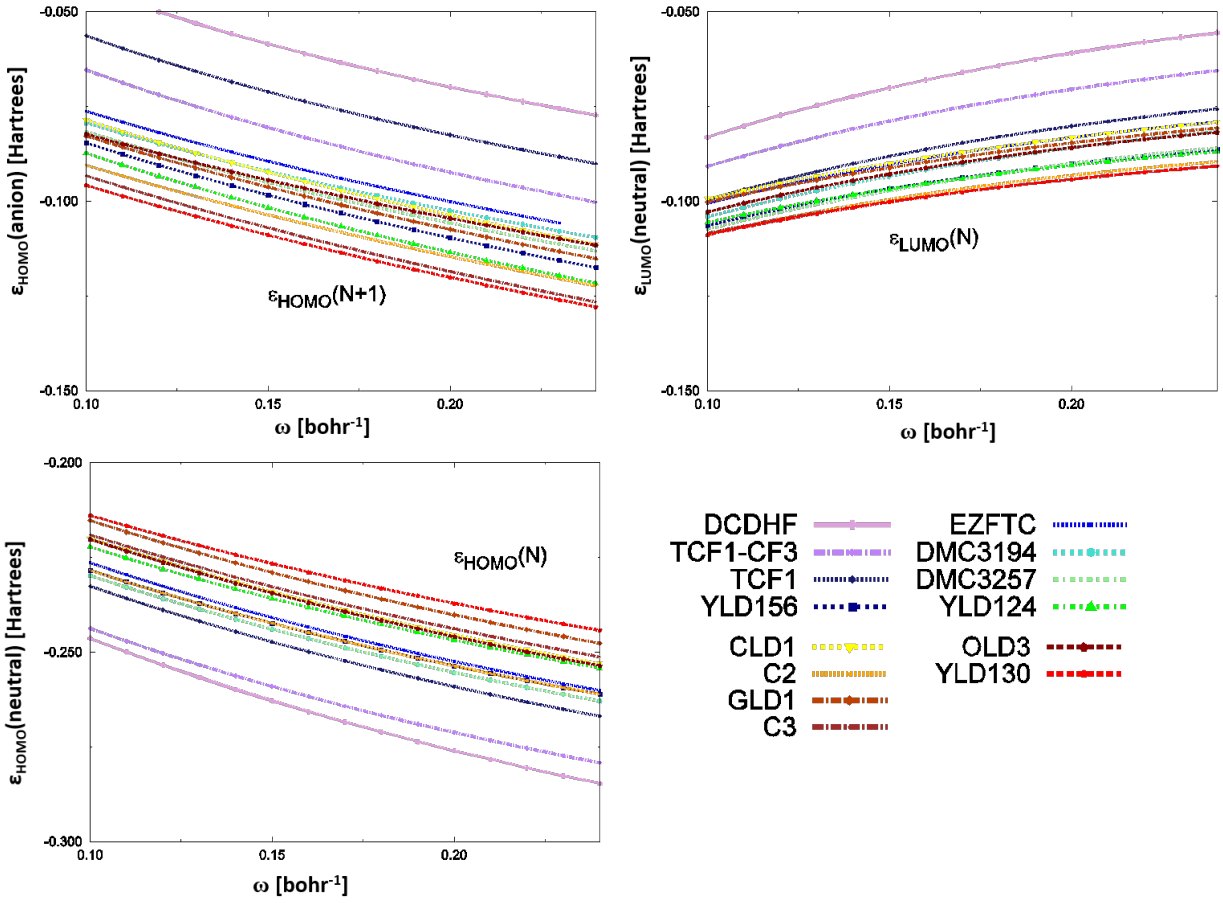

Figure B.2: **LC-ωPBE/6-31+G* orbital energies in vacuum.**

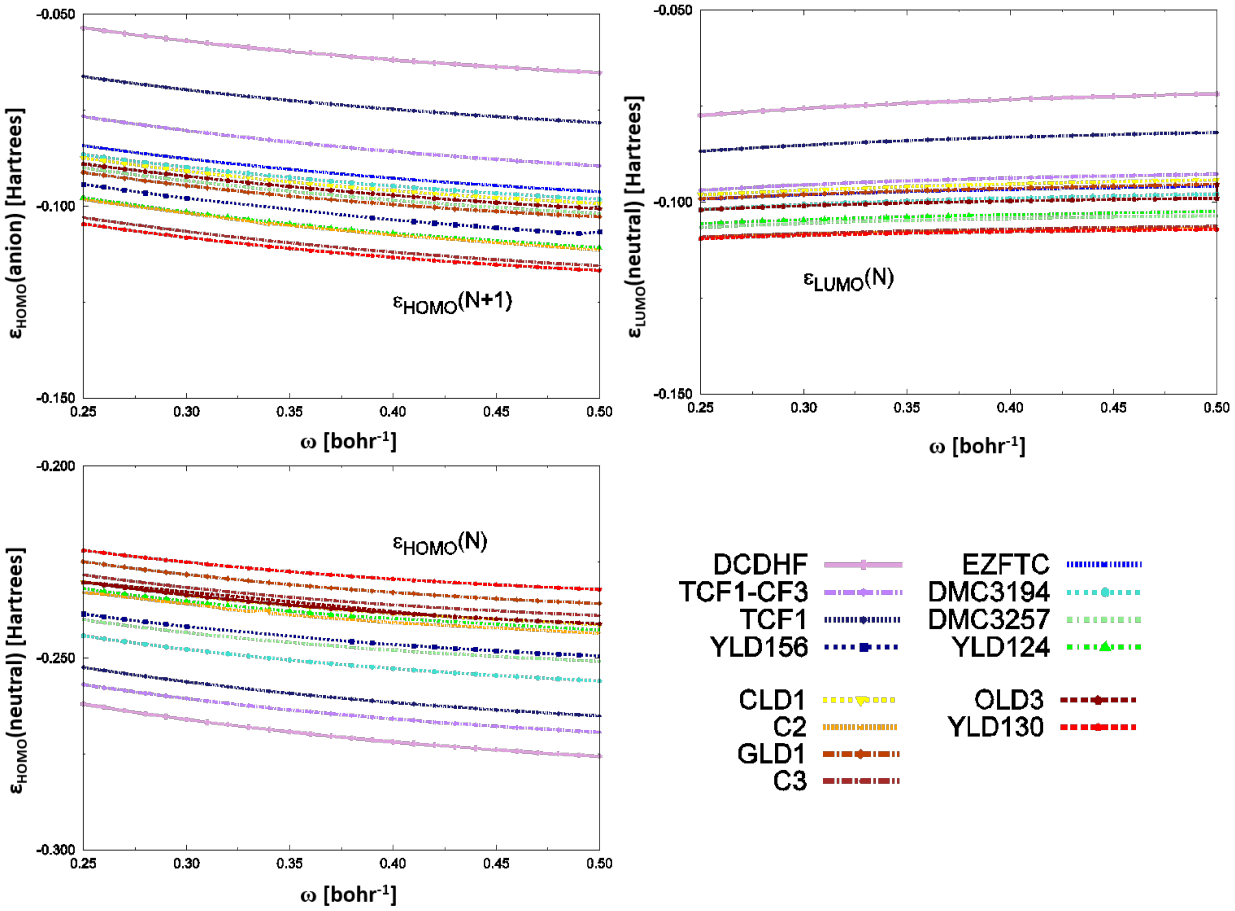

Figure B.3: **CAM-B3LYP/6-31+G* orbital energies in vacuum.**

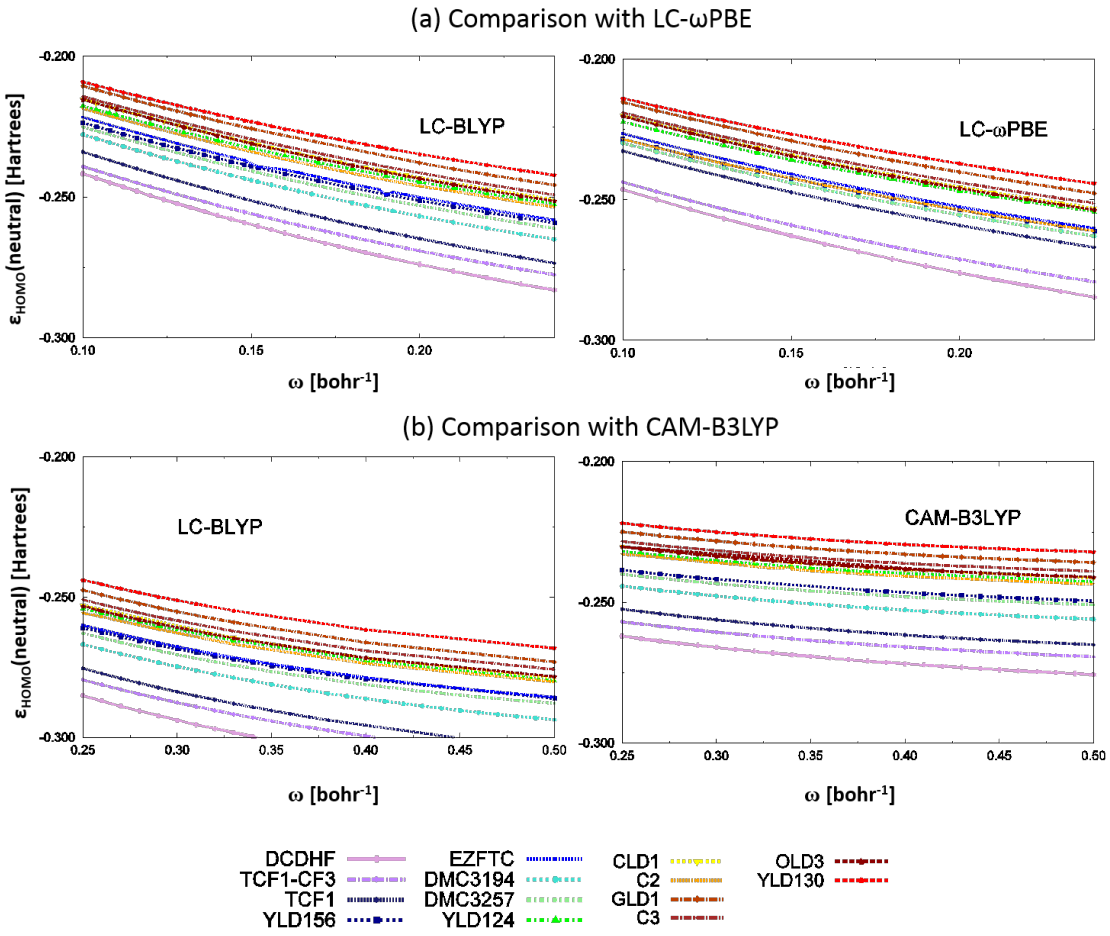

Figure B.4: **Side-by-side comparison of vacuum ϵ_{HOMO} energies computed using different LC/RSH functionals.** (a) LC-BLYP compared with LC-ωPBE; (b) LC-BLYP compared with CAM-B3LYP.

B.2 Koopmans' theorem plots

The following show the results for the optimally-tuned range-separation parameter, ω, according to the J_{GAP}-tuning method (Equation 3.3) for each of the functionals studied, including the results for Equations 3.1 and 3.2 shown in Figures B.5, B.6, and B.7.

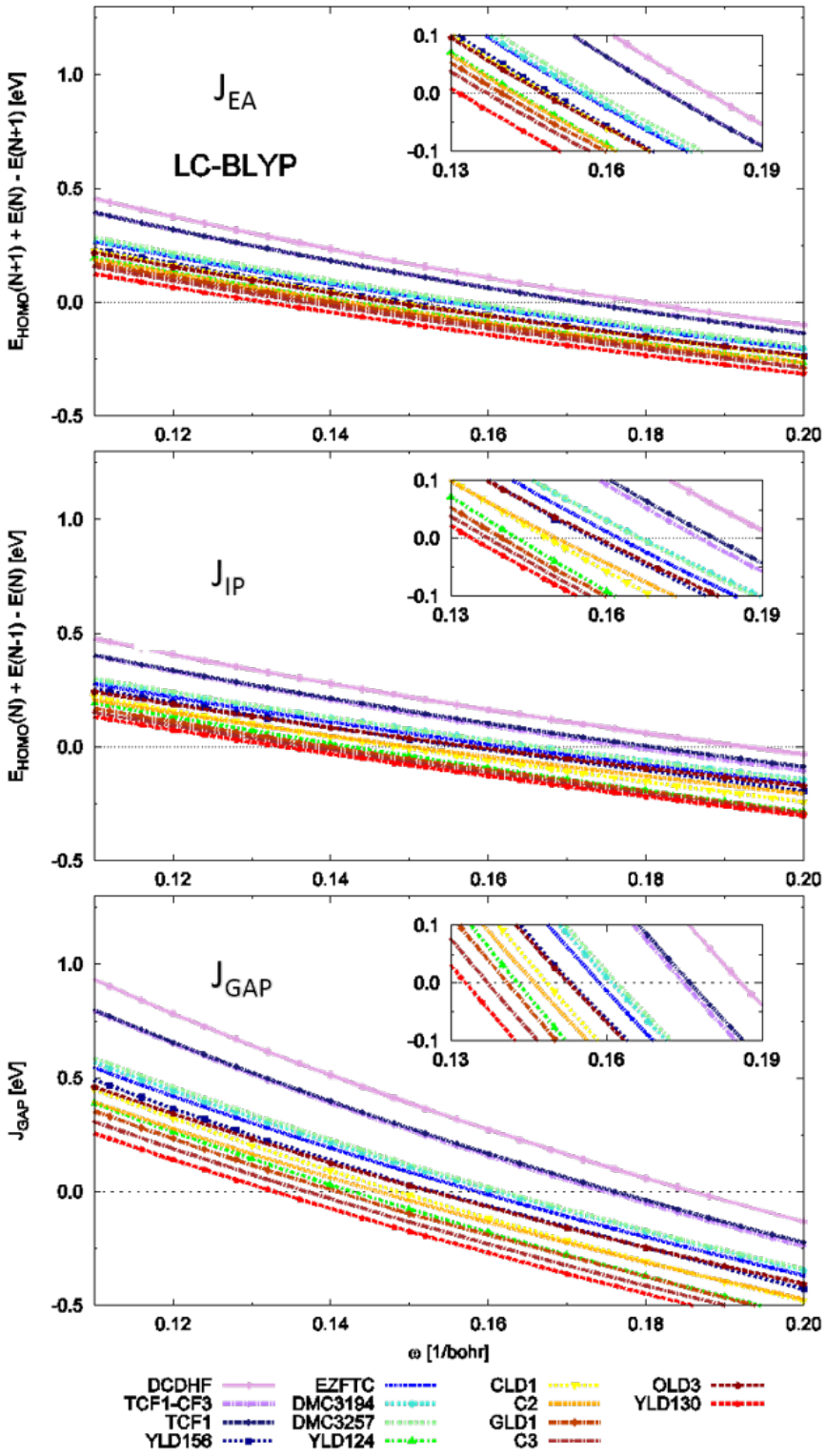

Figure B.5: J_{GAP}**-tuning method results for LC-BLYP:** J_{EA}**,** J_{IP}**, and** J_{GAP}**.**

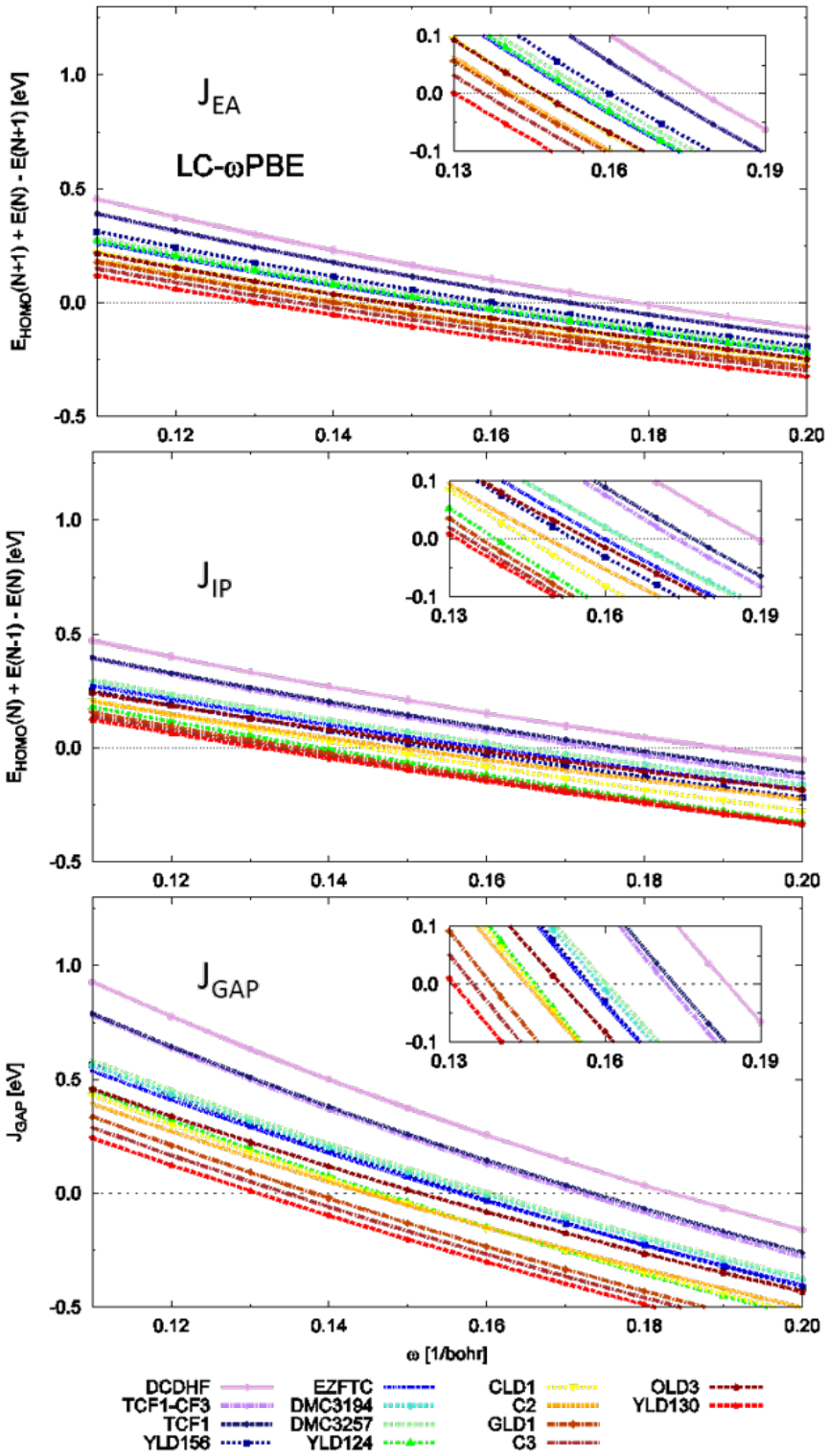

Figure B.6: J_{GAP}**-tuning method results for LC-**ω**PBE:** J_{EA}**,** J_{IP}**, and** J_{GAP}**.**

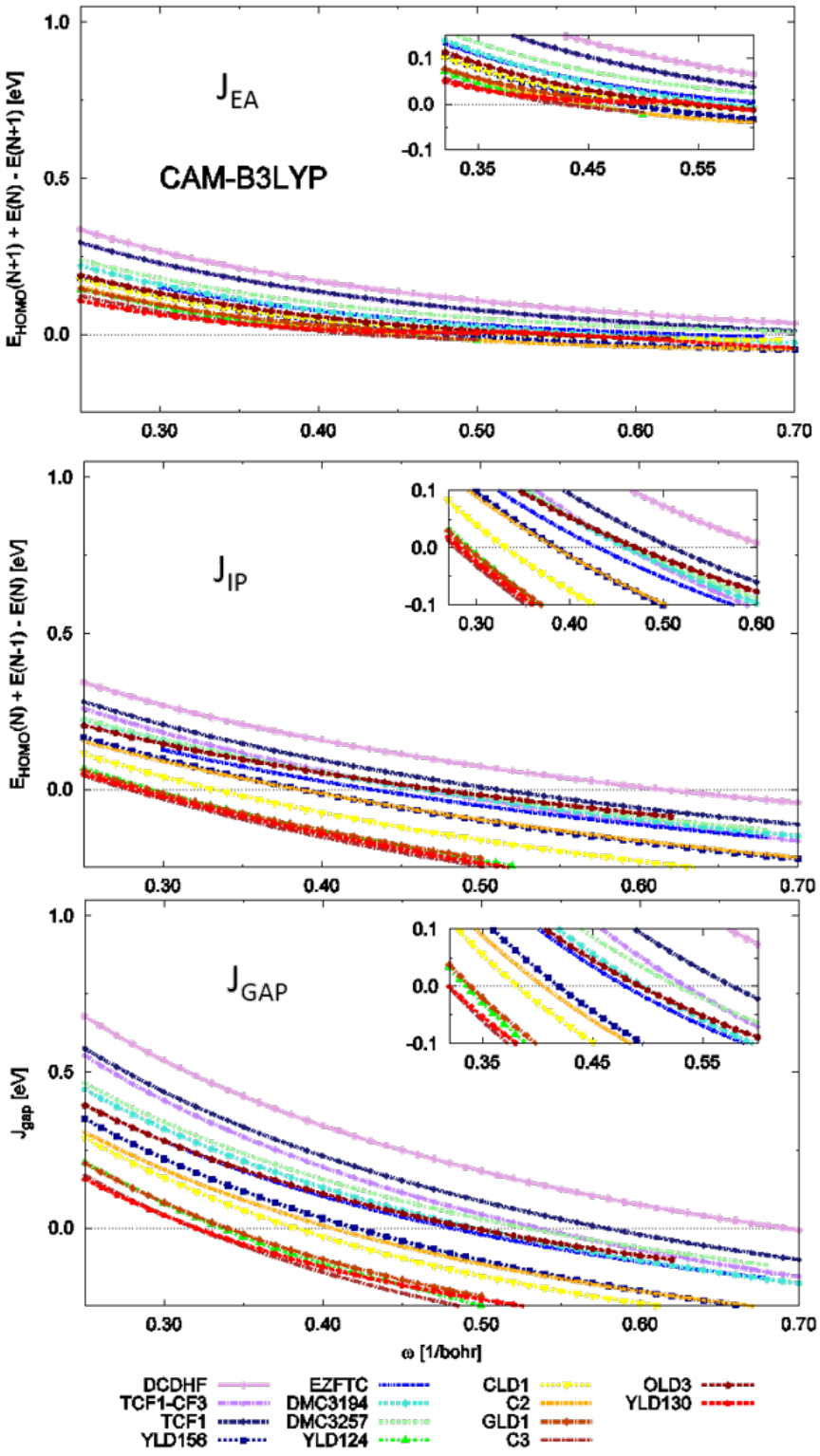

Figure B.7: J_{GAP}**-tuning method results for CAM-B3LYP:** J_{EA}**,** J_{IP}**, and** J_{GAP}**.**

The results of the ω-tuning calculations show a general correlation between molecular length (D-A length) and ω^* for each of the functionals used. A subset of the benchmark set four CLD-type systems which have identical donor (N,N-diethyl-aniline) and acceptor (TCF) units but varying conjugation length (n-units) of the polyene bridge, namely DCDHF (n=0), TCF1 (n=1, monoene), CLD1 (n=4, tetraene), and GLD1 (n=5, pentaene), shows a linear trend in ω^* with D-A length, as shown in Figure B.8. There is also correlation between ω^* and structural trends in bridge-character; namely, the J_{GAP} energy curves are partitioned according to each of the different bridge types in Table 2.1. The short bridge systems have largest predicted optimal ω^* ($\sim$0.18 $bohr^{-1}$, LC-BLYP); the FTC-type systems have moderate values, followed closely by the CLD-type systems ($\sim$0.16 and $\sim$0.14 $bohr^{-1}$, respectively, for LC-BLYP); and the longest system, the "hybrid" bridge YLD130 has the smallest predicted ω^* $\sim$0.13 bohr^{-1}, for LC-BLYP. The results are shown in Figure B.9.

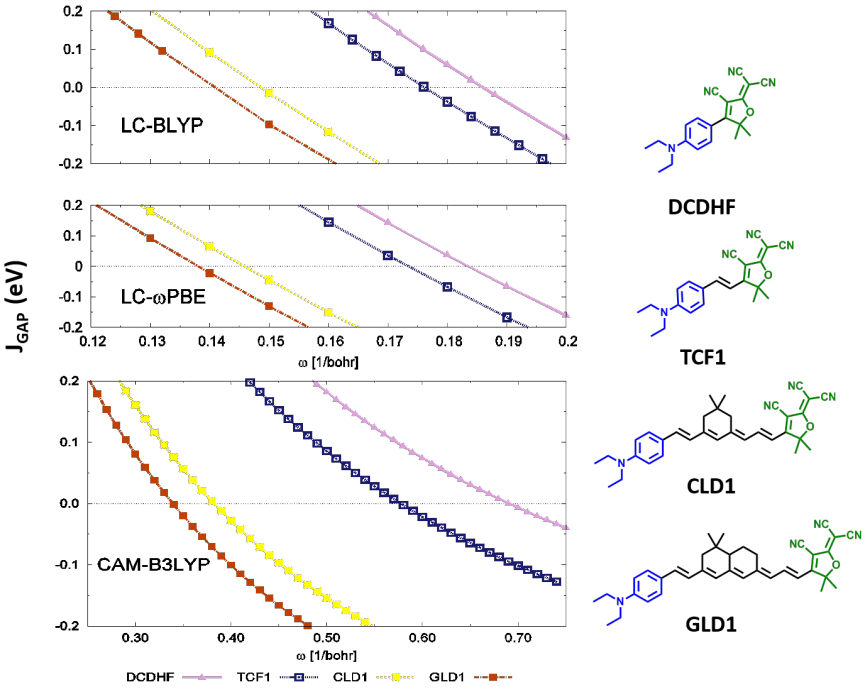

Figure B.8: **J_{GAP}-tuning method results with respect to extended polyene conjugation length.** Increasing conjugation length of the polyene bridge causes the J_{GAP}-tuned optimal range-separation parameter, ω, to shift closer to 0.0 $bohr^{-1}$.

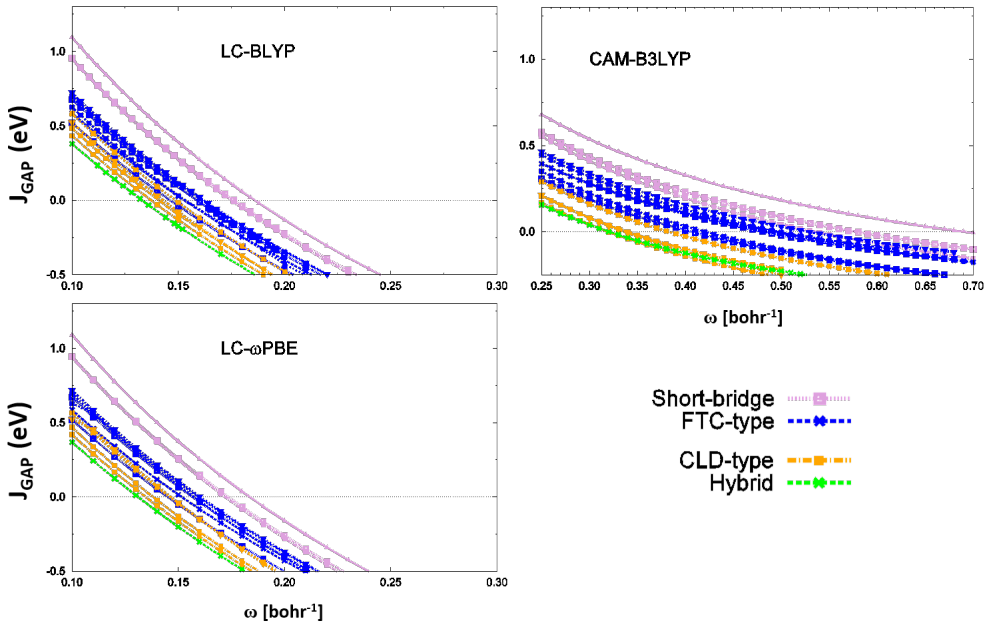

Figure B.9: **Structural Trends in J_{GAP}-tuning results.** Color-coded according to bridge class in Table 3.1; lilac: short-bridge systems (DCDHF, TCF1, TCF1-CF3), blue: FTC-type systems (EZFTC, YLD156, DMC3194, DMC3257, C2, OLD3), orange: CLD-type systems (CLD1, YLD124, GLD1, C3, YLD130), green: hybrid, YLD130. (Note that the abscissa and ordinate scales are customized to fit the data for the CAM-B3LYP plot.)

B.3 Orbital Energies with Solvent Effects

In comparison with vacuum results mentioned in Section 3.3, HOMO and LUMO energies were also computed using DFT in conjunction with solvent effects of a low-dielectric medium (chloroform) using the polarizable continuum model (PCM). Similar to the vacuum results, the behavior of the condensed-phase HOMO energies (ϵ_{HOMO}) are similar for both LC-ωPBE and LC-BLYP; whereas, the ϵ_{HOMO} energies from CAM-B3LYP vary over a wider range than for the LC-functionals. In general, the short-bridge molecules (DCDHF, TCF1, TCF1-CF3) have large energy gaps and the largest molecule (YLD130) has the smallest energy gap, as shown in Figure B.10.

Focusing on the vacuum and PCM orbital energies computed using LC-BLYP, shown in Figures B.1 and B.1 respectively, the $\epsilon_{LUMO}(N)$ values cover a similar energy range for vacuum and PCM calculations, with the PCM energies being only slightly higher ($\sim$0.005 hartrees difference). However, the $\epsilon_{HOMO}(N)$ values considerably change; the PCM neutral HOMO energies span 0.1

hartrees (∼2.72 eV), whereas the vacuum HOMO energies span 0.03 hartrees (∼0.82 eV). In general, the HOMO-LUMO energy differences for PCM are less than those computed in vacuum. For example, the vacuum HOMO-LUMO energy difference for the molecule DCDHF is nearly a factor of 2 greater (0.16 hartrees) versus the PCM HOMO-LUMO energy difference (0.1 hartrees).

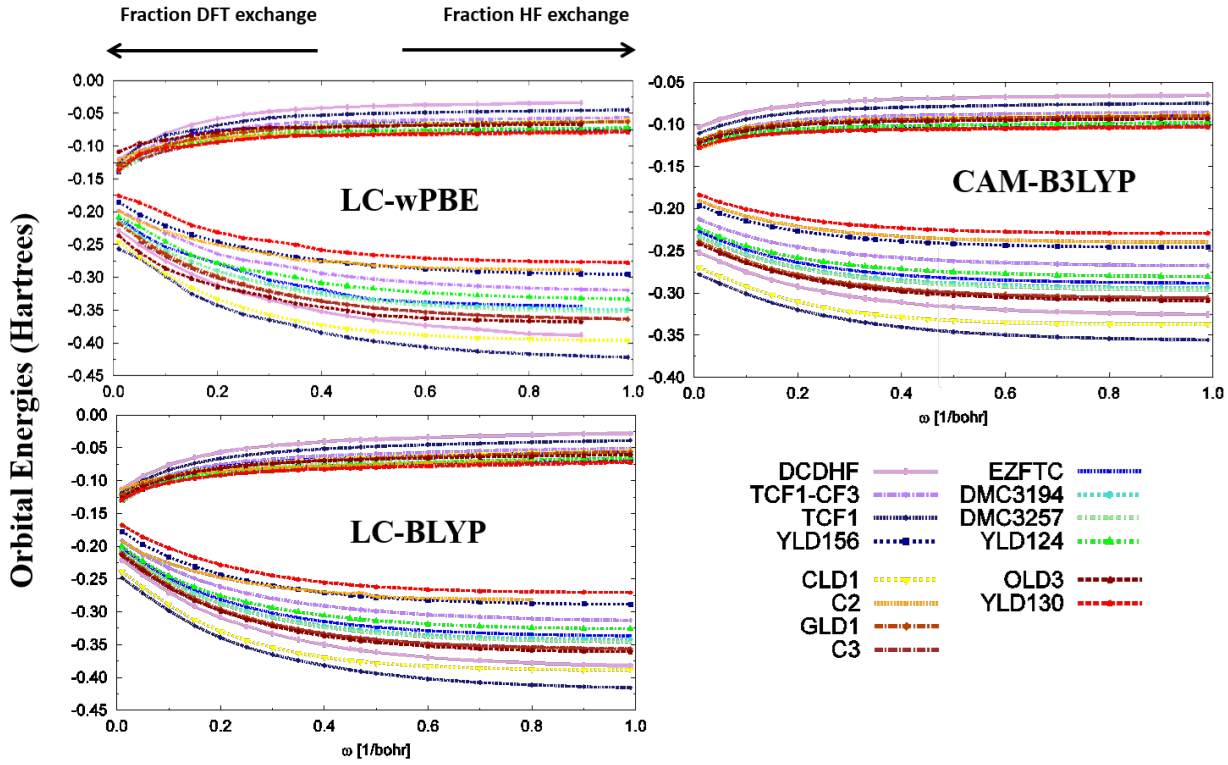

Figure B.10: **Orbital energies (HOMO, bottom; LUMO, top) for the linear-response TD-DFT calculations for LC-ωPBE, LC-BLYP, and CAM-B3LYP with PCM (chloroform) and 6-31+g* basis.** PCM-B3LYP/6-31+G* geometry was used for all calculations. Color scheme is organized according to D-A length as given in Table 2.1, from shortest (violet, DCDHF) to longest (red, YLD130).

B.4 Electronic Transition Energies with Solvent Effects

The ionization potential and electron affinity expressions which the J_{GAP}-optimal tuning method is based on are single-particle events, whereas the vertical excitation energies involve mixing of many single-particle contributions (e.g., HOMO→LUMO, HOMO-1→LUMO+1, etc.). The dom-

inant single particle contribution to the CT band observed in spectra of the D-π-A benchmarks is typically due to a strong $\pi \rightarrow \pi*$ HOMO-LUMO transition. The difference in highest occupied and lowest unoccupied molecular orbital energies, HOMO-LUMO, and the maximum oscillator strength vertical excitation energy for each of D-π-A molecule in the benchmark set are shown in Figure B.11. The general increase in both properties with increasing LR HF exchange shows that the HOMO-LUMO transition contributes to the primary CT transition, however, does not wholly describe this many-particle property as indicated by their nonlinear relationship over the range of ω. In general, as more LR HF exchange is included, the excited states split into more contributions. For example, the lowest energy (and strongest) transition for YLD124 computed with PCM-LCBLYP/6-31+G* is described completely by HOMO$\rightarrow$LUMO (i.e., "163$-$ $>$ 164") and HOMO$\leftarrow$LUMO contributions when ω is 0.01 bohr^{-1}:

```
 Excited State   1:      Singlet-?Sym    1.5698 eV  789.83 nm  f=2.5122  <S**2>=0.000
     163 ->164         0.71382
     163 <-164        -0.16060
```

whereas, for ω=0.99 bohr^{-1}, the first excited state is split into multiple contributions, as follows:

```
 Excited State   1:      Singlet-?Sym    1.9904 eV  622.90 nm  f=2.9551  <S**2>=0.000
     161 ->164        -0.10416
     162 ->164        -0.17121
     162 ->165         0.17574
     163 ->164         0.63782
```

The excited state properties of the other benchmark molecules behave similarly. It is no surprise that many published articles based on the J_{GAP}-optimal tuning method have applied it to predicting fundamental energy gaps (i.e., HOMO-LUMO energy differences), which produced favorable results [9], [145]. Based on this discussion, extending this method to the prediction of vertical excitation energies, especially with increasing amount of LR HF exchange (ω $>$0.15 bohr^{-1}), may not be as successful.

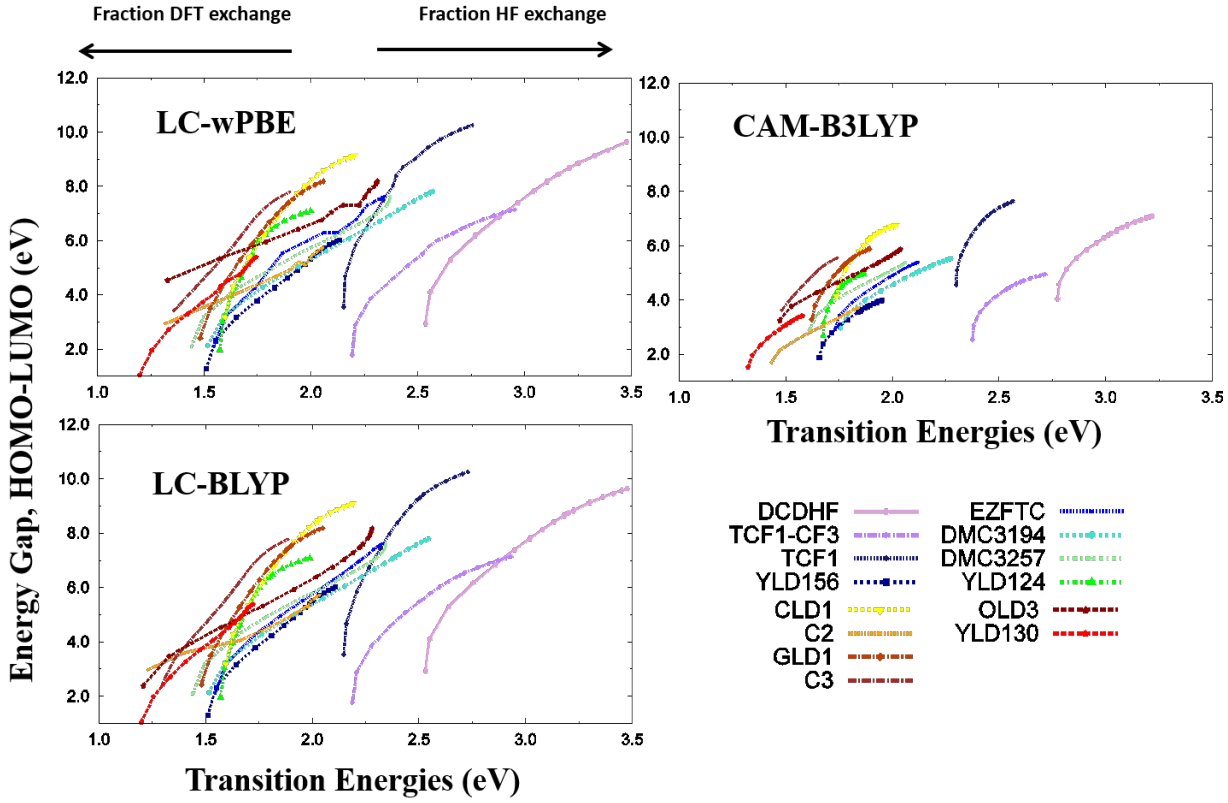

Figure B.11: **HOMO-LUMO energy gap versus Lowest Transition Energy (eV) for the linear-response TD-DFT calculations for LC-ωPBE, LC-BLYP, and CAM-B3LYP with PCM (chloroform) and 6-31+g* basis.** PCM-B3LYP/6-31+G* geometry was used for all calculations. Color scheme is organized according to D-A length (i.e., donor-acceptor length) as given in Table 3.1, from shortest (violet, DCDHF) to longest (red, YLD130).

B.5 Revisted: J_{GAP}-optimal tuning method

For the computation of J_{GAP}, we have applied the IP tuning to the anion ($N+1$ electron) system in Equation 3.2. Here we briefly investigate the effect of using $\epsilon_{LUMO}(N)$ in place of $\epsilon_{HOMO}(N+1)$ in Equation 3.2. For clarity, we focus on the results of only one of the benchmarks, DCDHF. As Figure B.12 illustrates, the result for J_{GAP} is dominated by the difference between $\epsilon_{HOMO}(N)$ and the IP of the neutral species, i.e. J_{IP} (Equation 3.1). Thus, the use of $\epsilon_{LUMO}(N)$ in place of $\epsilon_{HOMO}(N+1)$ for the calculation of J_{EA} is practically negligible for the calculation of J_{GAP}. This

has been reported elsewhere in the literature and is attributed to a minimization of the derivative discontinuity in the exchange functional [166].

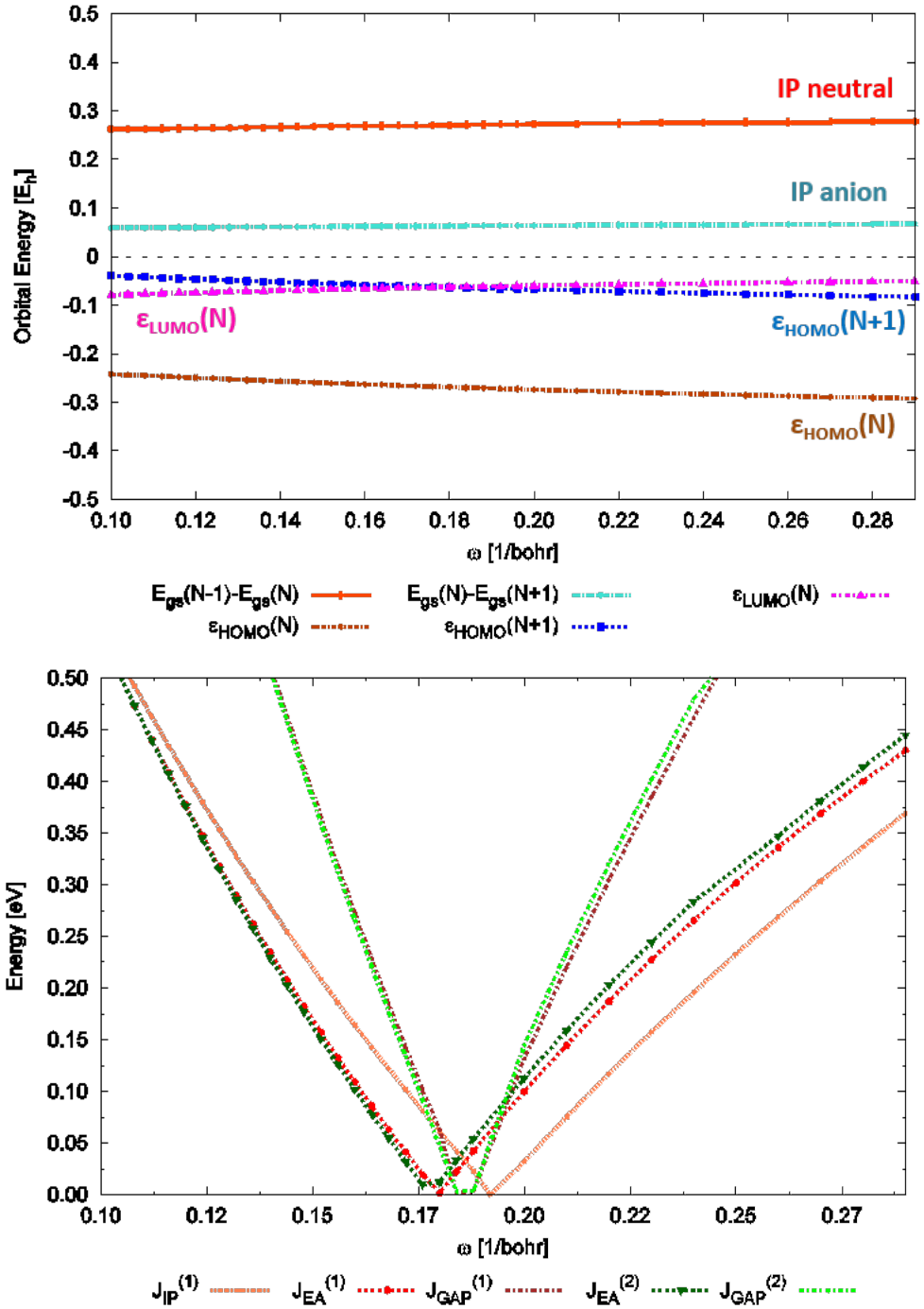

Figure B.12: **Use of $\epsilon_{LUMO}(N)$ in J_{EA}.** The change in J_{EA} using either $\epsilon_{LUMO}(N)$ or $\epsilon_{HOMO}(N+1)$ is negligible. Thus J_{IP} is a reasonable estimate of J_{GAP}.

Appendix C

CHAPTER 4 SUPPORTING INFORMATION

C.1 Hyperpolarizability trends for the various oligomers of the small molecule, DCDHF

The monomer geometry of DCDHF (see Table 2.1 for structure) was provided by crystallographic data collected by Peter Johnston and Dr. Werner Kaminsky of University of Washington [121]. The monomers were stacked in configurations analogous to the 'head-to-tail', 'π-stacked', and 'stair' configurations used to study YLD124. The number of DCDHF monomers per configuration range from 1 to 8. The molecular axis of the DCDHF monomer is taken to lie along the x axis with the y axis lying in the same plane perpendicular to x, as shown in Figure C.1. In the π-stacked arrangement the monomers are separated by 10 $\mathring{A}$ along the z axis. In the stair configuration, each monomer is separated by 6 $\mathring{A}$ along the z axis and shifted by 6 $\mathring{A}$ along the x axis relative to the previous monomer unit. For the head-to-tail arrangment, the center-to-center distance between each monomer is 17 $\mathring{A}$.

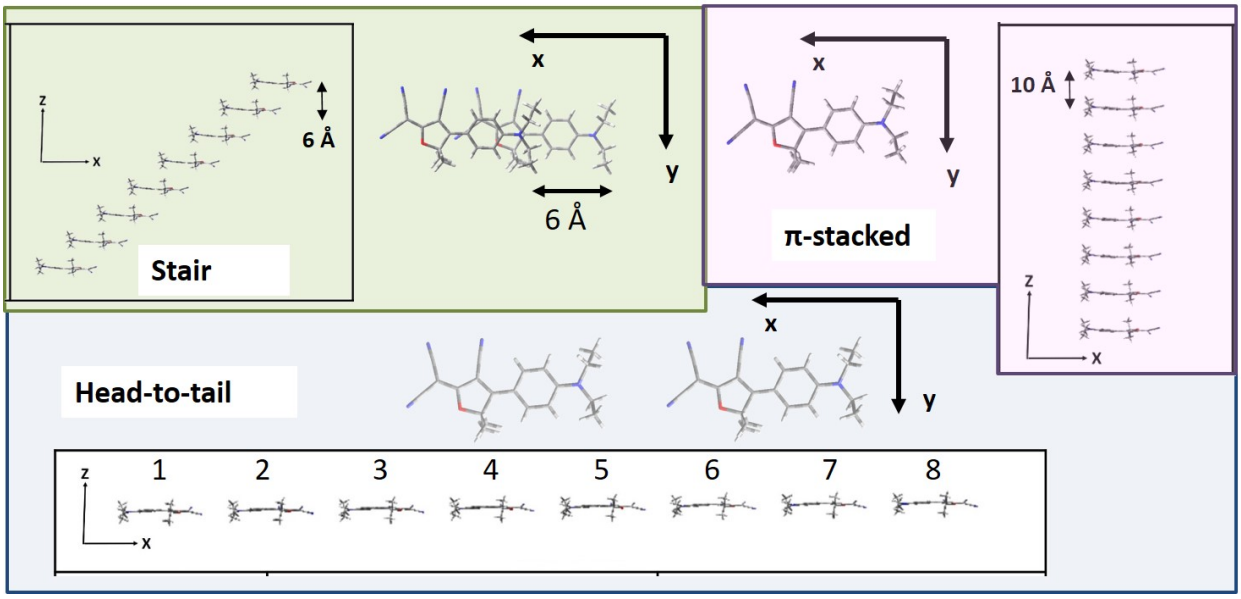

Figure C.1: **Generated Stacking Configurations of Interest for DCDHF oligomers.**

The frequency-dependent hyperpolarizability, $\beta_{zzz}(-\omega;\omega,0)$, was computed using wB97xD/6-31+G* in vacuum for each stacking type and plotted in Figure C.2. Similar to the YLD124 results in Figure 4.9, all but the head-to-tail arrangement result in less than an *additive effect* in the isolated molecule β modeled by the black line $n \times \beta_{monomer}$, where n is the number of molecules. The head-to-tail arrangement scales as $\beta_n^{head-to-tail} \approx 1.81 \times n\beta_{monomer} - 24.1$ with an R^2 fit of 0.9997. Therefore, the head-to-tail arrangement effectively increases each monomer β by 180% compared to the additive model. Also like the YLD124 data, the 'stair' arrangement of DCDHF is similar to the additive model and scales like $\beta_n^{stair} \approx 0.88 \times n\beta_{monomer} - 1.02$ with an R^2 fit of 0.9996 and is, thus, closest to the additive model. Like YLD124, the π-stacked arrangement in DCDHF reduces hyperpolarizability and scales like $\beta_n^{\pi-stack} \approx 0.63 \times n\beta_{monomer} + 10.2$ with an R^2 fit of 0.9999 (recall that $\beta_n^{\pi-stack} \approx 0.36 \times n\beta_{monomer}$). The difference in scaling may be attributed to each monomer in the DCDHF stack being 10 $\mathring{A}$ apart. As the oligomer size increases, the average contribution to the total hyperpolarizability from each monomer begins to reach a unique asymptotic limit depending on the different stacking types. For example, as the number of molecules increases the hyperpolarizability of each monomer in the head-to-tail arrangement approaches a constant of 1.8×

the hyperpolarizability of the isolated molecule. As the number of molecules increase for the other cases, the β of each monomer approaches a factor of 0.60 to 0.85 that of the isolated molecule depending on stacking type, as shown in Figure C.2. The $\beta_{zzz}(-\omega;\omega,0)$ values for the data shown in Figure C.2 are given in Table C.1.

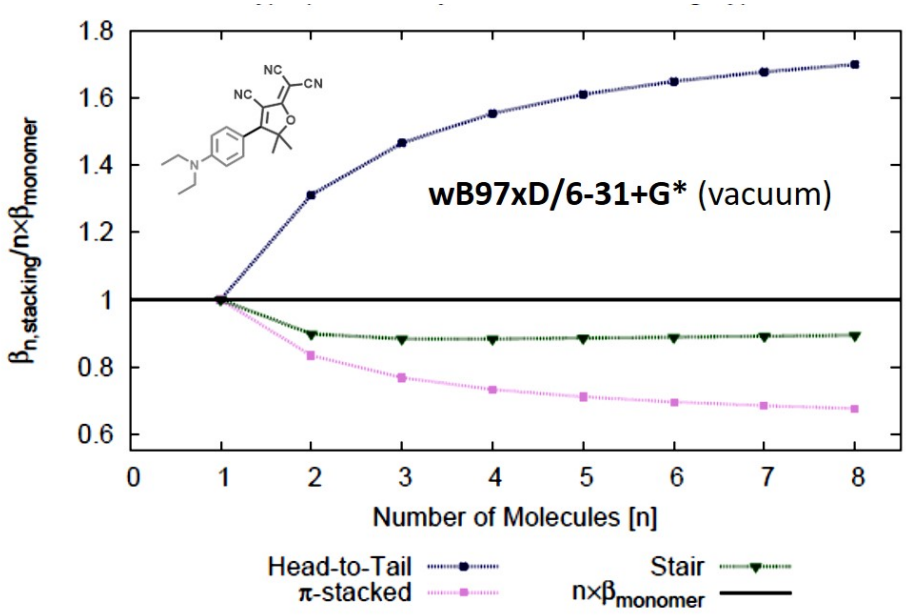

Figure C.2: **Ratio of Pockels $\beta_{zzz}(-\omega;\omega,0)$ of the dimer and trimer configurations with $n \times \beta monomer$.** Comparison of different assemblies of DCDHF oligomers with the additive model, $n \times \beta monomer$, represented by the black line where n is the number of molecules. Shown is the average contribution to the total hyperpolarizability from each monomer in an n-assembly.

Number of Molecules, n	$n \times \beta_{monomer}$	**Head-to-tail**	**π-stacked**	**Stair**
1	25.15			
2	50.30	65.97	41.95	45.19
3	75.45	110.59	57.99	66.72
4	100.60	156.33	73.77	88.89
5	125.75	202.49	89.44	111.41
6	150.89	248.87	105.04	134.14
7	176.04	295.35	120.61	156.99
8	201.19	341.91	136.15	179.93

Table C.1: **Pockels hyperpolarizability, $\beta_{zzz}(-\omega;\omega,0)$, at 1310 nm for different oligomer configurations of DCDHF.**

Frequency-dependent hyperpolarizabilities, $\beta_{zzz}(-\omega;\omega,0)$, were computed according to varying the position between two co-aligned monomers of DCDHF along a translation axis, x, and orbit angle, θ with different width (**w**) and height (**h**) of the arc, as illustrated at the top of Figure C.3. Similar to YLD124, the height/width of the arc was maintained at 10/14 ratio and β calculations were performed on the DCDHF dimers using CPKS method with wB97xD/6-31+G* in vacuum. The resulting contour plot of relative percentage error with the additive model, $2 \times \beta_{monomer}$, is shown in **Panel 2a** of Figure C.3. The height and width of the grid was then contracted by one-third to 6.7/9.3 height-to-width, as shown in **Panel 2b**. Unlike the previous case in which the 10/14 DCDHF dimer reaches its greatest reduction in β when the monomers are nearly eclipsed ($\theta \approx \pi/2$), the hyperpolarizability of the 6.7/9.3 DCDHF dimer is most reduced when the orbit angle approaches 0 or π. However, similar to all cases, the hyperpolarizability of the dimer increases as the monomers are pulled farther apart (< -10 $\mathring{A}$ or > 10 $\mathring{A}$).

Similar contractions of the grid were performed on YLD124 and the small molecule, pNA. Upon reducing the height-to-width of the arc to 8/10, the resulting contour plot for YLD124 experiences

at much as 60% reduction in overall hyperpolarizability (**Panel 1b**). These reductions cannot be explained by a simple dipole-dipole approximation, but rather are likely a result of significant molecular orbital mixing. The pNA molecules described in **Panel 3b** are pushed so close together ($< 3.5\ \mathring{A}$) so as to form mixed HOMO and LUMO structures which results in a non-monotonic change in overall hyperpolarizability as the orbit angle increases from 0 to $\pi/2$. However, when the molecules are far enough apart, the change in hyperpolarizability for YLD124, DCDHF, and pNA are qualitatively similar (**Panels 1a, 2a, and 3a**).

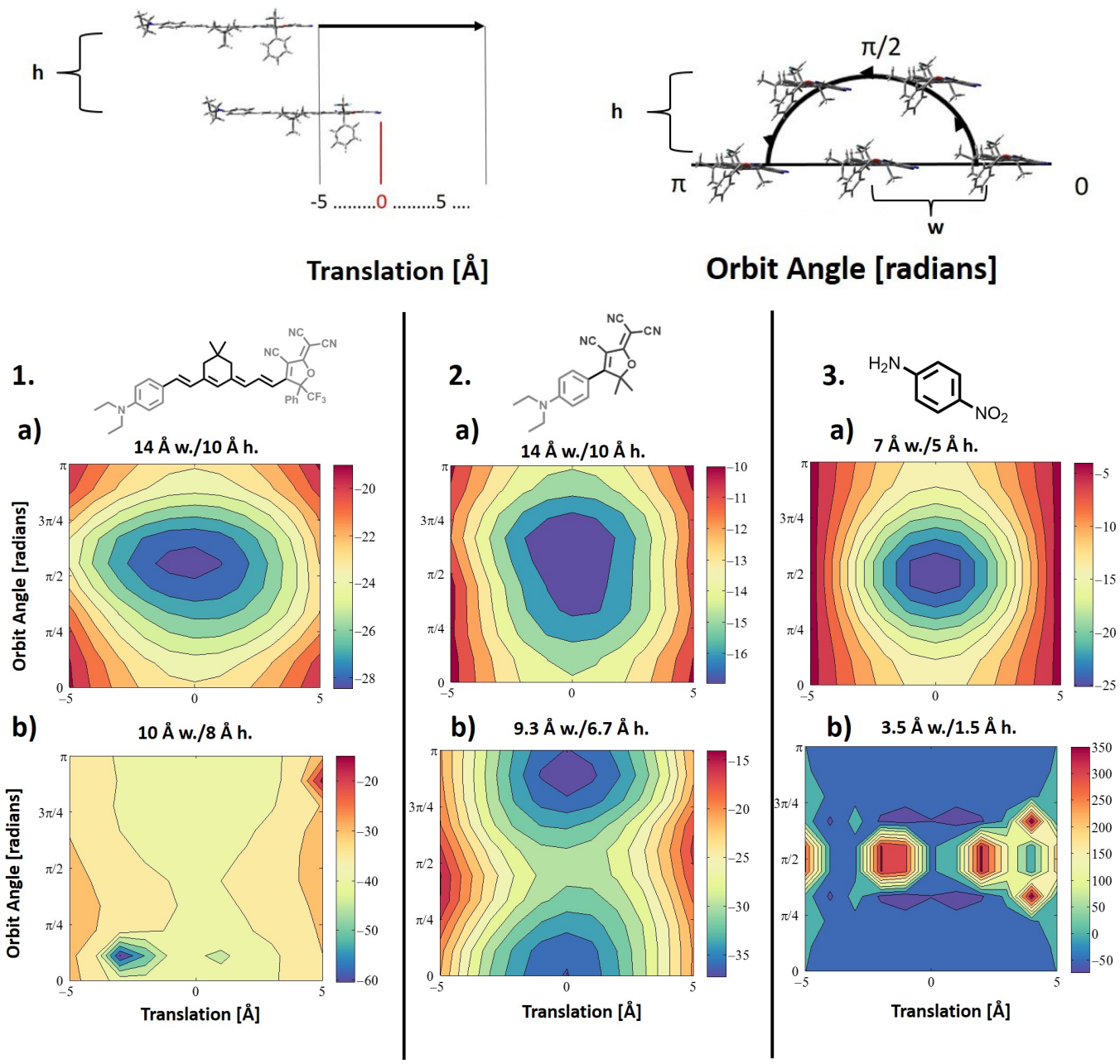

Figure C.3: **Effect of Relative Position of Acentric Monomers of YLD124, DCDHF, and pNA on Nonlinear Optical Response.** The first dipole hyperpolarizability consistent with the linear Pockels effect, $\beta_{zzz}(-\omega;\omega,0)$, is calculated at different relative positions 2 monomers of each of the systems listed above. One molecule is held static when the other half-orbits it along an arc from 0 to π. The molecule is simultaneosly tranversed along x which is co-aligned with the molecular axis. The height and width of the grid (i.e., distance between stationary and transient molecule) affects the quantitative and qualitative results of the contour plots.

C.2 Data Tables for Dimer Hyperpolarizability of YLD124 with 90° Roll, Pitch, and Yaw Angles

Each of the following tables corresponds to the contour plots shown in Figure C.4, shown below.

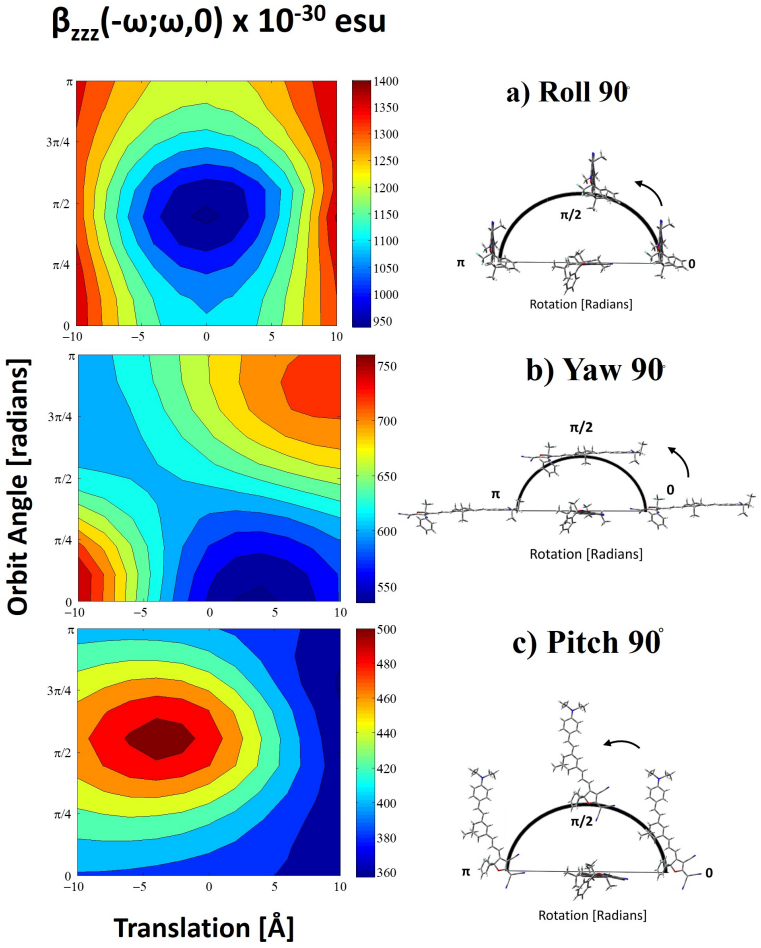

Figure C.4: **Change in Frequency-dependent Hyperpolarizability with Relative Orientation of YLD124 Monomers.** The linear Pockels hyperpolarizability, $\beta_{zzz}(-\omega;\omega,0) \times 10^{-30}$ esu, was computed in vacuum using wB97xD/6-31+G* for various YLD124 dimers. The orbital angle is illustrated, as well as Monomer 1 (stationary) with respect to Monomer 2 (transient), the latter which has been re-oriented according to a 90° shift along the roll, yaw, or pitch axis. Monomer 2 is simultaneously traversed along 'x' which is the molecular axis of Monomer 1, as illustrated in Figure 4.11. Panel a) shows changes in β when Monomer 2 is rolled 90°; Panel b) shows Monomer 2 rotated 90° about the yaw axis; and Panel c) shows Monomer 2 pitched downward by 90°.

θ \ x	**10**	**8**	**6**	**4**	**2**	**0**	**-2**	**-4**	**-6**	**-8**	**-10**
0	374	376	379	382	385	388	391	393	396	397	398
0.35	367	374	381	389	396	403	408	412	415	415	414
0.70	365	376	388	401	412	423	431	435	437	435	432
1.05	368	383	400	418	435	450	461	465	464	458	451
1.40	369	389	412	436	460	481	494	498	492	481	468
1.75	365	386	412	441	469	492	507	510	503	489	474
2.09	362	381	405	432	458	480	494	496	490	478	466
2.44	358	371	390	412	434	452	463	466	463	457	449
2.79	362	371	383	398	412	424	431	435	435	432	429
3.14	373	377	383	390	396	402	406	409	410	410	409

Table C.2: **Effect of Relative Position on Hyperpolarizability of Dimer Arrangement with Monomer 2 pitched downward by 90° with respect to Monomer 1.** Monomer 2 is moved about an orbit angle, θ, and translation axis, x, with respect to Monomer 1 which remains static. Note: The order is switched on the x-axis.

θ \ x	**-10**	**-8**	**-6**	**-4**	**-2**	**0**	**2**	**4**	**6**	**8**	**10**
0	1391	1300	1221	1160	1120	1107	1118	1152	1205	1271	1343
0.35	1390	1295	1212	1147	1106	1091	1103	1140	1197	1269	1349
0.70	1377	1271	1178	1106	1060	1045	1061	1106	1175	1262	1360
1.05	1353	1234	1130	1049	998	983	1005	1062	1149	1259	1385
1.40	1334	1210	1100	1013	957	939	961	1023	1122	1252	1405
1.75	1331	1220	1121	1041	988	966	978	1027	1111	1226	1366
2.09	1336	1249	1171	1109	1070	1056	1069	1109	1174	1262	1364
2.44	1347	1280	1220	1175	1147	1139	1153	1187	1240	1307	1381
2.79	1359	1305	1257	1221	1200	1195	1208	1237	1280	1333	1392
3.14	1370	1321	1278	1246	1227	1224	1235	1261	1299	1346	1398

Table C.3: **Effect of Relative Position on Hyperpolarizability of Dimer Arrangement with Monomer 2 rolled 90° with respect to Monomer 1.** Monomer 2 is moved about an orbit angle, θ, and translation axis, x, with respect to Monomer 1 which remains static.

θ \ x	**-10**	**-8**	**-6**	**-4**	**-2**	**0**	**2**	**4**	**6**	**8**	**10**
0	761	718	670	625	585	556	539	535	544	559	581
0.35	761	719	673	629	592	565	549	544	550	564	582
0.70	727	696	662	628	600	579	568	565	571	582	596
1.05	682	662	642	622	607	596	591	593	599	608	619
1.40	642	632	624	618	615	616	620	626	634	643	651
1.75	617	615	615	620	627	637	649	661	671	680	686
2.09	606	608	615	626	640	657	673	689	701	708	712
2.44	604	610	620	635	653	672	691	708	719	725	725
2.79	607	614	626	642	661	680	698	713	723	727	725
3.14	609	616	629	645	663	681	697	710	718	722	722

Table C.4: **Effect of Relative Position on Hyperpolarizability of Dimer Arrangement with Monomer 2 rotated by yaw angle of 90° with respect to Monomer 1.** Monomer 2 is moved about an orbit angle, θ, and translation axis, x, with respect to Monomer 1 which remains static.

C.3 Closer Look: Dimer and Trimer Spectra separately plotted

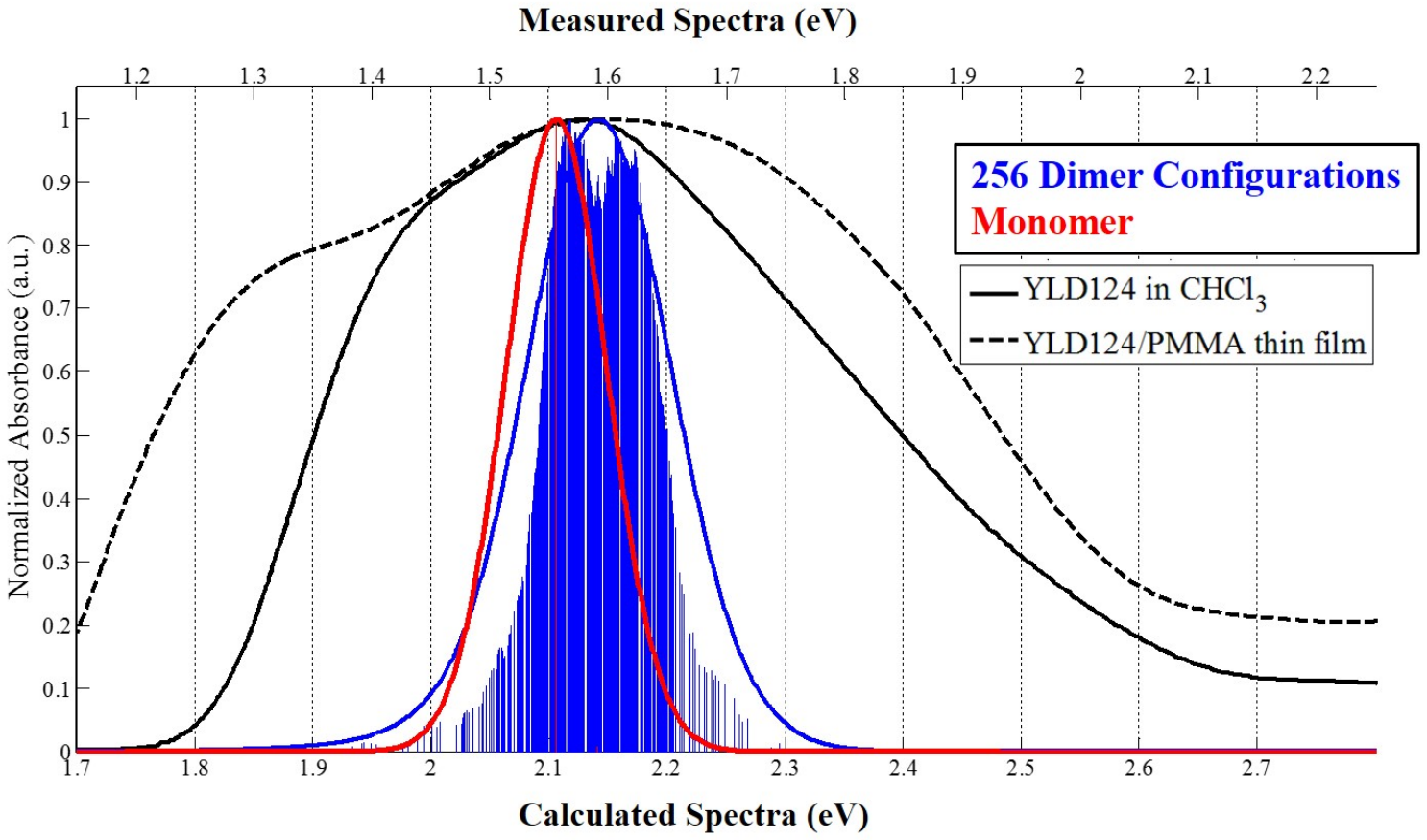

Figure C.5: **Measured Spectra of YLD124 compared with Simulated Spectrum of Total Dimer Configuration Results.** Measurements provided by I. Kosilkin are of YLD124 in chloroform solution (solid black curve) and 100% doped into a PMMA thin film (dotted black curve). The calculations are grouped and color coded according to monomer and dimer. The monomer curve is a single monomer calculation; the dimer curve represents 256 unique dimer configurations. The measured and computed energy ranges are shown on separate (top and bottom) axes.

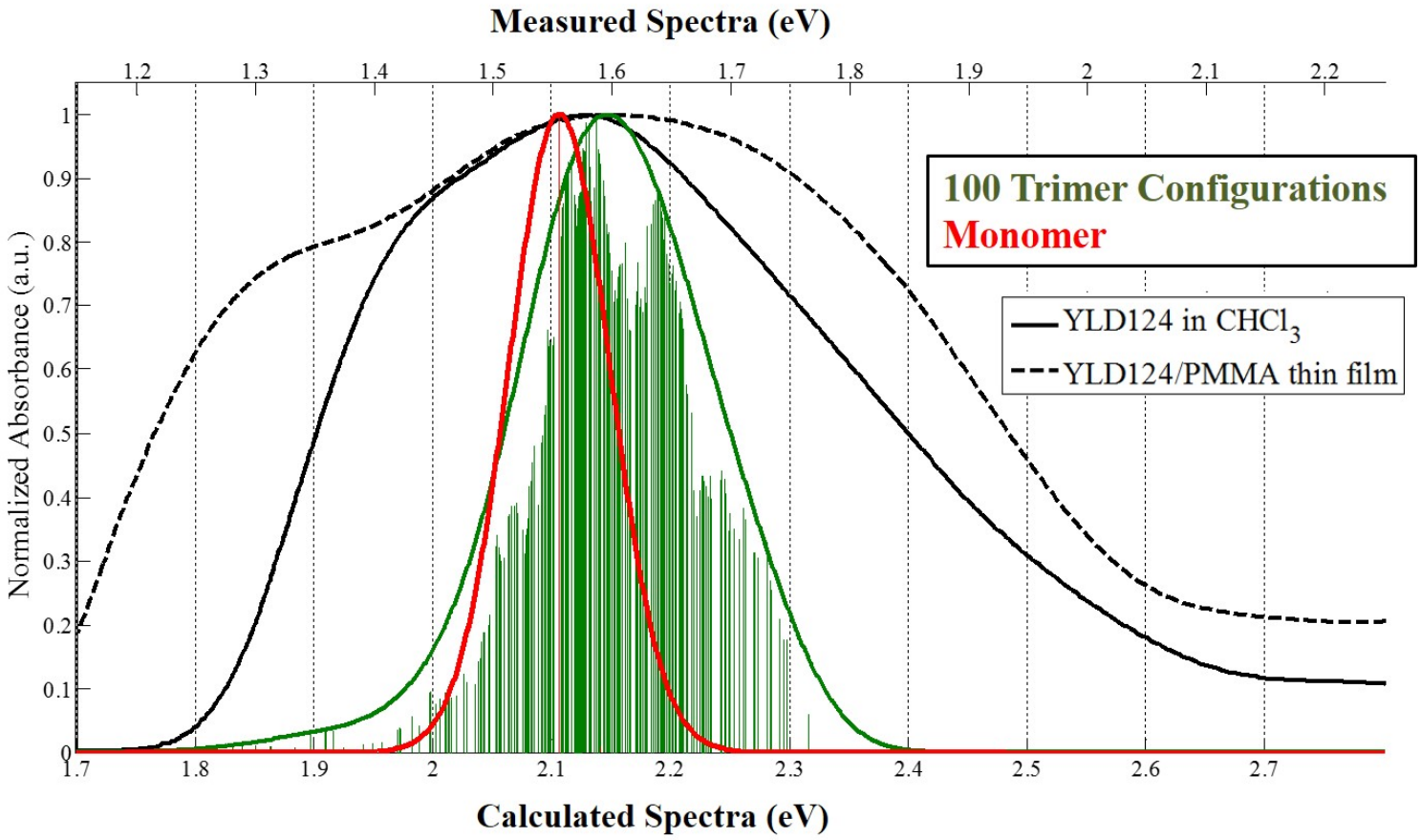

Figure C.6: **Measured Spectra of YLD124 compared with Simulated Spectrum of Total Trimer Configuration Results.** Measurements provided by I. Kosilkin are of YLD124 in chloroform solution (solid black curve) and 100% doped into a PMMA thin film (dotted black curve). The calculations are grouped and color coded according to monomer and dimer. The monomer curve is a single monomer calculation; the trimer curve represents 100 unique configurations. The measured and computed energy ranges are shown on separate (top and bottom) axes.

C.4 Molecular Orbitals and Orbital Energies of Selected Dimers in Categories I-VI

The following MO visualizations are based on dimers that are exemplary of the other dimer configurations of its category. The two lowest excited states are reported for each configuration, along with percentage of single particle contributions to each vertical excitation. The percentage of single particle contributions to the vertical excited states was determined using the same method as

Ref [237]. The percentage contributions are calculated using

$$\%contribution = \frac{\chi_i^2}{\sum_{i=1}^{n} \chi_i^2} \times 100\%, \tag{C.1}$$

where χ_i are the single-particle transitions corresponding to a given vertical excited state. In the Gaussian09 output for a 'td' calculation, the χ_i values are the CI coefficients printed next to each MO transition. For example, the output for a randomly selected YLD124 dimer is:

```
 Excited State   1:      Singlet-?Sym    1.9432 eV  638.03 nm  f=1.0627  <S**2>=0.000
     323 -> 327        0.13579
     323 -> 329       -0.10438
     325 -> 327        0.51464
     326 -> 327        0.10352
     326 -> 328        0.39993
```

where χ_1=0.13579 and so on. The transition "326 $\rightarrow$ 327" represents the HOMO-LUMO transition for this and all other YLD124 dimers (TBDMSO groups removed) in this study. In the following figures, the blue bars are the HOMO-1, HOMO, LUMO, and LUMO+1 states. The black arrows signify *intra*molecular CT between these states; whereas, the red arrows signify intermolecular CT. The insets illustrate the dimer geometry. Note that only the MO transitions with the top 2-4 percentage contributions are given for each vertical excitation. Other lesser percentage contributions from other transitions are added to make roughly 100%.

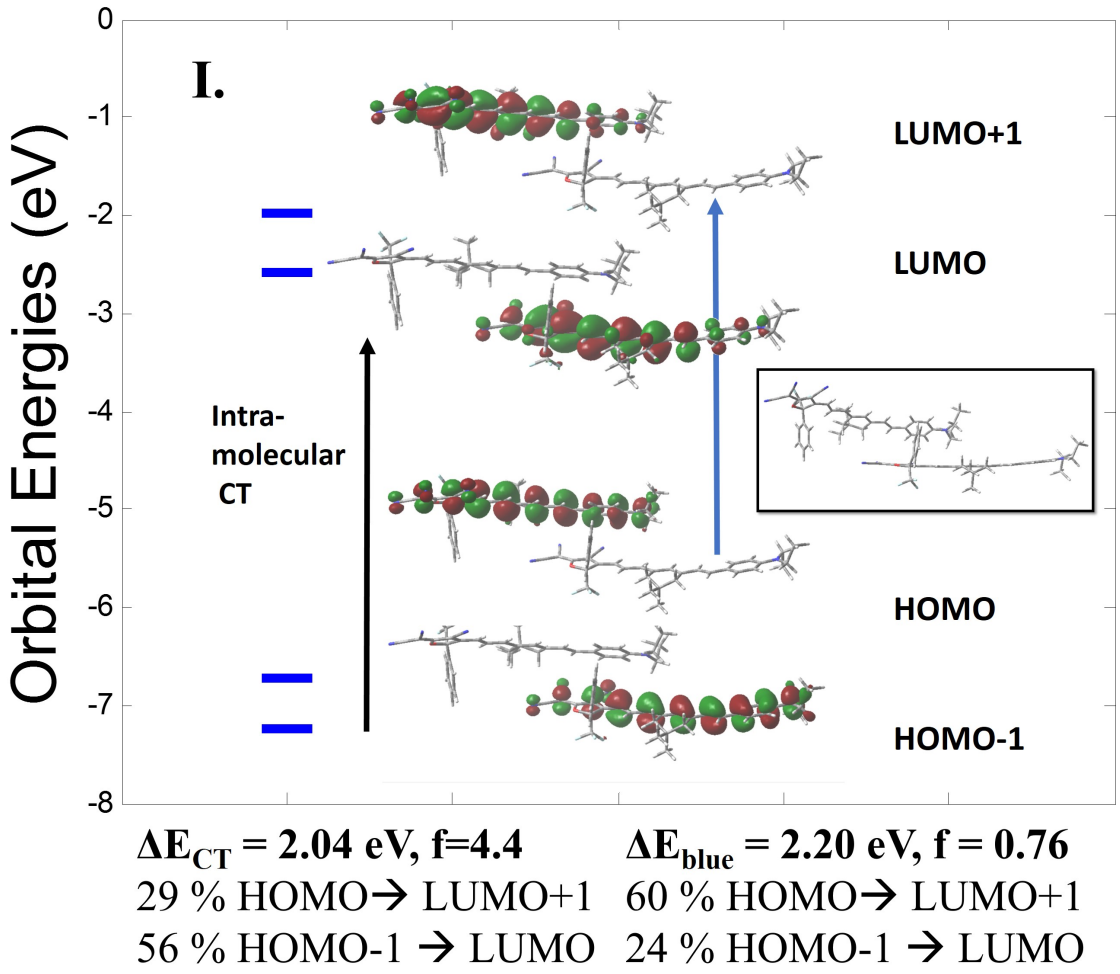

Figure C.7: **Orbital Energies and Molecular Orbitals for a Dimer in Category I.** The dimers in this category have large hyperpolarizabilities and form in a stair-like fashion. The first two excited states are described mostly by a combination of intramolecular CT occurring along monomer 1 and 2. There is little contribution from intermolecular CT states because the monomers are slightly rolled or shifted away from each other in this category. Accordingly, no ΔE_{red} is detected for this specific dimer, so the lowest energy transition is also the maximum oscillator strength transition, ΔE_{CT}. The second excited state transition occurs at 2.2 eV and is called "ΔE_{blue}", in keeping with the naming convention.

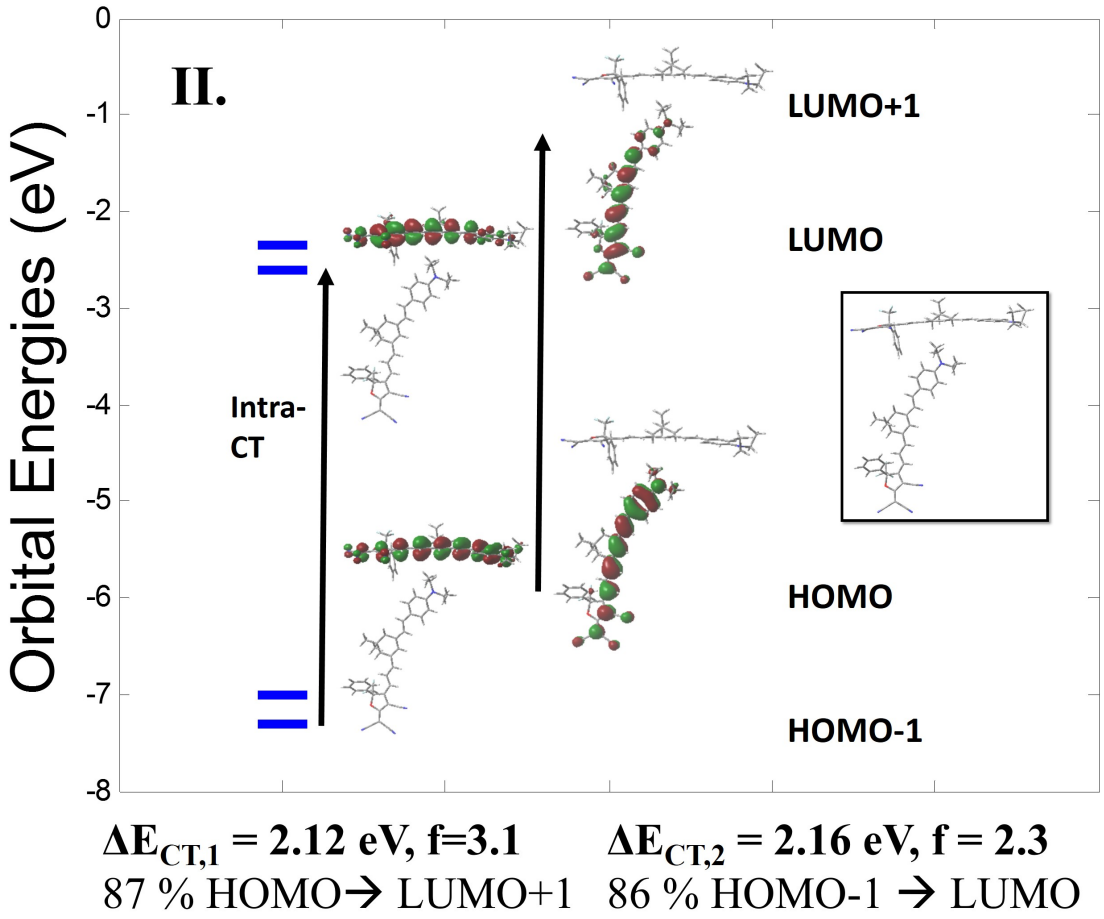

Figure C.8: **Orbital Energies and Molecular Orbitals for a Dimer in Category II.** The dimers in this category have moderate hyperpolarizabilities that are larger than the isolated molecule. The first two excited state transitions are very close in energy (only 0.04 eV difference) and thus are called $\Delta E_{CT,1}$ and $\Delta E_{CT,2}$. There is little mixing of states for these first two transitions. The lower energy transition is mostly described by intramolecular CT occurring along monomer 1 and the next lowest transition is mostly described by intramolecular CT occuring along monomer 2.

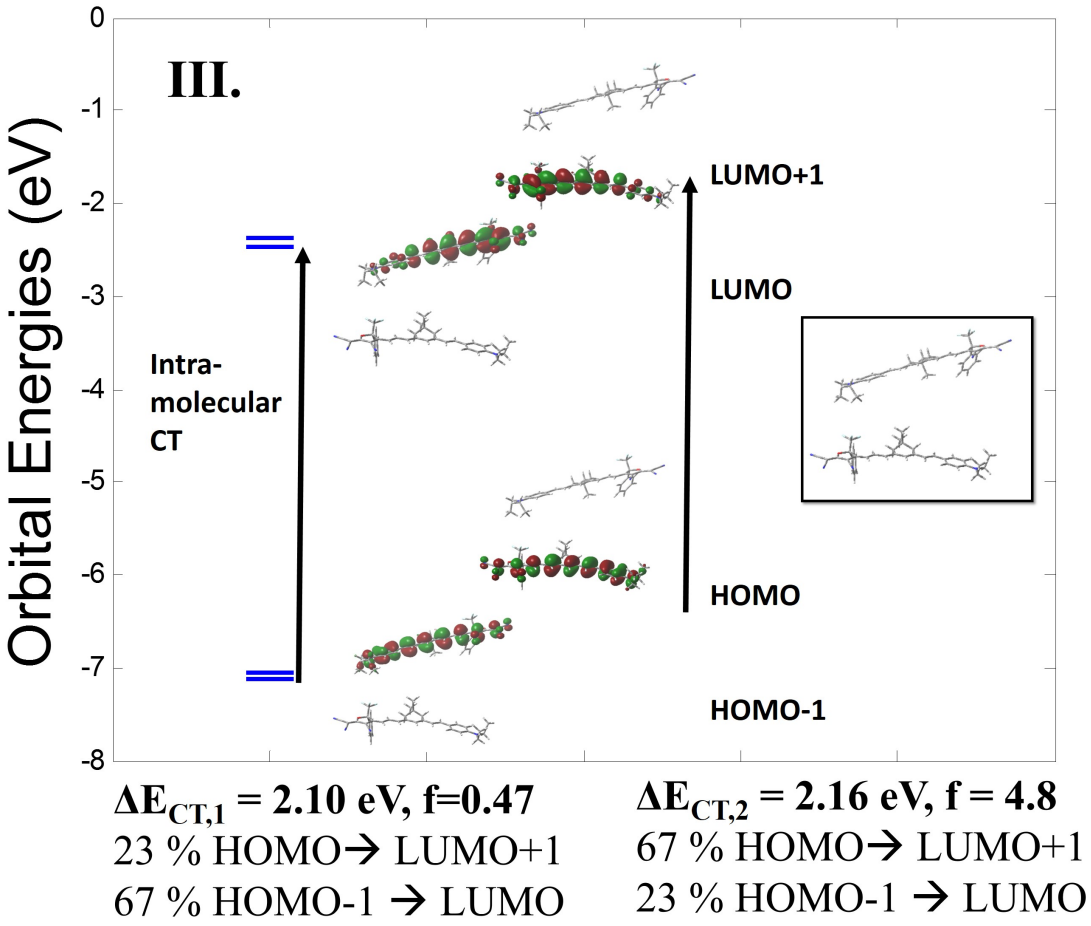

Figure C.9: **Orbital Energies and Molecular Orbitals for a Dimer in Category III.** The molecules in this category are separated on average by 15.2 $\mathring{A}$. Thus, there is little to no mixing with intermolecular CT states for the lowest excited state transitions.

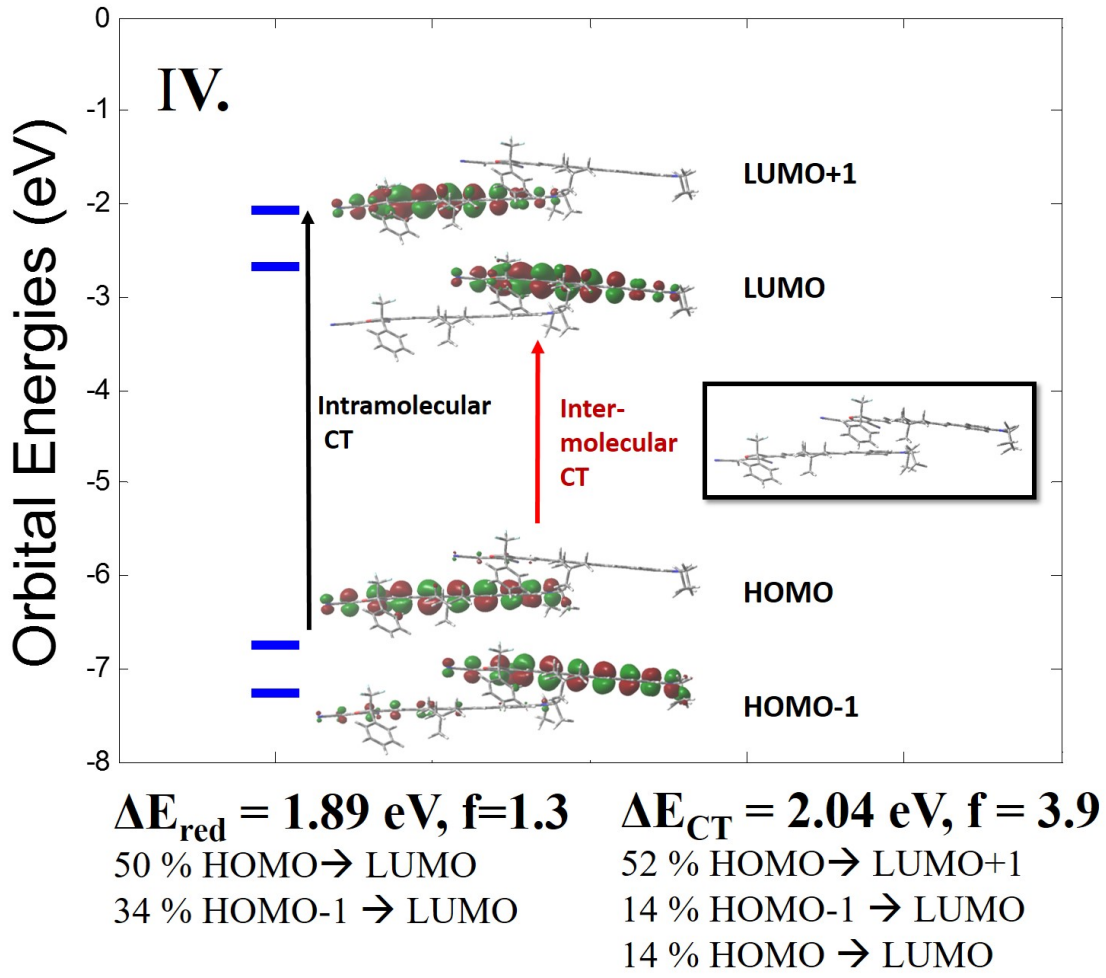

Figure C.10: **Orbital Energies and Molecular Orbitals for a Dimer in Category IV.** The dimers in this category are similar to **I**, but experience greater intermolecular orbital overlap which results in an Δ_{red} transition that is mostly described by intermolecular CT.

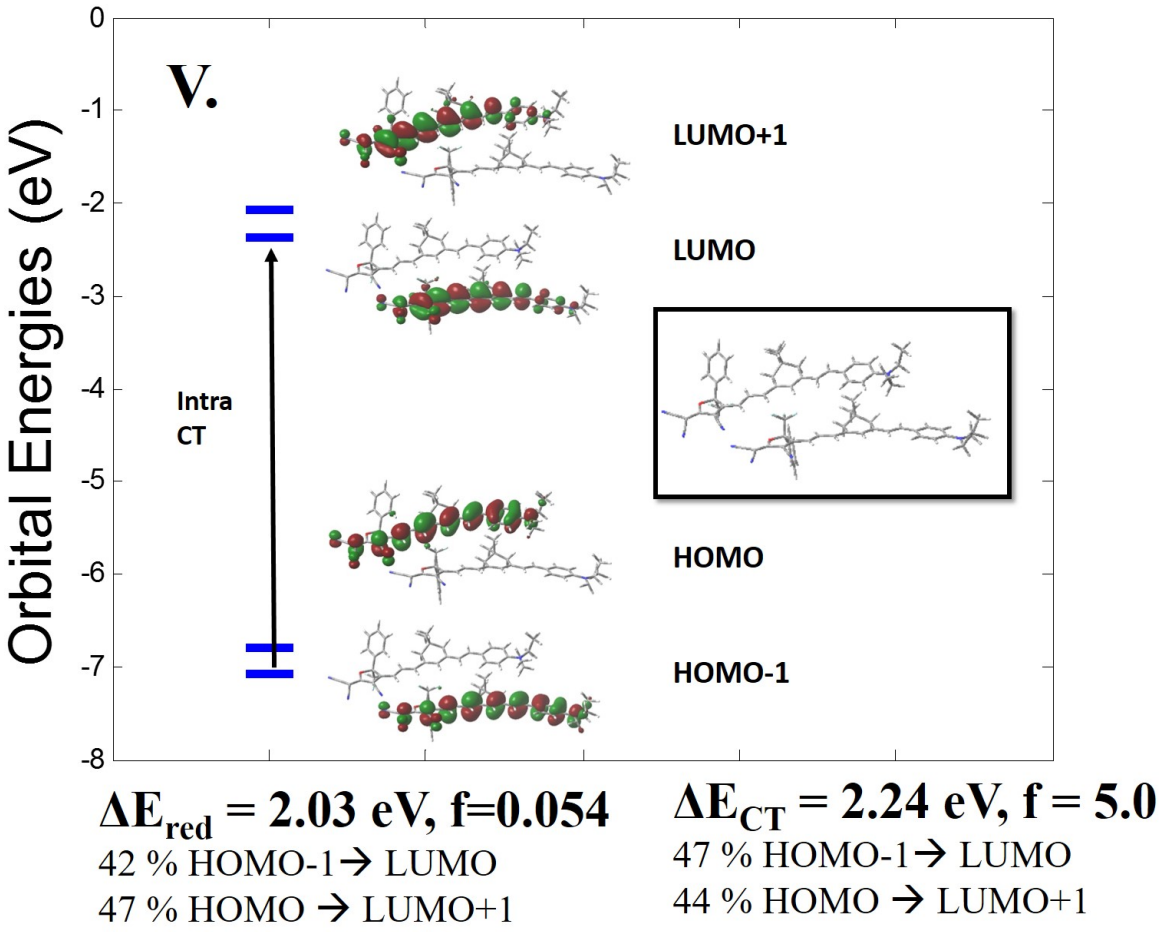

Figure C.11: **Orbital Energies and Molecular Orbitals for a Dimer in Category V.** The dimers in category **V** are generally non-centrosymmetric and the dipolar repulsions experienced by these configurations causes a notable blue-shift in ΔE_{CT}, consistent with H-aggregation.

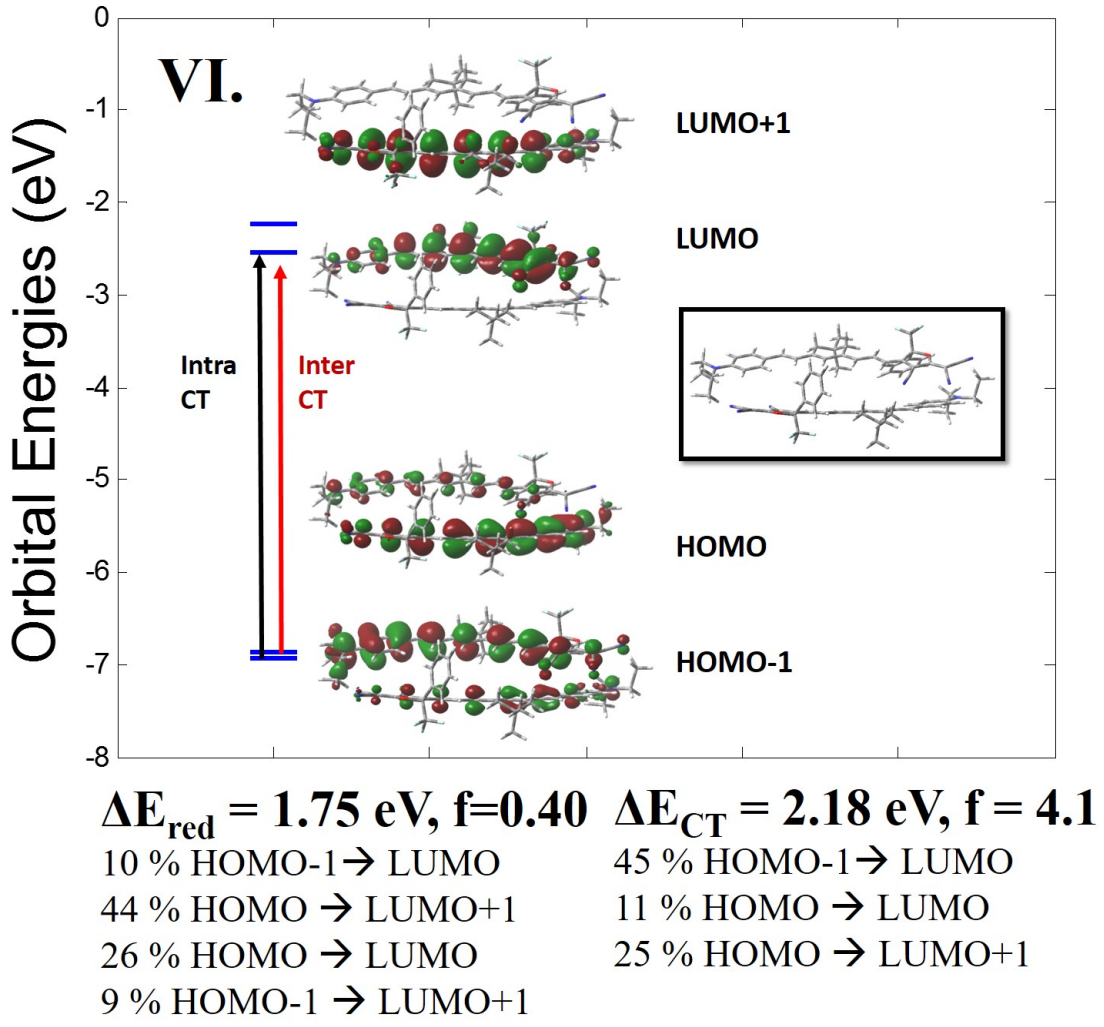

Figure C.12: **Orbital Energies and Molecular Orbitals for a Dimer in Category VI.** This category of dimers has the largest gaps between ΔE_{red} and ΔE_{red}. The dimers are mostly centrosymmetric and have hyperpolarizabilities smaller than the isolated molecule. The appearance of a low-energy shoulder from additional low-lying CT states is consistent with J aggregation.

C.5 Molecular Orbitals and Orbital Energies of Selected Trimers in Categories III, V, and VI

The following MO visualizations are based on trimers that are exemplary of the other trimer configurations of its category. The three lowest excited states are reported for each configuration, along with percentage of single particle contributions to each vertical excitation.The percentage of single particle contributions to the vertical excited states was determined using the same method as Ref [237], as explained above for the dimers. In the following figures, the blue bars are the HOMO-2, HOMO-1, HOMO, LUMO, LUMO+1, and LUMO+2 states. The insets illustrate the trimer geometry for each example. The visualization is enhanced with depth perception. Note that only the MO transitions with the top 2 percentage contributions are given for each vertical excitation. Other lesser percentage contributions from other transitions are added to make roughly 100%.

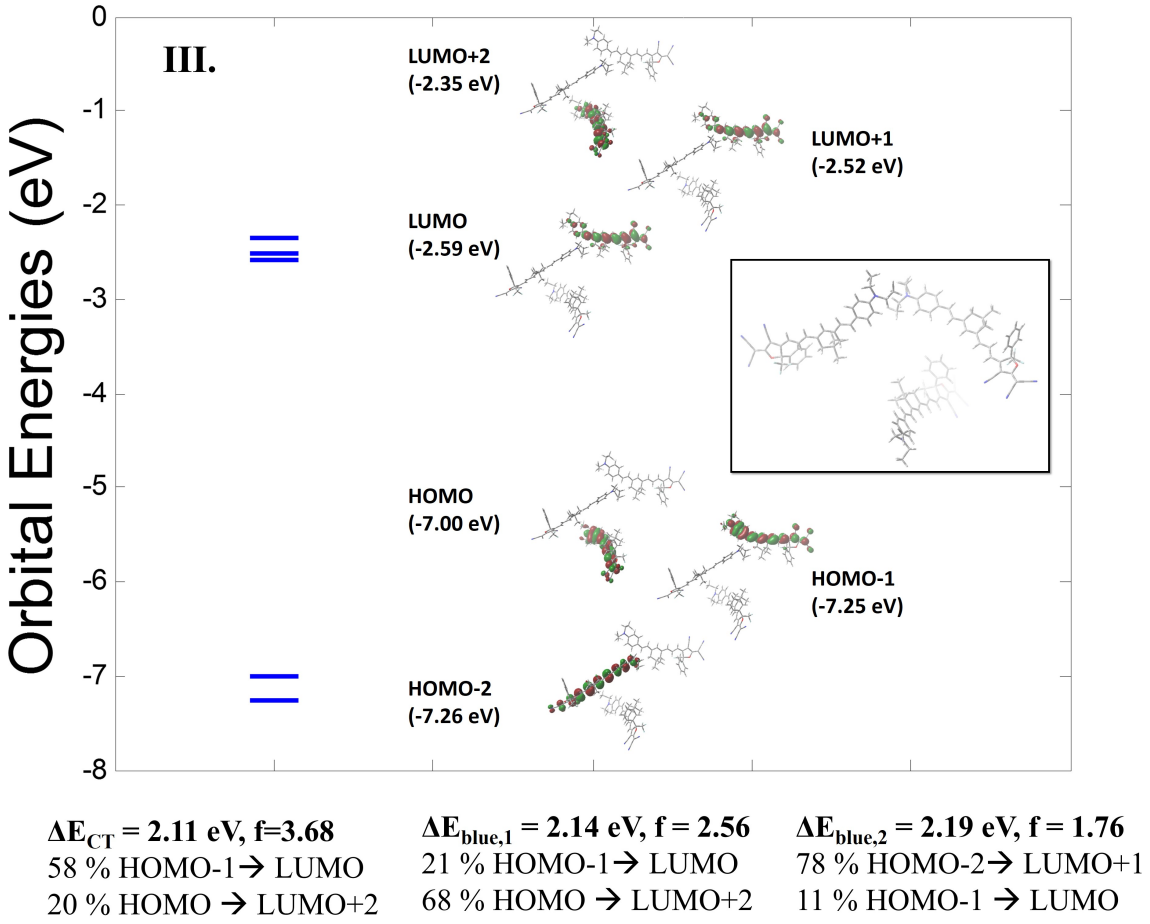

Figure C.13: **Orbital Energies and Molecular Orbitals for a Trimer in Category III.** The trimers in this category have modest hyperpolarizabilities (less than the isolated monomer) and tend to feature a centrosymmetric pair. There is little D/A overlap of any of the molecules, thus there is little to no mixing with intermolecular CT states for the lowest excited state transitions. The lowest transition energy corresponds to the primary CT transition, ΔE_{CT}.

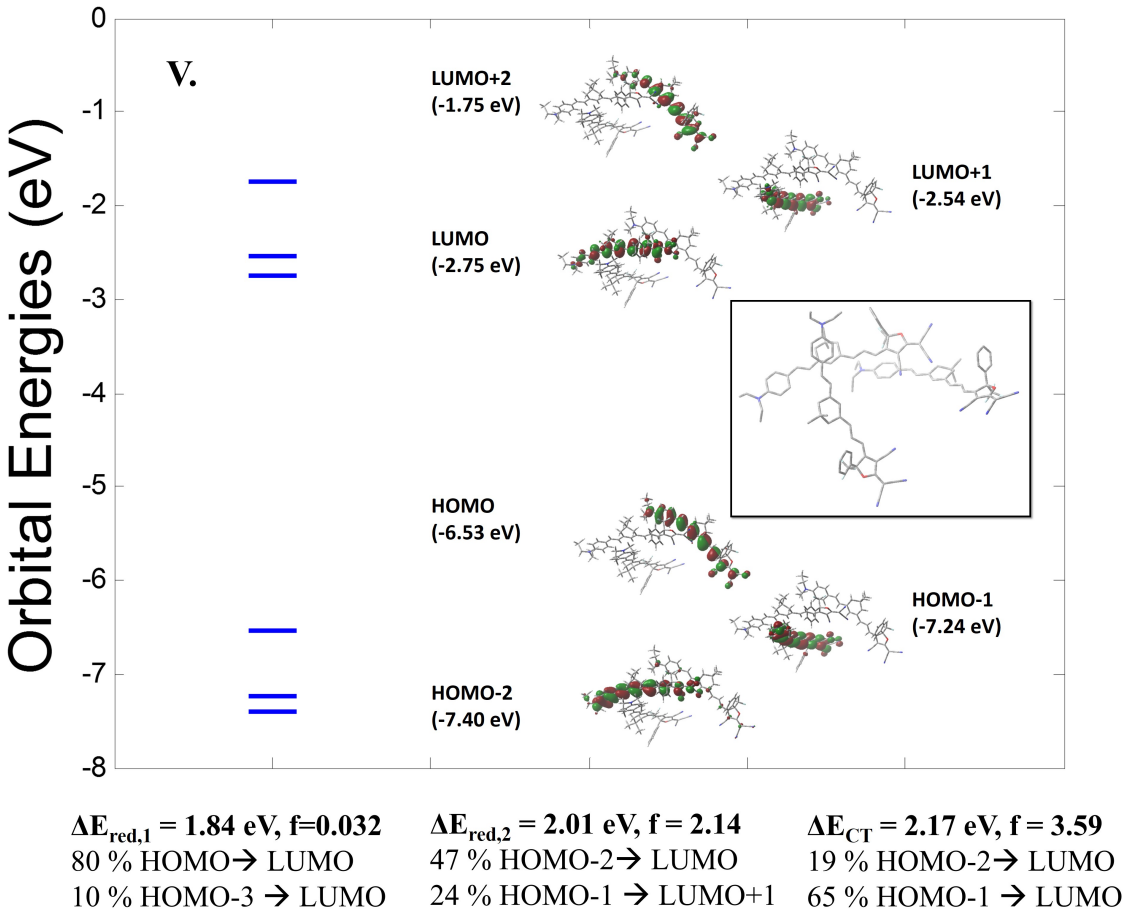

Figure C.14: **Orbital Energies and Molecular Orbitals for a Trimer in Category V.** The trimers in this category have moderate hyperpolarizabilities (greater than the isolated monomer). There is typically a pair of monomers that has D/A overlap, as illustrated in the example, which induces mixing with intermolecular CT states. The lowest transition energy, $\Delta E_{red,1}$, of the example shown has 80% contribution from HOMO→LUMO which corresponds to intermolecular CT. Also, the maximum oscillator strength transition, ΔE_{CT}, is blue-shifted by 0.07 eV with respect to the monomer peak.

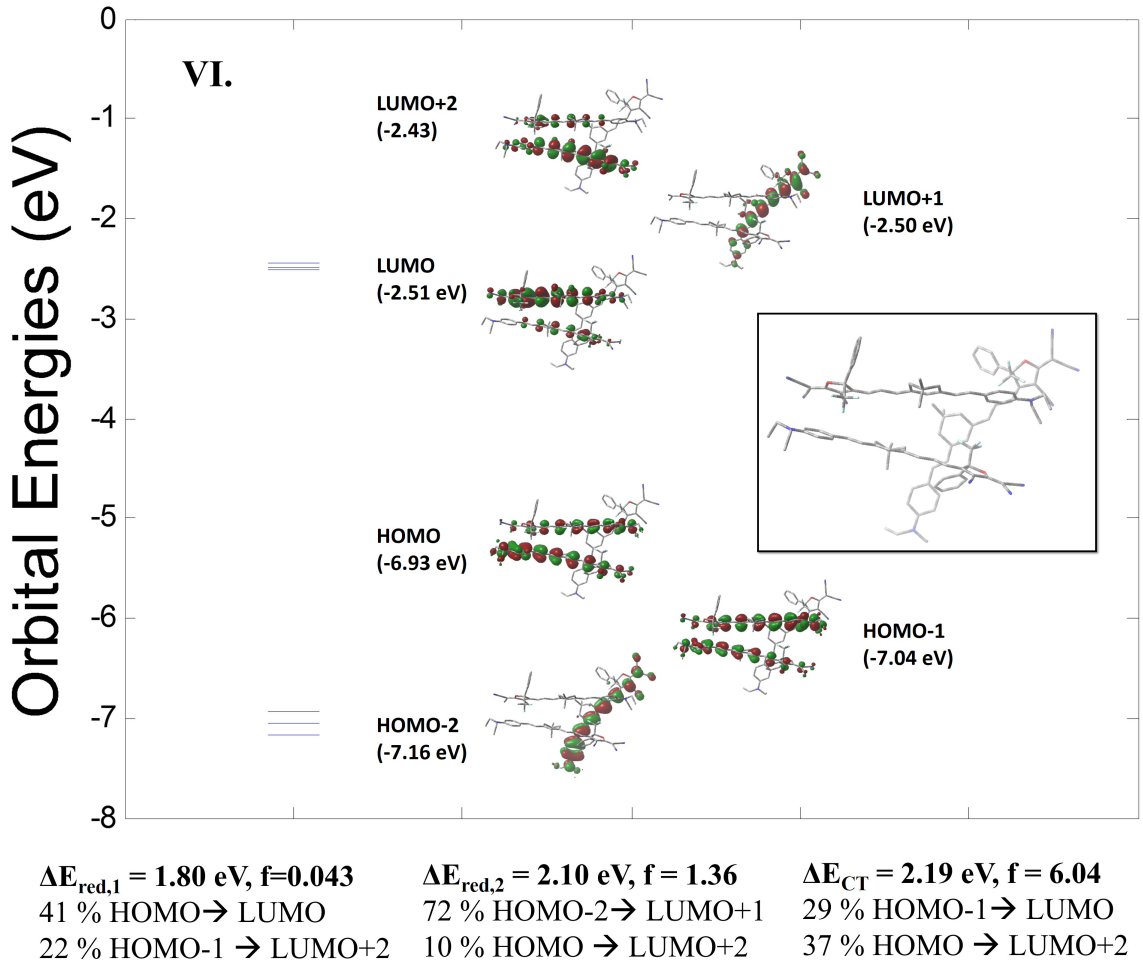

Figure C.15: **Orbital Energies and Molecular Orbitals for a Trimer in Category VI.** Similar to the dimers, this category of trimers features the largest gaps between ΔE_{CT} and ΔE_{red}. The trimers here have hyperpolarizabilities smaller than the isolated molecule and typically include a centrosymmetric pair of monomers. The appearance of additional low-lying CT states is consistent with J aggregation.

VITA

Kerry Ellen Garrett was born and raised in Spokane, WA. Kerry completed her ACS certified B.Sc. in Chemistry at Eastern Washington University in June 2010. Soon after, she moved to Seattle and began her graduate studies in Chemistry at the University of Washington. She fulfilled the requirements for her M.Sc. in Chemistry and also earned a M.Sc. in Applied Math from University of Washington in 2014. This dissertation completes the requirements for a Ph.D. in Chemistry.

BIBLIOGRAPHY

[1] Based on discussions with Andreas Tillack, c. 2015.

[2] C. Adamo and D. Jacquemin. "The Calculations of Excited-State Properties with Time-Dependent Density Functional Theory". In: *Chem. Soc. Rev.* 42 (2013), p. 845.

[3] A. J. P. Akelaitis et al. "Synthesis and electro-optic properties of amino-phenyl-thienyl donor chromophores". In: *Opt. Mater. (Amsterdam, Neth.)* 30 (2008), pp. 1504–1513.

[4] L. Alloatti et al. "100 GHz Silicon-Organic Hybrid Modulator". In: *Light: Science and Applications* 3.5 (2014), E173.

[5] J. Andzelm et al. "Performance of DFT Methods in the Calculation of Optical Spectra of TCF-Chromophores." In: *J. Chem. Theory Comput.* 5 (2009).

[6] P. Atkins. *Molecular quantum mechanics (2nd ed.)* Oxford [Oxfordshire] ; New York: Oxford University Press., 1983.

[7] J. Autschbach and M. Srebro. "Delocalization Error and "Functional Tuning" in Kohn-Sham Calculations of Molecular Properties". In: *Accounts of Chemical Research* 47.8 (2014), pp. 2592–2602.

[8] R. Baer, L. Kronik, and T. Stein. "Reliable Prediction of Charge Transfer Excitations in Molecular Complexes Using Time-Dependent Density Functional Theory". In: *J. Am. Chem. Soc.* 131.8 (2009), pp. 2818–2820.

[9] R. Baer, E. Livshits, and U. Salzner. "Tuned Range-Separated Hybrids in Density Functional Theory". In: *Annual Review of Physical Chemistry* 61 (2010), pp. 85–109.

[10] R. Baer and D. Neuhauser. In: *Phys. Rev. Lett.* 94 (2005), p. 043002.

[11] O. V. Baerends and E. J. Gritsenko. "The spin-unrestricted molecular Kohn-Sham solution and the analogue of Koopmans theorem for open-shell molecules". In: *J. Chem. Phys* 120 (2004).

[12] D. H. Bale. "Nonlinear Optical Materials Characterization Studies Employing Photostability, Hyper-Rayleigh Scattering, and Electric Field Induced Second Harmonic Generation Techniques." Thesis. 2007.

[13] D. H. Bale et al. "Dielectric Dependence of the First hyperpolarizability for Electro-Optic Chromophores". In: *J. Phys. Chem. B.* 115 (2011).

[14] H. Bartlett and R. J. Sekino. "Frequency-Dependent Nonlinear Optical-Properties of Molecules". In: *J. Chem. Phys* 85 (1986), pp. 976–89.

[15] A. Becke. "Perspective: Fifty years of density functional theory in chemical physics". In: *J. Chem. Phys.* 140 (2014), 18A301.

[16] A. D. Becke. "A New Mixing of Hartree-Fock and Local Density-Functional Theories". In: *J. Chem. Phys.* 98 (1993), p. 1372.

[17] A. D. Becke. "Density-functional exchange energy approximation with correct asymptotic-behavior". In: *Phys. Rev. A* 38 (1988), pp. 3098–3100.

[18] S. D. Bella, M. Ratner, and T. Marks. "Design of Chromophoric Molecular Assemblies with Large Second-Order Optical Nonlinearities. A Theoretical Analysis of the Role of Intermolecular Interactions." In: *J. Am. Chem. Soc.* 114 (1992), pp. 5842–5849.

[19] S. Benight et al. "Reduced Dimensionality in Organic Electro-Optic Materials: Theory and Defined Order". In: *J. Phys. Chem. B.* 114 (2010), pp. 11949–11956.

[20] A.F. Benner et al. In: *IBM J. Res. Dev.* 49 (2005), p. 755.

[21] N. S. Bonness Jr. "Development and Testing of New Theoretical Methods for Calculating Franck-Condon Factors and Density Functional Methods for Calculating (Hyper)polarizabilities". Thesis. 2008.

[22] M. Born and R. Oppenheimer. "Zur Quantentheorie der Molekeln." In: *Ann. Phys.* 84 (1927), p. 457.

[23] R. Boyd. *Nonlinear Optics*. San Diego, CA, USA: Academic Press, Inc., 1992.

[24] J. Brandrup et al. *Polymer Handbook*. New York, New York: Wiley and Sons, 1999.

[25] J.L. Bredas and S. Marder. "CHEM 535B – SPRING 2003, Chapter 9 – Nonlinear Optics". Accessed Nov. 2015 via quiz2.chem.arizona.edu/chem535/.

[26] J. Campo et al. "Practical Model for First Hyperpolarizability Dispersion Accounting for Both Homogeneous and Inhomogeneous Broadening Effects". In: *J. Phys. Chem. Lett.* 3 (2012), pp. 2248–2252.

[27] C.R. Cantor and P.R. Schimmel. *Techniques for the Study of Biological Structure and Function*. San Francisco, CA, USA: W.H. Freeman and Company, 1980, p. 349.

[28] M. E. Casida. "Time-Dependent Density-Functional Theory for Molecules and Molecular Solids". In: *J. Mol. Struct. (THEOCHEM)* 914 (2009), p. 3.

[29] D.M. Casimier et al. "Demonstration of a Low Vpi-L Modulator with GHz Bandwidth Based on Electro-Optic Polymer-Clad Silicon Slot Waveguides". In: *Proc. SPIE* 5351 (2004), pp. 243–252.

[30] J. Chai and M. Head-Gordon. In: *Phys. Chem. Chem. Phys* 10 (2008).

[31] B. Champagne and D. Bishop. "Calculations of Nonlinear Optical Properties for the Solid State". In: *Advances in Chemical Physics (Vol 126)*. Ed. by I. Prigogine and S. Rice. 2003. Chap. 2, pp. 41–92.

[32] B. Champagne and M. Wergifosse. "Electron Correlation effects on the first hyperpolarizability of push-pull pi-conjugated systems". In: *J. Chem. Phys* 134 (2011).

[33] B. Champagne et al. "Ab Initio Coupled Hartree-Fock Investigation of the Static First Hyperpolarizability of Model all-trans-Polymethineimine Oligomers of Increasing Size". In: *The Journal of Physical Chemistry A* 101.17 (1997), pp. 3158–3165.

[34] B. Champagne et al. "Assessment of conventional density functional schemes for computing the polarizabilities and hyperpolarizabilities of conjugated oligomers: An ab initio investigation of polyacetylene chains". In: *J. Chem. Phys* 109 (1998).

[35] B. Champagne et al. "Density functional theory investigation of the polarizability and second hyperpolarizability of polydiacetylene and polybutatriene chains: Treatment of exact and role of correlation". In: *J. Chem. Phys.* 125 (2006), p. 194114.

[36] D. S. Chemla, J. L. Oudar, and J. Jerphagnon. "Origin of the second-order optical susceptibilities of crystalline substituted benzene". In: *Phys. Rev. B* 12 (1975), p. 4534.

[37] A. Chen et al. *In Modified attenuated total reflection for the fast and routine electro-optic measurement of nonlinear optical polymer thin films, Organic Thin Films for Photonics Applications*. Long Beach, CA. 1997.

[38] Y.J. Cheng et al. "Demonstration of a Low Vpi-L Modulator with GHz Bandwidth Based on Electro-Optic Polymer-Clad Silicon Slot Waveguides". In: *Chem. Mater.* 19 (2007), pp. 1154–1163.

[39] Y.J. Cheng et al. "Donor-Acceptor thiolated polyenic chromophores exhibiting large optical nonlinearity and excellent photostability". In: *Chem. Mater.* 20.15 (2008), pp. 5047–5054.

[40] M. Chiba, T. Tsuneda, and K. Hirao. "Long-range corrected time-dependent density functional study on fluorescence of 4,4-dimethylaminobenzonitrile". In: *J. Chem. Phys* 126 (2007).

[41] E.Y. Choi, M. Jazbinsek, and O.P. Kwon. "Control of Nucleation of Organic Electrooptic Phenolic Polyene Crystals by Highly Polar Liquid Additive". In: *Crystal Growth & Design* 12.1 (2012), pp. 495–498.

[42] L.J. Clancy. *Aerodynamics*. Section 16.6. London, UK: Pitman Publishing Limited, 1975.

[43] K. Clays and A. Persoons. "Hyper-Rayleigh Scattering in Solution." In: *Rev. Sci. Instrum.* 63 (1992), pp. 3285–3289.

[44] CMDITR. *Photonics Wiki.* 2015. URL: `www.photonicswiki.org`.

[45] C. J. Cramer. *Essentials of computational chemistry: theories and models.* Chinchester, UK: Wiley and Sons, 2004.

[46] S. J. Cyvin, J. E. Rauch, and J. C. Decius. "Theory of Hyper-Raman Effects (Nonlinear Inelastic Light Scattering): Selection Rules and Depolarization Ratios for the Second-Order Polarizability". In: *J. Chem. Phys.* 43 (1965).

[47] Singer K. D., Kuzyk M. G., and Sohn J. E. "Second-Order Nonlinear-Optical Processes in Orientationally Ordered Materials: Relationship between Molecular and Macroscopic Properties". In: *J. Opt. Soc. Am. B* 4 (1987), p. 968.

[48] L. R. Dalton. "Rational design of organic electro-optic materials". In: *J. Phys.: Condens. Matter* 15 (2003), R897.

[49] L. R. Dalton and W. H. Steier. *Broadband Optical Modulators: Science, Technology, and Applications, Polymer Modulators.* New York, NY, USA: Taylor and Francis, 2011, pp. 221–254.

[50] L. R. Dalton, P. A. Sullivan, and D. H. Bale. "Electric Field Poled Organic Electro-optic Materials: State of the Art and Future Prospects". In: *Chem. Rev.* 110 (2010), pp. 25–55.

[51] L. R. Dalton et al. "From molecules to optochips: organic electro-optic materials." In: *Journal of Materials Chemistry* 9.9 (1999), pp. 1905–1920.

[52] L. R. Dalton et al. *Organic electro-optic silicon photonic materials and devices.* 2007.

[53] L. R. Dalton et al. "Synthesis and Processing of Improved Organic Second-Order Nonlinear Optical Materials for Applications in Photonics". In: *Chemistry of Materials* 7.6 (1995), pp. 1060–1081.

[54] Larry R. Dalton and K. S. Lee. *Polymers for Photonic Applications I: Advances in Polymer Science*. 2002.

[55] L.R. Dalton. "Organic electro-optic materials." In: *Pure Appl. Chem.* 76.7-8 (2004), pp. 1421–1433.

[56] L.R. Dalton et al. "Low (Sub-Volt) Halfwave Voltage Polymeric Electro-optic Modulators Achieved by Controlling Chromophore Shape". In: *Science* 288 (2000), p. 119.

[57] L.R. Dalton et al. "Organic Electro-Optic Materials". In: *Organic Thin Films for Photonic Applications*. Chap. 3, pp. 13–33.

[58] L.R. Dalton et al. "Progress toward Device-Quality Second-Order Nonlinear Optical Materials. 1. Influence of Composition and Processing Conditions on Nonlinearity, Temporal Stability, and Optical Loss". In: *Chem. Mater.* 10 (1998), pp. 146–155.

[59] L.R. Dalton et al. "Systematic Nanoengineering of Soft Matter Organic Electro-optic Materials". In: *Chemistry of Materials* 23.3 (2011), pp. 430–445.

[60] J. A. Davies et al. "Rational Enhancement of Second-Order Nonlinearity: Bis-(4-methoxyphenyl)hetero-aryl-amino Donor-Based Chromophores: Design, Synthesis, and Electrooptic Activity". In: *J. Am. Chem. Soc* 130 (2008), pp. 10565–10575.

[61] A. Davydov. *Theory of molecular excitons*. New York: Plenum Press, 1971.

[62] V. Dentan et al. In: *Opt. Commun.* 69 (1989), pp. 379–383.

[63] F. Ding et al. "An efficient method for calculating dynamic hyperpolarizabilities using real-time time-dependent density functional theory". In: *J. Chem. Phys.* 138 (2013), p. 064104.

[64] R. Ding and et al. "Demonstration of a Low Vpi-L Modulator with GHz Bandwidth Based on Electro-Optic Polymer-Clad Silicon Slot Waveguides". In: *Opt. Express* 18 (2010), pp. 15618–15623.

[65] Y. Ding et al. "Effective Electro-Optical Modulation with High Extinction Ratio by a Graphene-Silicon Microring Resonator". In: *Nano Letters* 15.7 (2015), pp. 4393–4400.

[66] A. Dreuw and M. Head-Gordon. "Failure of Time-Dependent Density Functional Theory for Long-Range Charge-Transfer Excited States: The Zincbacteriochlorin-Bacteriochlorin and Bacteriochlorophyll-Spheroidene Complexes". In: *J. Am. Chem. Soc.* 126 (2004), pp. 4007–4016.

[67] A. Dreuw and M. Head-Gordon. "Single-Reference ab Initio Methods for the Calculation of Excited States of Large Molecules". In: *Chem. Rev.* 105 (2005), pp. 4009–4037.

[68] A. Einstein. "Die Grundlage der allgemeinen Relativitatstheorie." In: *Ann. der Physik* 49 (1916), pp. 769–822.

[69] A. Elangovan and J. Davies. "Rational Enhancement of Second-Order Nonlinearity: Bis-(4-methoxyphenyl)hetero-aryl-amino Donor-Based Chromophores: Design, Synthesis, and Electrooptic Activity". In: *J. Am. Chem. Soc* 130 (2008), pp. 10565–10575.

[70] D.L. Elder et al. "Matrix-Assisted Poling of Monolithic Bridge-Disubstituted Organic NLO Chromophores". In: *Chemistry of Materials* 26.2 (2014), pp. 872–874.

[71] T. Engel and P. Reid. *Physical Chemistry, 3rd Ed.* San Francisco, CA, USA: Pearson Ed., Inc., 2013.

[72] J.F. Federici et al. In: *Semicond. Sci. Technol.* 20 (2005), S266.

[73] K. Firestone. "Frequency-agile hyper-Rayleigh scattering studies of nonlinear optical chromophores". Thesis. 2005.

[74] K. A. Firestone et al. "Frequency-Agile Hyper-Rayleigh Scattering Studies of Electro-Optic Chromophores". In: *Proc. SPIE* 5395 (2005), 0P1.

[75] M. A. Firestone, M. A. Ratner, and T. J. Marks. "Electric Field Poling in Polymeric Nonlinear Optical Materials. Relaxation Dynamics, Model, and Experiment." In: *Macromolecules* 28 (1995), pp. 6296–6310.

[76] M. E. Foster and B. M. Wong. "Nonempirically Tuned Range-Separated DFT Accurately Predicts Both Fundamental and Excitation Gaps in DNA and RNA Nucleobases". In: *J. Chem. Theory Comput.* 8 (2012), pp. 2682–2687.

[77] M. J. Frisch et al. *Gaussian 09, Revision D.01.* Computer Program. 2013.

[78] A. Furube et al. "Effect of Aggregation on the Excited-State Electronic Structure of Perylene Studied by Transient Absorption Spectroscopy". In: *The Journal of Physical Chemistry A* 110.20 (2006), pp. 6465–6471.

[79] K. Garrett et al. "Optimum Exchange for Calculation of Excitation Energies and Hyperpolarizabilities of Organic Electro-optic Chromophores". In: *Journal of Chemical Theory and Computation* 10.9 (2014), pp. 3821–3831.

[80] A.J. Garza et al. "Can Gap Tuning Schemes of Long-Range Corrected Hybrid Functionals Improve the Description of Hyperpolarizabilities?" In: *The Journal of Physical Chemistry B* 119.3 (2015), pp. 1202–1212.

[81] A.J. Garza et al. "Can Short and Middle Range Hybrids Describe the Hyperpolarizabilities of Long-Range Charge Transfer Compounds?" In: *The Journal of Physical Chemistry A* 118.50 (2014), pp. 11787–11796.

[82] S. J. A. van Gisbergen, J. G. Snijders, and E. J. Baerends. "A density functional theory study of frequency dependent polarizabilities and Van der Waals dispersion coefficients for polyatomic molecules". In: *J. Chem. Phys.* 103 (1995).

[83] S. J. A. van Gisbergen, J. G. Snijders, and E. J. Baerends. "Accurate density functional calculations on frequency-dependent hyperpolarizabilities of small molecules". In: *J. Chem. Phys* 109 (1998).

[84] D.C. Graham et al. "Optimization and Basis-Set Dependence of a Restricted-Open-Shell Form of B2-PLYP Double-Hybrid Density Functional Theory". In: *J. Phys. Chem. A* 113 (2009), pp. 9861–9873.

[85] S. Grimme. "Semiempirical hybrid density functional with perturbative second-order correlation". In: *J. Chem. Phys.* 124 (2006), pp. 034108–16.

[86] S. Grimme, F. Neese, and T. Schwabe. "Analytic derivatives for perturbatively corrected "double hybrid" density functionals: Theory, implementation, and applications". In: *J. Chem. Phys.* 126 (2006), pp. 124115–15.

[87] C. A. Guido et al. "On the Metric of Charge Transfer Molecular Excitations: A Simple Chemical Descriptor". In: *J. Chem. Theory Comput.* 9 (2013), p. 3118.

[88] M. Guillame, E. Botek, and B. Champagne. "Theoretical investigations of the linear and second-order nonlinear susceptibilities of the 3-methyl-4-nitropyridine-1-oxyde (POM) crystal". In: *J. Chem. Phys.* 121 (2004), pp. 7390–7400.

[89] D.R. Hartree. In: *Proc. Cambridge Phil. Soc.* 24 (1928), p. 111.

[90] R. Haunschild et al. "Many-electron self-interaction and spin polarization errors in local hybrid density functionals". In: *J. Chem. Phys.* 133 (2010).

[91] F. Haverkort, A. Stradomska, and J. Knoester. "First-Principles Simulations of the Initial Phase of Self-Aggregation of a Cyanine Dye: Structure and Optical Spectra". In: *The Journal of Physical Chemistry B* 118.29 (2014), pp. 8877–8890.

[92] L. M. Hayden et al. "Second-order nonlinear optical measurements in guest-host and side-chain polymers." In: *Journal of Applied Physics* 68 (1990), p. 456.

[93] L.M. Hayden et al. In: *J. Polym. Sci. (B) Polym. Phys* 41 (2003), p. 2492.

[94] T.F. Heinz, W.K. Tom, and Y. R. Shen. "Determination of molecular orientation of monolayer adsorbates by optical second harmonic generation". In: *Phys. Rev. A* 28.3 (1983), p. 1883.

[95] H.H. Heinze, F. Della Sala, and A. Gorling. "Efficient methods to calculate dynamic hyperpolarizability tensors by time-dependent density-functional theory". In: *J. Chem. Phys.* 116 (2002), p. 9624.

[96] M. Henderson et al. "Can short-range hybrids describe long-range-dependent properties?" In: *J. Chem. Phys.* 131 (2009), p. 044108.

[97] T. M. Henderson et al. "The importance of middle-range Hartree-Fock-type exchange for hybrid density functionals". In: *J. Chem. Phys* 127 (2007).

[98] P. Hohenberg. "Inhomogeneous Electron Gas". In: *Phys. Rev.* 136 (1964), B864.

[99] P. Hohenberg and W. Kohn. "Inhomogeneous electron gas." In: *Phys. Rev.* 136 (1964), B864.

[100] N. Holmgaard List et al. "Relation between Nonlinear Optical Properties of Push-Pull Molecules and Metric of Charge Transfer Excitations". In: *Journal of Chemical Theory and Computation* 11.9 (2015), pp. 4182–4188.

[101] J. Huo, K. Liu, and X. Chen. "1x2 Precise Electro-Optic Switch In Periodically Poled Lithium Niobate". In: *Opt. Express* 18 (2010), p. 15603.

[102] H. Iikura et al. "Long-range correction scheme for generalized-gradient-approximation exchange functionals". In: *J. Chem. Phys.* 115 (2001), pp. 3540–44.

[103] R. Improta. "The excited states of p-stacked 9-methyladenine oligomers: a TD-DFT study in aqueous solution". In: *Phys. Chem. Chem. Phys.* 10 (2008), pp. 2656–2664.

[104] Cisco Systems Inc. *Cisco Visual Networking Index: Global Mobile Data Traffic Forecast Update, 2014-2019.* Accessed Nov. 9, 2015 from www.cisco.com. 2015.

[105] C. M. Isborn et al. "Comparison of Static First Hyperpolarizabilities Calculated with Various Quantum Mechanical Methods." In: *J. Phys. Chem. A.* 111 (2007).

[106] Tomasi J., Mennucci B., and Cammi R. "Quantum Mechanical Continuum Solvation Models". In: *Chem. Rev.* 105 (2005), p. 2999.

[107] D. Jacquemin, C. Adamo, and et al. "First hyperpolarizability of polymethineimine with long-range corrected functionals." In: *J. Chem. Phys.* 126 (2007).

[108] D. Jacquemin, B. Champagne, and C. Hattig. "Correlated Frequency-Dependent Electronic first Hyperpolarizability of Small Push-Pull Conjugated Chains". In: *Chem. Phys. Lett.* 319 (2000), p. 327.

[109] D. Jacquemin et al. "Extensive TD-DFT Benchmark: Singlet-Excited States of Organic Molecules". In: *J. Chem. Theory Comput.* 5 (2009), p. 2420.

[110] D. Jacquemin et al. "Performance of an Optimally Tuned Range-Separated Hybrid Functional for 0-0 Electronic Excitation Energies". In: *J. Chem. Theory Comput.* 10 (2014), p. 1677.

[111] D. Jacquemin et al. "TD-DFT Performance for the Visible Absorption Spectra of Organic Dyes: Conventional versus Long-Range Hybrids". In: *J. Chem. Theory Comput.* 4 (2008), p. 123.

[112] S.-H. Jang et al. In: *Chem. Mater.* 18 (2006), pp. 2982–2988.

[113] E.E. Jelley. In: *Nature* 138 (1936), p. 1009.

[114] F. Jensen. *Introduction to Computational Chemistry*. West Sussex, England: Wiley and Sons, 2006.

[115] W. Jin et al. "Benzocyclobutene barrier layer for suppressing conductance in nonlinear optical devices during electric field poling". In: *Appl. Phys. Lett.* 104 (2014), p. 243304.

[116] L. E. v.d.L. Johnson. "Multi-Scale Modeling of Organic Electro-Optic Materials". Thesis. 2012.

[117] L. E. v.d.L. Johnson, B. H. Robinson, and L. R. Dalton. "Optimizing Calculations of Electronic Excitations and Relative Hyperpolarizabilities of Electrooptic Chromophores". In: *Accounts of Chemical Research* 47 (2014), pp. 3258–3265.

[118] P. Johnston. Univ. of Washington, Seattle, WA. Unpublished work. 2011.

[119] P. Kaatz and D. P. Shelton. "Two-photon fluorescence cross-section measurements calibrated with hyper-Rayleigh scattering". In: *Opt. Commun.* 157 (1998), pp. 177–181.

[120] O. Kaliski. *Organics for Electro-optical Applications*. 2002.

[121] W. Kaminsky. *Report: Crystal Structure Report for Dalton-Reid, ID-DCDHF-Et*. Sample Submitted by Peter Johnston. 2011. URL: `cad4.cpac.washington.edu/structures`.

[122] W. Kaminsky. *Report: Crystal Structure Report for Dalton-Reid, ID-YLD124*. Sample Submitted by Peter Johnston. 2012. URL: `cad4.cpac.washington.edu/structures`.

[123] M. Kamiya, T. Tsuneda, and K. Hirao. "A density functional study of van der Waals interactions". In: *J. Chem. Phys* 117 (2002).

[124] M. Kamiya et al. "Nonlinear optical property calculations by the long-range-corrected coupled-perturbed Kohn-Sham method." In: *J. Chem. Phys.* 122 (2005).

[125] I. Kaplan. *Intermolecular interactions : Physical picture, computational methods, model potentials.* Hoboken, NJ: Wiley and Sons, Inc., 2006, pp. 39–41.

[126] S. Karna and A. Yeates. *Nonlinear Optical Materials: Theory and Modeling.* Washington, DC: American Chemical Society., 1996.

[127] A. Karolewski, L. Kronik, and S. Kummel. "Using optimally tuned range separated hybrid functionals in ground-state calculations: Consequences and caveats". In: *J. Chem. Phys* 138 (2013).

[128] A. Karolewski et al. "Communication: Tailoring the optical gap in light-harvesting molecules". In: *J. Chem. Phys.* 134 (2011).

[129] A. Karton et al. "Highly Accurate First-Principles Benchmark Data Sets for the Parametrization and Validation of Density Functional and Other Approximate Methods. Derivation of a Robust, Generally Applicable, Double-Hybrid Functional for Thermochemistry and Thermochemical Kinetics". In: *J. Phys. Chem. A* 112 (2008), pp. 12868–12886.

[130] T.H. Kim. *An Iterative Technique for Solving the N-electron Hamiltonian: The Hartree-Fock method.* Accessed: December 2012 via web.mit.edu/kimt/www/8.06/.

[131] T. Kinnibrugh et al. "Influence of isomerization on nonlinear optical properties of molecules." In: *J. Phys. Chem. B.* 110.27 (2006), pp. 13512–22.

[132] S. Kirstein and S. Daehne. "J-Aggregates of Amphiphilic Cyanine Dyes: Self-Organization of Artificial Light Harvesting Complexes". In: *Int. J. Photoenergy* 2006 (2006), p. 1.

[133] B. Kirtman et al. "Calculation of electric dipole (hyper)polarizabilities by long-range-correction scheme in density functional theory: a systematic assessment for polydiacetylene and polybutatriene oligomers." In: *J. Chem. Phys.* 128.11 (2008), p. 114108.

[134] A.V. Kityk. "Absorption and Fluorescence Spectra of Heterocyclic Isomers from Long-Range-Corrected Density Functional Theory in Polarizable Continuum Approach." In: *J. Phys. Chem. A* 116 (2012).

[135] J. Klimes and A. Michaelides. "Perspective: Advances and challenges in treating van der Waals dispersion forces in density functional theory". In: *J. Chem. Phys.* 137 (2012), p. 120901.

[136] M.J. Kobrinsky et al. In: *Intel Technol. J.* 8 (2004), p. 129.

[137] W. Koch and M. C. Holthausen. *A Chemist's Guide to Density Functional Theory (2nd Ed.).* Weinheim: Wiley-VCH, 2001.

[138] W. Kohn and L. J. Sham. "Self-Consistent Equations Including Exchange and Correlation Effects". In: *Phys. Rev.* 140 (1965), A1133.

[139] L. Kollros. "Albert Einstein en Suisse Souvenirs." In: *Helv. Phys. Acta. Supp.* 4 (1956), pp. 271–281.

[140] T. Koopmans. In: *Physica (Elsevier)* 1.1-6 (1934), pp. 104–113.

[141] D. Korn. "Silicon-Organic Hybrid (SOH) IQ Modulator Using the Linear Electro-Optic Effect for Transmitting 16QAM at 112 Gbit/s". In: *Opt. Express* 12 (2013), pp. 13219–13227.

[142] K. Kornobis et al. "Electronically Excited States of Vitamin B12: Benchmark Calculations Including Time-Dependent Density Functional Theory and Correlated ab Initio Methods". In: *J. Phys. Chem. A* 115 (2011).

[143] T. Körzdörfer et al. "Long-range corrected hybrid functionals for pi-conjugated systems: Dependence of the range-separation parameter on conjugation length". In: *J. Chem. Phys* 135 (2011).

[144] I. Kosilkin. "Organic Materials for Electro-Optic and Optoelectronic Applications: Understanding Structure - Property Relationships". Thesis. 2012.

[145] L. Kronik et al. "Excitation Gaps of Finite-Sized Systems from Optimally Tuned Range-Separated Hybrid Functionals". In: *J. Chem. Theory Comput.* 8 (2012), pp. 1515–1531.

[146] N. Kuritz et al. "Charge-Transfer-Like $\pi- > \pi^*$ Excitations in Time-Dependent Density Functional Theory: A Conundrum and Its Solution". In: *Journal of Chemical Theory and Computation* 7.8 (2011), pp. 2408–2415.

[147] M. G. Kuzyk et al. "Second-Order Nonlinear-Optical Tensor Properties of Poled Films under Stress". In: *J. Opt. Soc. Am. B* 6 (1989), p. 742.

[148] Jonathan Lansey. *Matlab Central File Exchange: Beautiful and distinguishable line colors + colormap, linspecer.m.* July 2015. URL: `www . mathworks . com / matlabcentral/fileexchange`.

[149] M. Lauermann et al. "16QAM Silicon-Organic Hybrid (SOH) Modulator Operating with 0.6 Vpi and 19 fJ/bit at 112 Gbit/s". In: *IEEE J. Lightwave Technol.* (2014).

[150] A. Laurent and D. Jacquemin. "TD-DFT Benchmarks: A Review". In: *Int. J. Quantum Chem.* 113 (2013), p. 2019.

[151] A. Leach. *Molecular Modelling: Principles and Applications.* Harlow (UK): Prentice Hall, 2001.

[152] A. Lee and S. Colwell. "The determination of hyperpolarizabilities using density functional theory with nonlocal functionals". In: *The Journal of Chemical Physics* 101 (1994), p. 9704.

[153] C. Lee, W. Yang, and R.G. Parr. "Development of the Colle-Salvetti correlation-energy formula into a functional of the electron density". In: *Phys. Rev. B* 37 (1988), pp. 785–789.

[154] M. Lee et al. "Broadband Modulation of Light by Using an Electro-Optic Polymer." In: *Science* 298 (2002), pp. 1401–1403.

[155] I. Levine. *Quantum chemistry (6th ed.)* Upper Saddle River, N.J.: Pearson Prentice Hall., 2009.

[156] H. Li. "Nonlinear Optical Properties of Potential Sensitive Dyes". Thesis. 2007.

[157] Y. Liao. Univ. of Central Florida, Orlando, FL. Unpublished work. 2008.

[158] Y. Liao et al. "Systematic study of the structure-property relationship of a series of ferrocenyl nonlinear optical chromophores". In: *J. Am. Chem. Soc.* 127 (2005), p. 2758.

[159] S.-T. Lin and C.-S. Hsieh. "Triple-Wavelength Nd-Laser System By Cascaded Electro-Optic Periodically Poled Lithium Niobate Bragg Modulator". In: *Opt. Express* 20 (2012), p. 29659.

[160] T.C. Lin et al. "Molecular Origins of the High-Performance Nonlinear Optical Susceptibility in a Phenolic Polyene Chromophore: Electron Density Distributions, Hydrogen Bonding, and ab Initio Calculations". In: *The Journal of Physical Chemistry C* 117.18 (2013), pp. 9416–9430.

[161] D. Lingerfelt et al. "Dynamical Investigations of Inhomogeneous Vibrational Broadening in Diluted Magnetic Semiconductor Nanocrystals". In: *The Journal of Physical Chemistry C* 118.6 (2014), pp. 3266–3273.

[162] A. Liu et al. "A high-speed silicon optical modulator based on a metal-oxide-semiconductor capacitor." In: *Nature* 427 (2004), pp. 615–618.

[163] E. Livshits and R. Baer. In: *Phys. Chem. Chem. Phys.* 9 (2007), p. 2932.

[164] K. Lopata et al. "Excited-State Studies of Polyacenes: A Comparative Picture Using EOMCCSD, CR-EOMCCSD(T), Range-Separated (LR/RT)-TDDFT, TD-PM3, and TD-ZINDO". In: *Journal of Chemical Theory and Computation* 7.11 (2011), pp. 3686–3693.

[165] H. Lu et al. "6-Micron Interaction Length Electro-Optic Modulation Based On Lithium Niobate Photonic Crystal Cavity". In: *Opt. Express* 20 (2012), p. 20884.

[166] A. K. Manna et al. "Calculating High Energy Charge Transfer States Using Optimally Tuned Range-Separated Hybrid Functionals". In: *J. Chem. Theory Comput.* 11 (2015), pp. 1110–1117.

[167] S. Mao et al. "Progress toward Device-Quality Second-Order Nonlinear Optical Materials. 1. Influence of Composition and Processing Conditions on Nonlinearity, Temporal Stability, and Optical Loss". In: *Chem. Mater.* 10 (1998).

[168] S. R. Marder. "Organic nonlinear optical materials: where we have been and where we are going". In: *Chem. Commun.* (2006), pp. 131–134.

[169] S. Marder et al. "Relation Between Bond-Length Alternation and Second Electronic Hyperpolarizability of Conjugated Organic Molecules." In: *Science* 261 (1993), pp. 186–189.

[170] B. McCarthy et al. "Charge Transfer or J-Coupling? Assignment of an Unexpected Red-Shifted Absorption Band in a Naphthalenediimide-Based Metal-Organic Framework". In: *J. Phys. Chem. Lett.* 4 (2013), pp. 453–458.

[171] R. McWeeny. "Perturbation Theory for Fock-Dirac Density Matrix". In: *Phys. Rev.* 126 (1962), p. 1028.

[172] R. McWeeny. "Some recent advances in density matrix theory". In: *Rev. Mod. Phys.* 32 (1960), pp. 335–369.

[173] F. Michelotti et al. In: *Appl. Phys. Lett.* 67 (1995), pp. 2765–2767.

[174] P. Millie, F. Momicchioli, and D. Vanossi. "Exciton Effects in the Dimer and Higher Aggregates of a Simple Merocyanine Dye. A CS INDO CI Based Theoretical Study". In: *The Journal of Physical Chemistry B* 104.41 (2000), pp. 9621–9629.

[175] C. Moller and M. S. Plesset. "Note on approximation treatment for many-electron systems." In: *Phys. Rev.* 46 (1934), p. 618.

[176] P. Mori-Sanchez, A. J. Cohen, and W. Yang. "Localization and Delocalization Errors in Density Functional Theory and Implications for Band-Gap Prediction". In: *Phys. Rev. Lett.* 100 (2008).

[177] Metropolis N. et al. In: *J. Chem. Phys.* 21 (1953), p. 1087.

[178] M. et al. Nakano. "Localization and Delocalization Errors in Density Functional Theory and Implications for Band-Gap Prediction". In: *Chem. Phys. Lett.* 454 (2008), pp. 97–104.

[179] H. Naundorf. "Short Introduction to Quantum Chemistry Methods." In: (2005). Institute of Physical and Theoretical Chemistry, Freie Universitat Berlin.

[180] Y. Okuno, S. Yokoyama, and S. Mashiko. "Interaction between Monomeric Units of Donor-Acceptor functionalized Azobenzene Dendrimers: Effects on Macroscopic Configuration and First Hyperpolarizability". In: *J. Phys. Chem. B.* 105 (2001), pp. 2163–2169.

[181] D. Ostrowski et al. "The Effects of Aggregation on Electronic and Optical Properties of Oligothiophene Particles". In: *ACS Nano* 6.6 (2012), pp. 5507–5513.

[182] J. L. Oudar. "Optical nonlinearities of conjugated molecules. Stilbene derivatives and highly polar aromatic compounds." In: *J. Chem. Phys.* 67.446 (1977).

[183] J. L. Oudar and D. S. Chemla. "Hyperpolarizabilities of the Nitroanilines and their Relations to the Excited State Dipole Moment". In: *J. Chem. Phys.* 66 (1977), p. 2664.

[184] R. Palmer. "Low Power Mach-Zehnder Modulator in Silicon-Organic Hybrid Technology". In: *IEEE Photonics Technol. Lett.* 25 (2013), pp. 1226–1229.

[185] R. Palmer et al. "High-Speed, Low Drive-Voltage Silicon-Organic Hybrid Modulator Based on a Binary-Chromophore Electro-Optic Material". In: *IEEE Photonics Technol. Lett.* (2014).

[186] F. Pan et al. "Nature of Low-Lying Excited States in H-Aggregated Perylene Bisimide Dyes: Results of TD-LRC-DFT and the Mixed Exciton Model". In: *J. Phys. Chem. B.* 113 (2009), pp. 14581–14587.

[187] L. Pandey et al. "Lowest excited states and optical absorption spectra of donor-acceptor copolymers for organic photovoltaics: a new picture emerging from tuned long-range corrected density functionals". In: *Phys. Chem. Chem. Phys.* (2012). DOI: 10.1039/c2cp41724c.

[188] M. Paniccia, V. Krutul, and S. Koehl. *White Paper: Introducing Intel's Advances in Silicon Photonics*. 2004.

[189] G. Pescitelli, L. Di Bari, and N. Berova. "Application of electronic circular dichroism in the study of supramolecular systems". In: *Chem. Soc. Rev.* 43 (2014), p. 5211.

[190] P. Petelenz and B. Pac. "Is Dipole Moment a Valid Descriptor of Excited State's Charge-Transfer Character?" In: *Journal of the American Chemical Society* 135.46 (2013), pp. 17379–17386.

[191] A. D. Polyanin and V. F. Zaitsev. *Handbook of Nonlinear Partial Differential Equations*. 2000 N.W. Corporate Blvd., Boca Raton, Florida 33431: Chapman and Hall/CRC Press, 2004, pp. 779–782.

[192] Dalton L. R. et al. "Theory-inspired nano-engineering of photonic and electronic materials: Noncentrosymmetric charge-transfer electro-optic materials". In: *Solid-State Electron.* 51 (2007), p. 1263.

[193] B. Robinson and L.R. Dalton. "Monte Carlo Statistical Mechanical Simulations of the Competition of Intermolecular Electrostatic and Poling-Field Interactions in Defining Macroscopic Electro-Optic Activity for Organic Chromophore/Polymer Materials". In: *J. Phys. Chem. A* 104 (2000), pp. 4785–4795.

[194] B.H. Robinson, L.E. Johnson, and B.E. Eichinger. "Relation of System Dimensionality and Order Parameters". In: *J. Phys. Chem. B* 119.7 (2015), pp. 3205–3212.

[195] M.A. Rohrdanz and J.M. Herbert. "Simultaneous benchmarking of ground- and excited-state properties with long-range-corrected density functional theory." In: *J. Chem. Phys.* 129 (2008).

[196] M.A. Rohrdanz, K.M. Martins, and J.M. Herbert. "A long-range-corrected density functional that performs well for both ground-state properties and time-dependent density functional theory excitation energies, including charge-transfer excited states." In: *J. Chem. Phys.* 130 (2009).

[197] Y. Salamin et al. "Direct Conversion of Free Space Millimeter Waves to Optical Domain by Plasmonic Modulator Antenna". In: *Nano Letters* (Article ASAP).

[198] T. Saleh. *Fundamentals of Photonics. (1st Ed.)* New York, New York: Wiley-Interscience Publications., 1991.

[199] P. Salek et al. In: *J. Chem. Phys.* 117 (2002).

[200] F. Santoro et al. In: *Phys. Chem. Chem. Phys.* 12 (2010), pp. 4934–4948.

[201] M. Sarovar et al. "Ab-initio calculation of molecular aggregation effects: A Coumarin-343 case study". In: *J. Phys. Chem. B* 117 (2013), p. 11072.

[202] T. Sato, T. Tsuneda, and K. Hirao. "Long range corrected density functional study on weakly bound systems: Balanced descriptions of various types of molecular interactions". In: *J. Chem. Phys* 126 (2007).

[203] G. Scheibe. In: *Angew. Chem.* 49 (1936), p. 563.

[204] A. Schneider, M. Stillhart, and P. Gunter. *Highly Efficient Generation of THz Pulses Using Laser Pulses at Telecommunication Wavelengths*. 2006.

[205] A. Schneider et al. "Generation of terahertz pulses through optical rectification in organic DAST crystals: Theory and experiment". In: *J. Opt. Soc. Am. B* 23 (2006), p. 1822.

[206] L.I. Sedov. *Similarity and Dimensional Methods in Mechanics*. 2000 N.W. Corporate Blvd., Boca Raton, Florida 33431: CRC Press, Inc., 2008.

[207] H. Sekino et al. "Polarizability and second hyperpolarizability evaluation of long molecules by the density functional theory with long range correction". In: *J. Chem. Phys* 126 (2007).

[208] R. Serway and John W. Jewett. *Physics for scientists and engineers. 7th Ed.* Belmont, CA: Thomson-Brooks/Cole, 2008.

[209] Y. R. Shen. In: *Ann. Rev. Mater. Sci.* 16 (1986), pp. 69–86.

[210] Y. R. Shen. In: *Annu. Rev. Phys. Chem.* 40 (1989), pp. 327–350.

[211] Y. R. Shen. *The Principles of Nonlinear Optics*. New York, New York: Wiley, Inc., 1984.

[212] D. Silva et al. "Self Aggregation and Optical Absorption of Stilbazolium Merocyanine in Chloroform". In: *J. Phys. Chem. B* 118 (2014).

[213] K. D. Singer, J. E. Sohn, and S. J. Lalama. "Second harmonic generation in poled polymer films." In: *Applied Physics Letters* 49.5 (1986), p. 248.

[214] A.M. Sinyukov et al. In: *Appl. Phys. Lett.* 85 (2004), p. 5827.

[215] D. Skoog, J. Holler, and S. Crouch. *Principles of Instrumental Analysis, 6th Ed.* Belmont, CA: Thomson Brooks/Cole, 2007.

[216] S. Sok et al. "Solvent Induced Shift of the Lowest Singlet pi to pi* Charge-Transfer Excited State of p Nitroaniline in Water: An Application of the TDDFT/EFP1 Method". In: *The Journal of Physical Chemistry A* 115.35 (2011), pp. 9801–9809.

[217] J. W. Song et al. "Long range corrected density functional calculations of chemical reactions: Redetermination of parameter". In: *J. Chem. Phys* 126 (2007).

[218] J. W. Song et al. "Nonlinear optical property calculations of polyynes with long range corrected hybrid exchange correlation functionals". In: *J. Chem. Phys* 129 (2008).

[219] T. Stein, L. Kronik, and R. Baer. "Prediction of charge transfer excitations in coumarin based dyes using a range separated functional tuned from first principles". In: *J. Chem. Phys.* 131 (2009).

[220] P. J. Stephens and N. Harada. *Plotting UV-vis Spectra from oscillator and dipole strengths*. Gaussian Technical Notes. 2014. URL: `www.gaussian.com/g_whitepap/tn_uvvisplot.htm`.

[221] P.A. Sullivan and L.R. Dalton. "Theory Inspired Development of Organic Electro optic Materials". In: *Accounts of Chemical Research* 43.1 (2010), pp. 10–18.

[222] P. Sullivan et al. "Modeling the Optical Behavior of Complex Organic Media: From Molecules to Materials". In: *J. Phys. Chem. B* 113 (2009).

[223] S.S. Sun et al. "1,3-Bis(dicyanomethylidene)indane-Based Second-Order NLO Materials". In: *Chemistry of Materials* 8.11 (1996), pp. 2539–2541.

[224] K. Y. Suponitsky, Y. Liao, and A. E. Masunov. "Electronic Hyperpolarizabilities for Donor Acceptor Molecules with Long Conjugated Bridges: Calculations versus Experiment." In: *J. Phys. Chem. A.* 113 (2009).

[225] K. Y. Suponitsky, S. Tafur, and A. E. Masunov. "Applicability of Hybrid Density Functional Theory Methods to Calculation of Molecular Hyperpolarizability". In: *J. Chem. Phys.* 129 (2008), p. 044109.

[226] K. Suponitsky and A. Masunov. "Supramolecular step in design of nonlinear optical materials: Effect of π...π stacking aggregation on hyperpolarizability". In: *J. Chem. Phys.* 139 (2013), p. 094310.

[227] A. Szabo and N. Ostlund. *Modern Quantum Chemistry*. New York: McGraw-Hill, 1982.

[228] A. Tarnopolsky et al. "Double-Hybrid Functionals for Thermochemical Kinetics". In: *J. Phys. Chem. A* 112 (2008), pp. 3–8.

[229] Y. Tawada et al. "A long range corrected time-dependent density functional theory." In: *J. Chem. Phys.* 120 (2004).

[230] C. C. Teng and H. T. Man. "Simple reflection technique for measuring the electro-optic coefficient of poled polymers." In: *Applied Physics Letters* 56 (1990), p. 1734.

[231] A. Teshome et al. "Strategies for optimising the second-order nonlinear optical response in zwitterionic merocyanine dyes". In: *Opt. Mat.* 31 (2009).

[232] A. Tillack. "Electro-Optic Material Design Criteria Derived from Condensed Matter Simulations Using the Level-of-Detail Coarse-Graining Approach." Thesis. 2015.

[233] A. Tokmakoff. *5.74 Introductory Quantum Mechanics II, Spring 2009. (Massachusetts Institute of Technology: MIT OpenCourseWare)*. Accessed: January 2011 via www.ocw.mit.edu; License: Creative Commons BY-NC-SA.

[234] F. Trager. *Springer Handbook of Lasers and Optics, 2nd Ed.* Berlin ; New York: Springer Science and Business Media, 2012.

[235] T. Tsuneda et al. "On Koopmans' theorem in density functional theory". In: *J. Chem. Phys* 133 (2010).

[236] Pereverzev Y. V. et al. "Guest-host cooperativity in organic materials greatly enhances the nonlinear optical response". In: *J. Phys. Chem. C* 112 (2008), p. 4355.

[237] R. Aaron Vogt, Thomas G. Gray, and Carlos E. Crespo-Hernandez. "Subpicosecond Intersystem Crossing in Mono- and Di(organophosphine)gold(I) Naphthalene Derivatives in Solution". In: *Journal of the American Chemical Society* 134.36 (2012), pp. 14808–14817.

[238] O. A. Vydrov and G. E. Scuseria. "Assessment of a long range corrected hybrid functional". In: *J. Chem. Phys.* 125 (2006).

[239] O. A. Vydrov, G. E. Scuseria, and J. P. Perdew. "Tests of functionals for systems with fractional electron number". In: *J. Chem. Phys.* 126 (2007).

[240] O. A. Vydrov et al. "Importance of short-range versus long-range Hartree Fock exchange for the performance of hybrid density functionals". In: *J. Chem. Phys.* 125 (2006).

[241] A Warshel and M. Levitt. "Theoretical studies of enzymic reactions: Dielectric, electrostatic and steric stabilization of the carbonium ion in the reaction of lysozyme". In: *Journal of Molecular Biology* 103.2 (1976), pp. 227–249.

[242] C. Weimann et al. "Silicon-Organic Hybrid (SOH) Frequency Comb Sources for Terabit/s Data Transimission". In: *Opt. Express* 22.3 (2014), pp. 3629–3647.

[243] E.W. Weisstein. *Gaussian Function.* From MathWorld–A Wolfram Web Resource; Accessed via www.mathworld.wolfram.com/GaussianFunction.html. 2015.

[244] A. Willetts et al. In: *J. Chem. Phys.* 97.10 (1992), pp. 7590–7599.

[245] B.M. Wong, M. Piacenzab, and F.D. Salab. "Absorption and fluorescence properties of oligothiophene biomarkers from long-range-corrected time-dependent density functional theory." In: *Phys. Chem. Chem. Phys.* 11 (2009).

[246] O. Worz and G. Scheibe. In: *Z. Naturforsch.* 146 (1969), p. 381.

[247] K. Wu, J. Snijders, and C. Lin. "Reinvestigation of Hydrogen Bond Effects on the Polarizability an Hyperpolarizability of Urea Molecular Clusters". In: *J. Chem. Phys. B.* 106 (2002), pp. 8954–8958.

[248] F. Wurthner, T. E. Kaiser, and C. R. Saha-Möller. "J-Aggregates: From Serendipitous Discovery to Supramolecular Engineering of Functional Dye Materials". In: *Angew. Chem., Int. Ed.* 50 (2011), p. 3376.

[249] T. Yanai, D.P. Tew, and N.C. Handy. "A new hybrid exchange-correlation functional using the Coulomb-attenuating method (CAM-B3LYP)." In: *Chem. Phys. Lett.* 393.51 (2004).

[250] T. Yasukawa, T. Kimura, and M. Uda. "A AM1 Study of the effects of intermolecular interactions on hyperpolarizabilities of p-nitroanilines". In: *Chem. Phys. Lett.* 169.3 (1990).

[251] R. Zalesny et al. "Toward Fully Nonempirical Simulations of Optical Band Shapes of Molecules in Solution: A Case Study of Heterocyclic Ketoimine Difluoroborates". In: *The Journal of Physical Chemistry A* 119.21 (2015), pp. 5145–5152.

[252] F. Zernike and J. E. Midwinter. *Applied Nonlinear Optics.* Mineola, NY: Dover Publications, Inc., 1973.

[253] X.-F. Zhang, Q. Xi, and J. Zhao. "Fluorescent and triplet state photoactive J-type phthalocyanine nano assemblies: controlled formation and photosensitizing properties". In: *J. Mater. Chem.* 20 (2010), p. 6726.

[254] X. Zhou et al. "One-Dimensional Model Of A Plasma-Electrode Optical Switch Driven By One-Pulse Process". In: *Opt. Express* 14 (2006), p. 2880.

[255] J. Zyss and D.S. Chemla. "Quadratic Nonlinear Optics and Optimization of the Second-Order Nonlinear Optical Response of Molecular Crystals". In: *Nonlinear Optical Properties of Organic Molecules and Crystals (Vol 1).* Ed. by J. Zyss and D.S. Chemla. 1987. Chap. II-1, pp. 23–193.

[256] J. Zyss and J.L. Oudar. "Relations Between Microscopic And Macroscopic Lowest-Order Optical Nonlinearities Of Molecular-Crystals With One- Dimensional Or Two-Dimensional Units." In: *Physical Review A* 26.4 (1982), pp. 2028–2048.